Non linear dynamics in semiconductor lasers with optical feedback

Massimo Giudici

NON LINEAR DYNAMICS OF A SEMICONDUCTOR LASER WITH OPTICAL FEEDBACK

By

Massimo Giudici

Acknowledgements

I am grateful to Prof. Jorge R. Tredicce, my supervisor, for having convinced me to start a research activity. His optimism is probably the main reason that, three years ago, pushed me to leave a permanent position at Pirelli^{TM} Cables S.p.A for starting a Ph.D thesis. During my research project he has always created the best conditions for me both to perform the experimental work and to improve my understanding of non-linear dynamics and laser physics. I want to acknowledge Prof. Salvador Balle for his continuous and huge help during all my thesis and, especially, in the last year. The discussions with him have been fundamental for my understanding of semiconductor laser physics and his suggestions improved a lot this thesis. I am grateful to Prof. Maxi San Miguel for having invited me to teach at his university, solving the problem of funding my last year of thesis. I acknowledge Guillaume Huyet for his important contribution to my thesis project and I wish him a successful career in physics, as he deserves for his skill and ability. I acknowledge Gianni Giacomelli for his visits at INLN, always very fruitful both scientifically and gastronomically (sua la divulgazione transalpina della impagabile Brikka). I also enjoyed a lot the visit of Prof. Gabriel Mindlin who introduced me to the dynamical modeling of a time series. Thorsten Ackemann and Charlie Green have collaborated with me in different periods to the realization of the work. I would like to acknowledge them for their help and for what I learnt from them. Stephane Barland helped me a lot in the revision of this thesis. I am very grateful to Prof. Jorge Rocca and Prof. Carmen Menoni for their invitation to the Colorado State University: I really had great time there! In particular, I strongly acknowledge the help of Georgiy Vaschenko, whose skills on streak cameras allowed for one of the most important result of this thesis. I also acknowledge L. Giuggioli, S. Hegarthy, J. Ensenat, L. Furfaro for their contribution to some experimental parts of this thesis. I thank G. Lippi, N. Abraham, H. Grassi, M. Clerc, M. Argentina, N. Dokhane, C. Mirasso, J. Mulet, M. Santagiustina, M. Zimmermann, H. Solari, A. Yacomotti, E. Hernandez, P. Colet, C. Massoler and O. Piro for the helpful discussions.

I thank all the persons that contributed directly or indirectly to the realization

of this work. In particular, I acknowledge Roberta Proserpio, my girlfriend, for having stood me even when I was almost reduced to a computer part not separable from the keyboard, and my mother, whose contribution has been a necessary condition for the realization of this work.

The first two years of this thesis were funded by the TMR grant N. ERB4001GT of the European Community.

Nice, France — Massimo Giudici
September, 1999

Table of Contents

Introduction

Semiconductor lasers are the most important invention in the development of the opto-electronics technologies. The main reason for the success of these devices is that they achieve laser operation with sub-millimeter sizes, requiring a current supply of only a few milliamperes for emitting CW at ambient temperature (Ref. [1]). The manufacturing process is low cost and it guarantees highly reliable and easy-to-handle devices, since no alignment or setting procedure is required. The semiconductor media characteristics allow for very fast response to electrical modulation (several Gbytes/sec); hence the successful application of semiconductor laser in telecommunication industry. Moreover, by changing the semiconductor elements or the doping levels of the active medium it is possible to produce laser devices in a very wide range of emission wavelengths (400 nm - 1600 nm) covering, in this way, the optical fiber windows of low absorption (840 nm, 1150 nm, 1550 nm) and providing sources for spectral physics applications (optical pumping of Er-doped fibers at 980 nm, tunable narrow-linewidth sources for spectral characterization). For all these reasons, the technological impact of semiconductor lasers in opto-electronics has been impressive. Nowadays, in all-day life, this source has been largely implemented in the widest variety of warehouses (compact-disk players) and professional equipment (from dental surgery applications to industrial cutting or welding laser machines).

In this thesis we describe the dynamical behavior of the semiconductor laser when part of the light emitted is re-injected back into the laser. This experimental

configuration is very interesting both from the technological/applicational perspective, and from the laser dynamics investigation point of view. In fact, optical feedback is unavoidable whenever a reflective surface is located in front of the laser, i.e whenever the laser light has to be coupled into an optical fiber or used onto reflective substrates (compact-disks, for example). If the laser performance (linewidth, spectral purity, stability, modulation bandwidth) is affected by the optical feedback, the laser may become useless for many applications. Hence the need of describing and understanding the effects of the optical feedback on the laser behavior. The technological impact of optical feedback on the semiconductor laser applications is testified by the huge amount of literature developed on this subject in the last twenty years.

The effect of delayed feedback on dynamical systems has been studied in different branches of science such as physics (Ref. [2]), chemistry (Ref. [3]) and other fields (Ref. [4]). These systems, which are commonly encountered in nature, often show a complex behavior and they challenge many intuitive and theoretical descriptions. Feedback was originally perceived as a stabilizing factor. It was introduced in several types of systems (Ref. [5]), but in many cases the result was strong fluctuations of the variables. A laser system with feedback is a infinite dimensional dynamical system. The system may potentially exhibit very rich dynamics (possible presence of chaotic attractors) and this complexity makes such systems very interesting for general studies of non-linear dynamics.

Previous works show that the feedback improves the laser performance for a small range of parameters values, stabilizing the output and reducing the optical linewidth (Ref. [6]). On the other hand, for the widest part of parameter-space, optical feedback affects detrimentally the coherence of the laser emission (Refs. [7, 8]). In particular, for a moderate level of feedback, as the injection current is increased, the laser output becomes unstable and displays sudden power drops

followed by a slower recovery stage (Refs. [9, 10, 11]). The characteristic rate of such fluctuations ($10 - 100\ MHz$) is much smaller than the other typical frequencies of the system (relaxation oscillations, for example), hence the name *Low-Frequency Fluctuations* (LFF). As LFF appear in the intensity output the laser linewidth broadens up to tens of GHz and the coherence of the laser beam is strongly reduced (*Coherence-Collapse* as named in Refs. [8, 12, 13, 14]). LFF are characteristic of semiconductor lasers, including conventional edge-emitters and distributed-feedback semiconductor lasers (DFB), see Refs. [7, 15]. The fact that LFF do not appear in other kinds of lasers under optical feedback is attributed to the strong amplitude-phase coupling that exists in semiconductor lasers due to the linewidth enhancement factor (α) (Refs. [16, 17, 18, 19]).

Low-Frequency Fluctuations are the central issue of this dissertation. In spite of the fact that this phenomenon has been extensively studied and a huge literature exists on it, the discussion about the origin of LFF is still open. We have identified the bifurcation that is at the origin of this phenomenon and we have characterized the physical mechanism that induces this instability.

This thesis is organized as follows: in the first chapter we introduce some concepts on laser dynamics and on semiconductor laser physics as a theoretical background of our analysis on the LFF-instability. We present the Maxwell-Bloch equations for a two level laser and the instabilities described by this model. Semiconductor laser physics is introduced in the second part of this chapter underlining the difference with the two-level laser. We describe the *effective two-level model* for semiconductor media, leading to a realistic expression for the semiconductor susceptibility (Ref. [20]). This allows for writing a semiconductor laser model where the coherent coupling between the light and the active medium is taken into account, hence overcoming the approximation of the laser rate-equations. The optical cavity imposes the boundary conditions in the laser equations allowing

for a multi-mode description of the laser dynamics (Ref. [21]).

In the second chapter we describe the experimental results obtained in edge-emitting semiconductor laser. We start describing the solitary laser characteristics and the general parameter-space properties of the laser with feedback system (section one and two), locating the parameter regions explored in our experiments. The phenomenology of LFF is described in section three. Then, we report on the experimental characterization of the bifurcation at the origin of LFF (section four). For the first time, experimental evidence of *excitability* in an optical system is given. Moreover, the role of noise in the system is explored in detail leading to the first experimental observation of *Coherence Resonance*. Finally, on the base of the dynamical ingredients identified, we depict the simplest dynamical model able to describe the LFF-instability. Numerical simulations of this model show good agreement with the experimentally observed statistical properties of LFF, thus confirming the correctness of our interpretation. The physical mechanism at the origin of LFF is explored in section five. By means of time-resolved optical spectra obtained with very high time-resolution (streak camera measurements) we have been able to identify the role of the laser modes in the LFF-instability. In section six we compare our experimental evidences to the theoretical models existing in the literature. We conclude this chapter describing the results of the experiment with frequency-selective feedback.

In the third chapter we report on the experimental results obtained in Vertical-Cavity Surface-Emitting ($VCSEL's$) laser with optical feedback. Dynamics involving the two orthogonal linear polarizations components appears to be the dominant feature in this system. A theoretical model able to describe qualitatively the polarization behavior is presented.

In the Appendix A we describe the equipment used in the experiments and some technical aspect of the semiconductor laser laboratory. Finally, in Appendix

B, we review the most important experimental results presented in the literature concerning the statistical properties of the LFF time-intervals. This review allows for a comparison with our results of Chap. II

Chapter 1

Laser Physics and Instabilities

1.1 The Two-Level laser equations

This section is intended as an introduction to two-level laser physics and instabilities following the vast literature that developed this issue. Laser instability has been a field largely explored in the last twenty years and an exhaustive list of references on this subject would be necessarily very long. Here we can limit ourselves to reference those books which were our personal entry-point to the problem and on which this chapter is based (Refs. [22, 23, 24, 25, 26, 27]). The references listed in these books represent a very useful guide to navigate in the laser physics literature.

The importance of laser instabilities was first revealed in the early 1960's by a number of Russian physicist such as Uspensky, Fain and Khanin, Oraevsky and by Haken in Stuttgart. In 1975 Haken discovered the analogy between the laser equation and Lorenz equations for convective hydrodynamical system. The possibility of exploring chaotic dynamics in laser systems triggered a huge interest in the field of laser instabilities. Those behaviors, that were considered "annoying" from the point of view of laser engineering since they were affecting the *CW* performance of the laser, started to be investigated and classified. Instabilities mean a spontaneous break of temporal and spatial symmetry, since a

steadily driven laser starts to develop spatio-temporal fluctuations in its output. Changing the control parameters of the laser we may obtain a very rich variety of unstable behaviors. The laser parameter-space is a rich source of interest for non-linear dynamics. Non-linear dynamics provides the instruments to analyze the behavior of a non-stable dynamical system (Refs. [28, 29]). When, changing the control parameters, a dynamical system changes its spatio-temporal behavior, non-linear dynamics says that a bifurcation has occurred in the system. The identification of the type of bifurcation provides all the information required to describe the dynamical behavior of the system in the bifurcation neighborhood. In fact, the behavior types of any system when it bifurcates or, alternatively, the ways an instability develops, could be described by few very general equations called *normal-forms*. The laser dynamics investigation is very useful both for laser physics both for non-linear dynamics (Ref. [30]). Laser systems are real dynamical systems where instabilities develops with time-scale in general smaller than 10^{-3} s. Such fast time-scales make the experimental application of the non-linear dynamics instruments much easier in lasers than in other dynamical systems previously explored, like chemical systems or fluids. On the other hand the identification of the bifurcation offers valuable clues on modeling laser behavior and, by consequence, on internal mechanism of laser action.

The first paragraph is dedicated to the description of the operating principle on which a laser is based. The second treats the light-matter interaction in the Active Medium deriving the Maxwell-Bloch (or " Laser-Lorenz") equations. The boundary conditions of these equations are imposed by the optical cavity, considered in the third paragraph. Thus we obtain a set of equations describing the two-level laser. We look for the stationary solutions of these equations and, by performing a stability analysis, we analyze the instabilities predicted by this model.

1.1.1 Operating principles

A laser is essentially an oscillator operating at optical frequencies. It is composed by three basic ingredients: i)An Active Medium that, interacting with the electromagnetic field, provides the mechanism for the amplification of radiation, ii)An Optical Cavity that provides the positive feedback loop for the radiation, iii)A pumping mechanism that provides the energy for compensating the radiation losses due both to internal mechanisms and to the emission of radiation.

The "heart" of the laser is the Active Medium. In the interaction between light and matter there are three main processes that may occur: *Spontaneous emission*, *Stimulated Emission* and *Absorption*. Spontaneous emission implies the spontaneous decay of an electron from an excited state to a lower one, and we define as A_{21} its probability per unit of time. According to quantum mechanics, the atomic absorption of a photon of energy $h\nu$ implies an electronic transition from a level E_1 to a level E_2, where:

$$E_2 - E_1 = h\nu \tag{1.1.1}$$

Vice versa, the electronic transition from E_2 to E_1 implies the atomic emission of a photon of energy $h\nu$. So the law 1.1.1 could be read in two directions describing, from left to right, emission and, from right to left, absorption. Let us define B_{12} and B_{21} the atomic probability per unit of time and unit of radiation intensity for, respectively, absorption and stimulated-emission to occur. An Active Medium is a collection of atoms: we call N_2 the density of atom excited in the upper state with energy E_2 and N_1 the number of atoms in the lower state with energy E_1 we can write the net change of N_2 for unit of time:

$$\dot{N_2} = B_{12}E(\nu)N_1 - [A_{21} + B_{21}E(\nu)]N_2 \tag{1.1.2}$$

being $E(\nu)$ the radiation energy density. At the thermal equilibrium Maxwell-Boltzmann statics implies that:

$$\frac{N_1}{N_2} = e^{h\nu/KT} \tag{1.1.3}$$

Then

$$E(\nu) = \frac{A_{21}/B_{12}}{e^{h\nu/KT} - B_{21}/B_{12}} \tag{1.1.4}$$

This expression could be compared with Planck's radiation equation for radiation in equilibrium with matter and we obtain:

$$\frac{A_{21}}{B_{12}} = \frac{8\pi\nu^3}{c^3} \qquad \frac{B_{21}}{B_{12}} = 1 \tag{1.1.5}$$

Let us now calculate the probability of stimulated emission for unit of time (that is also the absorption probability) :

$$E(\nu)B_{21} = \frac{A_{21}}{e^{\frac{h\nu}{KT}} - 1} \tag{1.1.6}$$

This relation says that the field-matter interaction strength is proportional to the spontaneous-emission term. The net power generated by one unit of Active Medium volume in the interaction with a monochromatic plane wave is:

$$P = (N_2 - N_1)\frac{A_{21}h\nu}{e^{\frac{h\nu}{KT}} - 1} \tag{1.1.7}$$

The Active Medium amplifies the radiation when the upper level E_2 is more populated of atoms than the level E_1. Radiation amplification from a medium could be obtained if external energy is supplied to keep N_2 larger than N_1; the so-called *population inversion*. Population inversion is obtained and maintained through the laser pumping mechanism. In this way the Active Medium transforms the incoherent energy of the pumping into a quasi monochromatic electro-magnetic field.

The Optical Cavity provides a positive feedback loop: it brings back at the entrance of the Active Medium part of the radiation coming out from the medium. When an amplifier has a positive feedback loop a small amount of broad band noise is enough to drive the system to oscillate. Spontaneous Emission provides the initial noise in laser system. Then, if the pumping mechanism is strong enough, it is possible to achieve a stationary condition where the radiation gain compensates the radiation losses and emission of coherent light occurs steadily. Saturation of the gain, because of the finite pump rate of atoms, prevents the gain process to grow indefinitely. The minimum level of the pumping for which the condition gain equal to losses is obtained is called *laser threshold*. Further increase of the pump determines an increase of the gain saturation value. The excess of gain over the losses determines the intensity of the laser emission. It is worth to point out that light emission is not the only mechanism of losses, in semiconductor laser, for example, non radiative re-combination processes may occur as well. From the theoretical point of view, the laser could be described quite accurately by a semi-classical approach using Maxwell-Bloch equations to describe the light interaction with the medium and appropriate boundary conditions to take into account the optical cavity.

1.1.2 The Maxwell-Bloch equations

The Maxwell-Bloch equations are derived using the classical Maxwell equation to describe the electro-magnetic field and the Bloch equations to describe the medium. The Maxwell-Bloch approach is based on a self consistent approximation for which the electro-magnetic field interacting with microscopic dipoles creates a macroscopic polarization which acts as source for the electro-magnetic field that interacts again with the dipoles and so on. The classical treatment of the field lies on the fact that the field intensity is, inside the cavity, large enough for justifying

the classical approximation. We can write:

$$\nabla^2 E - \frac{1}{c^2}\partial_t^2 E = \mu_0 \partial_t^2 \mathbf{P} \tag{1.1.8}$$

being E the electric field and $\mathbf{P}$ the macroscopic atomic polarization.

Bloch equations for the matter interacting with an electro-magnetic field are derived from the Schroedinger equation, where the Hamiltonian of each atom could be written as:

$$H = H_0 + H_{int} = \frac{\hbar\omega_a}{2}\begin{pmatrix} 1 & 0 \\ 0 & -1 \end{pmatrix} - dE\begin{pmatrix} 0 & 1 \\ 1 & 0 \end{pmatrix} = \frac{\hbar\omega_a}{2}\hat{\sigma_z} - dE\hat{\sigma_x} \tag{1.1.9}$$

being $\hbar\omega_a$ the energy gap between the two electronics levels, E the electro-magnetic field, d the projection of the atomic electrical dipole moment in the direction of the field polarization, $\hat{\sigma}$ the Pauli matrices. The time evolution of the operators is given, in the Heisenberg representation, by:

$$\dot{\hat{\sigma}} = \frac{1}{i\hbar}[\hat{\sigma}, H] \tag{1.1.10}$$

Several approximations have been done to write the Hamiltonian in 1.1.9 :
i) The atom is described as a two-level system with unperturbed eigenstate $\mid \Psi_1 >$ and $\mid \Psi_2 >$ and unperturbed energies $E_1 = -\frac{\hbar\omega_a}{2}$ and $E_2 = \frac{\hbar\omega_a}{2}$. The state wave function could be written as

$$\mid \Psi >= a \mid \Psi_1 > + b \mid \Psi_2 > \tag{1.1.11}$$

being a and b the time-dependent complex amplitudes. ii) The second term of 1.1.9, describing the interaction dipole-field (H_{int}), assumes reflexion symmetry (not valid for the non centro-symmetric crystals). iii)We have neglected the center of mass effects considering only one-photon transitions. iv) We have neglected the vectorial character of the field assuming a single electro-magnetic field polarization axis. v) We have neglected the variation of the electric field inside the

atom assuming the dipole approximation. This approximation is based on the hypothesis that the term of the field $e^{i\vec{k}\bullet\vec{x}}$, where $\vec{k}$ is the wave-vector of the field and $\vec{x}$ is the position vector of the electron in respect with the atom nucleus, can be neglected. This holds as far as λ is much larger than the radius of the atom. Such a approximation is consistent with the semi-classical treatment of the field. vi) All atoms are identical, i.e. the medium is considered to be *homogeneously broadened*. This is not the case, for example, in gas lasers at low pressure where the velocity vector of the molecule separates the atoms in groups. Each group will contribute to the emission in a slight different way because of the Doppler effect and the radiation emission line will be *inhomogeneously broadened*.

In order to provide a description for the whole collection of atoms of the Active Medium we assume that all atoms contribute in the same way to the polarization (*homogeneously broadened system*). Then the macroscopic polarization for unit of volume of the medium is

$$\mathbf{P} = Nd < \hat{\sigma_x} > \tag{1.1.12}$$

being N the atomic density in the medium and d the atomic dipole. Performing the average on the Pauli operators we can realize that, given the wave function of 1.1.11:

$$\begin{aligned} < \hat{\sigma_z} > &= < \mid b \mid^2 > - < \mid a \mid^2 > \\ < \hat{\sigma_x} > &= < b^* a > + < a^* b > \end{aligned} \tag{1.1.13}$$

Therefore, $< \hat{\sigma_z} >$ is the difference between the probability of having an atom excited in the upper level and the probability of having an atom in the lower level, while the macroscopic polarization $\mathbf{P}$ could be written, according to 1.1.12 as a sum of two complex conjugate terms. Following 1.1.10 the time-evolution of

the mean value operators reads (omitting the operators hat):

$$\begin{aligned} < \dot{\sigma_x} > &= -\omega_a < \sigma_y > \\ < \dot{\sigma_y} > &= \omega_a < \sigma_x > +2\frac{dE}{\hbar} < \sigma_z > \\ < \dot{\sigma_z} > &= -2\frac{dE}{\hbar} < \sigma_y > \end{aligned} \tag{1.1.14}$$

The term $\frac{dE}{\hbar}$ it is the well known expression of the Raby frequency. It is worth to notice that the semi-classical treatment of the field allowed for writing $< E\sigma_x >= E < \sigma_x >$. We can define the new variables:

$$r = (< \sigma_x > -i < \sigma_y >)/2 \qquad r^* = (< \sigma_x > +i < \sigma_y >)/2 \qquad D =< \sigma_z >$$

We have then $< \sigma_x >= r+r^*$ and $< \sigma_y >= (r^*-r)/i$ that could be compared with the polarization decomposition described in 1.1.13. We write the time-evolution equations for the new variables:

$$\begin{aligned} \dot{r} &= -i\omega_a r - \frac{i}{\hbar} dED \\ \dot{r^*} &= i\omega_a r^* + \frac{i}{\hbar} dED \\ \dot{D} &= i\frac{2dE}{\hbar}(r^* - r) \end{aligned} \tag{1.1.15}$$

At this point we can return on the electric field equation 1.1.8 and separate the electric field term and atomic polarization term into a fast oscillating term and into a slow one:

$$\begin{aligned} E(z,t) &= \frac{1}{2} E_0(z,t) e^{i(k_c z - \omega_c t)} + E_0^*(z,t) e^{-i(k_c z - \omega_c t)} \\ r(z,t) &= r_0(z,t) e^{i(k_c z - \omega_c t)} \\ r^*(z,t) &= r_0^*(z,t) e^{-i(k_c z - \omega_c t)} \end{aligned} \tag{1.1.16}$$

where ω_c (and $k_c = \omega_c/c$) is not specified up to now except for being an optical frequency (of the order of $10^{15} Hz$) much larger than the typical time-scales evolution of the envelopes E_0, r_0, r_0^*. We can assume the so-called *Slowly Varying*

Envelope Approximation ($SVEA$) which lies on the fact that the variation scales in time and in space for the envelopes are much slower than the variation scales of the fast oscillating terms:

$$\omega_c |\, r_0 \,| >> |\, \partial_t r_0 \,|, \qquad \omega_c |\, E_0 \,| >> |\, \partial_t E_0 \,|, \qquad k_c |\, E_0 \,| >> |\, \partial_z E_0 \,| \quad (1.1.17)$$

We can also neglect the fast terms oscillating at $2\omega_c$ since they average to zero at the time-scales of the envelopes (*Rotating Wave Approximation*, RWA). Finally, we neglect transverse effects in the electrical field, looking only for plane wave solutions (*Plane Wave Approximation*, PWA). We can then write for the electrical field and atomic polarizations envelopes:

$$\partial_t E_0 + c\partial_z E_0 = i\frac{\omega_c N d}{\varepsilon_0} r_0 \qquad + c.c \qquad (1.1.18)$$

We can operate in the same way in eqts. 1.1.15 by replacing E with the expression 1.1.16 and, according to 1.1.17, applying $SVEA$ and RWA approximations to the field and to the polarization terms. We get, defining $P = -2ir_0$ and $P^* = 2ir_0{}^*$.

$$\begin{aligned} \dot{P} &= -i\delta_{AC} P - \frac{d}{\hbar} E_0 D \qquad + c.c \\ \dot{D} &= \frac{d}{2\hbar}(E_0 P^* + E_0^* P) \end{aligned} \qquad (1.1.19)$$

where $\delta_{AC} = \omega_a - \omega_c$.

The time-evolution eqts. 1.1.19 determines the evolution of the complex macroscopic polarization of the medium and of the population difference between the two level states when the electro-magnetic field interact with a collection of stable atoms. So far, no irreversible process has been considered. Since the atomic levels are not stable in general (except for the ground state) and have a limited lifetime when interacting with an electro-magnetic field, we have to introduce these irreversible processes in our description. There are no equations able to represent these phenomena in a fundamental way as the Schroedinger equation

does for the stable atomic state. For this reason, the atomic decay processes are introduced in a phenomenological fashion. The decaying of the population implies a decay of the polarization, but atomic polarization could decay for other reasons that do not involve population decay (elastic collision, for examples). Hence, the introduction of two different decay rates for polarization and population difference ($\gamma_\perp$ and $\gamma_{//}$).

In order to work as an amplifier, the Active Medium must have a higher probability of emitting rather than absorbing radiation. In other words, the emission rate must be larger than the absorption rate. At thermal equilibrium this is not possible, as it is easy to verify by using the Maxwell-Boltzmann statistics (see eqts. 1.1.3). Lasers cannot operate at thermal equilibrium; a constant injection of energy is required to maintain the emission rate larger than the absorption rate. This injection of energy is called pumping. Several pumping mechanism are employed in laser technologies. The most common is the incoherent optical pumping that excites continuously the atoms electrons to the upper levels. The effect of the pumping is incorporated into the population equation through a term D_o that increases the population difference between the upper and the lower levels. Equations 1.1.19 become, after re-scaling:

$$\begin{aligned} \frac{1}{c}\partial_t F + \partial_z F &= g\widetilde{P} + c.c. \\ \partial_t \widetilde{P} &= -\gamma_\perp(F\widetilde{D} + (1 + i\Delta_{AC})\widetilde{P}) + c.c. \\ \partial_t \widetilde{D} &= \gamma_{//}[\frac{1}{2}(F\widetilde{P}^* + F^*\widetilde{P}) - (\widetilde{D} - 1)] \end{aligned} \tag{1.1.20}$$

where: $F = \frac{dE_0}{\hbar\sqrt{\gamma_\perp\gamma_{//}}}$, $\widetilde{P} = \sqrt{\frac{\gamma_\perp}{\gamma_{//}}}\frac{P}{D_0}$, $\widetilde{D} = \frac{D}{D_0}$, $\Delta_{AC} = \frac{\omega_a - \omega c}{\gamma_\perp}$ and $g = \frac{-N\omega_c d^2 D_0}{2c\hbar\varepsilon_0\gamma_\perp}$. These equations describe the light matter interaction for a dissipative and pumped medium. Depending on the sign of the pump D_0 the Active Medium will behave as an amplifier or as an absorber. In the limit of weak field, $D \approx D_0$ and $\widetilde{D} \approx 1$; 1.1.20 may be solved by Fourier transforming and considering a monochromatic

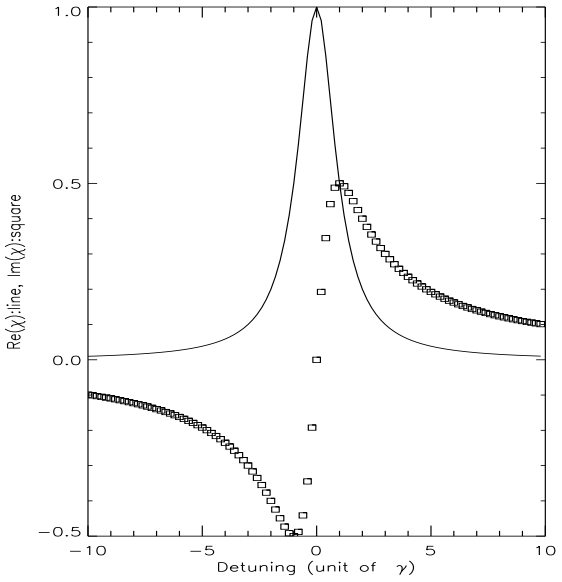

Figure 1.1: $\Re(\chi)$ (line) and $\Im(\chi)$ (square) as a function of the detuning $(\omega - \omega_a)$. The detuning is normalized to $\gamma_\perp$.

component of the field envelope $F = F(\widetilde{\omega}, z)e^{-i\widetilde{\omega}t}$. We obtain a scaled expression for the complex electronic susceptibility χ of the medium, defined as $\widetilde{P} = \chi F$:

$$\chi = \Re(\chi) + i\Im(\chi) = \frac{\gamma_\perp^2}{\gamma_\perp^2 + (\omega - \omega_a)^2} + i\frac{\gamma_\perp(\omega - \omega_a)}{\gamma_\perp^2 + (\omega - \omega_a)^2} \tag{1.1.21}$$

where $\omega = \widetilde{\omega} + \omega_c$. We plot $\Re(\chi)$ and $\Im(\chi)$ in Fig. 1.1. Solving the equation for the propagation of the field in the Active Medium we obtain the Bear's law:

$$F(\widetilde{\omega}, z) = F(\widetilde{\omega}, 0)\ e^{(g\ \Re(\chi)\ z)}\ e^{i(\frac{\widetilde{\omega}}{c} + g\ \Im(\chi))z} \tag{1.1.22}$$

Eqt. 1.1.22 says that a monochromatic field interacting with an amplifying Active Medium suffers both amplification and dispersion. In the hypothesis of weak field (which implies $D \approx D_0$) the field intensity is exponentially amplified by a factor proportional to the length of the Active Medium. The exponential amplification rate per unit of length is given by the real part of the electronic susceptibility and it is a function of the frequency detuning between the interacting field and the atomic transition frequency (Fig 1.1). This function is called *gain curve* and it has a symmetric Lorentzian shape, centered at detuning equal zero,

of width ($HWHM$) $\gamma_\perp$. Together with amplification, the field suffers dispersion. Remembering the starting field eqts. 1.1.16 and that, given the frequency and the wave number of a propagating field, the index of refraction n of the medium can be calculated as $n = ck/w$, we obtain:

$$n = 1 + c\ g\Im(\chi)/\omega_c \tag{1.1.23}$$

Eqt. 1.1.23 says that, in general, the value of the refraction index of the medium is different from the unpumped ($g = 0$) material refraction index value. The dependence of the dispersion with the optical field frequency is given by the imaginary part of the electronic susceptibility ($\Im(\chi)$), (Fig 1.1). This function says that no dispersion occurs if the frequency of the interacting field is not detuned respect to the atomic transition frequency. It worth noting that maximum dispersion occurs for detuning equal to $\gamma_\perp$. The dispersion curve could be obtained from the gain curve using Kramer-Kronig's relations.

1.1.3 The optical cavity

Besides the mechanism of gain, the laser requires a positive feedback loop. The laser optical cavity provide this effect (Fig. 1.2). Let us suppose that the electromagnetic field can propagate, along the ring cavity, just in one direction, as can be achieved experimentally inserting an optical diode in the cavity. In this way we can neglect the counter-propagating wave in the cavity and the subsequent standing-wave that is formed by the interaction between the two fields. If the cavity length is ℓ and the medium length is L the boundary condition reads:

$$F(0,t) = RF(L, t - \frac{\ell - L}{c}) \tag{1.1.24}$$

being R the power reflectivity of the mirrors 1 and 2. Now we can identify reference optical frequency ω_c for the electrical field and polarization in eqts. 1.1.16 as the resonant frequency of the empty cavity: $\omega_c = \frac{2j\pi c}{\ell}$, being j an

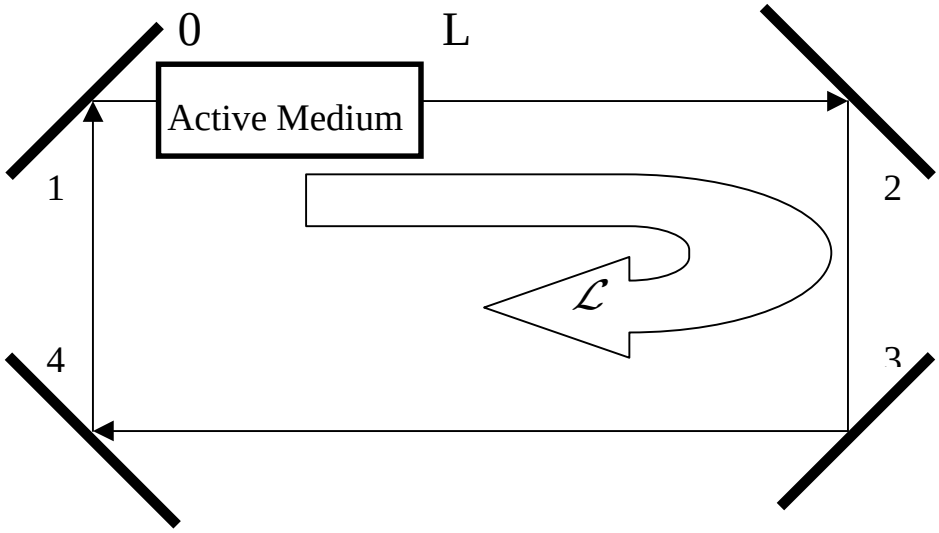

Figure 1.2: Schematic representation of a ring cavity. The mirrors labeled 1 and 2 have power reflectivity R, while mirrors 3 and 4 are ideal reflectors.

integer number. The five coupled eqts. 1.1.20 with the boundary condition of 1.1.24 describe theoretically the laser system.

We can look for the envelope-stationary solution of this system. Such solutions will have, in general, the form (omitting the tilde on $\widetilde{P}$ and on $\widetilde{D}$):

$$F(z,t) = F_{st}(z)e^{-i\omega t} \qquad P(z,t) = P_{st}e^{-i\omega t} \qquad D(z,t) = D_{st}(z) \qquad (1.1.25)$$

where ω is the frequency offset of the operating optical field respect to the reference frequency ω_c. If we called ω_L the lasing frequency, then $\omega_L = \omega_c + \omega$. We obtain, substituting the 1.1.25 into the 1.1.20,

$$\begin{aligned} P_{st}(z) &= -F_{st}(z)\frac{1 - i\bar{\Delta}}{1 + \bar{\Delta}^2 + \mid F_{st}(z) \mid^2} \\ D_{st}(z) &= \frac{1 + \bar{\Delta}^2}{1 + \bar{\Delta}^2 + \mid F_{st}(z) \mid^2} \end{aligned} \qquad (1.1.26)$$

where $\bar{\Delta} = \frac{\omega_a - \omega_L}{\gamma_\perp}$. Separating the modulus and the phase of the stationary field envelope $F_{st}(z) = \rho(z)e^{i\theta(z)}$ and substituting in the first of eqts. 1.1.20 and in the

boundary condition 1.1.24, we obtain

$$\rho^2(L) = \frac{2}{1-R^2}[gL - (1+\bar{\Delta}_j^2) \mid \ln R \mid] \tag{1.1.27}$$

$$\omega_j = \frac{\kappa\delta_{AC} + \alpha_1\gamma_\perp j}{\gamma_\perp + \kappa} \qquad j = 0, \pm 1, \pm 2... \tag{1.1.28}$$

The second equation could be expressed in terms of ω_L:

$$\omega_L^j = \frac{(\omega_c + \alpha_1 j)\gamma_\perp + \omega_a\kappa}{\gamma_\perp + \kappa} \qquad j = 0, \pm 1, \pm 2... \tag{1.1.29}$$

where $\kappa = \frac{c|\ln R|}{\ell}$ are the cavity losses for the field and $\alpha_1 = \frac{2\pi c}{\ell}$ is the free-spectral-range of the cavity or the separation between two longitudinal-modes. From eqts. 1.1.29 we realize that the operational optical frequency is a losses weighted average of the atomic resonant frequency and the frequency of one cavity mode. A stability analysis is necessary to find out which of the longitudinal-modes will be active. Anyway, eqt. 1.1.27 imposes already a selection between the possible operational resonant cavity modes. A necessary condition for a cavity mode to operate is that, at its frequency, gain must overcome the losses. This is the so-called threshold condition that reads:

$$(gL)_{thr,j} = (1+\bar{\Delta}_j^2) \mid \ln R \mid \tag{1.1.30}$$

From the first of eqts. 1.1.20, replacing the expression for P_{st} (first equation in eqts. 1.1.26) and considering the boundary conditions, we can obtain the longitudinal profile of the field modulus $\rho(z)$ at the steady-state conditions. The overall variation of $\rho(z)$ in Active Medium depends on the mirror reflectivity and on the degree of saturation. The typical increase of the field modulus is about 10% when $gL = 1.0$, $R = 0.9$ $\alpha_1 = 2.0$, and rises up to 65 % if $gL = 5.0$ and $R = 0.5$.

1.1.4 Stationary solutions and stability analysis

The general stability analysis of the Maxwell-Bloch equation is a quite challenging problem. The complications come from the spatial dependence of the field and of the atomic variables. A way to avoid this obstacle is to assume the so-called *Uniform (or Mean) Field Approximation.* Such approximation assumes

$$gL \longrightarrow 0 \qquad\qquad T \longrightarrow 0 \tag{1.1.31}$$

This approximation is not trivial, since, even if the gain per pass in the medium is assumed very small, the radiation will stay inside the cavity for many round trips, since $R \longrightarrow 1$. In this way the two effects compensate each other and the threshold condition could be fulfilled. Defining $C = \frac{gL}{2T}$, the threshold condition reads

$$(C)_{thr,j} = \frac{(1+\bar{\Delta}_j^2)}{2} \tag{1.1.32}$$

It is important to point out that, in this approximation, the stationary field profile is uniform along the cavity longitudinal coordinate. Applying the theorem of the mean value as integrating the first of 1.1.20, we have $\rho(L) \sim \rho(0)$. Numerical simulations using this approach reveal that one should assume values for gL and T that are unrealistically low ($gL < 0.1$, $T < 0.01$). Lugiato et al. in 1980 succeeded in implementing this limit in a more general way. They defined a new set of independent variables for the eqts. 1.1.20, 1.1.24:

$$\begin{aligned} z' &= z; & t' &= t + \frac{\ell - L}{c}\frac{z}{L}; \\ \widetilde{F}(z',t') &= F(z',t')e^{\frac{z'}{L}\ln R}; & \widetilde{P}(z',t') &= P(z',t')e^{\frac{z'}{L}\ln R}; \qquad \widetilde{D}(z',t') = D(z',t') \end{aligned}$$

By this transformation the two non-isochronous events at the boundary conditions become isochronous, and the Maxwell-Bloch equations take the form (omitting

the tilde):

$$\begin{aligned}
\partial_{t'}F + \frac{cL}{\ell}\partial_z F &= -\kappa(F + 2CP) && + c.c. \\
\partial_{t'}P &= -\gamma_\perp(FD + (1 + i\Delta_{AC})P) && + c.c. \\
\partial_{t'}D &= -\gamma_{//}[\frac{1}{2}(FP^* + F^*P)e^{(\frac{2z'}{L}|\ln R|)} + D - 1] && (1.1.33)
\end{aligned}$$

where we have redefined $C = \frac{gL}{2|\ln R|}$. The new equations differ from the equations 1.1.20 and 1.1.24 for having a phase velocity $\frac{cL}{\ell}$ instead of c and in including an explicit spatial dependence through the exponential factor. Now the boundary condition reads

$$F(0, t') = F(L, t') \tag{1.1.34}$$

that is the conventional periodic boundary condition of ordinary linear vibration problems. We can then introduce an appropriate modal decomposition of the Fourier type with related modal amplitude. The big advantage is that the new field amplitude $\widetilde{F}(z', t')$ is very uniform throughout the medium, even when the values for gL and T deviate slightly from the uniform-field approximation requirements. The Fourier decomposition of the variables in Maxwell-Bloch equation gives:

$$\begin{aligned}
\begin{pmatrix} F(z', t') \\ P(z', t') \end{pmatrix} &= e^{-i\omega t'} \sum_{n=-\infty}^{n=+\infty} u_n(z') \begin{pmatrix} f_n(t') \\ p_n(t') \end{pmatrix} && + c.c. \\
D(z', t') &= \sum_{n=-\infty}^{n=+\infty} u_n(z') d_n(t') && (1.1.35)
\end{aligned}$$

where the ortho-normal complete base on which the variables are projected is

$$u_n(z') = \frac{1}{\sqrt{L}} e^{ik_n z'} \qquad where \qquad k_n = \frac{2\pi}{L} n \tag{1.1.36}$$

ω is an unknown frequency offset that measures the frequency separation between the selected cavity reference and the optical laser frequency (ω_L). Since $D(z', t')$ is real $d_n(t') = d^*_{-n}(t')$. We can notice that, the introduction of an ortho-normal

and complete set of modal function was not possible in the frame of eqts. 1.1.20, 1.1.24, unless applying the mean-field approximation. In this limit the two pictures converge to one another. The Maxwell-Bloch modal amplitudes obey the following equations:

$$\begin{aligned}
\frac{d}{dt'}f_n &= i\omega f_n - \kappa(f_n + 2Cp_n) - ick_n\frac{L}{\ell}f_n \qquad + c.c \\
\frac{d}{dt'}p_n &= -\gamma_\perp\sum_{n'} f_{n'}d_{n-n'} + [1 + i(\frac{\omega_a - \omega_c - \omega}{\gamma_\perp})]p_n \qquad + c.c \\
\frac{d}{dt'}d_n &= -\gamma_{//}[-\frac{1}{2}\sum_{n'n''}(f^*_{n'}p_{n''}\Gamma_{n''-n'-n} + \\
&\qquad + f_{n'}p^*_{n''}\Gamma_{n''-n'-n}) + d_n - \delta_{n,0}]
\end{aligned} \tag{1.1.37}$$

where Γ_p is a coupling term between modes that reads:

$$\Gamma_p = \frac{1}{L}\int_0^L dz' e^{ik_p z'} e^{\frac{2z'}{L}|\ln R|} = \frac{1-R^2}{R^2}\frac{1}{2\mid \ln R \mid + ik_p L} \tag{1.1.38}$$

steady-state solutions can be obtained as usual setting the derivative to zero. In general the j^{th} steady-state is a linear combination of different n^{th}-order modal functions 1.1.36. Then, the longitudinal field profile modulus will not be perfectly homogeneous but it will contain the interference terms due to the presence of additional harmonic Fourier components.

It is worth noting that eqts. 1.1.37 are an exact description of the laser system without additional approximations beside those used in the Maxwell-Bloch picture of matter-radiation interaction. Thus eqts. 1.1.37 are useful as a starting point to implement approximations for the laser description. For example, from eqts. 1.1.37 it is possible to obtain improved solutions in the single-mode limit (normally obtained trivially retaining just the $n = 0$ field amplitudes in the 1.1.37).

The mean-field approximation applied to 1.1.37 implies vanishing mode-mode coupling: $\Gamma_p \longrightarrow \delta_{p,0}$. In this limit the j^{th} steady-state will be purely homogeneous and every single frequency field solution of 1.1.37 (i.e. every stationary

solution j^{th}) corresponds to a single spatial mode. We can then introduce new field and polarization amplitudes whose general expression is:

$$\bar{x}_n(t') = x_n(t')exp(-ick_nt') = x_n(t')exp(-i\alpha_nt') \tag{1.1.39}$$

We then obtain a new set of modal equations where the amplitudes are defined by 1.1.39. The stationary solutions are obtained by putting the derivatives to zero and the generic j^{th} stationary solution is identified by five strings of infinite modal components (omitting the bar on the atomic and field amplitudes):

$f_0^j, f_{\pm1}^j, f_{\pm2}^j \cdots \quad f_0^{*j}, f_{\pm1}^{*j}, f_{\pm2}^{*j} \cdots \quad p_0^j, p_{\pm1}^j, p_{\pm2}^j \cdots \quad p_0^{*j}, p_{\pm1}^{*j}, p_{\pm2}^{*j} \cdots \quad d_0^j, d_{\pm1}^j, d_{\pm2}^j \cdots$

that, in the uniform-field limit, takes the form

$$\begin{aligned} f_n^{(j)} &= [2C - (1+\bar{\Delta}_j^2)]^{\frac{1}{2}}\delta_{n,j} \qquad + c.c. \\ p_n^{(j)} &= -f_n^{(j)}\frac{1 - i\bar{\Delta}_j}{1 + \bar{\Delta}_j^2 + \mid f_n^{(j)} \mid^2} \qquad + c.c. \\ d_n^{(j)} &= \frac{1+\bar{\Delta}_j^2}{1 + \bar{\Delta}_j^2 + \mid f_n^{(j)} \mid^2}\delta_{n,0} \end{aligned} \tag{1.1.40}$$

where

$$\bar{\Delta}_j = \frac{\Delta_{AC} - j\alpha_1/\gamma_\perp}{1 + k/\gamma_\perp} \qquad \frac{\omega_j}{\gamma_\perp} = \frac{\kappa}{\gamma_\perp + \kappa}(\Delta_{AC} - j\frac{\alpha_1}{\gamma_\perp}) \tag{1.1.41}$$

The threshold condition for the stationary solutions j^{th} is

$$2C > 1 + \bar{\Delta}_j \tag{1.1.42}$$

Multiple solutions are possible if the medium has enough gain and/or the inter-mode spacing is small compared with the gain curve width. The two situations where steady-state solutions cannot or can coexist for the same parameters set are shown in Fig. 1.3. In the case of multiple steady-state solutions the stability analysis will reveal which solution is going to dominate.

In order to analyze the stability of the solution j^{th} let us linearize eqt. 1.1.37 around the stationary solution by setting

$$x_n(t') = x_n^{(j)}\delta_{n,j} + \delta x_n(t') \tag{1.1.43}$$

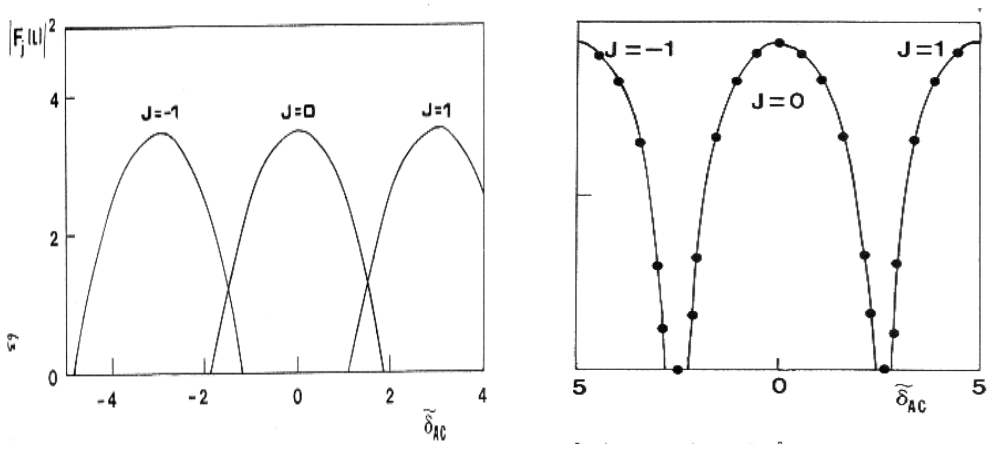

Figure 1.3: steady-state output intensity $\mid F_j(L) \mid^2$ for the solutions $j = 0, \quad \pm 1$ as a function of the detuning parameter Δ_{AC}. Parameters used (right): $gL = 2.0$, $R = 0.5$, $\frac{\gamma_{//}}{\gamma_\perp} = 2.0$, $\frac{\alpha_1}{\gamma_\perp} = 5.0$, (left): the same as right except for $\frac{\alpha_1}{\gamma_\perp} = 3.0$. From Ref. [22]

where x represents the general variable of 1.1.37. The infinite system of equation, after substitution, breaks up in blocks of five equations each block containing the perturbation variables $\delta f_{n+j}(t')$, $\delta f^*_{n-j}(t')$, $\delta p_{n+j}(t')$, $\delta p^*_{n-j}(t')$, $\delta d_n(t')$. Introducing the usual ansatz

$$\delta x(t') = e^{\lambda t'} \delta x(0) \tag{1.1.44}$$

where x represents the general perturbation variable, we find the fifth degree characteristic equation for the constant rate λ

$$\sum_{i=0}^{i=5} A_i(\alpha'_n)(\lambda/\gamma_\perp)^i = 0 \tag{1.1.45}$$

the coefficients A_i depends on the j^{th} stationary state parameters values and on the frequency α_n of the n-th Fourier mode. The steady-state j^{th} will be stable if and only if the real part of all of the five eigenvalues $\lambda^{(i)}_{n,j}$ are negative for all n. If it exists a value n' at which one or more eigenvalues have real positive parts this means that an instability is developing, causing the growth of of side-bands at frequencies $\pm\alpha_{n'}$. Then the field amplitude $F(z', t')$ departs from its uniform stationary configuration developing a spatio-temporal time structure. Numerical analysis have revealed that the eigenvalues relative to the atomic variables

(P, P^*, D) have large negative real parts. The remaining two eigenvalues are relative to the field degrees of freedom (F, F^*) and can be associated to the linearized evolution of the field amplitude and phase. Indeed the resonant phase eigenvalue has a zero real value in agreement with the marginal stability of the phase of the laser resonant mode at the steady-state. We can identify mainly two mechanisms of instability: the *amplitude instability* and the *phase instability.*

Amplitude instability occurs for zero value of detuning Δ_{AC} or for $\Delta_{AC} \ll \alpha_1$. This situation may occur in lasers with gain curve width larger than several free-spectral-ranges of the laser cavity and it requires large unsaturated gain g. In Fig. 1.4 we show the two largest real part of the eigenvalues of the eqt. 1.1.45 where $\alpha_1 = 3\gamma_\perp$ and $\Delta_{AC} = 0$. As the gain is increased over $gL = 2.0$ the real part of the eigenvalues $\lambda^{ampl}_{\pm 3,0}$ become positive. This means that an arbitrary perturbation at the frequencies $\alpha_3 = \pm 3\alpha_1$ grows exponentially in the linear regime and the cavity field becomes a superposition of the steady-state solution at the frequency ω_c and of growing side-bands at frequencies $\omega_c \pm \alpha_3$. Similar plots for the stationary solutions $j = \pm 1$ (also above the threshold for the parameters chosen) show that these are unstable for both the gain values of Fig. 1.4 (upper panel). This means that no stable state is available for the laser. Thus, after a transient, a persistent self pulsing develops, characterized by the beat-note between modal components (multiple of the free-spectral-range). Such kind of instability, appearing for high gain, is also known as Risken-Nummedal instability. If the laser gain is further increased, more than one side-band becomes unstable, the non-linear dynamics could become very complicate and develops the signatures of deterministic chaos. If the modal separation is small enough, increasing the gain one notes that the beat frequency or, alternatively, the modal frequency at which the eigenvalue real part become positive, increases.

Phase instability occurs when the gain curve width contains more than one free-spectral-range and the detuning is varied. The instability develops when δ_{AC} reaches the value at which multiple stationary solutions coexist. Fig. 1.4 (lower panel) shows that the real part of the phase eigenvalue $\lambda^{\phi}_{\pm 1,0}$ becomes positive for $\delta_{AC} = 1.2$. The subsequent evolution depends on the stability of the coexisting mode. If this one is stable, the laser operation is transferred to the stable state, with a discontinuous change of the asymptotic intensity-output and operating frequency ("winner takes all"). If the coexisting mode is unstable too, undamped pulsations develop and the system is not able to reach any stationary state. Whether the first or the second behavior takes place depends on whether the stability domains of the modes overlap or not. The linear stability analysis shows that the first case is favored for $\frac{\gamma_{//}}{\gamma_{\perp}} < 1$, while the instability is more of the "winner takes all" kind if $\frac{\gamma_{//}}{\gamma_{\perp}} \sim 1$. It is worth to add that the detuning value for which the mode hop occurs in the "winner take all" mechanism, depends on the direction of variation of the detuning: thus the system exhibits hysteretic behavior. This is not the case when there is no coexistence of stable domains.

The above described instabilities are of multi-mode type since they involve the running laser mode and, at least, a pair of side-bands. Instabilities could develop also in a single-mode laser. From eqts. 1.1.37 we can obtain the single-mode laser imposing that all variables with the index $n \neq 0$ vanishes and imposing that $\ell\gamma_{\perp}/c \longrightarrow 0$. In this conditions all the cavity modes, except the resonant one, are very far away from the atomic gain line and they do not play any role in the evolution of the system. If, in addition, we assume resonance between the atomic gain line and the only remaining cavity mode, the laser equation reduces to a set of equations isomorphic to the Lorenz model describing convective hydrodynamic instabilities. The new set of laser equations are unstable under the following conditions: i) $\kappa > \gamma_{\perp} + \gamma_{//}$, called bad cavity limit and ii) $2C > 1 + \frac{(\kappa+\gamma_{\perp}+\gamma_{//})(\kappa+\gamma_{\perp})}{\kappa-\gamma_{\perp}-\gamma_{//}}$,

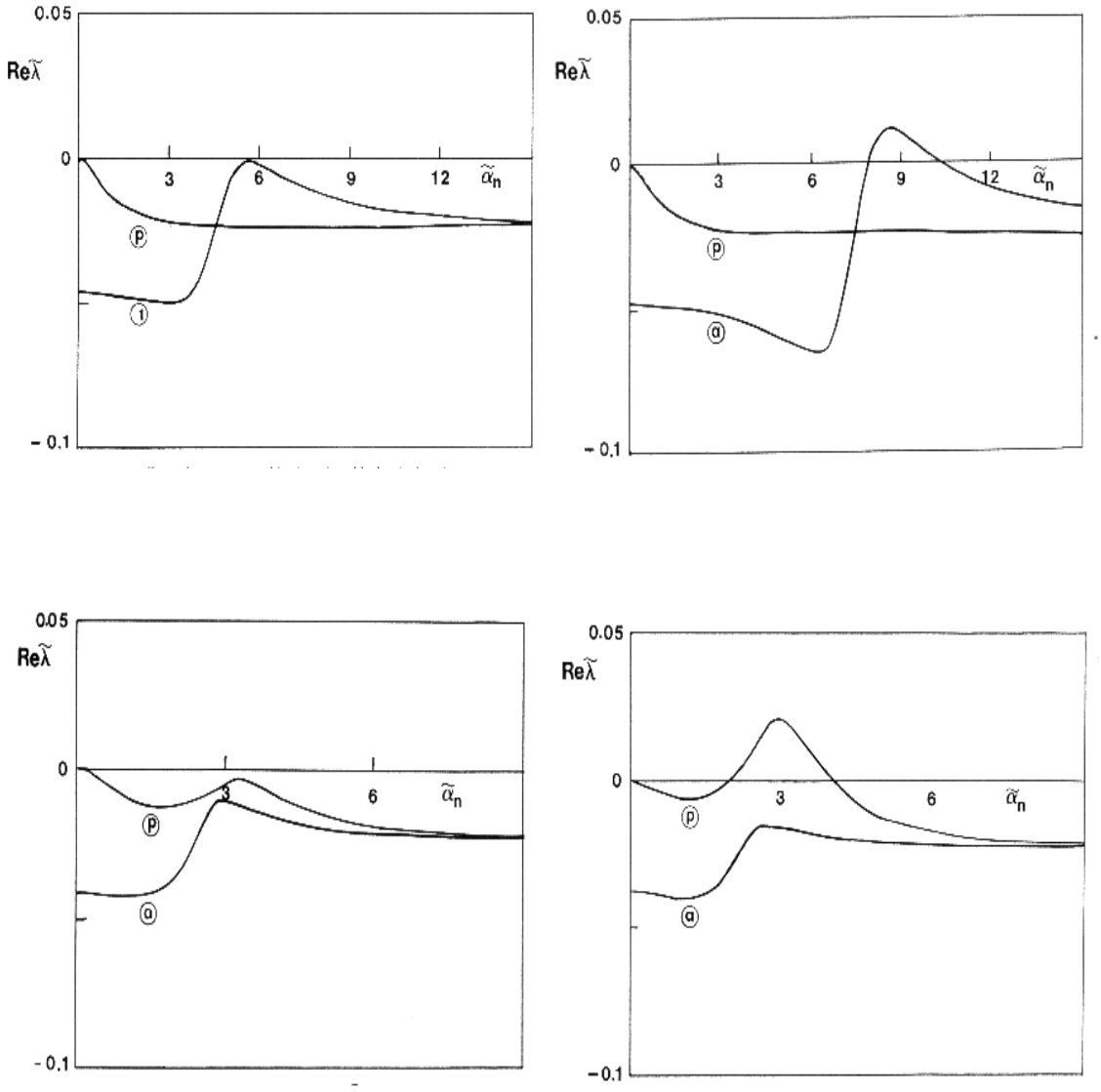

Figure 1.4: Two largest real part of the eigenvalues for $j = 0$ plotted as a function of $\frac{\alpha_n}{\gamma_\perp}$ viewed as a continuous variable. Upper Panel: $\Delta_{AC} = 0$, $R = 0.95$, $\frac{\alpha_\perp}{\gamma_\perp} = 3.0$, $\frac{\gamma_{//}}{\gamma_\perp} = 1.5$ $gL = 0.8$(left), $gL = 2$ (right). Lower Panel: $R = 0.95$, $\frac{\alpha_\perp}{\gamma_\perp} = 3.0$, $gL = 0.5$, $\frac{\gamma_{//}}{\gamma_\perp} = 0.8$ $\Delta_{AC} = 0.7$ (left), $\Delta_{AC} = 1.2$ (right). The line marked with a indicates the amplitude eigenvalue, the one with p the phase eigenvalue. From Ref. [22].

called high gain condition. The high gain condition sets a threshold (called second threshold) for which undamped pulsations set in. For the isomorphism with the Lorenz model, the self-spiking behavior that laser exhibits above the second threshold is deterministic chaos of Lorentz-type. In fact, the bifurcation sequence is more complicate than the one depicted here, we can reference Ref. [22] for a more exhaustive description.

1.2 Semiconductor laser

In the semiconductor lasers the three basic ingredients for the laser operation can be identified in this way:

i)The gain mechanism, in the simplest semiconductor laser structure, is provided by the electron-hole recombination in the depletion region of a forward biased p-n junction (homostructure). In modern devices this has been replaced by the double heterostructure and by the quantum-well heterostructure. ii)The pumping mechanism maintaining the population inversion in the junction, is provided by the injection of electrical current into the p-n junction. iii)The feedback mechanism is provided by the polished facets at the ends of the semiconductor block, forming, in this way, a Fabry-Pérot cavity. In more modern devices the cleaved facets have been replaced by a periodic index perturbation integrated along the laser structure acting as a grating (Distributed Bragg Reflectors (DBR) and Distributed Feedback (DFB) lasers). Quarter-wave DBR layers may be also stacked parallel to the wafer in order to obtain vertical emission (Vertical-Cavity Surface-Emitting Lasers). Lateral confinement of the field into the cavity may be obtained through dielectric waveguiding or through gain guiding. Sizing the transverse dimension of the waveguide allows to select single transverse-mode operation.

The p-n junction and its optical properties are described in the first paragraph together with the optical confinement technique most used. In the second paragraph we describe the electro-magnetic field propagation in a semiconductor medium, deriving the longitudinal-mode structure and the threshold condition. The semiconductor lasers present important differences in respect with the gas lasers or solid state lasers, for which the two-level Maxwell-Bloch equations were conceived. In particular, the energy-bands structure of a semiconductor medium

implies a different expression for the electrical susceptibility. Semiconductor media are conceptually similar to an ensemble of two-level atoms, though with different transition energies as defined by the electronic band structure and, more important, with different occupation of the electronic states. The problem of the evaluation of the susceptibility in a semiconductor medium is analyzed in the paragraphs three and four. In the third paragraph we describe the results of a phenomenological approach to the problem, leading to semiconductor laser rate-equations. In paragraph four we present a more fundamental approach; the semiconductor susceptibility is calculated taking into account the semiconductor energy-band structure. Introducing some approximations it is possible to obtain an effective two-level Maxwell-Bloch equations set for semiconductor laser. This set of equations provides an instrument to explore realistically the multi-mode dynamics of the semiconductor laser. In last part of paragraph four we present some numerical results showing the multi-mode behavior predicted by the effective two-level model. Finally, in the last paragraph, we will describe the Vertical-Cavity Surface-Emitting Lasers ($VCSEL's$) with particular emphasis on the polarization properties of these devices. This section is supposed to provide the essential concepts of semiconductor laser physics and it has been based on the Refs. [1, 20, 21, 31, 32, 33, 34, 35]

1.2.1 Operating principles

The optical properties of the *p-n* junction

Semiconductor materials are characterized by the existence of a relative small gap of forbidden energies, $(0.1 - 2\ eV)$ between the valence band of bonding electrons and the conduction band of free electrons. Hence, thermal energy or optical interactions (absorption of a photon whose energy is larger than the bandgap energy) may easily excite the uppermost valence electrons into the conduction

band and the vacancy left in the valence band behaves effectively as a positively charged free particle (hole). The Fermi-Dirac distribution describes the electrons (and holes) distribution through the energy state E:

$$f(E) = \frac{1}{e^{(E-E_f)/kT} + 1} \tag{1.2.1}$$

where E_f is the *Fermi energy level*, which identifies the borderline between empty states and filled states as $T \to 0$, k is the Boltzman constant, and T is the absolute temperature. It worth to notice that the Fermi energy does not correspond, in general, to any eigenenergy of an electron in the crystal. If the semiconductor crystal does not contain any defect, the Fermi energy is located at the center of the band-gap: all the valences states are filled, while the conduction states are empty. When the semiconductor is doped by donors or acceptors, the electron or hole population increases, filling states in the conduction band or generating holes in the valence band even for $T \to 0$. In this case the Fermi level may be pushed inside the conduction band (for donor doping) or inside the valence band (acceptor doping). When the semiconductor is not at the thermal equilibrium because of a current flow or other photoexcitation, *quasi-Fermi levels* for each one of the bands are used rather than the Fermi level. This description holds whenever the carrier scattering time within a band is much shorter than the equilibration time between the bands, which is always true for the large carrier density involved in $p-n$ junctions. Indeed, the timescale for intra-band relaxation is $\approx 10^{-13}s$ while for electron-hole recombination is $\approx 10^{-9}s$.

A $p-n$ junction is formed by two semiconductor blocks, one doped with donors (n) and the other with acceptors (p), in contact each other. When the two blocks are put in contact, there is an electrons flow from the n-type block to the p-type block and a counter-propagating flow of holes. This carriers diffusion re-establishes the equilibrium in the semiconductor. Prior to contacting the two

blocks, their Fermi levels were not matched; after a transient, an equilibrium state is reached and the two blocks have the same Fermi energy level. During the flow of carriers, several radiative electron-hole re-combinations may occur, although other kinds of re-combination mechanisms are possible. Eventually, a depletion region is created at the junction. This region presents, at its borders, electrons in excess (or negative charged acceptors) in the p-type block and holes in excess (or positive charged donors) in the n-type block. The consequent junction electric field prevents any further carrier diffusion. If the junction is forward biased by an external voltage overcoming the internal electrical field, carrier diffusion occurs into the junction. There is a small region at the junction where both holes and electrons are present. In this narrow region re-combination occurs and, in the case of radiative emission, a photon of energy $h\nu = E_g$, being E_g the semiconductor band-gap is emitted. This photon may be later absorbed trough the reverse process, generating a carrier pair. The level of current flowing in the semiconductor block for which stimulated-emission has the same probability to occur as absorption is called *transparency*. For currents below transparency, the semiconductor medium behaves as an absorber, for currents above it behaves as an amplifier. Defining the net rate of stimulated-emission, r_{st}, namely the difference between the stimulated photon rate and the absorption rate, the transparency condition is fulfilled when r_{st}=0. For a given photon energy, E=E_c-E_v=$h\nu$, r_{st} is proportional to the difference between the occupation probabilities of the electrons in the conduction band with energy E_c, $f_c(E_c)$, and the electrons in the valence band with energy E_v, $f_v(E_v)$. Such occupation probabilities, according to 1.2.1, read $(f_i(E_i) = (exp[(E_i - E_{fi})/kT] + 1)^{-1}$, $i = c, v)$, where E_{fc} and E_{fv} are the quasi-Fermi levels for the conduction and valence band. Beyond transparency, because net stimulated-emission occurs, the occupation probability in the conduction band at energy E_c is larger than the occupation probability in

the valence band at energy E_v, $f_c > f_v$, a condition equivalent to the population inversion introduced in the first section. Radiation emission may occur as spontaneous-emission or as stimulated emission. In the first case, photons are emitted in random directions and with arbitrary phases and the emitted light is incoherent. In the second case the process is initiated by an already existing photon which matches in phase, in frequency and in the direction of propagation, generating coherent light.

Radiative recombinations are not the only recombination mechanisms at the junction; electron-hole pairs may annihilate releasing their energy in form of lattice phonons instead of photons (non radiative recombination). This may happen through Auger recombinations, recombinations at defects, and surface recombinations. Non radiative recombinations affect the efficiency of the stimulated-emission process in the semiconductor and, therefore, the current threshold of the laser. Auger recombination involves four particle states (three electrons and one hole or two electron-hole pairs); the energy released at the recombination of a pair is absorbed by a carrier (electron or hole) which gets excited to a high energy state in the band. This electron or hole relaxes back to thermal equilibrium releasing energy in form of lattice vibrations (phonons). Auger effect is the dominant non radiative mechanism in narrow-gap lasers, especially at large temperature. It is responsible for the strong increasing of the threshold current for large temperatures. Recombination with defects occurs when a carrier interacts non radiatively with a defect in the active region. Defects are normally formed during the epitaxial growth of the semiconductor. A particular source of defects comes from the presence of surfaces interrupting the semiconductor lattice. At the edges of the active region or at the hetero-structure interfaces the crystal lattice geometry is broken. This causes the presence of many dangling bonds that can absorb impurities from the external environment.

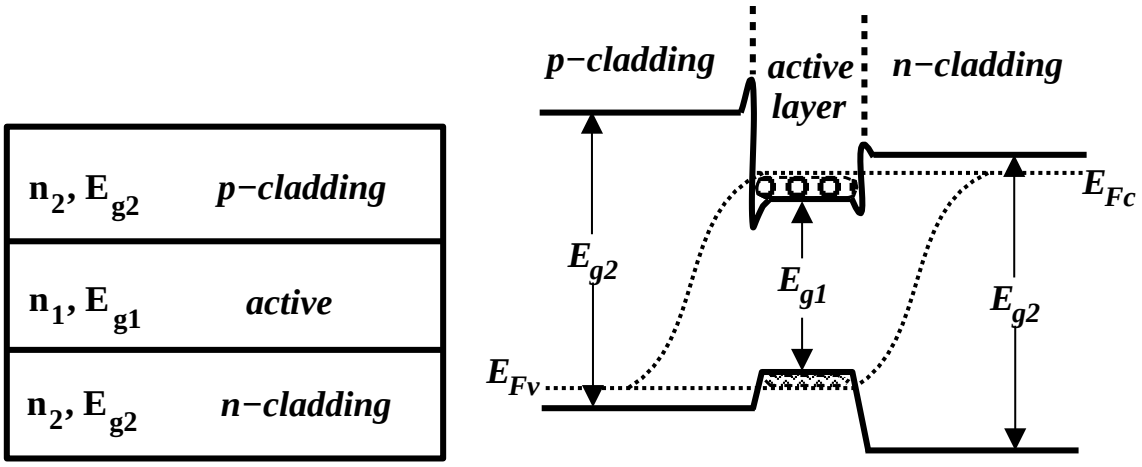

Figure 1.5: Left: Three-layer slab-waveguide heterostructure: $n_1 > n_2$, $E_{g1} < E_{g2}$. Right: Energy band diagram of a double heterostructure laser under forward bias.

Apart from the internal losses mechanisms, in the junction composed by the same band gap semiconductor (homostructure), the optical gain is limited by the very small size of the active region. In the homostructure the population inversion is reached only in the narrow portion of the junction where the electrons and holes are coexisting. The first diode lasers, based on this type of structure, had very large current threshold values ($> 50kA/cm^2$) and they were running just in pulsed mode at room temperature.

More efficient structures are double heterostructure and the quantum-well heterostructure (see Refs. [1, 36]); the modern semiconductor lasers are based on these solutions.

Double heterostructure lasers (DH) are formed by sandwiching a thin (100 to 200 nm thick) active layer of a given semiconductor material between two or more cladding layers of different semiconductor materials with wider band-gap. The cladding materials must posses almost the same lattice constant of the active layer in order to avoid formation of lattice defects during the growth of the wafers. The heterostructure provides better carrier confinement than the homostructure: the potential barriers at the heterojunctions prevent the outflow of electrons (holes) from the n-type region, while the bandgap difference helps

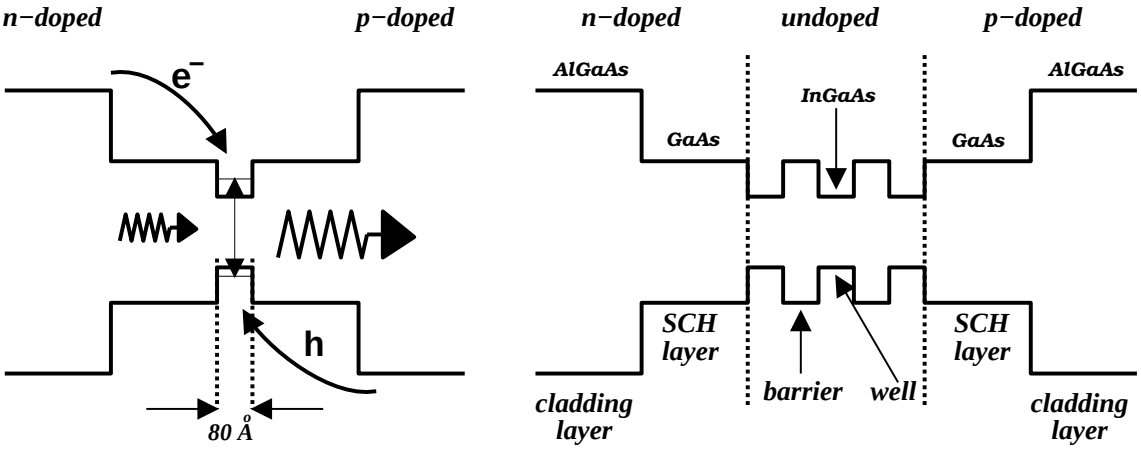

Figure 1.6: Band structure of a single (left) and multi quantum (right) well hetero-structure.

the injected carriers to be confined at the active region, as shown in Fig. 1.5. Moreover, the heterostructure provides optical confinement of the radiation: since the cladding layers have a smaller refractive index than the active layer, they originate a dielectric waveguide which confines, by total internal reflection, the generated photons in the vicinity of the active region.

A single quantum-well laser is similar to a conventional bulk heterostructure (Fig. 1.6), but with the active layer only a few nanometers wide ($< 20\ nm$), which requires sophisticated growth techniques. In a quantum well, carriers are confined along the direction normal to the quantum-well plane (quantization direction), and their energy and density of states become quantized. Coherent radiation occurs by stimulated electron-hole recombination between the quantized sub-bands of the conduction and valence bands. Because of the thin heterostructure, carriers are tightly confined, resulting in a better efficiency than in bulk laser diodes, and thus in lower threshold devices. However, optical confinement requires the addition of separate confinement heterostructure layers with a refractive index in between that of the cladding layers and the wells. Multiple quantum wells can also be produced by alternating narrow layers with low and high bandgaps, which allows for higher powers.

Different emission wavelengths may be obtained changing the semiconductor materials or the doping levels. Nowadays semiconductor lasers cover the optical spectrum from near ultraviolet to far infrared. It is important that the lattice vector of the two semiconductors of a specific heterostructure match each other to better than 0.1%. This requirement fixes the semiconductors pairs for obtaining a specific wavelength. Blue-green visible lasers are based on the $ZnSe$ family on $GaAs$ substrates, such as $ZnSSe$ and $ZnCdSe$. Red visible lasers, operating between 620 and 690 nm, are based on $Ga_{1-x}In_xP$ or $(Al_xGa_{1-x})_yIn_{1-y}P$ on $GaAs$ substrates. Laser diodes based on $Al_xGa_{1-x}As$ technology grown on $GaAs$ substrates emit at relatively higher wavelengths, from 750 to 870 nm, depending on the aluminum concentration. The other common group of lasers is based on $In_xGa_{1-x}As$ grown on $GaAs$ substrate or $In_{1-x}Ga_xAs_{1-y}P_y$ on InP substrates, having emission wavelengths in the near infrared area (980 to 1650 nm). Longer wavelength regions, from 1.7 to 4.4 μm, are covered by $InGaAsSb$ lasers on $GaSb$ substrates.

The optical confinement

In conventional semiconductor lasers, known as *edge-emitting lasers*, the resonator is a Fabry-Pérot cavity of partially reflecting facets, formed by cleaving the wafer along parallel crystal planes to create flat mirror facets. The presence of the resonator fixes the direction of propagation for the stimulated light emission.

The double heterostructure determines the mechanism for the optical confinement in the direction perpendicular to the junction plane. A third confinement mechanism is required to confine the radiation in the plane of the junction, perpendicularly to the direction of the radiation propagation. This confinement is obtained through two main techniques: *index guiding* or *gain guiding*. The first

one is obtained by building a dielectric waveguide laterally to the radiation propagation axis. In the second one, it is the gain profile, determined by the injected current profile, that confines laterally the radiation. The index waveguide may be sized in order to support just the fundamental transverse-mode. In this case, normal dimensions of the waveguide are hundreds of microns along the cavity axis, few microns along the direction perpendicular to the cavity axis, in the junction plane, hundreds of nanometer perpendicular to the junction plane.

In such a quasi planar waveguide built-in a semiconductor laser two polarization modes may propagate: the transverse electric (TE) and the transverse magnetic (TM). The TE modes have the electrical field vector perpendicular to the direction of propagation in the plane of the junction, while for the TM it is the magnetic field vector to have this direction. The facets reflectivity at the end of the cavity are larger for the TE-modes and the optical confinement is more efficient for the TE modes than for the TM modes. Hence the TE modes have a lower threshold gain than the TM modes and are strongly selected in edge-emitting laser diodes, unless the gain itself strongly favors TM.

Other techniques for building the optical cavity in edge-emitting lasers consist of a periodic index perturbation integrated along the laser structure and acting as a grating. In the Distributed Feedback (DFB) laser structure the grating region is built into the pumped part of the gain region, while in the Distributed Bragg Reflector (DBR) lasers the grating replaces the usual cleaved mirror on one or both sides of the resonator.

A completely different approach is employed in the Vertical-Cavity Surface-Emitting Lasers ($VCSEL's$, see Ref. [37]). In these lasers, the cavity is vertical and the mirrors, typically quarter-wave $DBRs$, are parallel to the wafer surface. It is worth noting that in quantum-well $VCSEL's$ the quantization direction coincides with the emission direction while in the other classes of quantum-well

laser diodes is always perpendicular. We will describe the $VCSEL's$ in details in the paragraph three.

1.2.2 Light-matter interaction in a semiconductor medium

The electro-magnetic field equation in a semiconductor laser medium reads:

$$\bigtriangledown^2 E - \sigma\mu_0\partial_t E - \frac{1}{c^2}\partial_t^2 E = \mu_0\partial_t^2 \mathbf{P} \tag{1.2.2}$$

The difference in respect with the 1.1.8 is the term containing the conductivity, neglected in case of gas lasers. Under steady-state condition and considering just the linear polarization we can write, after Fourier transforming:

$$\mathbf{P}_\omega = \epsilon_0\chi(\omega)E_\omega \tag{1.2.3}$$

χ is the electrical susceptibility, analogous to the scaled version introduced, for a two level laser, in 1.1.21. In general χ is a second rank tensor, in the case of isotropic medium it is a scalar. Dealing with semiconductor materials it is convenient to separate χ in two complex components: the first being the susceptibility in the absence of external pumping χ_o; the second being the additional contribution related to the pumping strength, χ_p. Omitting the notation for the dependence with ω:

$$\chi = \chi_o + \chi_p \tag{1.2.4}$$

Fourier transforming the 1.2.2, replacing the 1.2.3 we solve the equation for the field propagation in the Active Medium. We obtain for the complex index of refraction of the Active Medium, $\bar{\mu}$:

$$\bar{\mu} = \mu + i(\Lambda/2k_0) \tag{1.2.5}$$

where

$$\mu = (1 + \Re(\chi_o) + \Re(\chi_p))^{1/2} \tag{1.2.6}$$

$$\Lambda = \frac{k_0}{\mu}[\Im(\chi_o + \chi_p) + \sigma/(\epsilon_o\omega)] \tag{1.2.7}$$

μ is the refractive index of the medium, while Λ is the power-absorption coefficient. Eqts. 1.2.6 are very general and may be applied also to conventional two-level lasers. The index of refraction μ depends on the the external pumping. In general $\Re(\chi_p) << 1 + \Re(\chi_o)$ and we can approximate $\mu = \mu_b + \Delta\mu_p$, being μ_b the refractive index of the unpumped material and $\Delta\mu_p$ the change induced by the pumping.

$$\Delta\mu_p \approx \Re(\chi_p)/2\mu_b \tag{1.2.8}$$

In two-level lasers, $\Delta\mu_p = 0$ when there is no detuning between the frequency of the laser field and the atomic transition frequency. In the first section we have shown that the frequency of the laser field is close to the gain curve peak frequency; thus $\Delta\mu_p \approx 0$ for two-level lasers. For semiconductor lasers the term $\Delta\mu_p$ does not vanish at gain peak frequency. The reason of this difference lies on the band structure of the energy levels in the semiconductor medium and on the high density of charge carriers in the active region which determines band-gap shrinkage and band-filling. We will discuss this issue in paragraph four. Here we just underline that $\Delta\mu_p$ is normally negative and the correction term is of the order of 1% of the unpumped material index of refraction. The power absorption coefficient is given by the term $\Im(\chi_o)$ that accounts for the unpumped material absorption; the term $\Im(\chi_p)$ that accounts for the effect of external pumping on the material absorption and the term $\Lambda_{int} = \frac{k_0\sigma}{(\epsilon_o\omega\mu)}$ that accounts for several internal mechanism of internal losses as free-carrier absorption and scattering at the heterostructure interfaces. We can define the net gain g as

$$g = -\frac{k_0}{\mu_b}\Im(\chi_o + \chi_p) \tag{1.2.9}$$

Then the net absorption coefficient is given by

$$\Lambda = -\Gamma g + \Lambda_{int} \tag{1.2.10}$$

where Γ is the *confinement factor*, taking into account the spreading of the optical mode beyond the active region.

At this point it is easy to obtain the threshold condition and the resonant frequencies for the resonator. Threshold condition requires that the field reproduces itself after a round-trip, calling R_1 and R_2 the facet reflectivities at the two ends, ℓ the length of the cavity, and assuming single-mode operation, we have, separating real and imaginary part:

$$(R_1 R_2)^{1/2} e^{(-\Lambda \ell)} = 1 \tag{1.2.11}$$

$$sin(2\mu k_0 \ell) = 0 \tag{1.2.12}$$

The threshold condition for the gain is then

$$\Gamma g_{th} = \Lambda_m + \Lambda_{int} \tag{1.2.13}$$

where Λ_m is the mirror loss: $\Lambda_m = \frac{1}{2\ell} \ln(\frac{1}{R_1 R_2})$.

The lasing frequencies are given by the cavity-resonance frequency:

$$\nu = j \frac{c}{(2\mu\ell)} \qquad j \epsilon \mathbf{N} \tag{1.2.14}$$

The mode separation is given by $\Delta\nu = c/(2\mu_g \ell)$, where $\mu_g = \mu + \nu(\partial\mu/\partial\nu)$ is the group index of the dispersive semiconductor material. Thus, eqt. 1.2.8 indicates that longitudinal-mode frequencies and their separation depends on the external pumping.

We have now to relate the gain g with the pumping current J. It becomes unavoidable to describe the coherent response of the semiconductor material to the optical field. The problem is to find an expression for the susceptibility χ, relating the electrical field E and the polarization $\mathbf{P}$ induced. Several approaches are possible. The most complete one is the quanto-mechanical one, analogous to the approach explored for the gas laser. Defining the density matrix operator ρ

and the dipole-moment p, we have

$$\mathbf{P} = Tr(\rho p) = \sum_{c,v} (\rho_{cv} p_{vc} + \rho_{vc} p_{cv}) \tag{1.2.15}$$

The sum is over all the energy states per unit volume in the conduction and valence bands. The evolution of the density operator is given by

$$\dot{\rho} = \frac{1}{i\hbar}[H_0 - \overrightarrow{p} \bullet \overrightarrow{E}, \rho] - \frac{1}{2}[\gamma\rho + \rho\gamma] + \Upsilon \tag{1.2.16}$$

H_0 is the unperturbed Hamiltonian of the semiconductor, γ is the decay operator and Υ takes into account the carrier generation in the active region for the external pumping.

This approach is extremely complex for semiconductor lasers. In the γ operator are included both interband process and the intraband process (electron-electron scattering, electron-phonon scattering) and the latter are not yet well understood. Moreover the band structure and the density of states in the bands is required for writing H_0. Some progress has been done by the assumption of the parabolic density of states. We will discuss these improvements in the paragraph four.

A simpler way to deal with gain in semiconductor laser consists in assuming the gain dependence on carrier density as observed experimentally or as obtained numerically from eqt. 1.2.16 and incorporating this dependence phenomenologically in the laser equation describing the light-matter interaction.

In the next paragraphs we develop the problem of finding an expression for the susceptibility χ of the semiconductor media, for brevity we limit our analysis to bulk semiconductor structures.

1.2.3 The phenomenological description: Rate-Equations

The phenomenological approach is based on the fact that, in bulk semiconductor lasers, the gain calculated at the lasing frequency varies almost linearly with the injected carrier density and the same happens to the term $\Delta\mu_p$ in the expression of the refraction of index.

$$\begin{aligned} g(N) &= a(N - N_0) \\ \Delta\mu_p &= bN \end{aligned} \tag{1.2.17}$$

being N_0 the carrier density level at which the transparency occurs. Then aN_0 is the absorption coefficient of the unpumped material. It worth to point out that these equations are in good agreement with the experimental observations. We have now an expression for the pumping dependent susceptibility:

$$\chi_p = \mu_b(2b - ia/k_0)N \tag{1.2.18}$$

We can defined the so-called α (Ref. [38]) factor expressing the coupling between the real and the imaginary parts of the carrier dependent susceptibility:

$$\alpha = -2k_0\frac{\Re(\partial\chi/\partial N)}{\Im(\partial\chi/\partial N)} = \frac{\Re(\chi_p)}{\Im(\chi_p)} \tag{1.2.19}$$

The α factor is an important parameter for describing the light-matter interaction in semiconductor materials. It depends on the frequency detuning between the optical field frequency and the gain peak frequency of the material. When considering lasing operation in conventional edge-emitting lasers, this detuning is negligible because of the high density of longitudinal-modes below the gain curve. In the frame of the phenomenological eqts. 1.2.17, valid at the lasing frequency, we have $\alpha = -\frac{2k_0 b}{a}$. Since b is negative, α is a positive dimensionless number. This factor reveals the main difference between the semiconductor laser and the two-level ones, as we anticipated when describing the dependence of the

refraction index on the pumping rate. The equivalent for α in a two-level medium is the detuning between the gain peak frequency and the optical field frequency and it vanishes at resonance. This is not true for semiconductor laser where, in spite of the negligible detuning between the lasing frequency and the gain peak, the α factor takes values from two to six (Refs. [38, 39]). These values marks the difference between the α factor and the detuning of the two level lasers. No laser action is expected for a detuning value so large: it would be equivalent for the laser to emit at a frequency which is detuned from the gain peak five times the gain curve $HWHM$ width, which is unphysical. From this point of view it is difficult to apply the two-level Maxwell-Bloch equations to the semiconductor laser, unless introducing the α factor phenomenologically.

The α factor for a semiconductor medium is calculated in a fundamental way in paragraph four, following the approach depicted by eqt. 1.2.16 with the assumption of the parabolic density of states. The origin of α lies on the gain curve of the semiconductor media. Because of the presence of energy bands rather than two energy levels, the gain curve is asymmetric (Ref. [40]) and it is peaked at a frequency for which the carrier induced refraction index is not zero. On the contrary, in two-level lasers, the gain curve has a symmetric Lorentzian shape and Kramer-Kronig's relations imply the absence of dispersive effects at the gain peak.

The α factor has a strong impact on the spectral properties of the laser and also on its stability when perturbed by external mechanisms. The laser field linewidth has been found to be enhanced by a factor $(1 + \alpha^2)$ (Ref. [40]), hence the name *linewidth enhancement factor* often attributed to α.

The phenomenological eqts. 1.2.17 allow for relating gain and dispersion with the carrier density at the lasing frequency. In order to be able to write the semiconductor laser equations we need an expression that related the carrier

density N with the current density J. This is obtained through a rate-equation for the electrons. The total charge neutrality guarantees that the rate-equation for the holes is derivable from the one for the electrons.

$$\dot{N} = D(\bigtriangledown^2 N) + \frac{J}{qd} - R(N) \tag{1.2.20}$$

D is the diffusion coefficient of the carrier density, the second term takes into account the injection rate of the carrier through external pumping, $R(n)$ considers the carrier loss due to the different recombination processes.

When the semiconductor laser is strongly index guided and the active region is much smaller compare to the diffusion length, the diffusion term may be neglected. Then at the steady-state we have simply $J = qdR(N)$. The expression of $R(N)$ should take into account all the recombination process. The most suitable form for $R(N)$, valid if the doping level of the active region is much smaller than the carrier density injected, is given by

$$R(N) = A_{nr}N + BN^2 + CN^3 + R_{st}N_{ph} \tag{1.2.21}$$

The term $A_{nr}N$ takes into account the non radiative recombination, BN^2 consider the spontaneous-emission, CN^3 describes the Auger effect and, finally, $R_{st}N_{ph}$ where N_{ph} is the intracavity photon density and $R_{st} = (c/\mu_g)g(N)$ expresses the stimulated recombination that leads to the coherent emission of radiation. It worth to point out that this phenomenological model assumes the coefficient A, B and C independent of the pumping level. In fact, this approximation is rather crude since it is well known that B depends on the carrier density, while the Joule heating of the Active Medium, because of the pumping current flow, affects remarkably C. Remembering 1.2.20, 1.2.13 we can write the threshold condition for the pumping current:

$$J_{th} = qdN_{th}/\tau_e(N_{th}) \tag{1.2.22}$$

being:

$$N_{th} = N_0 + (\Lambda_m + \Lambda_{int})/(a\Gamma) \qquad \tau_e(N_{th}) = (A_{nr} + BN_{th} + CN_{th}^2)^{-1} \quad (1.2.23)$$

being τ_e the recombination time of the carriers. We can also obtain the intracavity photon density relationship with the pumping current:

$$N_{ph} = \eta_i(\tau_p/qd)(J - J_{th}) \quad (1.2.24)$$

where η_i is the internal quantum efficiency introduced phenomenologically, v_g is the group velocity and τ_p is the lifetime of the photon in the cavity.

$$\tau_p^{-1} = v_g(\Lambda_m + \Lambda_{int}) \quad (1.2.25)$$

When threshold is reached the carrier density stays locked to the value n_{th} while the light emission increases with increasing the pumping current. The power emitted by the laser is given by $P_{out} = \frac{1}{2}h\nu v_g \Lambda_m V N_{ph}$, being $V = Lwd$ the active region volume. Hence, we obtain

$$P_{out} = \frac{h\nu}{2q}\frac{\eta_i \Lambda_m}{\Lambda_m + \Lambda_{int}}(I - I_{th} - \Delta I_L) \quad (1.2.26)$$

being ΔI_L the possible increase of the leakage current with the current I. Eqt. 1.2.26 takes into account the fact that the increase of the emitted power is not increasing linearly with the pumping, for large of the current. Three contributions are predicted to contribute to power saturation:
i)The increase of leakage current with I, through the term ΔI_L, ii)The increase of I_{th} with I because of junction Joule heating that reduce the recombination carrier time τ_e. Recombination rate increases, as we have already mentioned, because of the increase of the contribution from the Auger effect C with the temperature, iii)The internal loss Λ_{int} increases with I.

The phenomenological approach describes quite well the characteristics of emission of a semiconductor laser. It is natural then to extend this procedure to describe the laser dynamics.

Semiconductor laser Rate-Equations

The phenomenological approach leads to the semiconductor rate equations. These are obtained solving the field propagation eqt. 1.2.2-1.2.3 with the assumptions 1.2.17-1.2.18. The field can be developed on the basis formed by the laser cavity resonance frequencies; assuming $SVEA$ approximation and single transverse-mode profile we end up with:

$$\begin{aligned} \dot{E} &= \frac{1+i\alpha}{2}[\Gamma G(N) - \tau_p^{-1}]E \\ \dot{N} &= \frac{J}{qd} - A_{nr}n + BN^2 + CN^3 - G(N)\mid E \mid^2 \end{aligned} \tag{1.2.27}$$

where $G(N) = a\frac{N-N_0}{1+\epsilon|E|^2}$; ϵ is the non-linear-gain coefficient and it has been introduced phenomenologically in order to take into account the saturation of the gain. Dividing the slowly varying part of the electric field E in amplitude and phase: $E = \sqrt{I}e^{i\phi}$ we can replace the field equation in 1.2.27 by:

$$\begin{aligned} \dot{I} &= [\Gamma a\frac{N-N_0}{1+\epsilon\mid E \mid^2} - \tau_p^{-1}]I \\ \dot{\phi} &= \frac{1}{2}\alpha a\Gamma\frac{N-N_0}{1+\epsilon\mid E \mid^2} \end{aligned} \tag{1.2.28}$$

We have already commented that the validity of these equations lies on the fact that the polarization decay rate depends on the intraband phenomena which have a timescale much shorter than the carrier and photon lifetimes. According to the number of degrees of freedom of this laser system, semiconductor laser can be classified a class B laser. It worth to remember that adiabatic elimination of the fast variables must be employed with great care in presence of laser instabilities (Ref. [22]). This establishes a limitation for using the rate eqts. 1.2.28 in order to describe a laser instability, possibly because of external mechanism (feedback, optical injection). Moreover, in 1.2.27, the boundary conditions, represented by the optical resonator, have been imposed by including the facet loss term α_m in the photon lifetime 1.2.25. A rigorous approach would require (see section one)

to consider the spatial dependence of E along the cavity, and then the integration of $E(z)$ through the longitudinal direction imposing the boundary conditions at the facets. These approximations are particularly severe when rate eqts. 1.2.28 are extended to describe the multi-mode semiconductor laser. Then, eqts. 1.2.28 are written for each mode with different field-carrier density coupling terms, since the gain coefficient changes with optical field frequency and they read:

$$\begin{aligned} \dot{I_m} &= [\Gamma_m G_{(m)}(N) - \tau_{p(m)}^{-1}] I_{(m)} \\ \dot{N} &= \frac{J}{qd} - A_{nr} N + BN^2 + CN^3 - \sum_m (G_{(m)}(N) \mid E_{(m)} \mid^2) \end{aligned} \quad (1.2.29)$$

Since the rate-equations picture neglects the spatial dependence of the electromagnetic field in the cavity, the spatial dependence of the mode-carrier coupling and the mode-to-mode coupling are not considered. As shown in the first section for a two-level laser, such mechanisms are fundamental in order to describe realistically the dynamics of a multi-mode laser. Moreover, in eqts. 1.2.29 the gain coefficient changes with optical field frequency, but the corresponding spectral dependence of the refraction index change on carriers (through the α factor) is not taken into account. Thus, eqts. 1.2.29 are not a valid tool to predict semiconductor laser instabilities. However, in spite of those limitations, the rate-equations model is quite useful for small-signal analysis of the laser: it describes rather accurately phenomena like noise properties, transient response and intensity modulation. In addition, several features like spectral variation of the lasing frequency due to thermal effects, band-filling or band shrinkage can be added phenomenologically to the model through suitable coefficients. In this way, physical mechanisms of very complex theoretical description may be implemented in a unified and simple approach that, under certain conditions, is reliable enough to predict the laser response to a small perturbation.

A more rigorous approach should be based on the derivation of an equation

able to describe the coherent field-semiconductor medium interaction. We have already mentioned, when introducing the eqt. 1.2.16, the difficulties of deriving an expression for the electrical susceptibility of the semiconductor lasers. In particular, one of the problems comes from the complexity of the energy band structure of semiconductor media. Two approaches have been explored: the microscopic description (Ref. [41]) and the effective two-level model (Ref. [20]). The microscopic approach tries to evaluate the susceptibility of the semiconductor media starting from the electronic structure of the crystal, considering or not many-body effects (Refs. [42, 43, 44]). The limitation of these models is their complexity and that they apply strictly only to *CW* laser operation or to small signal analysis. Anyway this exact approach is extremely useful when we want to relate macroscopic properties of the semiconductor media with their band structure.

The effective two level model consists in reducing, after opportune approximations, the band structure of the semiconductor material to an effective two-level system. Then, semiconductor laser equations analogous to Maxwell-Bloch are obtained, allowing for the modeling of the laser dynamics. In fact, since Maxwell-Bloch equations consider explicitly the coherent coupling between the optical feedback and the semiconductor medium, they enable large-signal analysis, four-wave mixing analysis and they consider the possibility of multi-mode operation. Moreover, the effective two-level model incorporates phenomenologically the main results of the microscopic theories, including thermal effects and many-body interaction. We will describe this approach in the next paragraph.

1.2.4 The effective two-level description

This paragraph is based on the paper by S.Balle, Optics Comun. **119**, 227 (1995)

The effective two-level model is based on the Maxwell-Bloch equations as obtained in the first section with all the related approximations assumed (RWA, SVEA, Plane Wave Solution). The difference concerns the slowly varying amplitude of the non-linear polarization of the medium that, for the semiconductor laser, has to be obtained taking into account the semiconductor band structure. This derivation is based on the calculation of the electrical susceptibility of the semiconductor medium that, in a two-band approximation, reads

$$\chi_E(\omega) = -\frac{2i}{V\varepsilon_0}\sum_k \mid M_{cv}(k) \mid^2 \frac{f_c(k) - f_v(k)}{i[E_{cv}(k) - \hbar\omega] + \gamma(k)} \tag{1.2.30}$$

being V the crystal volume, $E_{cv}(k) = E_c(k) - E_v(k)$ the energy difference between the conduction and the valence band states, $M_{cv}(k)$ is the electric dipole element between the conduction and the valence band states, $\gamma(k)$ is the transition linewidth, $f_c(k)$ and $f_v(k)$ are the quasi-equilibrium Fermi-Dirac distributions functions for the electrons in the conduction and in the valence bands and the summation is performed over all k vector in the first Brillouin zone. Eq 1.2.30 would require a numerical treatment for realistic band structure and finite temperature. Here we assume: i) parabolic bandstructures: $E_c = E_g/2 + (\hbar^2 k^2)/(2m_c)$, $E_v = -E_g/2 - (\hbar^2 k^2)(2m_v)$ (m_c and m_v being the effective mass in the conduction and in the valence band respectively), ii) $M_{cv}(k) = M$, iii) $\gamma(k) = \hbar/T_2$, that is considering the electric dipole strength and the transition linewidth independent of k. The contributions to $\chi_E(\omega)$ cannot be evaluated analytically except at zero temperature, replacing the summation by an integral. Then, considering the quasi-Fermi level close to the bottom of conduction band and just the frequency

relevant to the lasing process, we obtain

$$\chi_E(\omega) = \chi_L(\omega) + \frac{\mid M \mid^2}{\varepsilon_0 \hbar} \frac{N - N_0(1 - i\alpha_0)}{z} \tag{1.2.31}$$

where $N = N_e + N_h$ is the carrier density out of equilibrium, $z = \omega - E_g/\hbar + i/T_2$, $\chi_L(\omega)$ includes the terms not depending on N directly, and $N_0(1 - i\alpha_0)$ is defined as:

$$N_0(1 - i\alpha_0) = N^{eq} \frac{iT_2^{eq}}{T_2[(\omega_g - \omega_g^{eq})T_2^{eq} + i]} \tag{1.2.32}$$

where the terms N^{eq}, T^{eq} and ω_g^{eq} are the carrier density, the polarization decaying rates and the emission frequency at the gap for the semiconductor being at the equilibrium, i.e. when no current is injected. The main approximation in this last equation is to neglect the frequency dependence of α_0 by assuming $\omega \to \omega_g$. In this way, upon Fourier transforming to the time domain, and after including the linear term in the effective refraction index and losses for the electric field yields a simple equation for the temporal evolution of the non-linear polarization. Considering that the electric field is oscillating at a frequency ω_0 with a slowly varying amplitude E, the evolution equation for the slowly varying amplitude of the non-linear material polarization, P, then reads:

$$\begin{aligned}
\partial_t A &= \frac{1}{2n^2}\left[i\frac{c^2}{\omega_0}\left(\partial_z^2 A + k_0^2 A\right) + i\sqrt{\frac{\omega_0}{\hbar\varepsilon_0}} P - \frac{1}{\tau_p} A \right] \\
\partial_t N &= J - \gamma_e(N)N - \frac{2i}{\hbar}\sqrt{\frac{\hbar\omega_0}{\varepsilon_0}}\left(A^* P - A P^*\right) + \Delta\partial_z^2 N \\
\partial_t P &= \left[-\frac{1}{T_2} + i(\omega_0 - \omega_g) \right] P - \\
&\qquad -i\Gamma\frac{|\mu|^2}{\hbar}\sqrt{\frac{\hbar\omega_0}{\varepsilon_0}}(N - N_0 + i\alpha_0 N_0)A
\end{aligned} \tag{1.2.33}$$

where A denotes the modal amplitude of the optical field normalized in such a way that $|A|^2$ corresponds to photon density, $k_0 = n\omega_0/c$, τ_p is the photon lifetime inside the cavity due to losses, and n is the effective refraction index in the active

region. T_2 is the polarization lifetime, and N_0 is the transparency carrier density at frequency ω_g. J is the injection current density into the active region per unit time (in carriers per unit time and unit volume), $\gamma_e(N) = 1/\tau_e$ is the nonradiative decay rate of the injected carriers, which in general may depend explicitely on the carrier density (Ref. [1]), Δ is the effective carrier diffusion coefficient, and Γ is the modal confinement factor into the active region (defined as the fraction of modal power confined within the active region). The physical origin of α_0 comes from the electronic structure of the semiconductor materials; the band structure allows for the spreading of the transition energies, all nearly resonant. As a consequence, the complex electrical susceptibility, which takes into account all the possible transitions, cannot be purely imaginary even at the gain peak. The presence of the parameter α_0 in 1.2.33 implies three fundamental differences between semiconductor laser and conventional two-level lasers: i)the gain and the refraction index spectral shapes of the Active Medium are asymmetric and ii)the gain is maximum where the dispersion does not vanish, iii)the gain and the refraction index spectral shapes depends on the carrier density. The gain peak shift to larger frequency and increases to larger values as N increases. In this third point thermal and many-body effects play an important role as well. Considering these effects in addition to the parameter α_0 and incorporating them in a term α_{eff} it is possible to calculate the α factor obtaining values close to the experimental ones (Ref. [39]). The derived α_{eff} is equivalent to the phenomenological term introduced in the last paragraph.

In general, T_2 and ω_g may depend on both carrier number and on Joule heating related to the value of J. Increasing the temperature in the active region leads to a redshift of the frequency of the gain peak (see §II.1.2) and to a reduction of the maximum gain (Ref. [42]). These effects are not taken into account in the model 1.2.33, since we have supposed $T = 0$.

Moreover, as N increases, many-body effects induce a bandgap shrinkage (Ref. [45]) and they lead to an increased carrier scattering which reduces T_2 (Ref. [44]) and modify the width of the gain curve. These changes due to variations of the carrier density do not affect the Lorentzian shape of the gain spectrum characteristic of the two level model. The eqts. 1.2.33 enable the analysis of the effects of carrier density on both ω_g and T_2.

In order to gain insights into these effects, we can assume a linear dependence of γ_p and of ω_g with the carries. Thus, through the linear coefficients, we can account for the above mentioned effects in a phenomenological way.

$$\gamma_p = 1/T_2 = 1/T_2^0 + r(N - N_0); \qquad \omega_g = \omega_g^0 + s(N - N_0) \tag{1.2.34}$$

The steady-state complex susceptibility is then given by

$$\chi(\omega) = -ia \, \frac{D + i\alpha_0}{1 + \rho D - i(\theta - \sigma D)} \, , \tag{1.2.35}$$

where $a = \Gamma N_0(|\mu|^2 T_2^0/\hbar)(\hbar\omega_0/\varepsilon_0)^{1/2}$ determines the differential gain, $\theta = (\omega_0 + \omega - \omega_g^0)T_2^0$ is a normalized frequency detuning, $D = N/N_0 - 1$, and $\rho = rN_0T_2^0$ and $\sigma = sN_0T_2^0$. The gain spectrum is determined as $g(\omega) = (-\omega_0/nc)\Im(\chi(\omega))$, where n is the refraction index of the Active Medium, and the additional change in the refraction index is given by $\Delta n = (1/2n)\Re(\chi(\omega))$. In semiconductor media, at difference with the conventional two-level system, the resulting gain spectrum is not symmetric about its peak, and the gain peak no longer corresponds to zero dispersion (see Figs. 1.7).

Moreover, the gain peak shifts towards larger frequencies as the carrier density increases, as experimentally observed in the experiments at constant temperature (Ref. [46]). As pointed out before, the asymmetry of the gain spectrum depends only on the value of α_0; the dependence on N of both T_2 and ω_g leads only to a variation of both the frequency of the gain peak and the gain bandwidth, but the gain spectrum keeps a lorentzian shape. Moreover, because of band-filling,

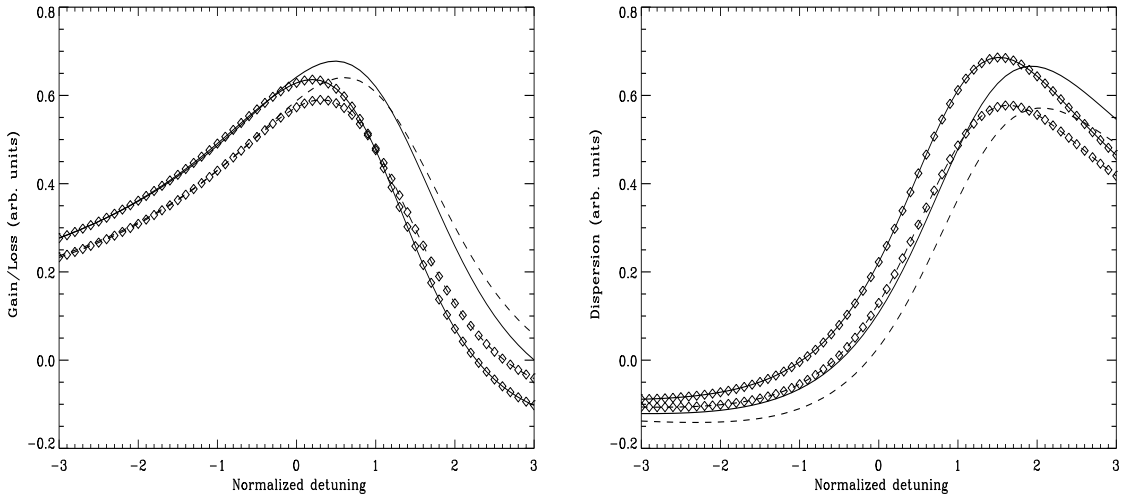

Figure 1.7: (right)Gain spectrum as a function of the normalized detuning θ obtained for $\rho = 0.75$ and $\sigma = 1.2$ for $\alpha_0 = 0.9$ (solid line) and $\alpha_0 = 0.7$ (dashed line). Lines with no symbols correspond to $N = 1.99N_t$ and lines with symbols to $N = 1.79N_t$. (left) Dispersion spectrum for the same parameters as above. The value $\rho = 0.75$ used in Fig. 1.7 implies that the polarization decay rate increases five times when going from $N = 0$ to $N = 2N_0$ thus giving about 80% reduction in the maximum gain due to both thermal and many-body effects; also, the value $\sigma = 1.2$ corresponds to the case where the frequency of the gain peak exhibits a blueshift of about 7 nm when going from $N = 0$ to $N = 2N_0$. From Ref. [20].

the parameter α_0 yields a carrier-induced shift in the frequency of the gain peak even for $s = 0$. When $r = s = 0$, the gain peak occurs at

$$\theta_p = \frac{1}{\alpha_0}\left(D - \sqrt{D^2 + \alpha_0^2}\right) , \tag{1.2.36}$$

so the frequency of the gain peak exhibits a blue-shift towards $\theta = 0$ as the carrier density increases. However, the total shift in the frequency of the gain peak in Fig. 1.7 contains also the contribution arising from $\sigma \neq 0$. The effective α parameter can be identified with the phenomenological term defined by eqt. 1.2.19, which now depends on both the frequency and carrier density. In order to match the observed values of α, it is crucial to take into account the dependence on the carrier density of both ω_g and T_2, otherwise α_{eff} essentially corresponds to detuning and hence it is restricted to small values.

The effective α factor has been computed for different injection levels as a function of frequency, some of which are displayed in Fig. 1.8. Fig. 1.8 (left

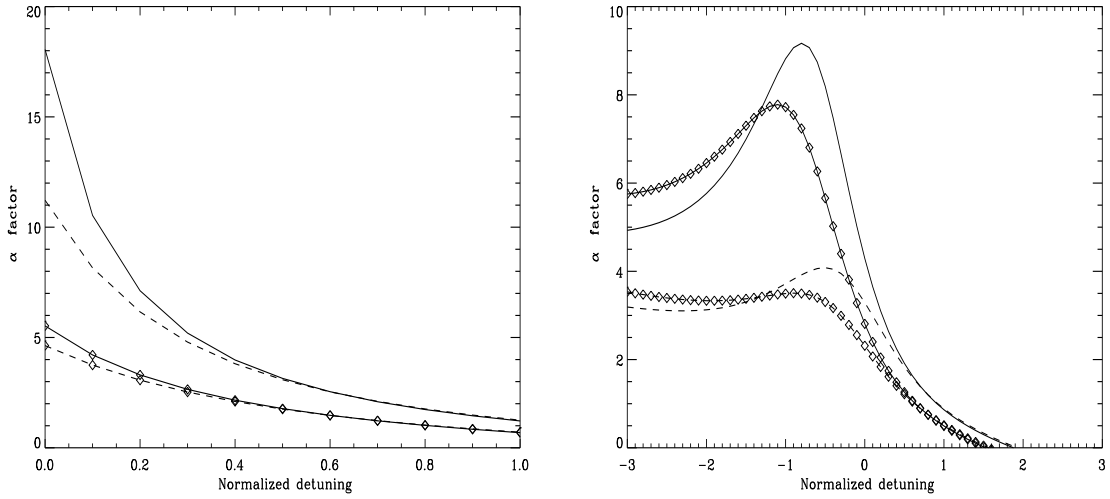

Figure 1.8: (left panel) α_{eff} in the region of maximum gain of Fig. 1.8. (right panel) α_{eff} obtained for $\rho = 0.75$ and $\sigma = 1.0$ for $\alpha_0 = 0.9$ (solid line) and $\alpha_0 = 0.7$ (dashed line). Lines with no symbols correspond to $N = 1.79N_t$ and lines with symbols to $N = 1.59N_t$. From Ref. [20].

panel) shows α in the region close to the gain peak in Fig. 1.7, and for the same parameter values; α is a uniformly decaying function of the normalized detuning θ. However, in Fig. 1.8 (right panel) α shows a rather different behaviour, with a very marked bump in the vicinity of the gain peak (now located around $\theta = 0$); the existence of this bump has been experimentally observed in Ref. [47].

Amplified Spontaneous Emission (ASE) spectrum can be computed from eqts. 1.2.33 for different levels of current injection. Below threshold the stimulated-emission contribution to the carrier density dynamics can be neglected and the spontaneous emission is assumed being proportional to the carrier density and homogeneously distributed through the entire laser modes spectrum. Then, the amplified spontaneous-emission spectrum can be calculated easily from the evolution equations for the electric field and the non-linear polarization by expanding the field in terms of the longitudinal-modes of the Fabry-Pérot laser. The result is plot in Fig. 1.9; the longitudinal modal resonances are superimposed to the asymmetric shape of the gain curve of the Active Medium (Refs. [46, 48]).

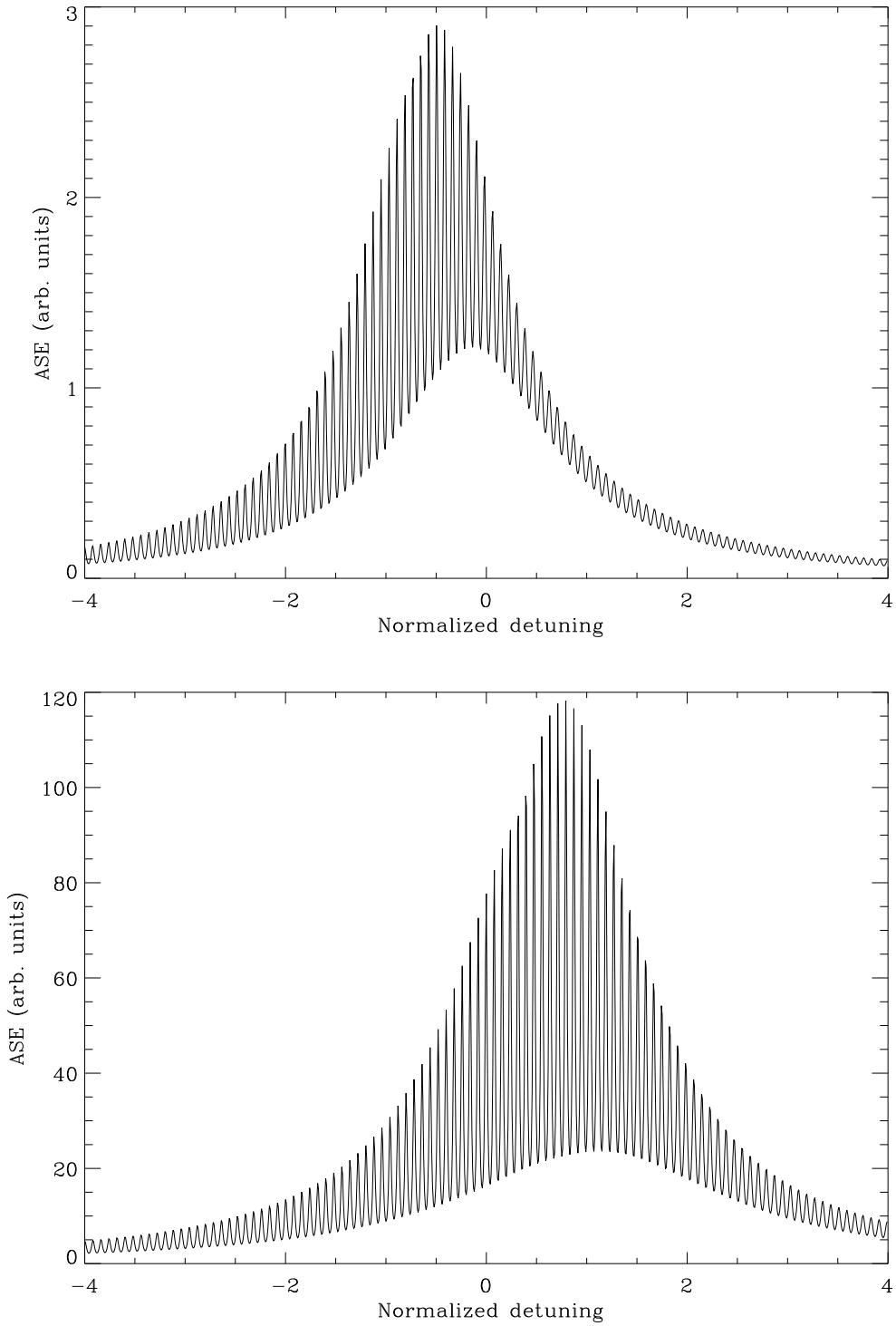

Figure 1.9: Amplified Spontaneous Emission spectrum for the parameters in Fig. 1.9. The upper panel corresponds to $N = N_t$, while the lower panel corresponds to $N = 1.99N_t$. The modes are located symmetrically around $\theta = 0$ with an intermode spacing of $\delta\theta = 0.08$. Note that only about 100 modes on the 500 considered appear to effectively contribute to the ASE. From Ref. [20].

Equations 1.2.33, with boundary condition describing the laser cavity, can be used to simulate the dynamical behavior of the semiconductor laser. This could be useful to understand the observed general multi-mode behavior (see §II.1.2) of the semiconductor lasers, even when they are pumped far above threshold. In fact, because of the extremely short intra-band carrier scattering, semiconductor lasers have an homogeneously broadened gain profile and, therefore, they are expected to exhibit mostly single-mode character. This is not confirmed experimentally. For pumping current close to the laser threshold, the semiconductor lasers optical spectra show several longitudinal-modes excited whose relative power vary with the pump current. In index guided semiconductor lasers the mode-suppression-ratio (MSR, the ratio between the main mode power and the most intense side mode power) increases with the pumping current and, eventually, only one longitudinal-mode dominates on the others (a laser is said to be single-mode when MSR exceed 20 dB). Gain guided lasers maintain their multi-mode character far above threshold and additional technique need to be employed to force a single-mode behavior. Moreover, even for largely pumped index guided lasers, every laser instability (maybe induced by an external perturbation as it is the case for the optical feedback) is coupled to a very rich multi-mode dynamics. In the following paragraph we will describe the physical mechanisms that rule the longitudinal-modes competition and we will show numerical results on the multi-mode dynamics. The same effective two-level approach has been applied to quantum-well lasers in Ref. [49]

Multi-mode semiconductor laser dynamics

This paragraph is based on the paper by M.Homar, S.Balle, M. San Miguel, Optics Comun. **131**, 380 (1996)

The number of lasing modes with significant power depends on the operating conditions of the laser, and it is determined by several mechanism such as *Spontaneous Emission Noise*, *Spatial Hole Burning* (SHB), phase sensitive interactions such as *Four Wave Mixing* (FWM) and *Diffusion* processes.

i)*Spontaneous Emission Noise.* It is well known that the rate of spontaneous-emission into each cavity mode in semiconductor lasers is four or five orders of magnitude larger than in both gas and solid state lasers. This, together with the large gain rate of semiconductor active media, determines the multi-mode optical spectra typical of the semiconductor laser when pumped close to the threshold (Ref. [50]). The large amplified spontaneous emission is "colored" by the comb of the laser cavity modes lying below the gain curve (as shown in Fig. 1.9). Thus, at currents near or slightly above threshold, the power carried by the mode at the peak of the gain spectrum is comparable to the amplitude of the secondary modes. These sides modes eventually saturate at large injection currents, as it would occur normally in a homogenously broadened laser. Single-mode output is achieved only at currents appreciably above threshold when the primary mode power is substantially larger than the power of the secondary modes. Spontaneous emission noise is the dominant mechanism for multi-mode excitation close to the laser threshold; it becomes less relevant for pumping currents well above threshold.

ii)*Spatial Hole Burning, SHB* The low reflectivity of the laser facets in edge-emitting bulk devices prevents us for applying the uniform-field approximation, as done in §I.1.4. Thus, the mode-to-mode coupling between the slow varying

modal amplitudes (the term expressed by eqt. 1.1.38 in the first section) cannot be neglected. This coupling term takes into account the competition between the longitudinal-modes for the maximal gain via the modal profiles. In fact, despite the field intensities are maximal at the laser facets to compensate the losses due to the low reflectivities, each modal profile affects the longitudinal profile of carrier density in a slightly different way.

In addition, the fast spatial oscillating term e^{ikz} of the electric field inside the Fabry-Pérot laser cavity, determines a population "grating" along the cavity axes. The electric field depletes the carriers in the location of the Active Medium where the electric wave field has a trough, while does not affect the location in correspondence with the nodes. Thus, each longitudinal-mode affect the spatial dependence of the carrier density with a different wavelength fast varying term. The longitudinal-modes compete for the maximal gain through the corresponding grating generated in the carrier density profile. In §I.1.3 this coupling is represented by the sum between different modal components in eqts. 1.1.37 and it is worthwhile to remark that it survives to the uniform-field approximation. In absence of carrier diffusion this short range SHB is negligible only very close to the laser threshold, while, further above threshold, it causes the excitation of side modes, giving rise to multi-mode laser emission. Anyway, for semiconductor laser in general, it is less important than the SHB generated by the modal profiles, since carrier diffusion is strong enough to wash out the grating effects in the carrier density profile.

iii) *Carrier Diffusion.* As we have seen, Carrier Diffusion washes out the population grating, limiting the SHB effects. Thus it contributes to enforce single-mode emission, even at large pumping current values. However, smaller values of the diffusion coefficient do not fully eliminate multi-mode emission far

above threshold and it allows for several competing modes, leading to mode-beating and mode-hopping.

In order to analyze the dynamics of the modes competition in semiconductor lasers, let us consider the laser eqts. 1.2.33 where we inserted the phenomenological assumptions 1.2.34. As done for calculating the amplified spontaneous emission spectrum a spatially distributed noise term $\xi(z,t)$ is added to the polarization equation. This term acts as a polarization source and it models independent spontaneous-emission process in different points of the cavity.

We can decompose the electric field amplitude into two counter-propagating waves (Travelling-Wave description),

$$A(z,t) = A^{+}(z,t)e^{ik_c z} + A^{-}(z,t)e^{-ik_c z} \ ,$$

where $A^{+}(z,t)$ is the slowly varying envelope of the electric field propagating forward and $A^{-}(z,t)$ is the slowly varying envelope of the electric field propagating backwards. The set of coupled equations for $A^{+}(z,t)$, $A^{+}(z,t)$, $P(z,t)$ and D are obtained as in Ref. [51]. The obtained set of equations including Travelling-Wave equations for the field which must be solved in conjunction with boundary conditions imposed by the cavity mirrors. This will result in a structure of the field power spectrum without a priori assumptions on the laser longitudinal-mode structure. Denoted by r_1 and r_2 the field amplitude reflectivities of the cavity facets placed at $z = 0$ and $z = \ell$, respectively, the boundary conditions for the field are:

$$A^{+}(z=0,t) = r_1 A^{-}(z=0,t) \qquad\qquad A^{-}(z=\ell,t) = r_2 A^{+}(z=\ell,t) \tag{1.2.37}$$

together with the boundary condition for the longitudinal carrier density

$$\left[\partial_z D\right]_{z=0,\ell} = 0 \ . \tag{1.2.38}$$

The spatial variations in polarization and carrier number over wavelength distances can be treated by means of a Fourier series expansion,

$$P(s,t) = e^{ik_c z}\sum_{p=0}^{\infty} P_{(p)}^{+} e^{2ipk_c z} + e^{-ik_c z}\sum_{p=0}^{\infty} P_{(p)}^{-} e^{-2ipk_c z}$$

$$D(z,t) = D_{(0)}(z,t) + \sum_{p=1}^{\infty}\left[D_{(p)}(z,t)e^{2ipk_c z} + D_{(p)}(z,t)^{*} e^{-2ipk_c z}\right] \qquad (1.2.39)$$

These equations can be studied following the procedure in Ref. [51], truncating the expansion after the first harmonic and keeping only the "grating terms" $p = 1$. This truncation gives rise to a set of coupled equations for $A^{\pm}$, $P_{(0)}^{\pm}$, $P_{(1)}^{\pm}$, $D_{(0)}$ and $D_{(1)}$.

Integration of traveling wave equations starting from random initial conditions for the electric field and for various values of the injection current and carrier diffusion constant, allows the dynamical analysis of the multi-mode dynamics. In particular, the parameters influence on the mode competition dynamics can be investigated. This work has been performed in Ref. [21].

A sample of the main different situations that can be found with this Traveling Wave model is summarized in Fig. 1.10 where the time-evolution of the total output power $I(t) = |A^{+}(z = \ell, t)|^2$ and dominant frequency (inset) are shown for different values of the injection current and of the carrier diffusion coefficient. The crucial role of carrier diffusion is evident. For a diffusion $\Delta = 1.6\ 10^{-5}$ (top panel) the laser reaches single-mode emission after a short transient . Residual chirping associated with the carrier density modulation due to relaxation oscillations can be observed in the dominant frequency (see inset). The same qualitative behavior is observed for two levels of injection current, $D = 1.1D_{th}$ or $D = 1.8D_{th}$. For lower carrier diffusion ($\Delta = 0.4\ 10^{-5}$) (central and bottom panel) laser emission becomes multi-mode, with a number of active modes that depends on the carrier injection level. Close to threshold mode beating between two main modes is observed in the total output power (central panel) with a fast modulation of $I(t)$

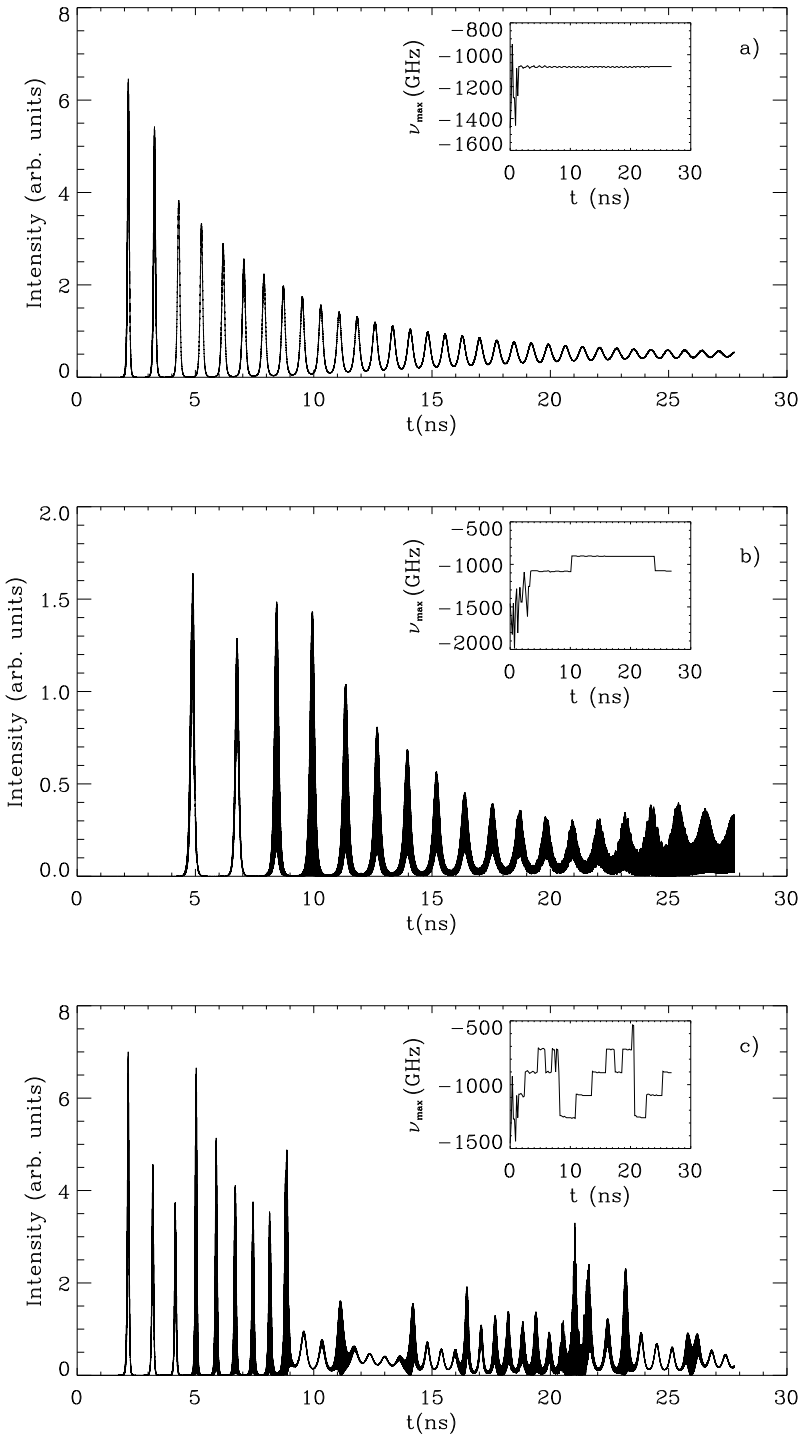

Figure 1.10: Time evolution of the total output power, $I(t)$, for different levels of injection current and diffusion coefficients: a)$D = 1.8D_{th}$ and $D_c = 2cm^2s^{-1}$ ($\Delta = 1.6\ 10^{-5}$); b)$D = 1.1D_{th}$ and $D_c = 0.5cm^2s^{-1}$ ($\Delta = 0.4\ 10^{-5}$); c)$D = 1.8D_{th}$ and $D_c = 0.5cm^2s^{-1}$. D_c is the not scaled version of the diffusion constant. In the inset we plot the frequency carrying the largest power in the time-resolved optical spectrum for each case. From Ref. [21].

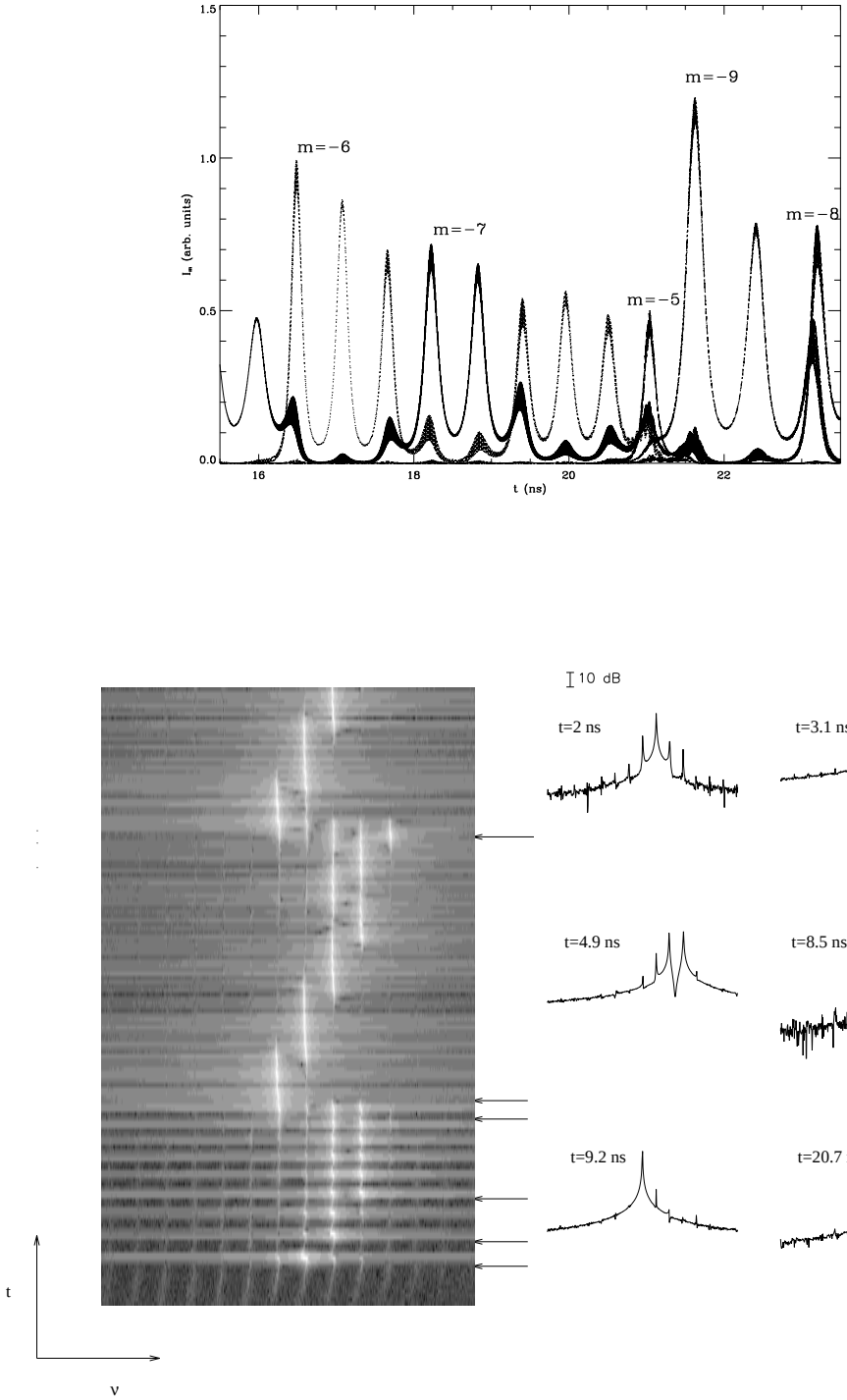

Figure 1.11: upper panel) Output power associated with different active modes as a function of time for $D = 1.8D_{th}$ and $\Delta = 0.4\ 10^{-5}$. (The zero mode is considered the one closest to zero frequency). (lower panel, Left): Time-resolved optical spectrum for the case $D = 1.8D_{th}$ and $\Delta = 0.4\ 10^{-5}$. The power level is displayed in a time and frequency plot on a 16-level gray scale, with black corresponding to the lowest value and white to the highest. Time runs from $t = 0$ to $t = 28\ ns$ on the vertical axis while frequency runs from $-2777.78\ GHz$ to $0\ GHz$ on the horizontal axis. (lower panel, Right): selected samples of the time-resolved optical spectrum taken over different time windows. The starting time for each window is displayed, and their positions in the left panel indicated by arrows. From Ref. [21].

at an oscillation frequency of 171 GHz corresponding to the longitudinal-mode spacing. The two active modes compete but coexist at all times. Higher above threshold (bottom panel) $I(t)$ displays a complicated sustained dynamics which is associated with a recurrent hopping among four (and even five) active modes, as can be observed in the inset.

A more direct description of the mode competition in the situation of Fig. 1.10 (lower panel) is given by looking at the output power associated with each of the active modes (Fig. 1.11, upper panel). There are time windows where the laser emits almost in a single mode (e. g. between 12 and 13 ns), but in other time windows several longitudinal-modes are active. In general, the dominant mode hops in a recurrent way, and it is worth noting that, differently to the case in Fig. 1.10 (central panel), some of the active modes switch-on and off without coexisting at all times. This mode hopping dynamics in can be better explored by looking at the time-resolved optical spectrum, as shown in Fig. 1.11 (lower panel). Mode competition and hopping are clearly displayed, showing time windows of quasi single-mode operation followed by mode hops and time windows of mode coexistence. It is also evident the effects of frequency chirp associated with transient relaxation oscillations as a drift in the positions of the modal peaks; this effect is especially clear in the initial regime (before 9 ns, say), and it also induces the characteristic chirp-induced broadening of the modal peaks in the time-resolved optical spectrum.

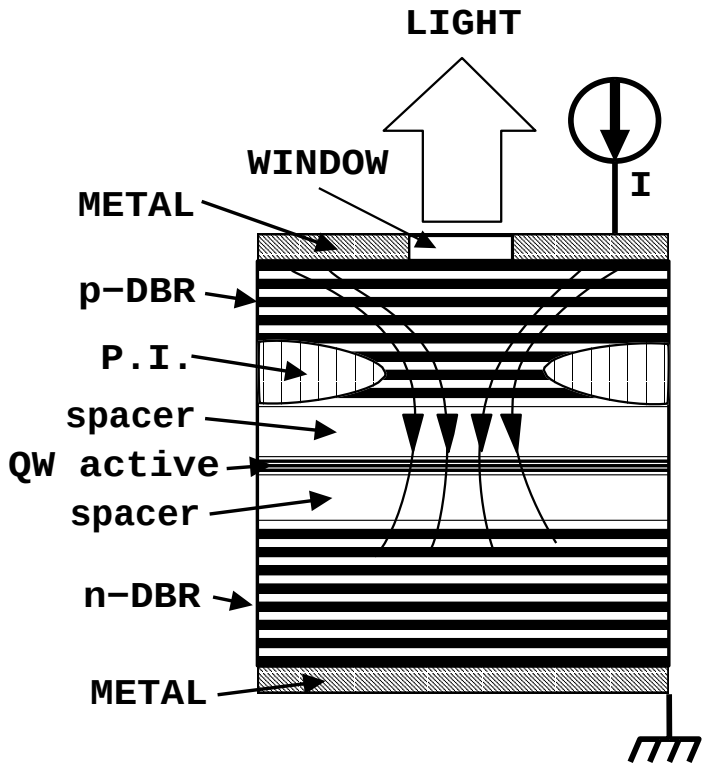

Figure 1.12: Typical $VCSEL's$ structure.

1.3 The Vertical-Cavity Surface-Emitting Lasers ($VCSEL's$)

The $VCSEL's$ are semiconductor lasers where the cavity axis is orthogonal to the semiconductor wafer layers (Refs. [52, 53]). The concept of a vertical cavity structure together with the standard semiconductor growth technology allow the creation, from a single wafer chip, of many $VCSEL's$ arrays whose optical and electrical properties homogeneity is assured (Ref. [54]). The parameters of each array (number of elements, geometry, distance between elements, single addressability) are easily controllable during the manufacturing process. Apart from the evident reduction of production costs comparing to conventional edge-emitting laser arrays or single elements, the $VCSEL's$ present many advantages also in the optical/electrical performances: short cavity length ($\approx 1\mu m$) ensuring single-longitudinal-mode operation, threshold current typically of the order of few mA

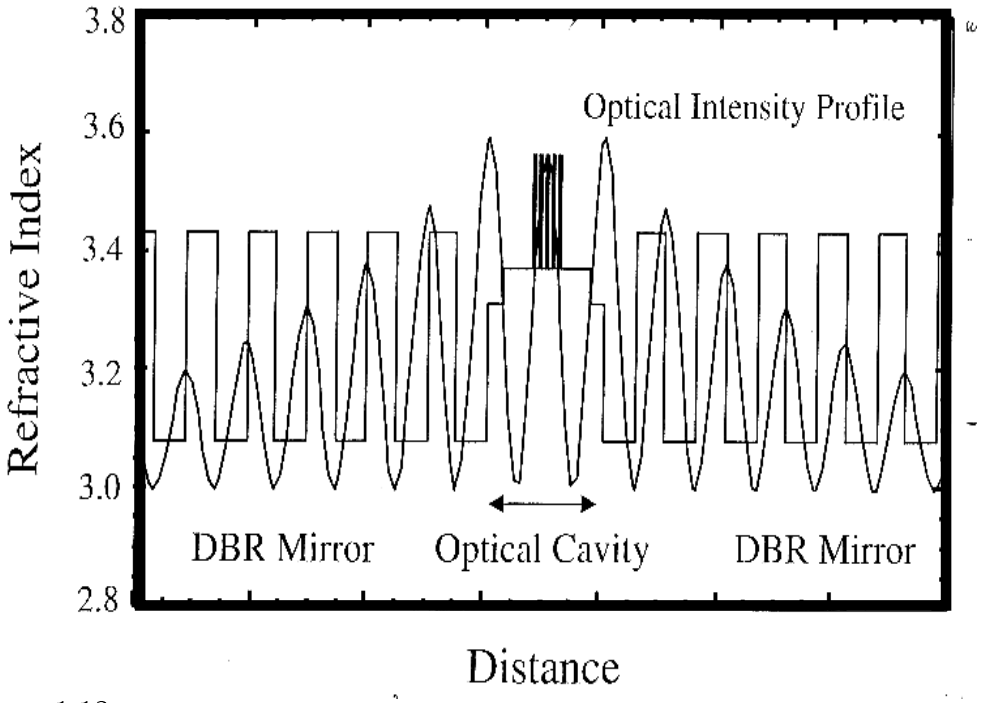

Figure 1.13: Standing wave intensity distribution in the central region of a $VCSEL$. The active region thickness is one-quarter of the operating wavelength, divided by the refraction index. Note the refraction index variation of the DBR layers. From Ref. [54]

due to their large gain and large mirrors reflectivity, a small divergence output beam with high coherence and high spectral purity.

The $VCSEL's$ structure is shown in Fig. 1.12. The vertical cavity is formed by DBR mirror consisting of alternating semiconductor layers of quarter-wave thick high and low-refractive index. Because of the short active region, $VCSEL's$ have lower round-trip gain than conventional edge-emitting lasers. In order to lower the threshold current, large reflectivity is required for the laser cavity mirrors. Power reflectivity of $\sim 99.9\%$ is achieved by stacking together tens of DBR pairs. The DBR mirrors clad a gain region composed by one or several quantum-wells. For optimizing the modal gain the quantum-well structures are placed at the antinodes of the standing-wave of the resonant longitudinal-mode of the $VCSEL$ cavity (Ref. [55]). Fig. 1.13 shows the standing-wave intensity distribution in the central region of a $VCSEL$ (left) and a typical reflectivity spectrum (right) for a GaAs MQW laser wafer (Ref. [54]).

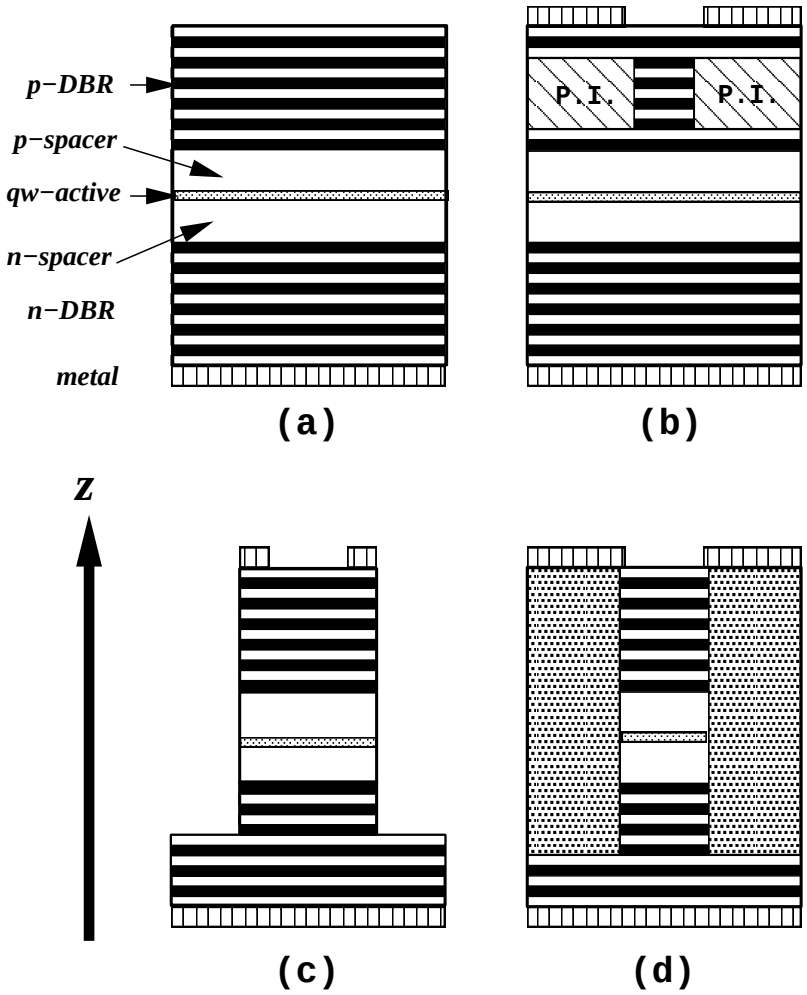

Figure 1.14: $VCSEL$ structures: (a) $VCSEL$ wafer; (b) gain-guided; (c) air-posted; (d) buried heterostructure.

In order to confine the radiation in the plane orthogonal to the cavity axis, several techniques are employed:

i) *Gain-guiding*: proton-implantation is employed to produce a surrounding large-resistance region which drives the injected carriers into the active region (current confinement) (Refs. [56, 57]). The large gain region generated at the center of the proton-implanted region provides optical confinement.

ii) *Index-guided* $VCSEL's$ use either mesa-etched, buried heterostructure, or native oxide processes to produce a transverse refractive index profile to induce optical waveguiding. Air-post $VCSEL's$ (Fig. 1.14(c)) (Ref. [58]) have strong

waveguiding because the large refractive index difference between the heterostructure and the air. Weakly index-guided $VCSEL's$ can be built, e.g., by re-growing a cladding layer around the air-post structure with a lower refractive index than the active region (Fig. 1.14(d)) (Ref. [59]). This structure, referred to as buried heterostructure, allows for simultaneous current and optical confinement. An alternative way of producing index-guided devices is through a native oxide process, in which a specific layer of $AlAs$ in the $VCSEL$ structure is selectively transformed into a native oxide which has a low refractive index and a large resistivity (Ref. [60]).

The effective $VCSEL's$ cavity length is of the order of one to a few times the emission wavelength. Therefore, the longitudinal eigenmode separation is of tens of nm, and only one longitudinal-mode falls within the gain spectrum. $VCSEL's$ are intrinsically single-longitudinal-mode devices. As a consequence of this feature, the electrical and optical characteristics of $VCSEL's$ are strongly affected by thermal effects. Both the cavity mode and the gain peak frequencies shift as the temperature of the active region changes. The resonant frequency of the cavity mode red-shifts with a rate of $0.5-1$ Å$/C^0$ (Refs. [61, 62, 63]) because of the heat-induced changes in the background refraction index and, indirectly, through temperature-dependent changes in the carrier number. The gain profile red-shifts at ≈ 3 Å$/C^0$ because of bandgap shrinkage with temperature (Refs. [64, 65]). The different dependence rate on temperature yields, as current is increased, a detuning of the gain peak with the cavity resonance and the gain available for laser action decreases, inducing saturation of the output light. Joule heating is strongly effective in $VCSEL's$ because of the large series resistance resulting from the DBR mirrors stack through which the current flows. large reflectivity mirrors require sharp interfaces that increase their series resistance. This results in large operating voltages and correspondingly large dissipated powers occur during CW

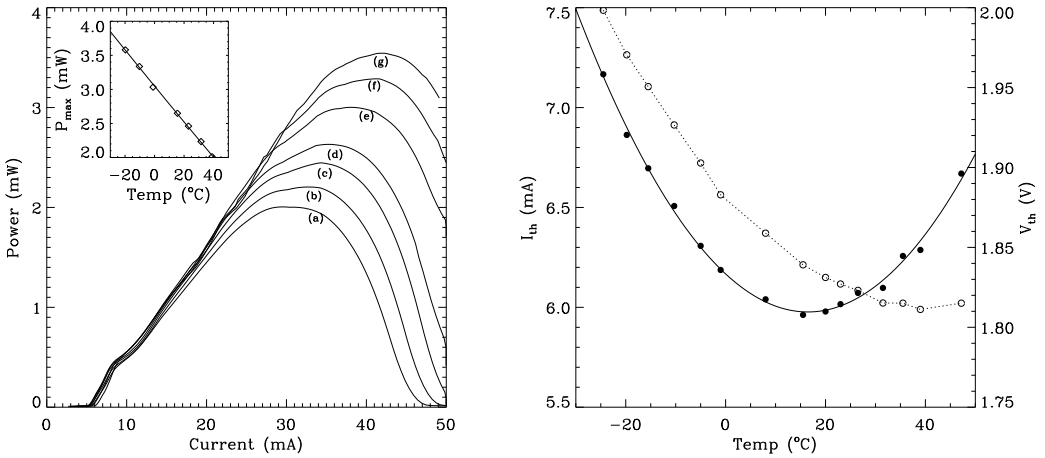

Figure 1.15: (left) L-I characteristic for a 15 μm active-region diameter $VCSEL$ taken at different substrate temperatures (a) 39.0, (b) 31.5, (c) 23.0, (d) 15.5, (e) -1.0, (f) -10.3, and (g) -19.8 C^0; the inset shows the dependence of the maximum output power emitted by the $VCSEL$ for the labeled temperatures. (right) Dependence of the CW current (solid circles) and bias voltage (open circles) at the lasing threshold on the substrate temperature. From Ref. [35].

operation of the device. For most applications, the effects of temperature changes on the device must be minimized.

Broad area $VCSEL$ devices easily have a rather large Fresnel number which favors the appearance of transverse patterns. Studies of the mode profile in the near field and/or far field have been combined with spectral information taken at low (Ref. [56]) and high resolution (Refs. [66, 67]) in order to analyze the transverse-mode structure of $VCSEL's$. transverse-modes of typical $VCSEL's$ are nearly Gauss-Laguerre or Gauss-Hermite (TEM) modes. The fundamental transverse-mode, commonly termed as the TEM_{00} mode, has a Gaussian beam pattern. The sequence of appearance of transverse-modes in $VCSEL's$ with increasing current is, typically, similar for many structures. Emission in the fundamental Gaussian transverse-mode occurs for current values just above the threshold while higher-order transverse-modes can be successively excited as the current is increased.

1.3.1 Polarization characteristics of $VCSEL's$

Contrary to the edge-emitters, $VCSEL's$ do not have a strong mechanism fixing the polarization axis. The high degree of transverse symmetry of the $VCSEL$ cavity and the cubic crystal impose no constraints on any type of polarization (linear, circular, elliptical) or the preference of the polarization direction. On the other hand, the presence of linear anisotropies in the $VCSEL$ cavity breaks the transverse symmetry favoring one polarization axis. Although several $VCSEL's$ display stable linearly polarization emission close to threshold (Refs. [68, 69]), the polarization state of the emitted light is, in many cases, dependent on the injected current. Many experiments have shown that $VCSEL's$ may switch from emitting linearly polarized light to emitting polarized light of the orthogonal linear polarization as the current is changed above the lasing threshold, a phenomenon known as polarization switching. Some authors have also reported polarization bistability (Ref. [70]) and hysteresis of the switching current (Ref. [71]). Emission on both linearly polarized modes (polarization coexistence) with different emission frequencies (Refs. [68, 72]), as well as in both linearly polarized modes with the same emission frequency (elliptically polarized light) (Ref. [73]) have also been reported. All these polarization behaviors are observed to occur close to threshold within the fundamental transverse-mode regime. For larger injection currents, the excitation of high-order transverse-modes may be accompanied by changes in the polarization state of the output light. A commonly observed feature in $VCSEL's$ is that the first order transverse-mode tends to lase in the polarization orthogonal to that of the fundamental TEM_{00} mode. For larger currents, the power in the dominant polarization typically saturates while the power in the orthogonal polarization rapidly increases (Refs. [72, 74]). Abrupt polarization switching between high-order modes has also been observed (Ref. [72]). Polarization-resolved measurement of the $VCSEL's$ optical spectrum close to

threshold, have revealed a splitting of the operating frequency of the two polarization modes. In some cases the two frequencies are unresolved within experimental accuracy ($< 2 - 3\ GHz$) (Refs. [66, 72]). In other works the reported frequency separations are about $10 - 12\ GHz$ (Refs. [68, 70, 75]) while a wide range, from 5 to 20 GHz, has also been reported (Ref. [76]). The same splitting has been found, for larger current, for the polarization components of the same high-order mode (Ref. [77]). These features indicate the presence of linear birefringence (or linear phase anisotropy) in the $VCSEL$ cavity which breaks the frequency degeneracy of the transverse-modes with orthogonal polarizations. Therefore, linear birefringence and $VCSEL's$ anisotropies are device characteristics affecting the polarization behavior.

Several efforts have been made to control the $VCSEL's$ polarization by playing with these parameters (Ref. [78]). Solutions proposed were based on anisotropic transverse cavity geometries (Ref. [68]), anisotropic stress produced from an elliptical etched hole (Ref. [79]), anisotropic gain from a fractional layer superlattice (Ref. [80]), polarization selective optical feedback (Ref. [81]). Woerdman and coworkers developed an experimental all-optical technique, referred to as the *hot-spot technique*, to manipulate the $VCSEL$ birefringence almost at will in either a reversible (Ref. [82]) or a permanent (Ref. [83]) way. Using this technique, this group performed a systematic experimental study of $VCSEL$ anisotropies which allowed the identification of the physical mechanisms for the transverse symmetry breaking. From these studies, it turns out that the dominant anisotropy in $VCSEL's$ is a linear birefringence between the preferred crystal axes, which is caused by both the elasto-optic (Ref. [82]) and the electro-optic (Ref. [76]) effects.

An explanation for the polarization state selection in the fundamental mode of $VCSEL's$ has been given in terms of the degree of matching between the gain peak and the polarization mode frequencies (Ref. [84]). The birefringence induced

splitting of the mode frequencies leads to different gains for the two modes. This explication was supported by the analysis of the $VCSEL's$ emission as the mean frequency of the two polarization modes was shifted all along the gain curve and as the strain induced anisotropies was varied, changing both the frequency splitting and the gain differences for the modes. Within this framework stable polarization emission occurs when the gain difference favors the same polarization mode at any current value (Ref. [84]). Polarization switching is expected when there is an exchange of the relative gain of the two polarized modes as the current is increased (Ref. [72]). Coexistence of both linearly polarized states occurs if the gain difference is small (small birefringence). Several theoretical works have been developed to include in a coherent model the polarization modes competition for the gain together with other experimentally observed polarization features (Ref. [85]).

From a more fundamental point of view, the polarization state of light emitted by a laser depends on both the angular momentum of the quantum states involved in the material transitions and on the laser cavity. Emission of a quantum of light (a photon) with right (left) circular polarization corresponds to a transition in which the projection of the total material angular momentum on the direction of propagation changes by $+1$ (-1) in units of $\hbar$. However, the anisotropies, geometry and waveguiding effects of the cavity can lead to a preference for a particular polarization state of the laser light. These two ingredients can compete or be complementary, their relative importance depending on the type of laser.

A fundamental model, called Spin Flip Model (SFM), has been developed by San Miguel, Feng, and Moloney in Ref. [86] which considers the polarization of the laser field by including the magnetic sublevels of the conduction and valence bands in unstrained quantum-well $VCSEL$ media. The SFM model considers the coupling of the vector optical field to the two allowed transitions between the

conduction band and the heavy hole band in unstrained quantum-well media. The evolution equation for the vector optical field of circularly polarized components is derived from Maxwell's equations for a gain-guided $VCSEL$, and includes transverse effects through the optical diffraction term. The evolution equations for the material dipole densities and the carrier densities for each transition are derived using a density matrix formalism, and extended spatially in the transverse plane by considering carrier diffusion. Coupling between the circularly left and right polarized transitions is assumed to occur via spin-flip relaxation processes. The polarization and transverse-mode dynamics of $VCSEL's$ are described in terms of two coupled sets of semiclassical two-level Maxwell-Bloch equations, one for each circularly polarized transition.

Regalado et al. in Refs. [87, 88] have used the SFM for analyzing the polarization properties of a $VCSEL$ emitting on the fundamental transverse-mode. The single-mode operation allows the derivation of a rate-equations model which includes the characteristic cavity anisotropies of $VCSEL's$, birefringence and dichroism, as well as the saturable dispersion through the α-factor. This simple model describes the allowed linearly and elliptically polarized steady-states. Moreover, the stability analysis of these solutions allows the prediction of the different polarization behaviors as the $VCSEL$ parameters are changed. We describe the main results of this approach in the following paragraph, following the Ref. [88].

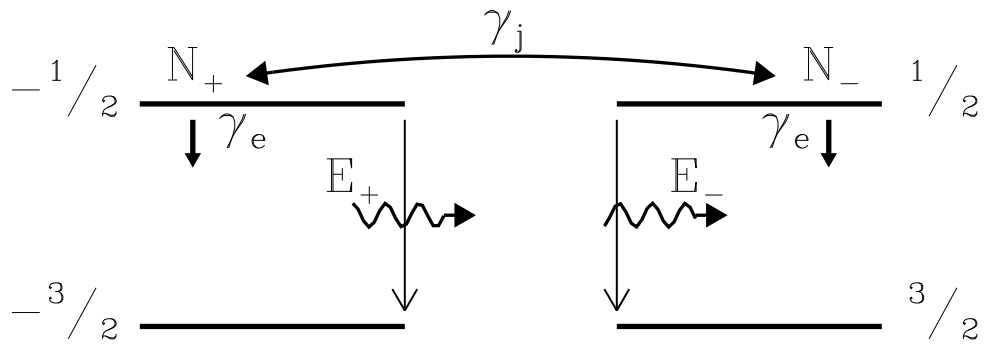

Figure 1.16: Four level model for polarization dynamics in $VCSEL's$. From Ref. [88]

Rate-equation model for polarization dynamics in $VCSELs$*

∗ this paragraph is based on the paper: J. Martín-Regalado, M. San Miguel, N. B. Abraham, and F. Prati, "Polarization Properties of Vertical-Cavity Surface-Emitting Lasers", IEEE Journal of Quantum Electronics **33**, 765 (1997)

Fig. 1.16 shows the schematic band structure of quantum well $VCSEL's$. From this scheme, applying a rate-equations approach is possible to derive the following equations valid for a single transverse-mode operating devices. A more rigorous derivation can be performed from the SFM (Ref. [86]) after introducing the simplification of single transverse-mode operation and after the adiabatical elimination of the material dipole polarization. Then, for fundamental transverse-mode operation, $VCSEL's$ equations read:

$$\begin{aligned} \dot{F}_{\pm} &= \kappa(1+i\alpha)(D \pm d - 1)F_{\pm} - (\gamma_a + i\gamma_p)F_{\mp} \\ \dot{D} &= -\gamma(D-\mu) - \gamma(D+d)|F_+|^2 - \gamma(D-d)|F_-|^2 \\ \dot{d} &= -\gamma_s n - \gamma(D+d)|F_+|^2 + \gamma(D-d)|F_-|^2 \end{aligned} \tag{1.3.1}$$

where $F_{\pm}$ is the scaled version of the slowly varying amplitudes of the left $(-)$ and right $(+)$ circularly-polarized optical fields. $D = (D_+ + D_-)/2 = a(N - N_0)/\kappa$, being $N - N_0$ the total carrier distribution referred to the transparency value N_0.

$d = (D_+ - D_-)/2 = an/\kappa$, being n is the difference of the carrier distributions associated with the transitions σ_+ and σ_- respectively. κ is the field decay rate, α is the linewidth enhancement factor, γ is the decay rate of the total carrier population, μ is the injection current normalized to threshold, and γ_s is the decay rate of the carrier population difference through spin-flip relaxation processes, $\gamma_p = 0$, $\gamma_a = 0$ are, respectively, the linear phase anisotropy and the linear amplitude anisotropy. Eqts. 1.3.1 may be written in terms of the orthogonal linear components of the electric field:

$$F_x = \frac{F_+ + F_-}{\sqrt{2}} \qquad F_y = -i\frac{F_+ - F_-}{\sqrt{2}} \tag{1.3.2}$$

Typically $\gamma^{-1} \approx 1$ ns and $\kappa^{-1} \approx 1$ ps and the spin mixing processes described by γ_s occur on an intermediate time-scale. Hence, the dynamics of d cannot be in principle adiabatically eliminated.

The equations 1.3.1 for $\gamma_a = 0$, $\gamma_p = 0$ describe polarization dynamics in a perfect isotropic $VCSEL$, and predicts the preference of quantum-well material for linearly polarized emission. The orientation of the linearly polarized modes is not fixed by the non-linear field-matter interaction in this model. Therefore, any amount of linear birefringence or linear-gain anisotropy resulting from material or cavity anisotropies restricts the linearly polarized solutions to one of two specific states along the linear anisotropy axes, that we call here the $\hat{x}$-and $\hat{y}$ directions.

The parameter γ_p represents the effect of a different index of refraction (implying different emission frequency) for each linear polarization as a consequence of the birefringency of the crystal. γ_p leads to a frequency difference of γ_p between the $\hat{x}$– and $\hat{y}$-polarized solutions. In addition, the two polarization modes may have a slightly different gain-to-loss ratio that can be related to the anisotropic gain properties of the crystal, the slightly different position of the frequencies of the modes with respect to the gain profile, and/or different cavity geometries for the differently polarized modes. These effects are included in the parameter γ_a

which leads to different thresholds for the linearly polarized solutions. The values of these parameters depend critically on $VCSEL$ designs.

The system of equations 1.3.1 has a variety of stationary solutions. The arbitrary steady-state solution reads

$$F_{\pm} = Q_{\pm} e^{i(\omega_{\pm} t \pm \psi) + i\theta} \quad D = D_0 \quad d = d_0 \tag{1.3.3}$$

where θ is the global phase that can be ignored or set to zero without loss of generality, and ψ is a relative phase which indicates the direction of linear polarization in the transverse plane of the laser.

In absence of anisotropies ($\gamma_a = \gamma_p = 0$) the stable solutions are linearly polarized but oriented in an arbitrary direction of the quantum-well plane (Ref. [86]). For $\gamma_p \neq 0$, and when there are no amplitude (gain or loss) anisotropies ($\gamma_a = 0$), we obtain four types of steady-state solutions. For each of these solutions the phase anisotropy breaks the rotational invariance of the orientation of the field (polarization) vector, that is, the relative phase ψ is no longer arbitrary. Two of these types of solutions have orthogonal linear polarization. We will call these states the $\hat{x}$– and $\hat{y}$-polarized solutions (modes).

For the linearly polarized modes the circularly polarized components have equal amplitudes and frequencies, but differ of $\pi/2$ in the relative phase . The other two types of solutions are elliptically polarized solutions for which the circularly polarized components have equal frequencies but different amplitudes. The stability analysis of these stationary solutions allows the determination of the lasing polarization state as the parameters are changed. We have plotted in Fig. 1.17 the stability domains for the linearly $\hat{x}$- and $\hat{y}$-polarized solutions in the $(\gamma_p - \mu)$ stability diagram. The $\hat{x}$-polarized solution is always stable for any current $\mu < \mu_x$, which occurs below the solid line. The $\hat{y}$-polarized solution is stable when $\mu > \mu_y$, which occurs to the left of the dashed line. Therefore, the stability diagram is divided into four different regions with different stability

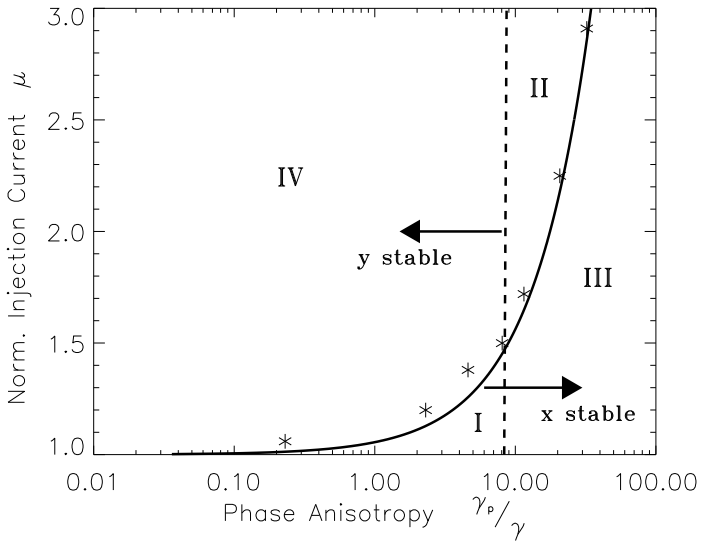

Figure 1.17: Stability diagram for the steady-state solutions. The $\hat{x}$-polarized state is stable below the continuous line (μ_x), while the $\hat{y}$-polarized state is stable to the left of the dashed line (μ_y). Elliptically polarized solutions are stable within the narrow region between the solid line and the stars. The following parameters have been used: $\kappa = 300\ ns^{-1}$, $\gamma = 1\ ns^{-1}$, $\gamma_s = 50\ ns^{-1}$ and $\alpha = 3$. From Ref. [88].

for the linearly polarized solutions: region I, where both linearly polarized states are stable, region II where both are unstable, and regions III and IV where only $\hat{x}$-or $\hat{y}$-polarized solutions are stable, respectively. The stability of the $\hat{x}$– and $\hat{y}$-polarized solutions can be interchanged by changing the sign of γ_p. Finally, the linear stability of elliptically polarized solutions has also been examined. The elliptically polarized solution is stable in a narrow domain of parameters in which μ is close to but larger than μ_x.

More complicate is the case where anistropies both in amplitude and in phase are considered ($\gamma_a \neq 0$). In this case the $\hat{x}$– and $\hat{y}$-polarized modes have different thresholds. Moreover, these linear polarized solutions have different steady-state amplitudes and different optical frequencies even in absence of phase anisotropy. We consider two cases in which a small amplitude anisotropy is introduced in the system. In the first case γ_a is negative (Fig. 1.18, left) and $\hat{x}$-polarized emission is "favored" because its lasing threshold is lower than the threshold of

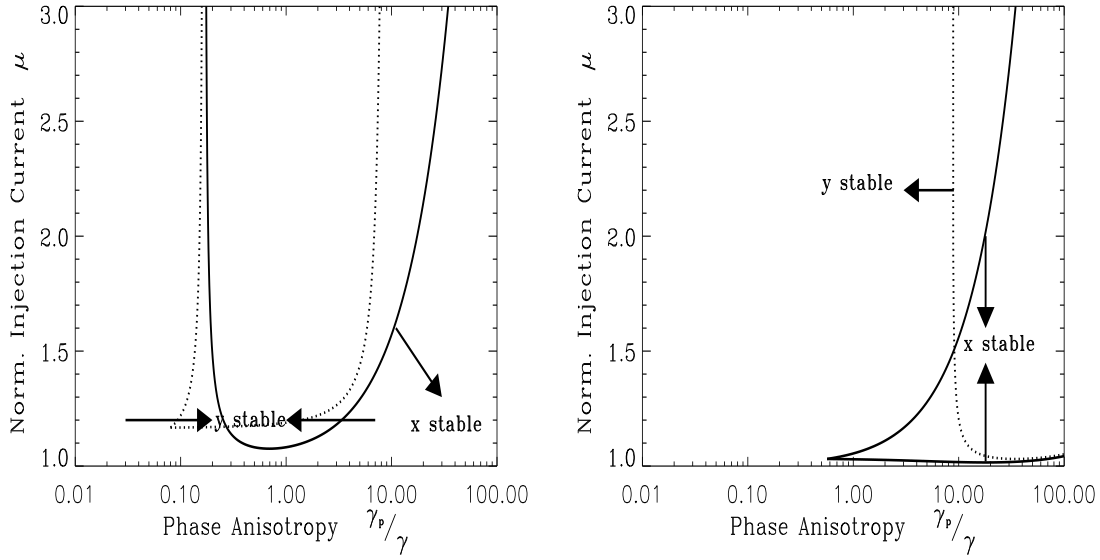

Figure 1.18: (left) Stability diagram for γ_a =-0.1γ; other parameters as in Fig. 1.17. The $\hat{x}$-polarized mode has the lowest threshold. (right) Stability diagram for γ_a =0.1γ; other parameters as in Fig. 1.17. $\hat{y}$-polarized mode has the lowest threshold. From Ref. [88].

the orthogonal polarization state. The other situation is when γ_a is positive (Fig. 1.18, right) and the $\hat{y}$-polarization is "favored" because its lasing threshold is lower than that of the $\hat{x}$-polarized state.

In the stability diagram for $\gamma_a = -0.1\gamma$ (shown in Fig. 1.18 (left)), the $\hat{x}$-polarized solution is stable below the solid line, while the $\hat{y}$-polarized solution is stable inside the zone bounded by the dashed curves. There are zones in which only one mode is stable, zones of bistability and zones in which neither linearly polarized mode is stable. As the birefringence (γ_p) goes to zero, only the $\hat{x}$-polarized solution is stable. In a large domain given roughly by $\mu > 1.1$ and $0.03 < \gamma_p/\gamma < 8.0$ only the $\hat{y}$-polarized mode is stable, indicating that despite the $\hat{x}$-polarized solution is favored by the gain anisotropy, the emission will switch to $\hat{y}$-polarized emission as the current is increased near threshold, an effect of the combination of saturable dispersion and birefringence similar to that which appeared in Fig. 1.17. In the stability diagram for $\gamma_a = 0.1\gamma$ (shown in Fig. 1.18 (right)), the $\hat{x}$-polarized solution is stable in the region between the solid curves,

while the $\hat{y}$-polarized solution is stable to the left and below the dashed curve. As in Fig. 1.18 (left) there are also zones where either one, both or none of the linearly polarized states are stable. As the birefringence (γ_p) goes to zero, only the $\hat{y}$-polarized (lower threshold) solution is stable. For $\gamma_p > 10.0\gamma$ and as the current is increased, there is a switching of stability from the mode with larger gain-to-loss ratio ($\hat{y}$-polarized mode) in favor of the weaker mode ($\hat{x}$-polarized mode).

The main difference between the situation with amplitude anisotropy and the case of isotropic gain of Fig. 1.17 is the different thresholds of the two modes. The somewhat unexpected consequence is that when the injection current is increased, the weaker mode does not always gain stability where the solution exists. Most strikingly the weak mode does not gain stability for any value of the current when the birefringence is small. These two effects are those which indicate the importance of the gain anisotropy, giving stability only to the mode with the larger gain-to-loss ratio. However, important zones remain near threshold, accessible for typical values of many $VCSEL's$, in which the saturable dispersion and the birefringence combine to induce switching to the mode with the lower gain-to-loss ratio.

Chapter 2

The Edge-emitting semiconductor lasers with optical feedback

In this chapter we report on the experimental characterization of semiconductor edge-emitting lasers with optical feedback. The main issue of our work is the analysis of the Low-Frequency Fluctuations (LFF) phenomenon, appearing for moderate-to-strong feedback levels. Our investigation is devoted to shed light on this instability, both on its dynamical nature and on the physical mechanism at its origin.

In the first section we describe the experimental set-up and the main characteristics of the solitary laser. We also define the control parameters and we specify the parameter ranges that we have experimentally explored. In the second section we provide an overview of the dynamical regimes the system exhibits as the control parameters are scanned, LFF phenomenon is then located in the general parameter-space. In the third section we present the experimental characterization of the LFF phenomenology. Then (section four), we argue, from non-standard experimental test, the dynamical origin of this phenomenon. We demonstrate experimentally that the semiconductor laser with optical feedback

behaves like an *excitable-medium* and we clarify the role of noise in the LFF-instability. Moreover, by controlling the noise level, we provide the first experimental evidence of *Coherence Resonance* in an optical system.

The second part of the experimental work, devoted to the identification of the physical mechanism at the origin of LFF, is presented in section five. In order to resolve the fast time-scales of semiconductor laser dynamics a monitoring system with high bandwidth is required. We have employed this system also for monitoring the spectral-resolved intensity output of the laser. In this way the intensities of the internal-cavity-modes active during the LFF-instability can also be monitored with high time-resolution. Such measurements allow us to identify unambiguously the role of laser modes in the LFF-instability. In section six we compare our results with the models in the literature. Finally, in section seven, we report on the experiment with frequency-selective optical feedback, gaining further insights into the physical mechanism at the origin of LFF.

2.1 Preliminary considerations

The experiments described in the following sections have been performed on a time duration of three years and, of course, many different kinds of laser devices were used. In the following experimental reports we describe just the general features, ignoring the details relative to the particular kind of device. For this reason we do not trace systematically the device characteristics, unless when it is important to explain differences from the "standard" behavior. In this case Appendix A provides detailed information on each device used. For several reasons, mainly historical, we assume as standard the behavior obtained with the edge-emitting laser $Hitachi^{TM}$ HLP 1400. In the feedback literature, this laser is the most used in the experiments and its characteristics are the most referenced in the theoretical works.

2.1.1 Experimental Set-up

The basic experimental set-up configuration used is the one showed in Fig. 2.1. The stability of the temperature of the laser submount is better than 0.01^oC. An AR-coated collimator is placed at the laser output in order to reduce the beam divergence. An external mirror is placed in front of the laser in order to re-inject into the laser cavity part of the light emitted. This distance can be varied between $0.1\ m$ and $1.0\ m$. The intensity-output is detected by $2-3\ GHz$ bandwidth silicon avalanche photodiodes. The signal is analyzed by a spectrum analyzer ($22\ GHz$ bandwidth), and a digital oscilloscope ($500\ MHz$ analogue bandwidth). Part of the output beam is reflected into a scanning Fabry-Pérot analyzer to check the spectral characteristics of the laser output. An Acousto-Optic Modulator controls the feedback level.

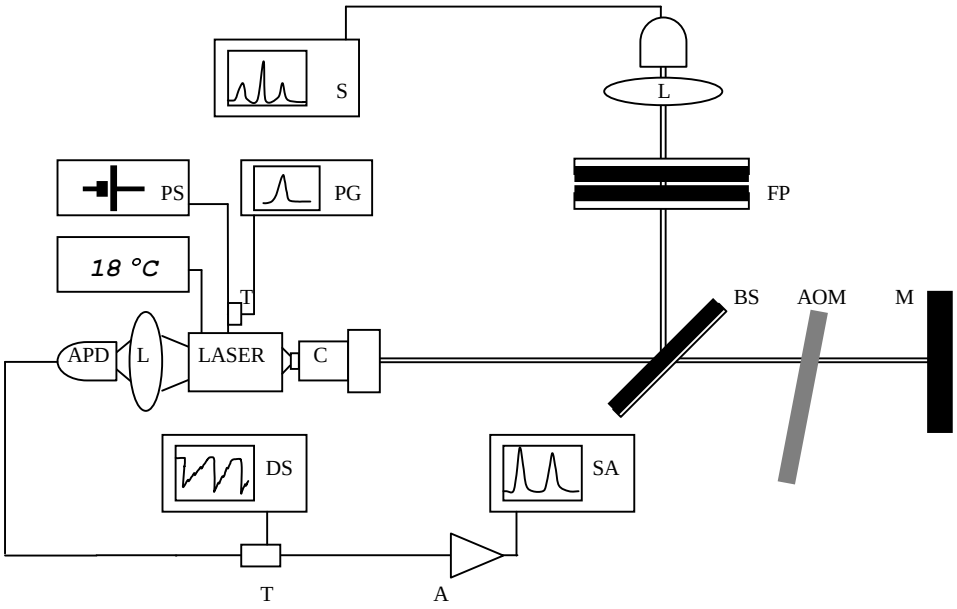

Figure 2.1: Experimental Set up: L lens, S scope, PG pulse generator, PS power supply, FP Fabry-Pérot interferometer, APD Avalanche Photodiode, C collimating lens, BS beam splitter, AOM acousto-optic modulator M mirror, DS digital scope, SA spectrum analyzer, A microwave amplifier, T T-coupler

2.1.2 The solitary laser

In our experiments the most used device is the commercial $Hitachi^{TM}$ HLP 1400 edge-emitting laser whose active region is made of $GaAlAs$. The emission wavelength is around 840 nm, the cavity length is approximately 300 μm and the frequency separation between the longitudinal-mode is 125 GHz. The power reflectivity of the cavity mirrors is defined by the index gap semiconductor/air and it is $R \approx 35\%$. In Fig. 2.2 we show the Light Output vs. Pumping Current Intensity (L/I) curve of one of this laser with and without optical feedback and in Fig. 2.3 we show the noise spectrum and the optical spectrum of the same laser without feedback for different levels of pumping current. We can notice that, in the case shown, the solitary laser threshold $I_{th,sol}$ is at 48 mA.

The laser without optical feedback operates in a single-longitudinal-mode ($MSR > 20\ dB$) for currents above 51.8 mA. For lower current values several

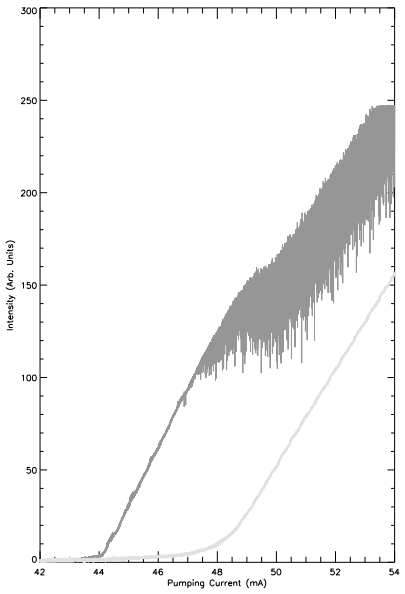

Figure 2.2: Light Output / Pumping Current Intensity curves for the solitary laser and laser with feedback (darker trace).

longitudinal-modes are active. We can notice that the mode-suppression-ratio increases with increasing the pump, as the spontaneous-emission noise relevance decreases (see §I.2.4).

The impact of the pumping current on the laser emission characteristics is two-fold: it controls the carrier density level in the active region and it affects the temperature of the active region by Joule heating.

The temperature changes modify both the band structure of the semiconductor and the refractive index of the active medium. The carrier distribution in the conduction band is affected by the temperature according to the Fermi-Dirac distribution:

$$\frac{dN}{dE} = \rho_c(E)\frac{1}{1+\exp\left[(E-E_{fc})/kT\right]} \tag{2.1.1}$$

where $\rho_c(E)$ is the conduction-band density of states and E is measured from the bottom of the conduction band. In a bulk system, like the laser considered here, $\rho_c(E) = 4\pi(\frac{2m_c}{h^2})^{3/2}\sqrt{E}$, while in a quantum-well laser: $\rho_c(E) = \frac{2m_c}{h^2}$. An expression analogous to 2.1.1 describes the hole distribution in the valence band.

According to 2.1.1, the increasing of the temperature determines a redistribution of the carrier towards higher energy states. As a consequence, in a bulk system, because of the dependence of the conduction-band density of states on the energy, the distribution peak lowers and shifts to smaller energy. Therefore, for increasing temperature, the gain peak decreases and red-shifts, while the gain curve broadens on the high energy side. In a quantum well laser, because of the constant density of states, the distribution peak is at the edge of the band, where the carrier density is affected only at large temperature. Hence, quantum well lasers are less sensible to temperature increasing.

The refractive index of the active medium is affected by temperature changes. For $GaAs$ the temperature coefficient of the refractive index of the unpumped material is $5.5 \times 10^{-4}\ /K$. Since the index of refraction increases, the comb of cavity resonant frequencies red-shifts. The decrease of the frequency ν_0 depends on the internal-cavity order, according to: $\frac{d\nu_0}{\nu_0} = -\frac{d\mu}{\mu}$, being μ the unpumped index of refraction of the active medium. The frequency modal separation Δ is also affected: $\frac{d\Delta}{\Delta} = -\frac{d\mu}{\mu}$. Calling j the order of the resonance ν_0, the shift rate of ν_0 with a variation in the index of refraction is j times the shifting rate of Δ. The shift rate of ν and Δ with the pumping rate because of thermal effects, depends on the thermal mass of the laser system. Typical values are $40K/W$ for $GaAs/Al_xGa_{1-x}As\ DH$ lasers.

The increase of carrier density in the active region, as mentioned in §I.2.4, modifies the band structure affecting the real and the imaginary part of semiconductor susceptibility. Band-filling determines, in bulk lasers, a blue-shift and an increase of the gain peak as well as a broadening of the gain curve towards the high energy side. Band-gap re-normalization, a many-body effect arising from the screened Coulomb interaction between electrons and hole, determines a red-shift of the gain peak. The gain curve shifts to the red, thus decreasing the frequency

of the band edge. For standard carrier densities ($\approx 10^{18}/cm^3$), if the carrier density is increased without inducing Joule heating of the active region (perfect thermal stabilization of the device), the band-filling effect is dominant.

Band-filling and many-body effects affect also the refraction index of the semiconductor medium, as shown by the α factor. In §I.2.4 we have seen that α_0 changes depending on the detuning between the field frequency and the band-gap. For long cavity lasers as the $Hitachi^{TM}$ HLP1400, the natural lasing frequency is very close to the gain peak and the above mentioned detuning is negligible. Then, α is positive and the increase of carrier density determines a decrease of the refraction index and, as a consequence, a blue-shift of the lasing frequency. In $VCSEL's$, the short cavity allows for lasing frequency very detuned respect to the gain curve. When the detuning is large and positive, α takes negative value and the lasing frequency red-shifts with increasing carrier density.

As the laser pumping current is increased, the carrier density in the active region increases and, at the same time, the semiconductor medium heats up. In Fig. 2.3 the dominant feature is the red-shifting effects of the gain peak; warming up effects appear to dominate on band-filling effects. For low current levels, the gain curve is evidenced by the colored spontaneous emission at the resonant frequencies of the laser cavity. The modal power envelope shifts to the red as current is increased (see the change from 49.2 mA to 49.8 mA). When the laser is single-mode, the gain peak shifting induces mode hops to the closest red detuned longitudinal-mode as the current is increased (see the jump at 51.8 mA). The red-shift rate could be estimated to be 15 GHz/mA (0.36 Å/mA). Finally, we remark that the shift of the cavity resonant frequencies is negligible compared to the shift of the gain curve. As a consequence, the shift in lasing frequency appears as jumps between consecutive higher wavelength modes rather than a continuous shift.

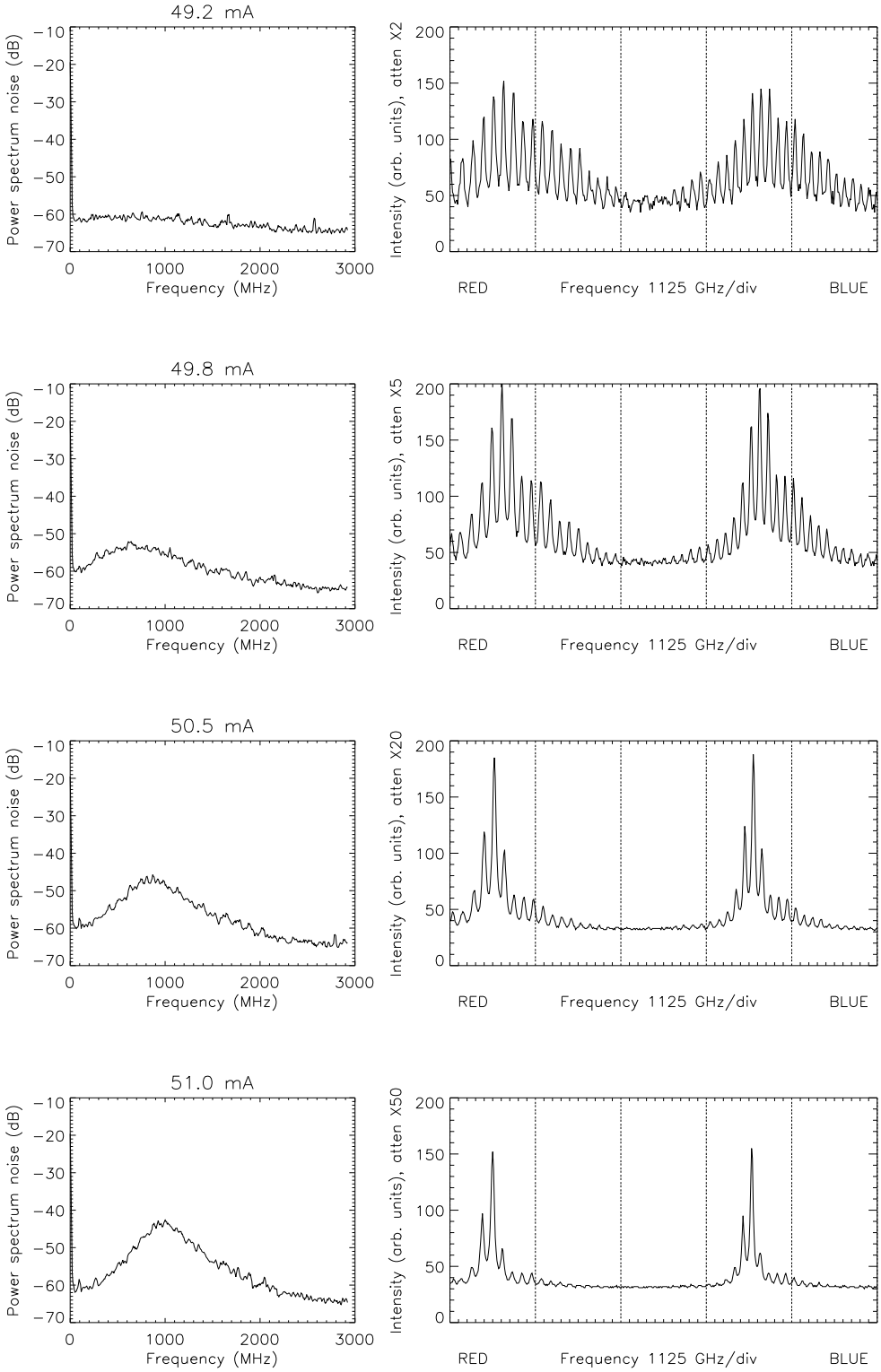

Follows in the next page ⟶

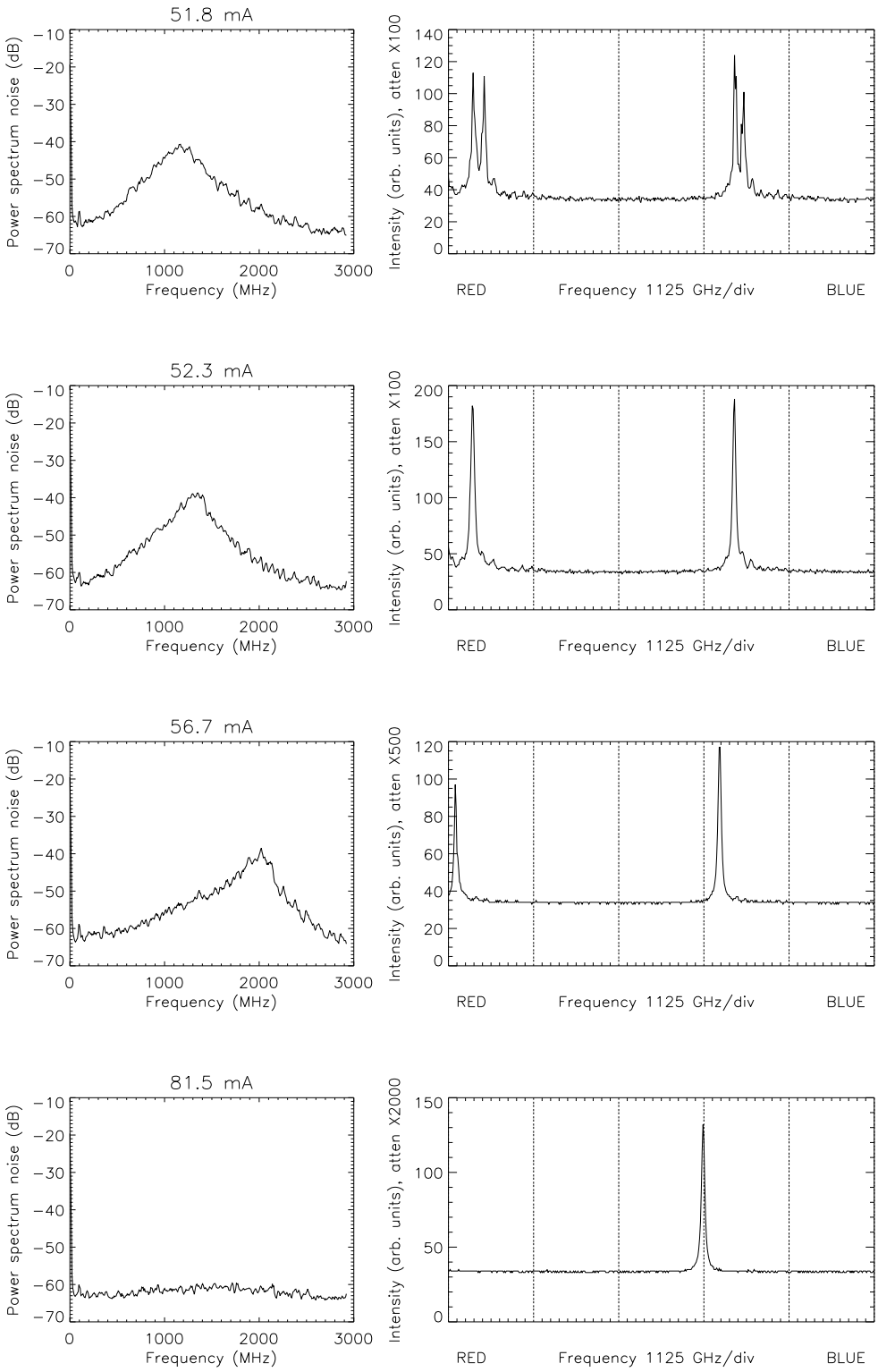

Figure 2.3: Solitary laser emission characteristics vs. Pumping Current: Power Spectrum and Optical Spectrum.

2.1.3 Definition and measures of the parameters

In the feedback configuration there are four main parameters that could be changed: the pumping current, the feedback level, the external-cavity length and the feedback phase. The pumping current is changed by the power supply. The cavity length is changed on a coarse scale by placing the external mirror at different distances from the laser. The feedback phase is controlled by wavelength tuning of the external-cavity length, obtained by moving the external mirror by a piezo-electric positioner.

The amount of feedback depends on the optical components inside the external-cavity (reflectivity of the external-cavity mirror, beam splitters inside the external-cavity, etc.) and on a coupling factor taking into account the quality of the alignment and of the mode matching between the emitted and the returned beams. The mode matching is controlled by acting on the collimating lens close to the laser cavity, the alignment is controlled by the micro-metric screws that tilt the external mirror. Experimental groups define and measure the amount of light fed back into the laser in different ways. In order to make comparisons between different experimental and theoretical works described in the literature, it is opportune to revise the different ways to quantify the feedback level. In general, the feedback is described by a delay term added to the solitary laser rate equation:

$$F E(t-\tau) \tag{2.1.2}$$

where τ is the time delay because of an external cavity round-trip ($\frac{c}{2l}$), being l the external-cavity length and F is the feedback rate, defined as:

$$F = \frac{1-R_1}{\tau_{in}}\sqrt{\frac{R_{ext}}{R_1}} \tag{2.1.3}$$

being R_1 the power reflectivity of the laser mirror where the light is fed back, τ_{in} the laser cavity round trip time and R_{ext} the effective power reflectivity of

the external mirror. R_{ext} is an effective term including all the losses experienced by the field in the external-cavity, because of the optics inside the cavity, to the feedback beam mode matching and alignment. Then, the real system is described simply as the solitary laser plus an external mirror of reflectivity R_{ext}. In fact, R_{ext} gives the power ratio between the light power emitted by the laser and the light power returned into the laser cavity. The feedback level, κ^2, is defined as the ratio between the light inside the laser and the light returned into the laser cavity. It is normally expressed in dB and it is related to F by:

$$\kappa^2 = (F\tau_{in})^2 \tag{2.1.4}$$

In the feedback literature the three parameters F, κ^2, or R_{ext} are the most commonly used to quantify the feedback level.

Experimentally it is difficult to estimate the real fraction of light that is reinjected into the laser. One could measure easily the ratio between the light power emitted by the solitary laser and then, the light returned just before the collimator, like in Ref. [89], but the losses for the coupling between the laser and the external field (collimator) are not taken into account. A possible way to quantify the coupling ratio between laser and collimator is proposed in Refs. [90, 91], where the solitary laser light power is measured before and after the collimator placed in its working position. In this way the laser/collimator coupling ratio R_{coupl} is measured and it is assumed to be the same even for the reversed propagation path of the field. Calling R_{cav} the power ratio between the light returned to the collimator by the external-cavity and the light transmitted by the collimator, the fraction of light returned into the laser is estimated to be $R_{ext} = R_{coupl} \cdot R_{cav} \cdot R_{coupl}$. In fact, this measurement gives just a rough estimation of the collimator/laser coupling coefficient: the problem of mode matching between the returned beam and the laser cavity is not taken into account by the measuring detector. This is proven by modifying slightly the laser/collimator distance around the position for which

the beam is focused onto the external mirror: the measure of the coupling ratio by a detector (active region diameter larger than 0.5 mm) is not significantly affected while, in the system, the feedback level changes dramatically.

In order to quantify the feedback level we have preferred to use an indirect method where, rather than measuring the light fed back, we have measured the feedback effects in the laser characteristics. In fact, when a laser is subjected to optical feedback, the threshold decreases linearly, on a wide feedback range, with the feedback rate F, since re-injecting back into the laser cavity part of the light emitted is equivalent to reducing the losses of the laser. Using the rate eqts. 1.2.27, the re-injected field term 2.1.2 changes the level of the total losses $1/\tau_p$. If the external-cavity is at least two orders of magnitude longer than the optical length of the laser cavity, the phase effect of the feedback is negligible on the system output power (see the next section or Refs. [10, 92]). Therefore we can assume the maximum constructive interference between the returned field and the field in the cavity and, according to 1.2.27 with 2.1.2, we have the new threshold condition: $G = 1/\tau_p - 2F$. Calling $I_{th,feed}$ the current threshold of the system with feedback, we have:

$$\frac{I_{th,sol} - I_{th,feed}}{I_{th,sol}} = 2\frac{F}{1/\tau_p} \tag{2.1.5}$$

that holds if $1/\tau_p(I_{th,feed}) \approx 1/\tau_p(I_{th,sol})$, i.e. if α_{int} does not change a lot with current. Eqt. 2.1.5 enables us to relate the threshold reduction with the other parameters used to quantify the feedback strength. In our experiments we express the feedback level with the threshold reduction induced (in percentage) ξ:

$$\xi = [100 \times \frac{(I_{th,sol} - I_{th,feed})}{I_{th,sol}}]\% \tag{2.1.6}$$

Since this measure involves the effect of the feedback on the laser, it takes into account all the losses suffered by the light in traveling in the external-cavity.

2.1.4 Feedback level setting: alignment condition and mode-matching

Once the external-cavity mirror is in place and the collimating lens at its working distance from the laser, the alignment between the feedback beam and the laser is optimized by tilting the external mirror until reaching the position at which the feedback level is maximum (minimum laser threshold). One may think that the feedback level may be changed by tilting the external mirror, i.e. modifying the feedback beam alignment quality. In fact, by this method other effects are introduced as well. The misalignment between the returned and emitted beams could introduce multiple pass resonances in the external-cavity, due to the fact that the beam is reflected by the chip substrate surface, one or several times, before returning into the laser cavity (Refs. [11, 93, 94]). Anyway, the experimental investigation of the system behavior as the external mirror is tilted is exposed in Ref. [95]. Another effect that is possibly introduced is an asymmetry in the re-injected beam profile in the active region, with the consequence of a inhomogeneous feedback profile through the active medium.

Once found the best alignment, the feedback level may be improved further by changing the position of the collimating lens. It turned out that the feedback level depends critically on lens focusing point (see Ref. [11]) and it is maximized when the collimating lens is focusing the laser beam on the surface of the external mirror. Since the cavity is symmetric around the external mirror, beam focusing on the mirror surface implies that the returned beam at the laser facet is the image of the beam at the emission source. The fact that this method realizes a better mode matching than beam collimation is probably due to the strong astigmatism of the laser beam. In fact, even setting the collimator at its working point, the collimation is never perfect and the beam spreads slightly as it travels inside the external cavity.

In our experiment we have always maintained perfect alignment and mode matching condition.

Since we want to study the effect of the delayed field re-injection, without any spatial effect spuriously coupled, we do not tilt the external mirror in order to control the feedback level. For the same reason, we have always set the position of the collimators in order to have a perfect mode matching between the emitted and the re-injected fields. We have changed the feedback level using the methods described in the Appendix A.5.1.

Many experimental works in the literature show set-up where the feedback is applied onto the back laser facet. In some devices, the laser chip is mounted on open mounting that enables the propagation of the back emission light (typically $Hitachi^{TM}$ HLP 1400). Since the laser chip has not the back facet on the edge of the mounting, the emitted light, partly reflected by the mounting base, interferes with itself, exactly as in a Lloyd interferometer. The consequence is that the back beam presents interference fringes. For this reason we strongly dislike the experimental configuration using such a beam as feedback beam. In our opinion, in such configuration, it is impossible to guarantee mode matching and, because of the interference fringes, frequency non-selective feedback. On the other hand, this back beam, once properly focused, is very useful for the detection of the output power of the system.

In our feedback experiment we have explored feedback levels involving threshold reduction larger than 1% (typically from 5% up to 25%). In terms of F this would mean (assuming $1/\tau_p = 6.31 \times 10^{11}\ s^{-1}$) larger than $3.15 \times 10^9\ s^{-1}$ (typically from $1.57 \times 10^{10}\ s^{-1}$ up to $7.9 \times 10^{10}\ s^{-1}$), in terms of κ^2 (assuming $\tau_{in} = 8\ ps$) this would mean larger than $-32\ dB$ (typically from $-18\ dB$ up to $-4\ dB$), in terms of R_{ext} this would mean (assuming $R_1 = R_2 = 0.31$) larger than 4×10^{-4} (0.04%), typically from 0.01 (1%) up to 0.26 (26%).

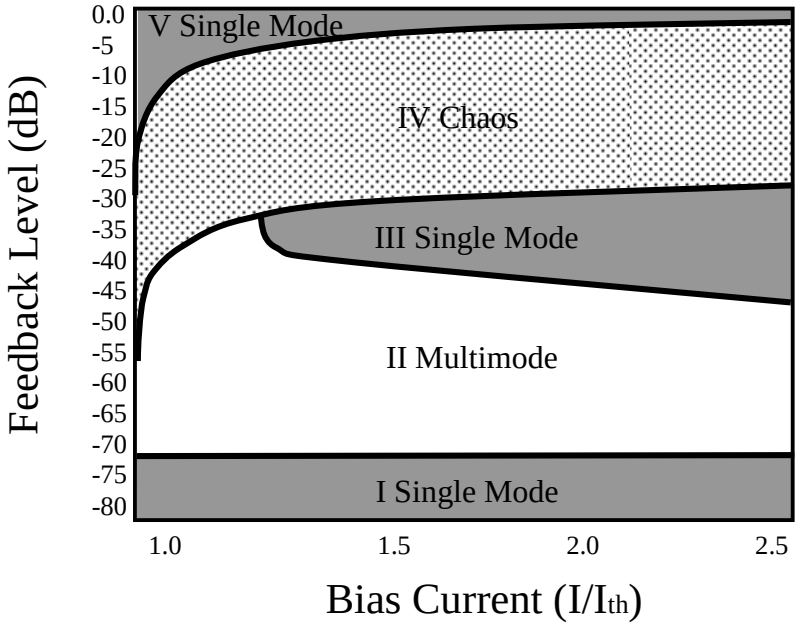

Figure 2.4: Parameter space for a DFB laser with feedback: pumping current and feedback level. From Ref. [96]

2.2 Global description of the parameter-space

2.2.1 Parameter-space overview

In this paragraph we want to describe briefly the general parameter-space of the system laser with optical feedback. We have not performed this characterization based on wide control parameters variation ranges, since it has been already performed by other groups, and it is fully available in the literature (Refs. [7, 14]). We want to describe the general phenomenology of the system in order to locate the parameter-space region where we have performed our analysis. In Fig. 2.4 we report a qualitative mapping of the parameters space according to Ref. [14]. The system is composed by a single-mode semiconductor laser with an external reflector at a distant variable from 10 cm to 100 cm.

We can notice that feedback starts to affect the laser behavior already at -80 dB. At -70 dB (regime II) the system starts to admit multiple stable solutions that correspond to external-cavity-modes. Increasing the feedback level the

system could lase on an increasing number of different external-cavity-modes and spontaneous-emission noise could induce mode hopping (Refs. [14, 96]). Regime I and II are called *weak feedback* regimes. The *weak feedback* regimes have been experimentally studied in Ref. [91] for low biasing current ($I < 1.5 \cdot I_{th,sol}$). In Ref. [91] it turns out that the spectral characteristics of a semiconductor laser with optical feedback depend on the feedback level and on the laser characteristics. It is possible to define two critical levels for the feedback: the first, r_a, is the level for which, if $r < r_a$, the laser is always single-mode no matter the feedback phase (regime I), the second, r_b, is the level for which, if $r_a < r < r_b$, the system emits on a single or on several external-cavity-modes depending on the feedback phase. Anyway, for $r_a < r < r_b$, the Mode-Suppression-Ratio is always larger than 20 dB even when, because of noise-induced hopping among external-cavity-modes, the emission is multi-mode. For $r_a < r < r_b$ the optical linewidth of the compound system can be much narrower than the solitary laser (0.1 MHz against 17 MHz in Ref. [91]). In this regime, the feedback improves the laser performance, especially using short cavity, where the wide separation between external-cavity-modes makes the single-mode operation very robust (Ref. [92]). While for $r < r_b$ only one internal-cavity-mode is active, several internal-cavity-modes are excited for $r > r_b$ and the MSR falls down abruptly; we are in regime IV. In regime III, obtained for $I > 1.5 \cdot I_{th,sol}$, the feedback improves again the stability of the solitary laser and the optical line gets narrowed (Refs. [97, 98, 99, 100]).

In regime V (*strong feedback* level) feedback improves the coherence properties of the laser. It must be pointed out that such strong feedback level requires AR coating of the laser facet exposed to feedback and perfect alignment and mode matching conditions.

The regime IV (*moderate feedback* level) is dynamically very rich and it is the most explored in the literature. Going from the regime III to the regime IV

a quasi-periodic route to chaos has been found in Ref. [101]. Here it is shown experimentally that the laser main mode is destabilized by a Hopf bifurcation (at a feedback level = $-43\ dB$) and a limit cycle takes place at the frequency of the relaxation oscillation of the solitary laser. Continuing to increase the feedback level this limit cycle gets larger and distorted, and, at $-31\ dB$, the trajectory presents the characters of a chaotic attractor. The interpretation of quasi periodic route to chaos is supported by observing the power spectrum as the feedback level is increased. From $-44\ dB$ to $-32\ dB$ it shows increasing intensity peaks at the inverse of the external-cavity round-trip time (ν_{ext}), then it shows frequency locking between ν_{ext} and the relaxation oscillation of the solitary laser (f_r) and finally it shows broadening of the peaks, testifying the appearance of the chaotic attractor. The frequency locking region is very sensible to the experimental conditions like pumping current and external-cavity length; hence Mork et al. claimed that the route to chaos may be interrupted by frequency locking. These experimental evidences are coherent with a calculated bifurcation diagram predicting quasi periodic route to chaos. Further confirmations come from the fact that the calculated bifurcation diagram predicts the coexistence of two attractor whose existence has been showed experimentally. It is important to underline that the laser is a DFB laser, the pumping current is $1.8 \cdot I_{th,sol}$, the external-cavity length is of the order of 15 cm and it is tuned such that an external-cavity resonance coincides with the solitary active laser mode. This prevents, for low feedback level, the excitation of other external-cavity-modes.

2.2.2 The effects of the feedback phase

The tuning of the cavity length on wavelength scales affects the emission characteristics of the system. The relevance of the feedback phase depends, in general, on the external-cavity length and on the feedback level. For weak feedback levels

we may represent the system as a laser cavity perturbed by a weak fraction of the field emitted, returned into the laser cavity with a phase difference due to the delay accumulated during the external-cavity round-trip. When the external-cavity length is tuned on a wavelength scale, the phase relationship between the field emitted and the field re-injected changes. Since the interference condition is altered, the stability of the active laser mode is affected and the system jumps to another external and/or internal-cavity-mode, where the interference condition is more convenient. The mechanism of this instability depends, among other things, on the relationship between external-cavity length (L_{ext}) and internal-cavity optical length (L_{int}^{opt}). This relationship determines the matching between the frequencies of the external and of the internal-cavity-modes and, as a consequence, whether the system will hop to the closest external cavity mode, continuing lasing close to the same internal-cavity-mode, or it will hop to an external-cavity-mode far apart more than one internal-cavity free spectral range.

For large cavity lengths it is necessary to consider that the spectral density of external-cavity resonances grows, changing consequently the mechanisms of the mode hopping. Finally, for a given cavity length, the feedback level affects the stability of the modes since it is directly related to the finesse of the external resonator. We now describe how these considerations come into play in the experiments.

In Ref. [16] they investigate the effects of weak feedback on the L/I curve of the laser for short external cavities ($L_{ext} < 20 \cdot L_{int}^{opt}$). Then, the separation between external-cavity-modes is of the same order of magnitude than the separation between internal-cavity-modes. For an external-cavity of 1 cm the spacing of the external-cavity-modes is of 15 GHz, and it becomes the same as the internal-cavity-mode spacing if $L_{ext} \approx L_{int}^{opt} \approx 3.5 \cdot L_{int}$, i.e. typically $L_{ext} \approx 1$ mm, because of the active medium refractive index. For $L_{ext} < 20 \cdot L_{int}^{opt}$, if the solitary

laser is emitting on a single-longitudinal-mode, the compound system emits on a single external-cavity-mode for a wide range of feedback level (Ref. [92]), because of the large detuning among the solitary laser peak and the other external-cavity-modes. In this situation, the tuning of the external-cavity length on wavelength scale generates a modulation of the system output, exactly as expected from scanning a low finesse Fabry-Pérot (Refs. [16, 91]). Since Joule heating makes the output wavelength of the solitary laser increase continuously as the pumping current increases (0.092 Å/mA, or, in terms of external-cavity-modes separation, 0.26 modes/mA in Ref. [16]), the same modulation is present (with a period of $\frac{1}{0.26}$ mA), in the L/I curve, for a fixed length of the external-cavity (Fig. 2.5).

The amplitude of the undulation depends on L_{ext} and it is maximized when it corresponds to a multiple integer of L_{int}^{opt}. In this condition (Fig. 2.5, lower panel), the optical spectrum shows that, in the interval of pumping current corresponding to each L/I undulation period, the active external cavity mode is always the same, and, at the successive undulation period, the system has jumped abruptly to the next external-cavity-mode (at higher wavelength for increasing current). The active external-cavity-mode is the one closest to the solitary laser peak; as this peak moves to higher wavelength because of the current increasing, the system hops on the external-cavity-mode better tuned to the solitary laser frequency. In the situation where $L_{ext} = nL_{int}^{opt} + \Delta L$ (Fig. 2.5, upper panel), the situation is more complicate: increasing the current, starting from the bottom of an undulation, the optical spectrum shows that the system jumps from one internal-cavity (say the mode of order m) mode to the closest one $m+1$ at smaller wavelength. This hopping from one internal-cavity-mode to the next one continues up to the next bottom of the undulation, there the system has jumped abruptly back at the mode $m-1$, the closest higher wavelength internal-cavity-mode to the mode where the system was lasing at the preceding bottom of the L/I curve. This

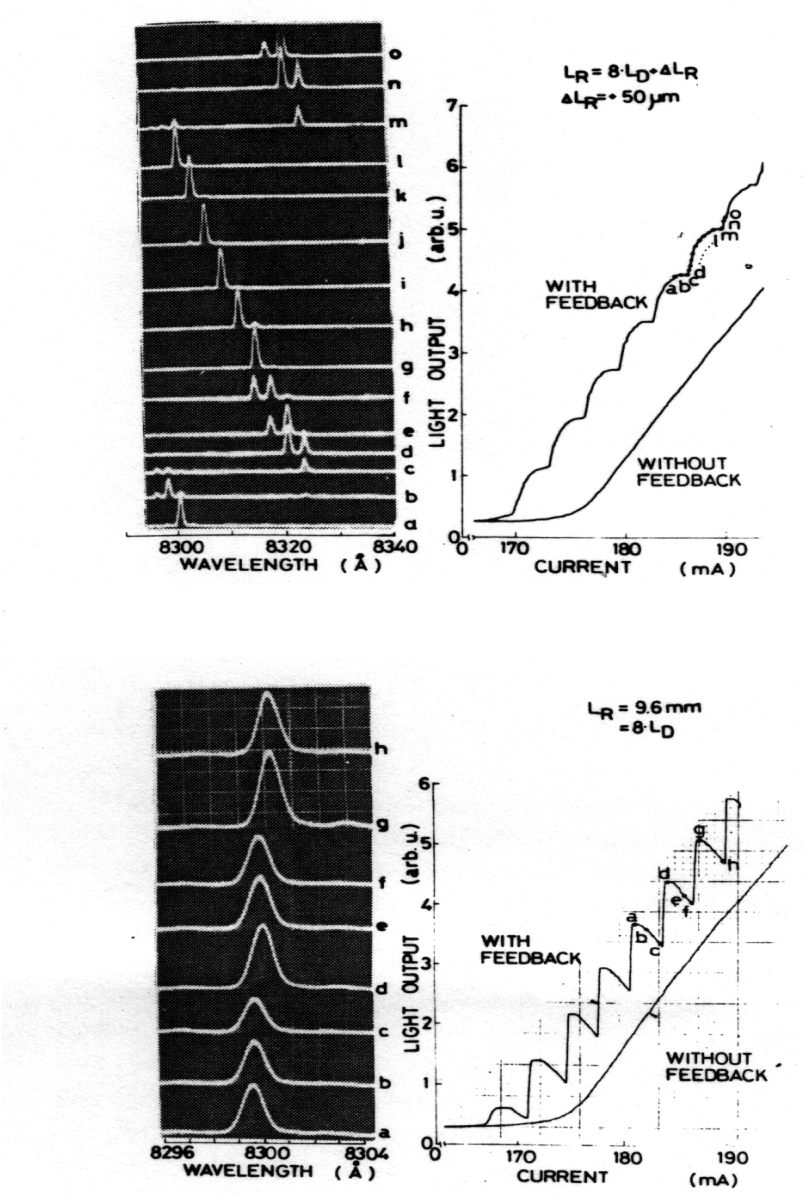

Figure 2.5: Spectral changes and output undulation with current increase, when L_{ext} is greater by 50 μm than the nearest integral multiple of L_{int}^{opt} (above) and when L_{ext} is equal to an integral multiple of L_{int}^{opt} (below). From Ref. [16]

phenomenology is repeated through all the ripples of the L/I curve. The difference between the two behaviors is due to the frequency matching between the combs of the internal and of the external cavity modes. When $L_{ext} = nL_{int}^{opt}$ there is always the same detuning between all the internal-cavity-modes and the closest external-cavity-modes; the active external-cavity-mode is always the closest one to the lasing mode. The lasing mode retains the control on the selection of the external-cavity-mode, because no other internal-cavity-mode is better tuned with respect an external-cavity-mode. When $L_{ext} = nL_{int}^{opt} + \Delta L$, this is not true anymore. In this case the system realizes a better matching using an internal-cavity-mode different from the one active in the solitary laser case. Let us suppose that, at a certain pumping current level, the internal mode m (the solitary lasing one) is resonant with the external-cavity-mode m'; increasing the current, the comb of internal-cavity moves, and the mode m and m' are not perfectly tuned anymore. Depending on ΔL, it could be that now the modes $m+1$ and $m'+n'$ are the best tuned and then the system emits on the mode $m'+n'$. The system chooses different internal-cavity-modes in order to maximize the feedback interference and, as a consequence, the intensity-output varies smoothly as the current is increased (Fig. 2.6).

In Fig. 2.6 (from: Ref. [16]) we show the amplitude of the output undulation of the L/I curve as the length of the cavity is changed. The maxima corresponds to $L_{ext} = nL_{int}^{opt}$, where the system is extremely sensible to the feedback phase. It worth noting that, as the length of the cavity is increased, the height and the separation of the peaks decrease because of the increasing density of external-cavity-modes.

In Fig. 2.7 we show the output power versus external-cavity length curves for different feedback levels (from: Ref. [89]). The minima corresponds to the lengths at which $L_{ext} \approx nL_{int}^{opt}$. Around these cavity length values, the system emits always

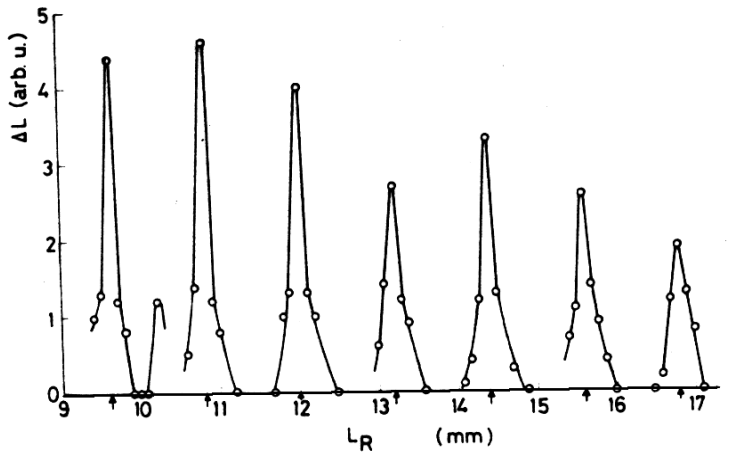

Figure 2.6: Amplitude of output undulation of the L/I curve as L_{ext} is changed. The arrows indicate where $L_{ext} = nL_{int}^{opt}$. From Ref. [16]

on the same internal-cavity-mode and the intensity-output decreases strongly for the destructive interference between the field emitted and field fed back. Instead, when $L_{ext} \neq nL_{int}^{opt}$, the system emits on different internal-cavity-modes and the effect on the power output is smoother.

When the external-cavity length is increased over $L_{ext} > 100 \cdot L_{int}^{opt}$, the spectral density of the external-cavity resonances is very high. For such lengths, a variation on a wavelength scale of the external-cavity does not perturb remarkably the intensity-output of the system (Fig. 2.7, left panel); the spectral density provides good internal/external cavity modes matching for any ratio between L_{ext} and L_{int}^{opt}. In other words, the high spectral density of the external-cavity-mode breaks the competition between internal and external-cavity-modes.

The feedback level, increasing the finesse of the external resonator, increases the undulational amplitude of the L/I curve and the sensibility to the feedback phase as the cavity length is varied (Fig. 2.7, right panel, Ref. [89]).

Our experimental work has been dedicated to the regime IV and V (it moderate-to-strong feedback levels) and we have always used fairly long external-cavity ($L_{ext} = 15 - 100\ cm$). In this experimental conditions, the system is not critically

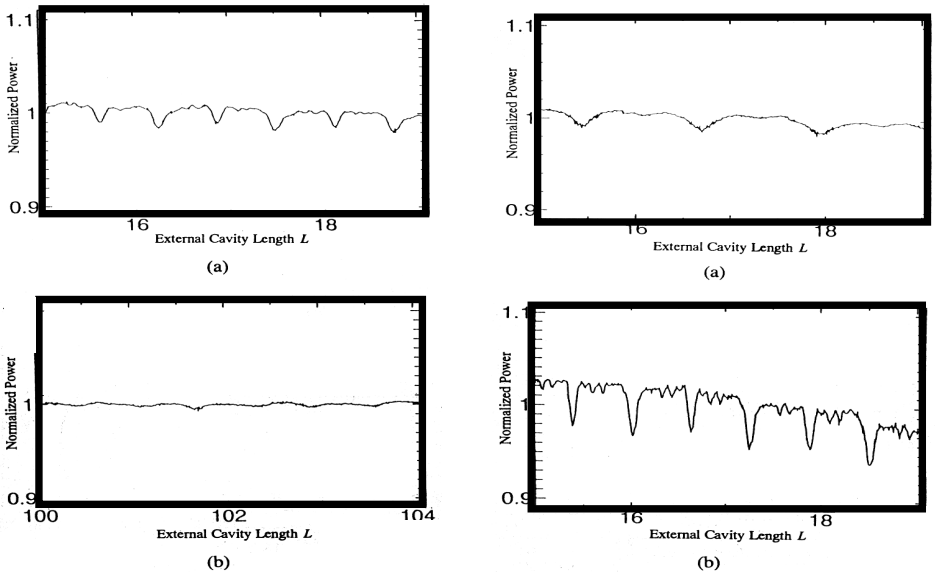

Figure 2.7: Experimental results of the output power as a function of the external-cavity length for different cavity locations. On the left: $R_{eff} = 0.248$, a) $L = 15 - 19\ mm$, b) $L = 100 - 104\ mm$. On the right: $L = 15 - 19\ mm$ a) $R_{eff} = 0.0115$, b) $R_{eff} = 0.387$. From Ref. [89]

sensitive to the feedback phase wavelength scale tuning of the external-cavity and the results obtained are qualitatively valid for any cavity length in the above mentioned range as in Ref. [10].

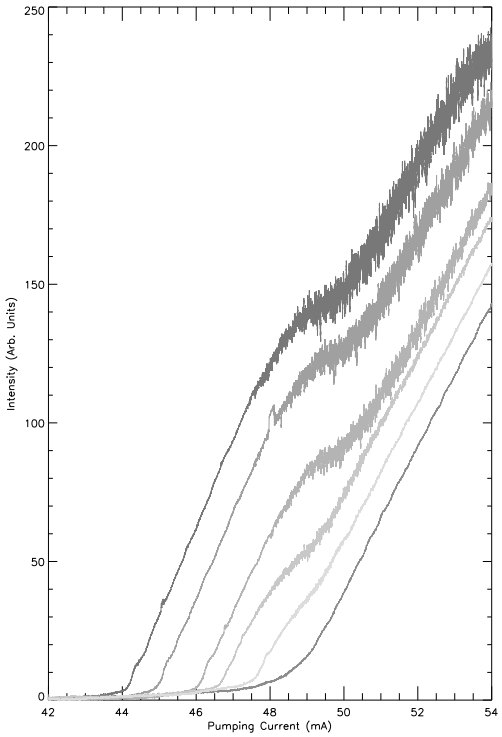

Figure 2.8: Light Output / Pumping Current curves for different feedback levels.

2.3 The Low-Frequency Fluctuations (LFF)

In Fig. 2.2 we have shown the L/I curve for the laser system with optical feedback from a distant reflector ($L_{ext} = 63\ cm$, $\tau_{ext} = 4.2\ ns$). In Fig. 2.8 we show the L/I curve for different levels of feedback, we used low bandwidth detector ($< 1\ MHz$). From these curves we can estimate the amount of feedback ξ by comparing the threshold of the system with feedback $I_{th,feed}$ with the threshold of the solitary laser $I_{th,sol}$. In the case of Fig. 2.2 we have $I_{th,feed} = 44\ mA$ which is equivalent to a feedback level of $\xi = 9.3\%$ of threshold reduction.

The shape of the curves shown in Fig. 2.8 is typical for feedback level involving threshold reduction (ξ) from 2% up to 20% (feedback level from $-32\ dB$ up to $-2\ dB$, or $0.04\% < R_{eff} < 33\%$) (Refs. [11, 96, 102]). We remark a kink around the threshold of the solitary laser. By monitoring the laser output with

a 100 MHz detector (Fig. 2.2), we notice that this kink is due to drops of the laser intensity, appearing abruptly with large amplitude at a given pump level. These features in the L/I curves give already important indication on the nature of the instability at the origin of the drops. It appears evident from Fig. 2.2 that these fluctuations could not be originated by a super-critical Hopf bifurcation. In fact, in this case, the instability would appear with small amplitude oscillations, increasing as the control parameter is changed.

In Fig. 2.8, where the output power has been averaged on a long time-scale, the appearance of power drops induces an abrupt decrease of the Slope Efficiency of the system. Kink in the L/I curve are, for laser engineering, the most relevant effect of feedback in a laser system, since the quality of a device is often related to the maximum power achievable *kink free*, i.e. in the linear range of the L/I curve.

In order to describe the emission characteristics of semiconductor laser with optical feedback we plot in Figs. 2.9, 2.10, 2.11 the time intensity-output, the noise (or power) spectrum and the optical spectrum of the system as the control parameters are changed. The bandwidth of the time-series is limited by the scope bandwidth (500 MHz). The power spectra are limited by the detector bandwidth ($\approx$ 2 GHz). In order to detect the entire set of the laser internal longitudinal-mode, the free spectral range of the interferometer has been set at $\approx$ 3200 GHz, limiting the resolution to $\approx$ 20 GHz. In Fig. 2.9 the external-cavity round-trip is $\tau_{ext} = 4.2\ ns$, we show the behavior of the system as pumping current is increased and the feedback level is $\xi = 12\%$. In Figs. 2.10-2.11 the external cavity round-trip is $\tau_{ext} = 3.2\ ns$, we have fixed the pumping current (respectively, at $I = 1.09 \cdot I_{th,sol}$ and $I = 1.2 \cdot I_{th,sol}$) and we have changed the feedback level. Decreasing this parameter we obtain the same sequence of behaviors as increasing the current. In order to achieve very large feedback level, the experiment of Figs.

2.10-2.11 has been performed with an $Hitachi^{TM}$ HLP1400 partially AR-coated ($\approx 1\%$) on the output facet. For a feedback level $9\% \lesssim \xi \lesssim 25\%$ the system exhibits three main regimes as the pumping current (I) is changed.

•**Stable-regime.** Appearing for $I_{th,feed} < I < I_{lff}$, being I_{lff} the pumping current value at which the power drops occur. I_{lff} depends on the feedback level but it is always $I_{lff} \gtrsim I_{th,sol}$ for $9\% \lesssim \xi \lesssim 25\%$.

This regime (Fig. 2.9a, 2.10a, 2.11a) is characterized by a constant intensity-output at low-frequency (0-100 MHz). The corresponding power spectrum can be flat or composed by narrow peaks at the multiple of the external-cavity resonant frequencies (ν_{ext}), depending on the feedback level. If the feedback level is very strong ($\xi \gtrsim 15\%$) the power spectrum shows no noise in excess at any electrical frequency and the corresponding optical spectrum shows single internal-cavity-mode operation (Fig. 2.10a, 2.11a). We can conclude that the laser emit on a single external-cavity-mode.

From the optical spectrum we remark that, when $I_{th,sol} < I < I_{lff}$, the Mode-Suppression-Ratio (MSR) of the system with feedback is larger than the solitary laser MSR at the same current (compare the optical spectrum of Fig. 2.3 at $I = 49.2\ mA$ with the one of Fig. 2.9). In these conditions, the properties of coherence of the laser are improved by the feedback (regime V in Fig. 2.4). Moreover, a comparison between the lasing absolute frequencies of the system with and without feedback reveals that, in the feedback configuration, the lasing peak is red-shifted of several internal-cavity free spectral ranges in respect with the solitary laser lasing modes. The amount of this frequency shift increases with the feedback level and it is due mostly to the decrease of the carrier density stationary value induced by the laser threshold reduction. This change occurs at injection current almost constant since the carriers injected in excess respect to the new threshold value increases the photon density stationary value. Then,

according to the consideration of §II.1.2, band-filling effect dominates on the thermal effect and the gain curve shifts to the red for the carrier density decrease.

If the feedback is not very strong (Fig. 2.9a), $9\% \lesssim \xi \lesssim 15\%$, $I_{lff} \approx I_{th,sol}$, the power spectrum shows narrow noise peaks at the resonant frequencies of the external-cavity (ν_{ext}). These peaks correspond to the beating notes between external-cavity-modes: the first peak at ν_{ext} is given by the beating note of adjacent external-cavity-modes, the second peak, at $2 \cdot \nu_{ext}$, correspond to the beating note of external-cavity-modes separated by two orders and so on. These frequency components can be resolved in the time signal provided they fall inside the oscilloscope bandwidth; this condition is verified, for the peak at ν_{ext}, if $L_{ext} > 30\ cm$. In the time trace, this component appears as a small sinusoidal modulation of the output intensity.

In Fig. 2.9a the power spectrum shows, at the right side of each external-cavity resonance, a broad and lower noise peak. We have not observed this side peak in the power spectrum of the stable-regime when using the AR-coated laser of Fig. 2.10-2.11, even for equivalent feedback levels. This suggests that the presence of side peaks is connected to some property of the solitary laser. Moreover, the broad peaks, as the pumping current is increased, broaden and move to higher frequencies. Since the broad peaks are located only on a side of the narrow peaks at ν_{ext} and since there is no peak in the power spectrum at the frequency difference between the peaks at ν_{ext} and the side peaks, we can conclude that these peaks are not originated by a beating between an external-cavity-mode and a broad side peak. The double-peaked structures in the power spectrum seems rather originated by the beating itself between different external-cavity-modes. The origin of this double-peaked intensity noise spectrum has been explained in Ref. [103] as due to correlation between the lasing mode and sub-threshold external-cavity-modes, leading, in the beating note, to strong suppression of the

intensity noise. The dip in between the two peaks is then originated by the strong anti-correlation between the noise in the active mode and the noise in the sub-threshold external-cavity-modes.

•**Coherence-Collapse: LFF-regime.** Appearing for $I_{lff} < I < I_{cc}$, being I_{cc} the highest pumping current at which the LFF features are still recognizable in the time trace.

Increasing the pumping current from the stable-regime we approach a value of pumping current at which sudden intensity breakdowns appear in the time signal (Fig. 2.9b). The power drops are followed by slower relaxation to the previous power level, this recovery is stepped by the round-trip time of the external-cavity τ_{ext} and it lasts 12-16 τ_{ext}. The amplitude of the fluctuation is almost the same for every breakdown. The rate of the fluctuations increases with the pumping current (Figs. 2.9b,c,d) and, for the same pumping level, it increases with decreasing feedback levels (Figs. 2.10b,c,d). Moreover, the drops rate depends on the external-cavity length, which fixes the recovery time and, therefore, imposes an upper limit ν_{max} to the breakdown rate. This highest rate corresponds to the situation where each drop occurs immediately after the recovering of the one before (Fig. 2.9d), then $\nu_{max} \approx (12 \cdot \tau_{ext})^{-1}$. For a typical cavity length ($L_{ext} = 50\ cm$, $\tau_{ext} = 3\ ns$), the maximum drop frequency will be around 30 MHz. Since this frequency value is much smaller than the other frequencies of the system (relaxation oscillation or external-cavity free-spectral-range), the above described fluctuations have been called Low-Frequency Fluctuations (LFF).

The noise spectrum shows strong and broad noise components in the low-frequency region of the spectrum, corresponding to the presence of LFF, and broad peaks at the external-cavity resonant frequencies. The optical spectrum, in the LFF-regime, shows always multiple internal-cavity-modes. Crossing I_{lff} from the stable-regime, this fact is evident in Figs. 2.9b, 2.10b, 2.11b: as power

drops start to appear in the time signal, the optical spectrum shows a sudden decrease of the MSR; several internal longitudinal-modes become active at the blue side of the mode lasing in the stable-regime, covering the spectral interval up to the solitary laser lasing frequency (dash line in the optical spectra of Figs. 2.9d,e). In addition, the linewidth of each modal peak has broadened up to 40 GHz, indicating a frequency chirp of each mode during the fluctuations. In this condition the coherence properties of the laser are lost, hence the name *Coherence-Collapse*.

In Fig. 2.9(b-e) it is possible to observe how the features of the fluctuations evolve, increasing the current from I_{lff}. Passing I_{lff}, LFF starts to appear in the time signal grouped in bursts. These bursts are formed by few fluctuations when $I \approx I_{lff}$ and appear quite seldom in the time-series (Fig. 2.9b). In this condition the noise spectrum may jump between the situation associated to the stable-regime (power spectrum in Fig 2.9a) and the one typical of the LFF-regime, due to the fact that the sweeping time of the spectrum analyzer and the bursts rate are of the same order. Increasing the pumping current the bursts become more and more frequent in the time trace, up to have LFF all over the time trace (Fig. 2.9c). The interval of currents for which the LFF-regime is alternating in time with the stable-regime depends on the feedback level. For feedback level $\xi \approx 9\%$, the "burst region" is very narrow and gets broader for increasing feedback level. In the time-series, once the LFF-regime is totally settled down (Fig. 2.9c), the LFF time-intervals decrease for increasing current, while the LFF amplitude is not significantly affected. Corresponding to the increasing rate of LFF, the optical spectrum shows an increasing number of internal-cavity-modes with a consequent further decreasing of the MSR. This trend continues up to the current value at which the interval between the power drops is equal to their recovery time. In this condition a drop occurs as the intensity has recovered after the preceding drop.

The intrinsic duration of the LFF (that involves the breakdown plus the recovery stage) locks with the drop rate and the corresponding low-frequency peak in the power spectrum narrows in correspondence to almost-periodic LFF in the time signal (Fig. 2.9d).

If the current is further increased there is a limit (I_{cc}) at which the LFF features (drops plus stepped recovery) are lost in the time-series. This starts to appear in localized time-intervals (when $I \approx I_{cc}$) (Fig. 2.9e) and then it extends to the whole time-series.

•**Fully-developed Coherence-Collapse (CC-regime).** Appearing for $I > I_{cc}$.

The time signal in this regime is highly irregular, the corresponding power spectrum shows excess noise at all frequencies and the MSR in the optical spectrum is very low (Figs. 2.9e, 2.11c). In the CC the laser coherence has dropped to few tenths of millimeters.

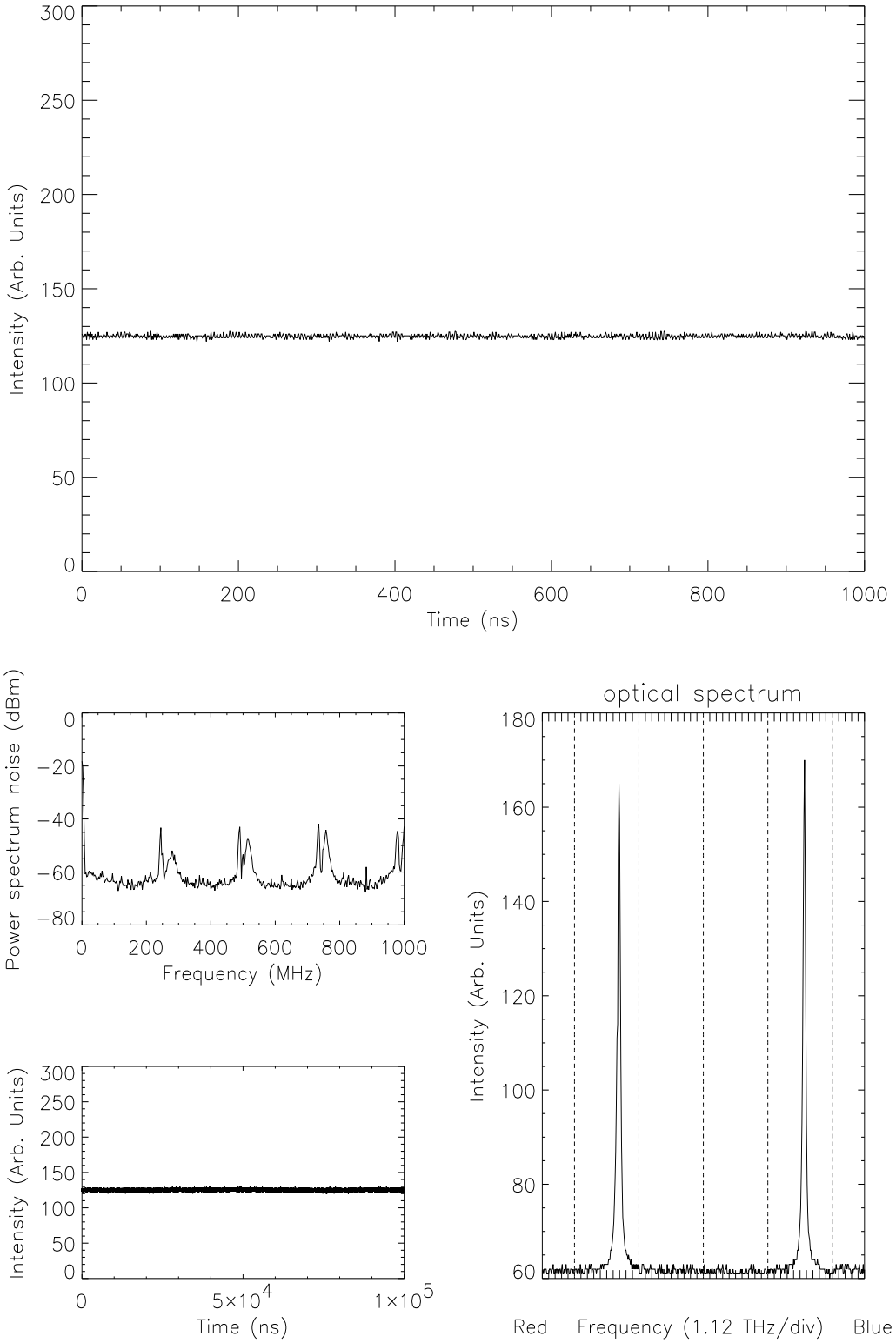

Figure 2.9: (a) Laser emission characteristics with feedback level $\xi = 12\%$, $\tau_{ext} = 4.2\ ns$ and $I/I_{th,sol} = 1.02$.

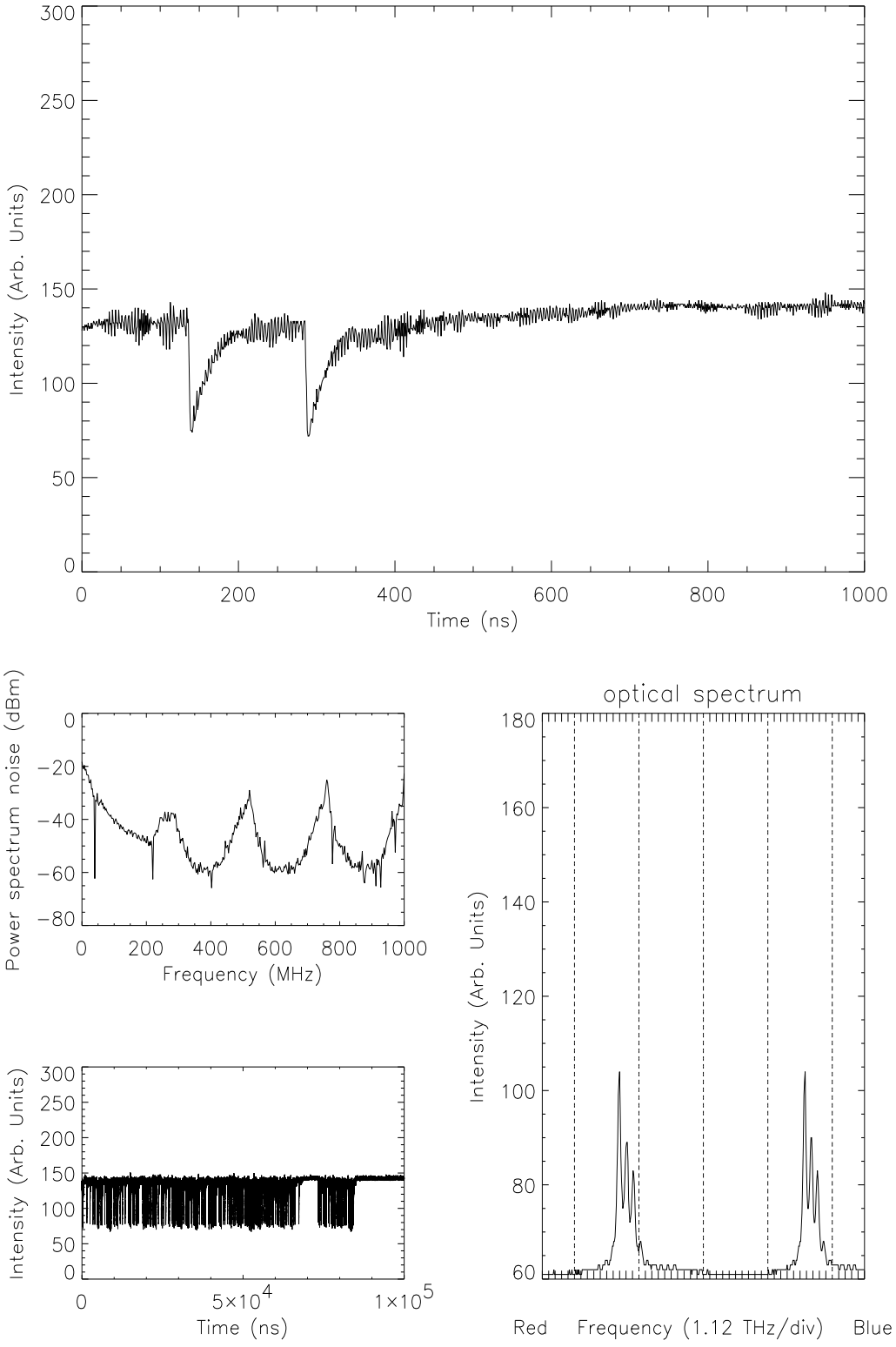

Figure 2.9: (b) Laser emission characteristics with feedback level $\xi = 12\%$, $\tau_{ext} = 4.2\ ns$ and $I/I_{th,sol} = 1.03$.

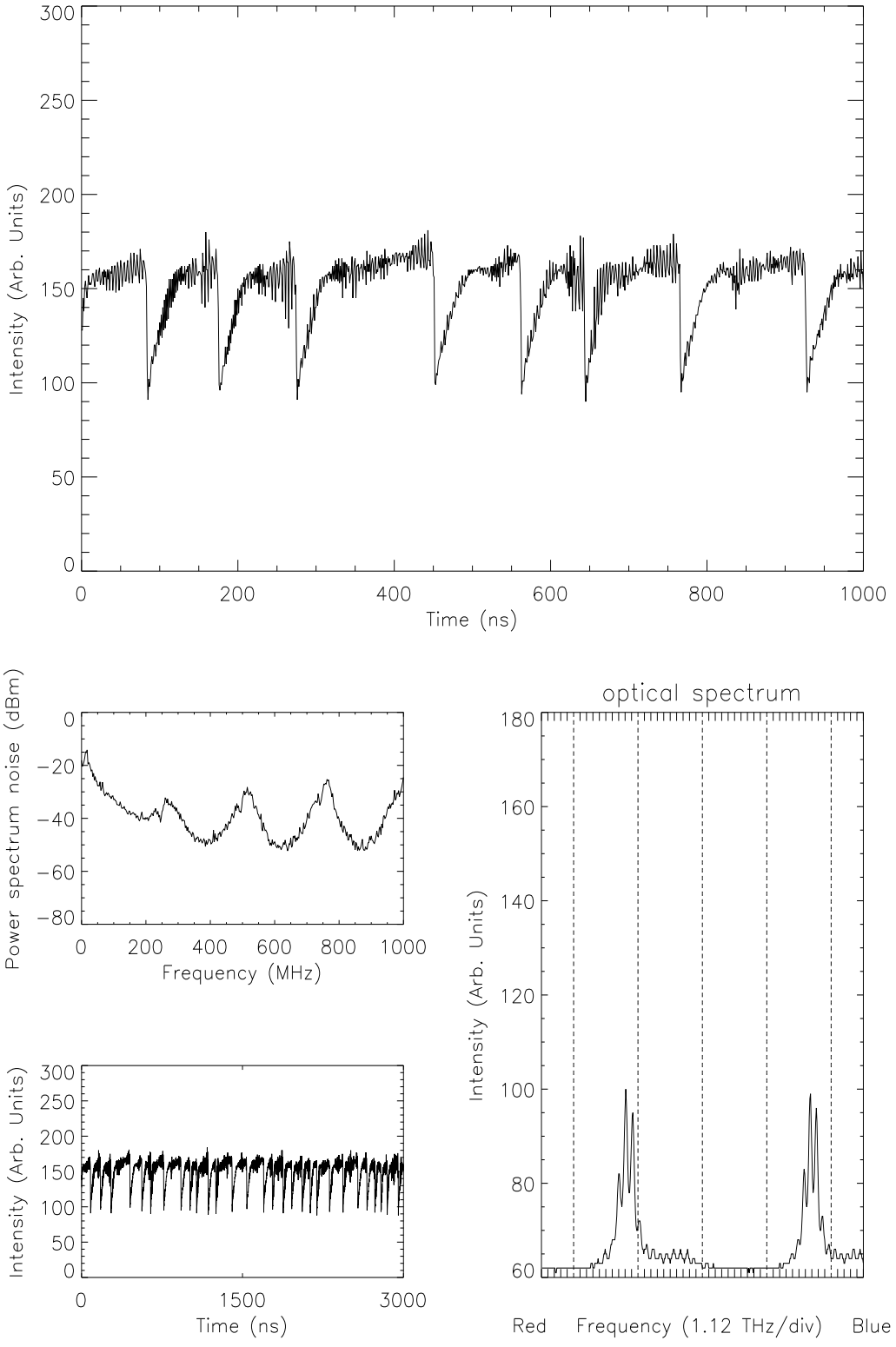

Figure 2.9: (c) Laser emission characteristics with feedback level $\xi = 12\%$, $\tau_{ext} = 4.2\ ns$ and $I/I_{th,sol} = 1.08$.

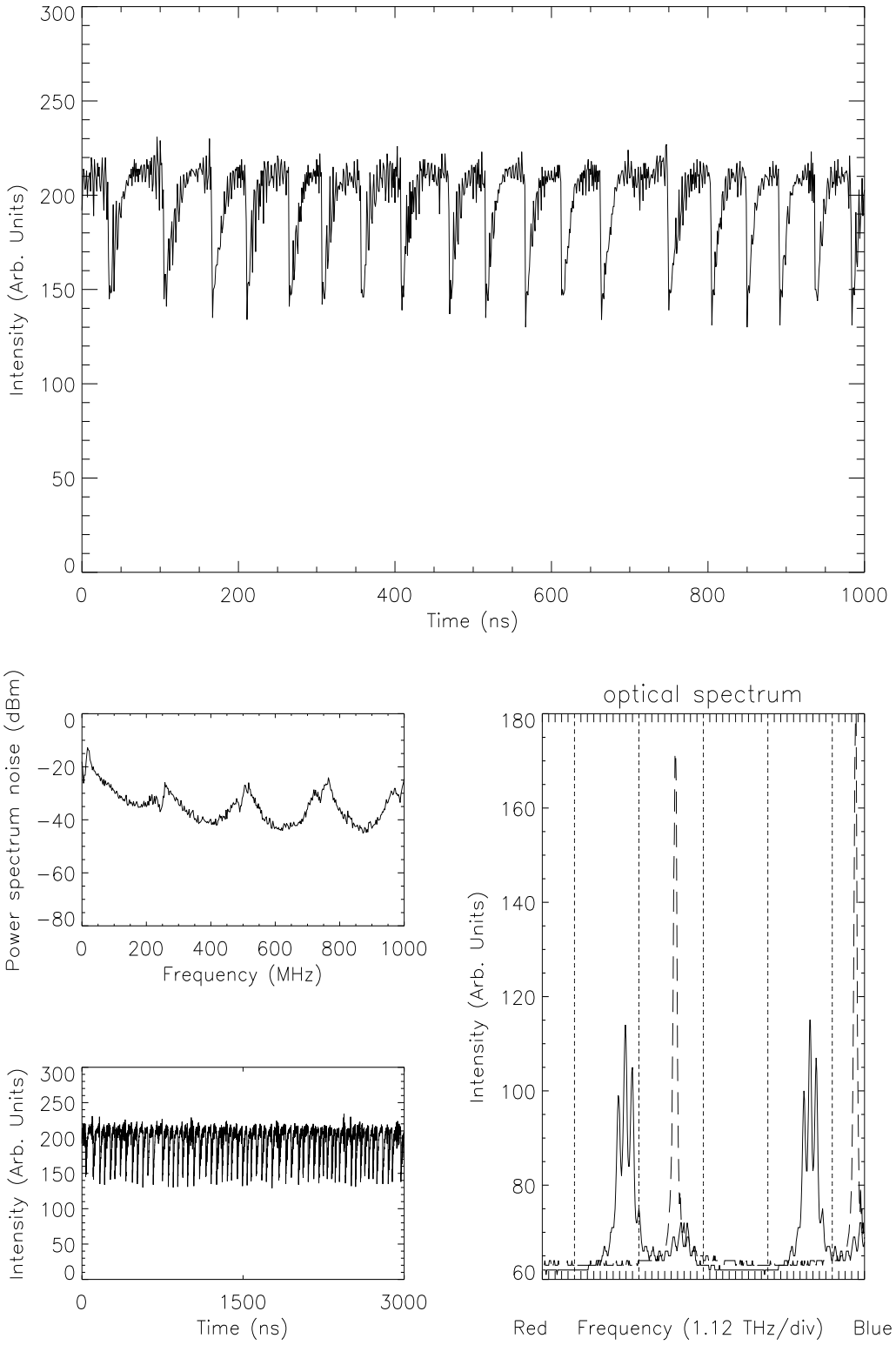

Figure 2.9: (d) Laser emission characteristics with feedback level $\xi = 12\%$, $\tau_{ext} = 4.2\ ns$ and $I/I_{th,sol} = 1.14$. In the optical spectrum we have added for comparison the solitary laser optical line at the same current (dashed trace).

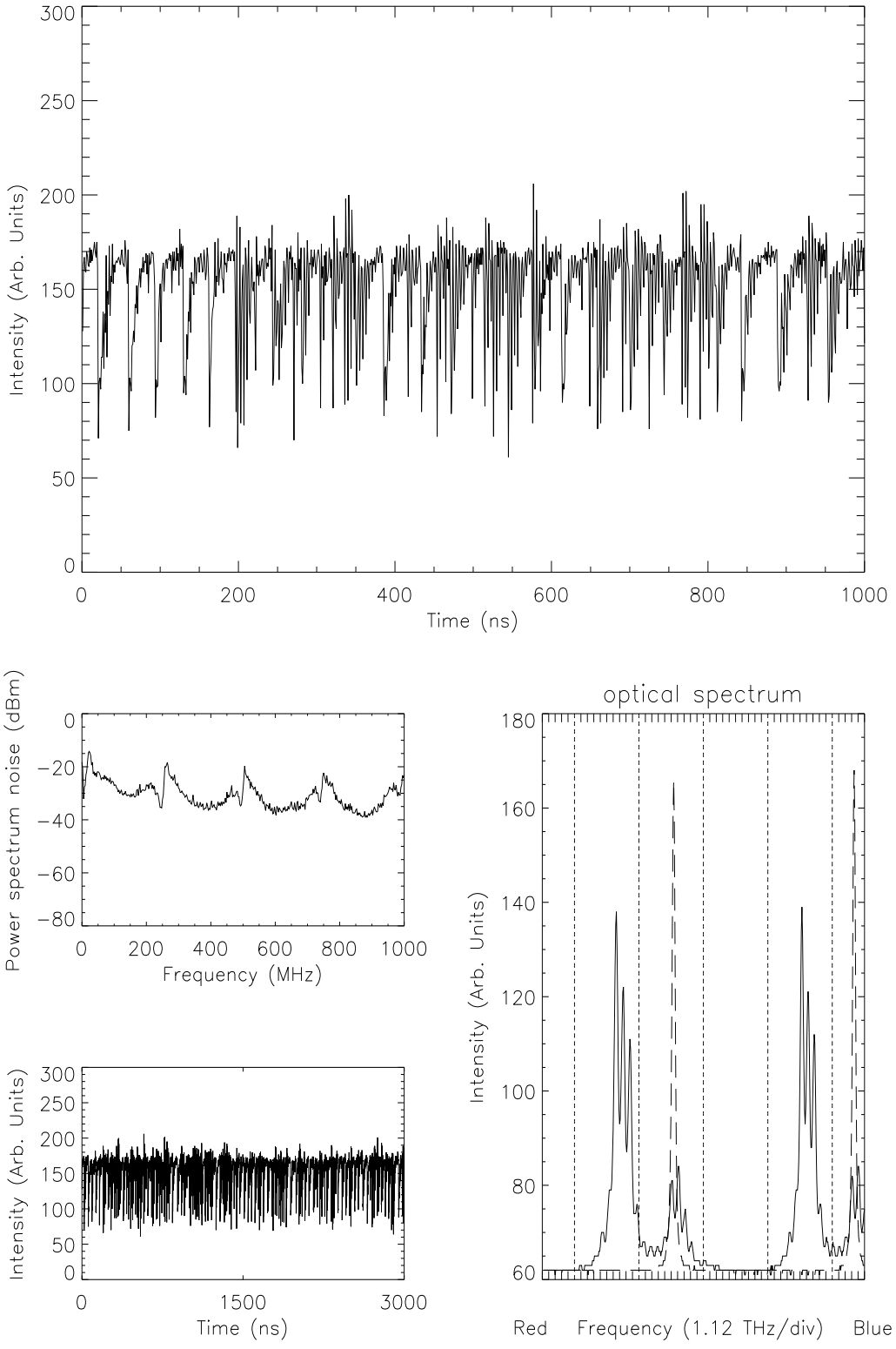

Figure 2.9: (e) Laser emission characteristics with feedback level $\xi = 12\%$, $\tau_{ext} = 4.2\ ns$ and $I/I_{th,sol} = 1.24$. The time-series has a vertical offset of -128 arb. units in respect with the other time-series of Fig. 2.9. In the optical spectrum we have added for comparison the solitary laser optical line (attenuated in intensity by a factor of four in respect with the other traceof Fig. 2.9) at the same current (dashed trace).

In Fig. 2.10 ($I = 1.09 \cdot I_{th,sol}$) we observe the three regimes, previously identified versus pumping current, for the following values of feedback level:

$13\% < \xi < 25\%$: stable single-mode emission on the internal-cavity (Fig. 2.10a).

$11\% < \xi < 13\%$: LFF appears seldom in time (Fig. 2.10b) and multi internal-cavity-mode operation of the system.

$6\% < \xi < 11\%$: LFF(Fig. 2.10c-d) extended to all the time-scale, increasing in frequency and getting almost-periodic, The MSR in the optical spectrum gets lower as the LFF rate increases. Fully-developed Coherence-Collapse settles down for feedback level smaller than 5% at this pumping current value.

For $I = 1.2 \cdot I_{th,sol}$ (Fig. 2.11) we observe the same sequence, even if, in this case, the fully-developed Coherence-Collapse is reached for larger feedback values.

$18\% < \xi < 25\%$: stable single-mode on the internal-cavity (Fig. 2.11a).

$14\% < \xi < 18\%$: LFF seldom appearing in time (Fig. 2.11b).

$5\% < \xi < 8\%$: Coherence-Collapse fully-developed (Fig. 2.11c).

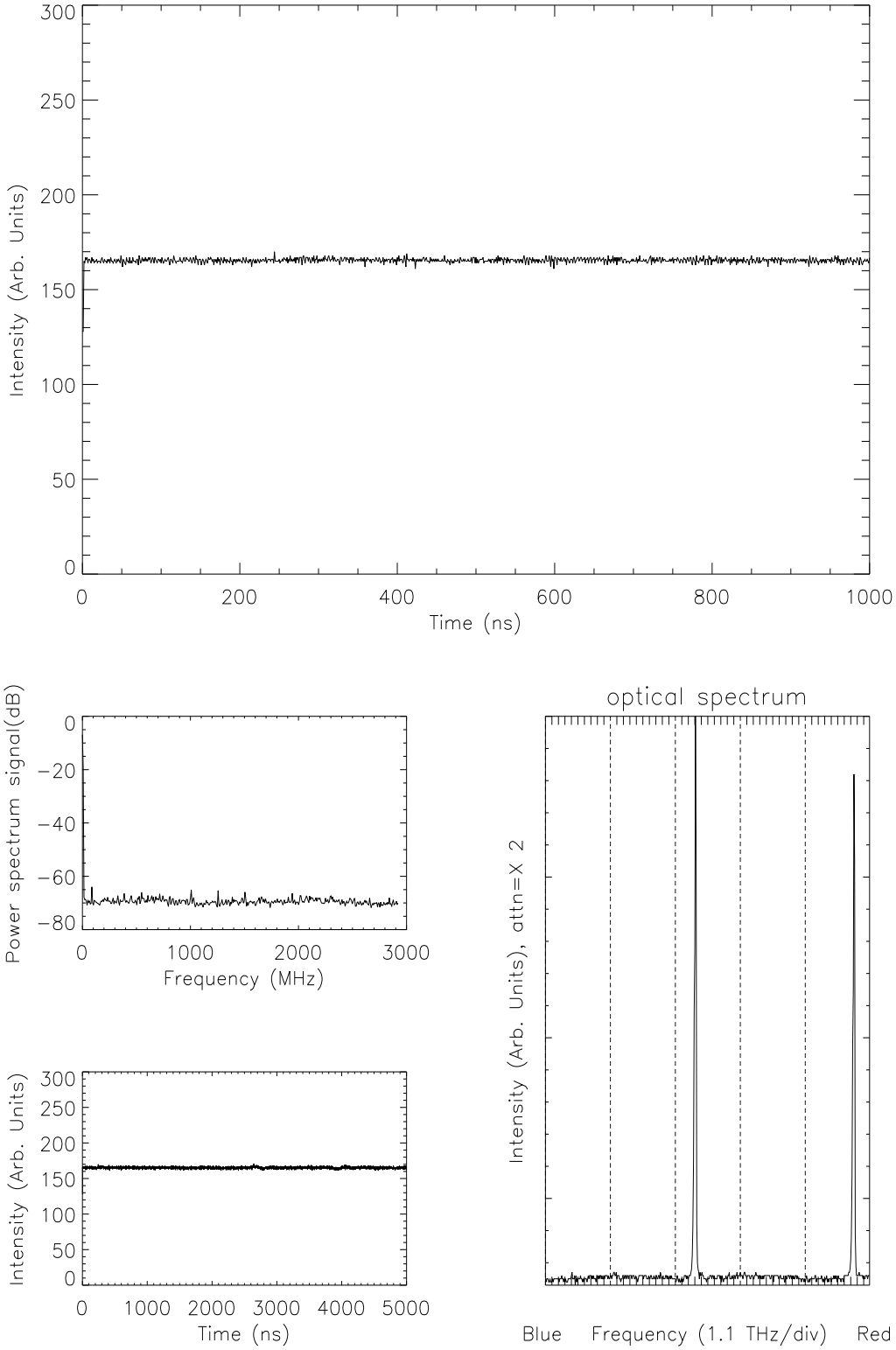

Figure 2.10: (a) Laser emission characteristics with feedback level $\xi = 24\%$, $\tau_{ext} = 3.2\ ns$ and $I/I_{th,sol} = 1.09$. The vertical scale in the optical spectrum is reduced by a factor of two in respect with Figs. 2.10b-d.

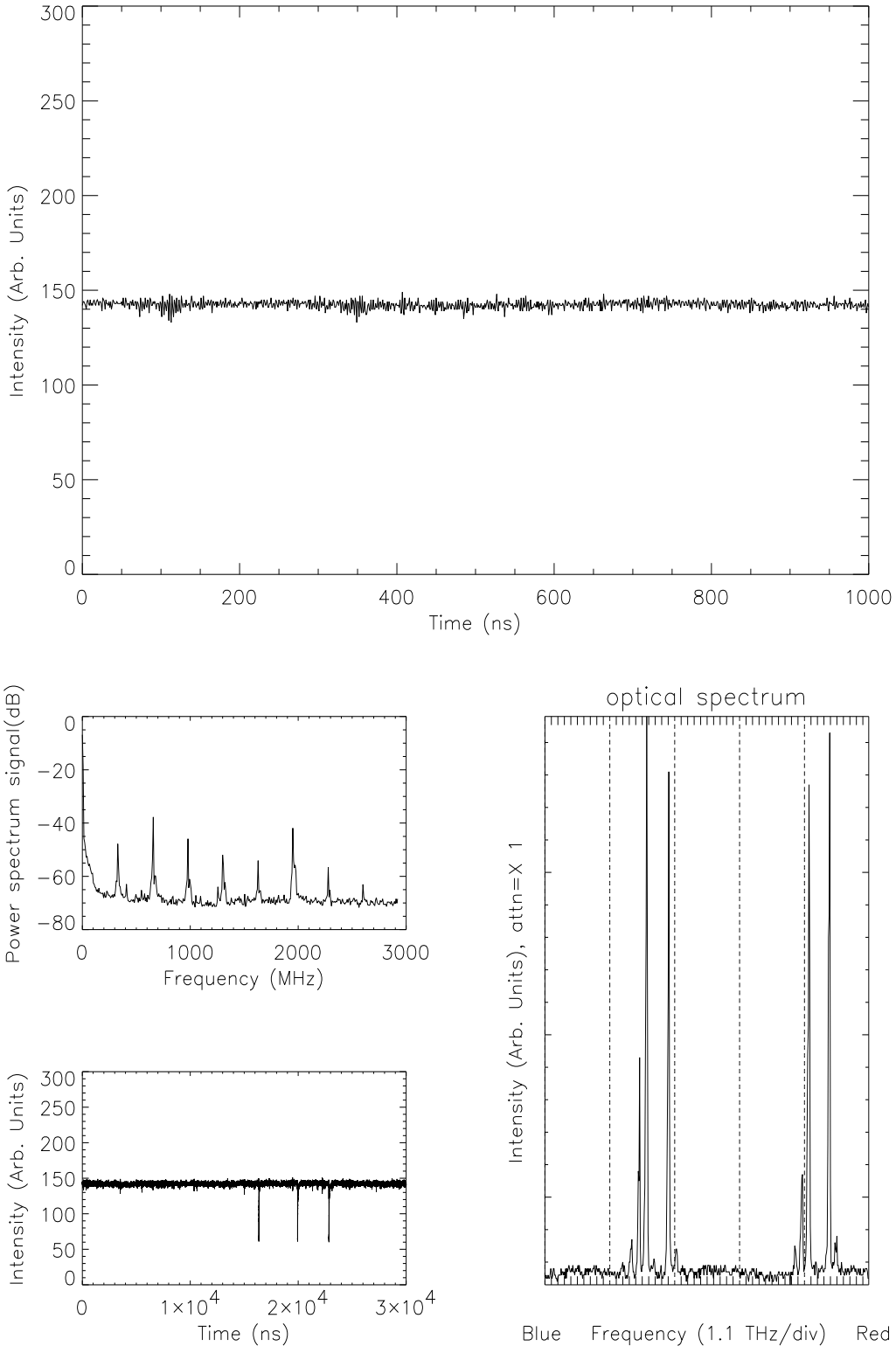

Figure 2.10: (b) Laser emission characteristics with feedback level $\xi = 13\%$, $\tau_{ext} = 3.2\ ns$ and $I/I_{th,sol} = 1.09$.

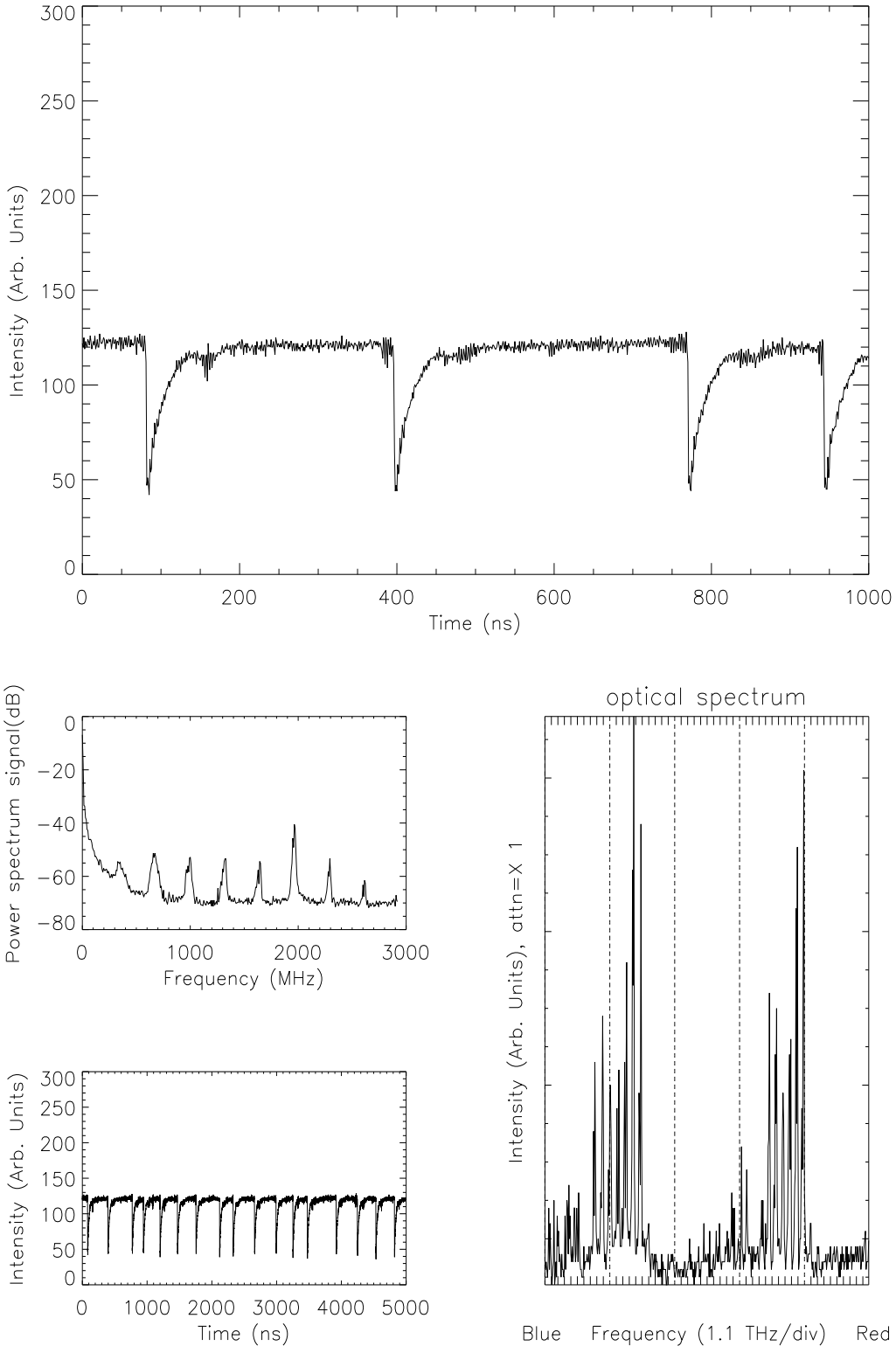

Figure 2.10: (c) Laser emission characteristics with feedback level $\xi = 9\%$, $\tau_{ext} = 3.2\ ns$ and $I/I_{th,sol} = 1.09$.

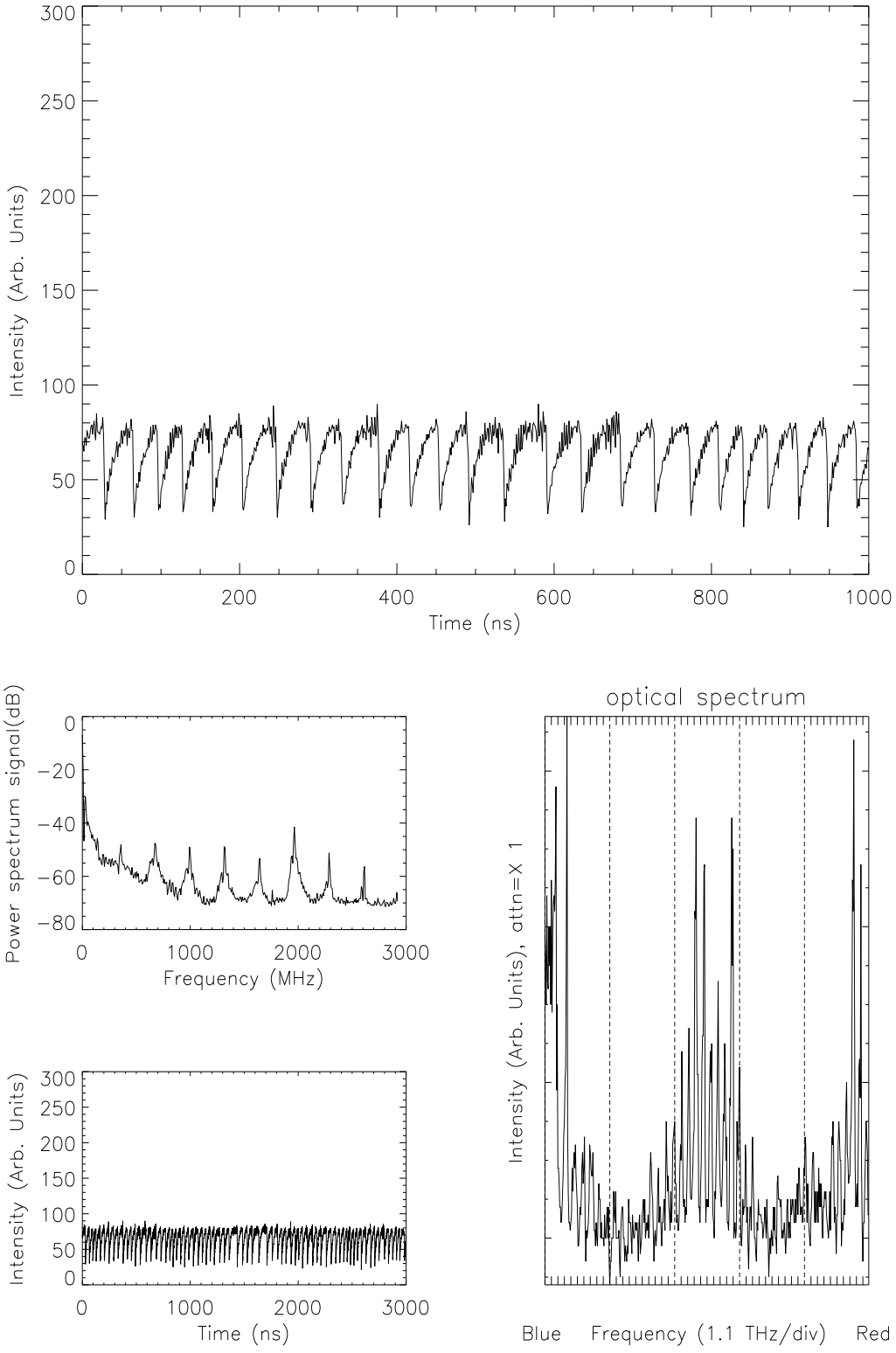

Figure 2.10: (d) Laser emission characteristics with feedback level $\xi = 6\%$, $\tau_{ext} = 3.2\ ns$ and $I/I_{th,sol} = 1.09$.

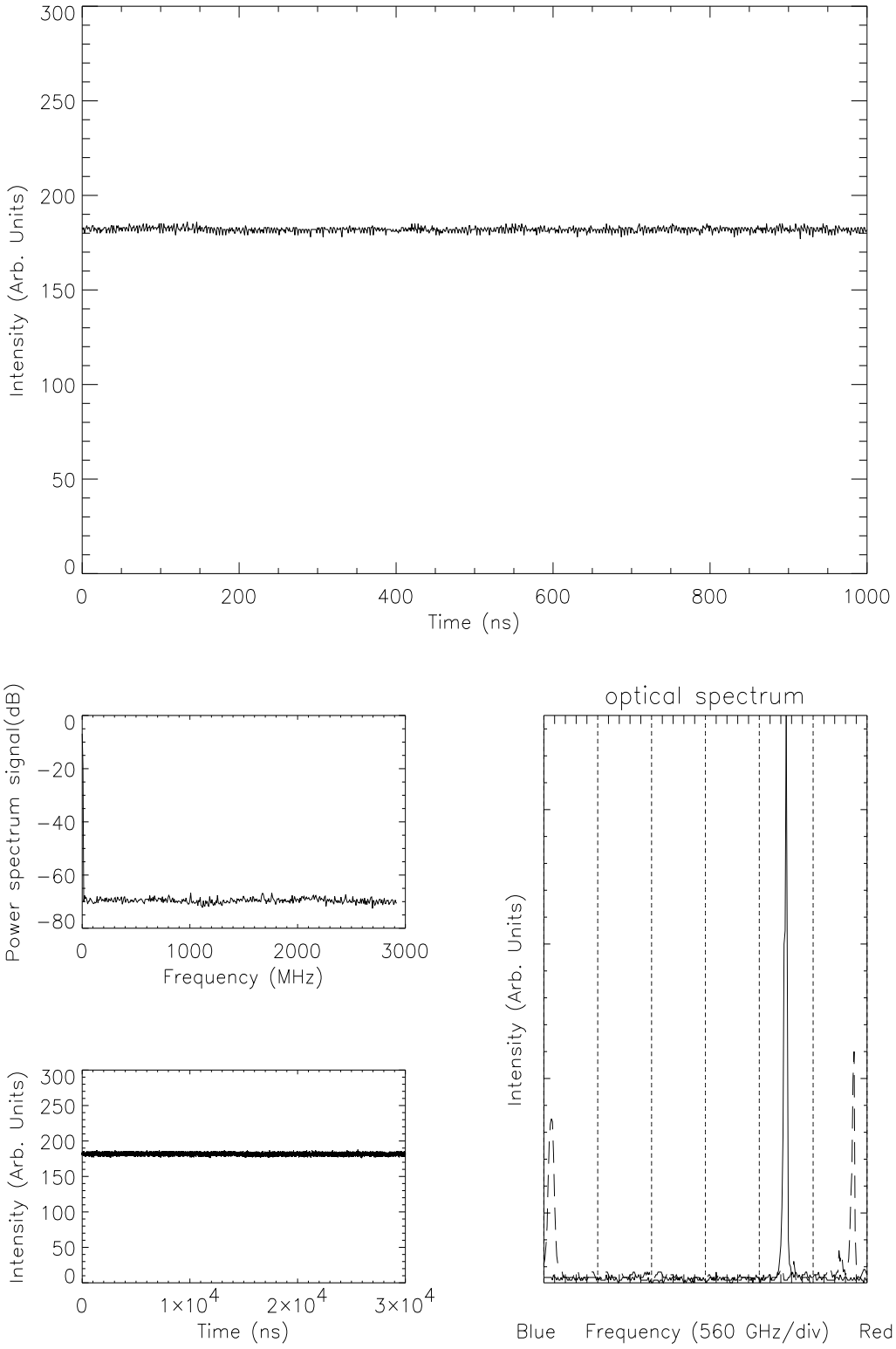

Figure 2.11: (a) Laser emission characteristics with feedback level $\xi = 20\%$, $\tau_{ext} = 3.2\ ns$ and $I/I_{th,sol} = 1.2$. In the optical spectrum we have added for comparison the solitary laser optical line at the same current (dashed trace). The vertical scale of the optical spectrum is attenuated in intensity by a factor of two in respect with Fig. 2.11b.

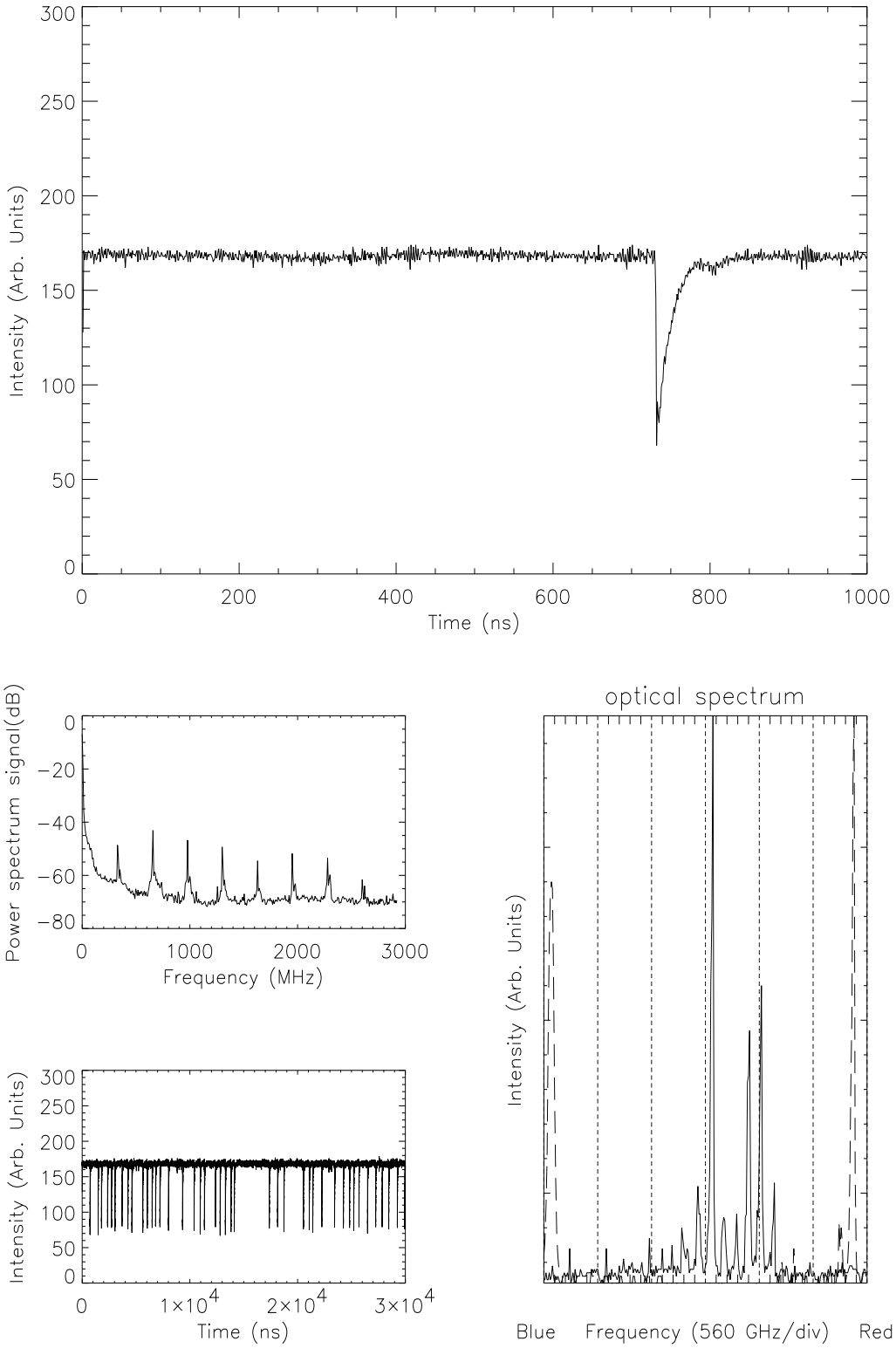

Figure 2.11: (b) Laser emission characteristics with feedback level $\xi = 18\%$, $\tau_{ext} = 3.2\ ns$ and $I/I_{th,sol} = 1.2$. In the optical spectrum we have added for comparison the solitary laser optical line at the same current (dashed trace).

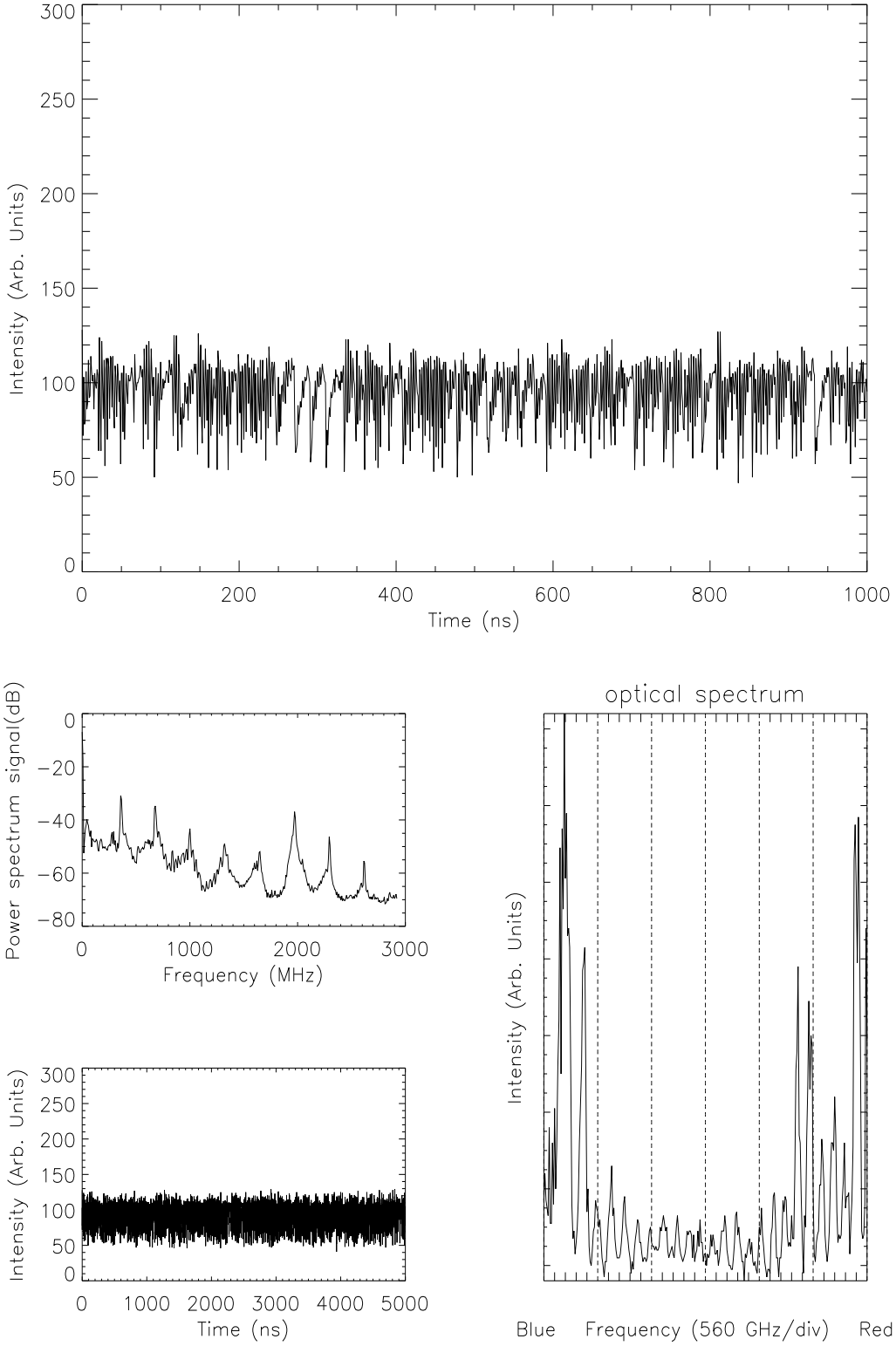

Figure 2.11: (c) Laser emission characteristics with feedback level $\xi = 6\%$, $\tau_{ext} = 4.2\ ns$ and $I/I_{th,sol} = 1.2$. The vertical scale of the optical spectrum is magnified in intensity by a factor of two in respect with the optical spectrum in Fig. 2.11b.

In Fig. 2.12 we represent the qualitative parameter-space around the laser threshold for moderate-to-strong feedback levels. I_{lff} increases with the feedback level and for feedback level $\xi < 9\%$ it goes below $I_{th,sol}$. The current interval of the stable-regime decreases as feedback level decreases and, below $\xi < 6\%$, the regime of stability disappears. At this feedback level and for lower ones, for $I_{th,feed} < I < I_{th,sol}$, the power spectrum shows a broad noise component at low-frequency and noise peaks at multiple of ν_{ext}. These lasts are broader then the ones characteristic of the stable-regime. Moreover, the low-frequency peak and the peaks at multiple of ν_{ext} appear all together in the power spectrum as $I \approx I_{th,feed}$. For greater pumping current, they broaden and get higher approaching, without sudden changes, the noise spectrum figure typical of the LFF-regime. In the time domain, accordingly, as the current is increased, LFF amplitude increases gradually from a negligible value. As $I \approx I_{th,feed}$ the LFF amplitude does not grow anymore, instead the LFF rate keeps increasing until the system enters in the CC regime. Therefore, the abrupt transition from the stable-regime to the LFF-regime with non zero amplitude fluctuations it is not observed if $\xi < 6\%$.

It is important to point out that, for a given point in the parameter-space, the LFF amplitude is almost the same for every drop. LFF are breakdowns of the intensity-output from an high intensity level determined by the feedback rate, down to an intensity level close to the one of the solitary laser. Increasing the pumping current, the solitary laser intensity increases and so it does the lowest level at the drop. Since the high intensity level before the drop increases too (see L/I curves), the LFF amplitude is not very affected by pumping current variation. On the other hand, if we increase the feedback rate, the highest level before the drop moves up and the LFF amplitude grows. If $I \leq I_{th,sol}$ the lowest level at the drop corresponds to the off state; in this condition the fluctuation amplitude

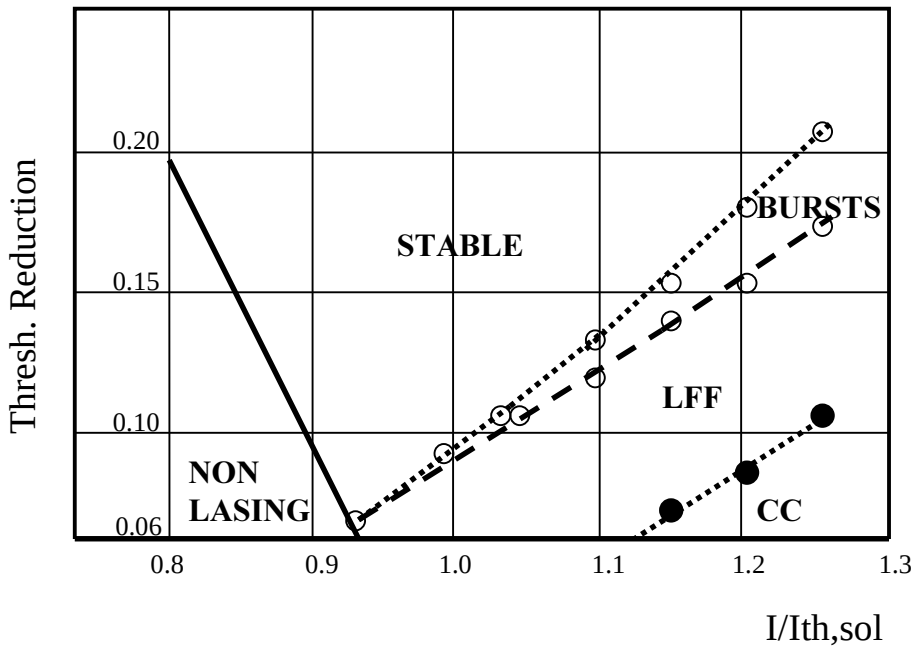

Figure 2.12: Qualitative parameter-space around laser threshold for moderate-to-strong feedback levels

is 100% of the level before the drop. It worth to note that all these considerations have been done analyzing the time intensity on a 500 MHz bandwidth scope. This bandwidth limit could hide several important features, as it will be clear in section five.

2.4 LFF: characterization of the dynamics

In this section we describe the experimental analysis performed on the transition between the stable-regime and the LFF-regime for feedback level $\xi > 6\%$. The aim is two-fold: i) understand whether the nature of the Low-Frequency Fluctuations is deterministic or stochastic; ii) in case of determinism, identify the bifurcation type at the origin of the instability.

2.4.1 Stochastic or deterministic nature?

This question is very important and not only from a theoretical point of view. Understanding the nature of LFF means being able to prevent them to occur: if their nature is deterministic they can not be avoided, unless setting the control parameters in the stable-regime. On the other hand, if LFF are stochastic fluctuations they could be avoided reducing the noise sources in the system (improving the power supply, thermal stabilization, etc.). In order to obtain information on this issue we perform statistical measurements on the LFF phenomenon.

The first experimental test consists in performing an averaging of the time-evolution between consecutive drops crossing a prefixed intensity threshold. We trigger the oscilloscope on the maximum of the derivative of the intensity each time the intensity becomes lower than the threshold value, and we average the traces of 10^4 events. In the LFF-regime, close to the stable-regime (64 mA, 66 mA in Fig. 2.13) we observe that, around the drop, the averaged LFF trace is strongly similar to the single LFF traces; the fast oscillations present just before the drops and in the recovery stage are not washed out by the averaging process. The washing out takes place only after the recovery of the intensity. This feature indicates that, around the drop, the system is exhibiting an intensity behavior that is always the same for all the LFF. Let us associate to each LFF an orbit in the phase-space. No matter the dimension of the phase-space associated to

our system, we can reduce an orbit to its projection onto a plane containing the intensity-output variables $(I, \dot{I})$ that are easily detectable. We call *LFF-orbit* the projection of the orbit associated to a Low-Frequency Fluctuation. Since, fixed the parameters, the time intensity behavior around the drops is similar for every drop, the LFF-orbit is almost the same for each LFF. On the other hand, the fact that the system looses correlation before the next drops, shows that the triggering mechanism of the drops is likely to have a stochastic nature. Hence we can try a first hypothesis on the nature of low-frequency fluctuations: they have a deterministic nature but, at least in the LFF-regime, they are noise-induced. In this contest we can define a time t_o as the LFF-orbit time or the time taken by the system to run along the LFF-orbit. We also define a time t_a as the system waiting-time (also called firing-time or escaping-time or activation-time) between the end of the recovery stage of an LFF and the next departure. Then the total time-interval between two Low-Frequency Fluctuations will be $T = t_o + t_a$. The loss of correlation between two drops indicates that, in the LFF-regime, noise is controlling t_a while t_o, by definition, is fixed by the deterministic evolution of the Low-Frequency Fluctuation.

In the fully-developed Coherence-Collapse regime (68 mA, 70 mA in Fig. 2.13) we note that the structure of the oscillations is never completely washed out and determinism plays the most relevant role. These observations indicate that a bifurcation does exist somewhere in the parameter-space. This bifurcation is "anticipated" by noise which plays a relevant role close to the critical point. Deterministic behavior takes over at larger pump rates.

In order to gain more insights on the dynamics of the system in the LFF-regime, we have analyzed the statistics of the time-interval T between pulses. The $LeCroy^{TM}$ 7200 allows direct statistical measurements. Given a time trace it is possible to specify some features that identify a particular *event*. The scope is

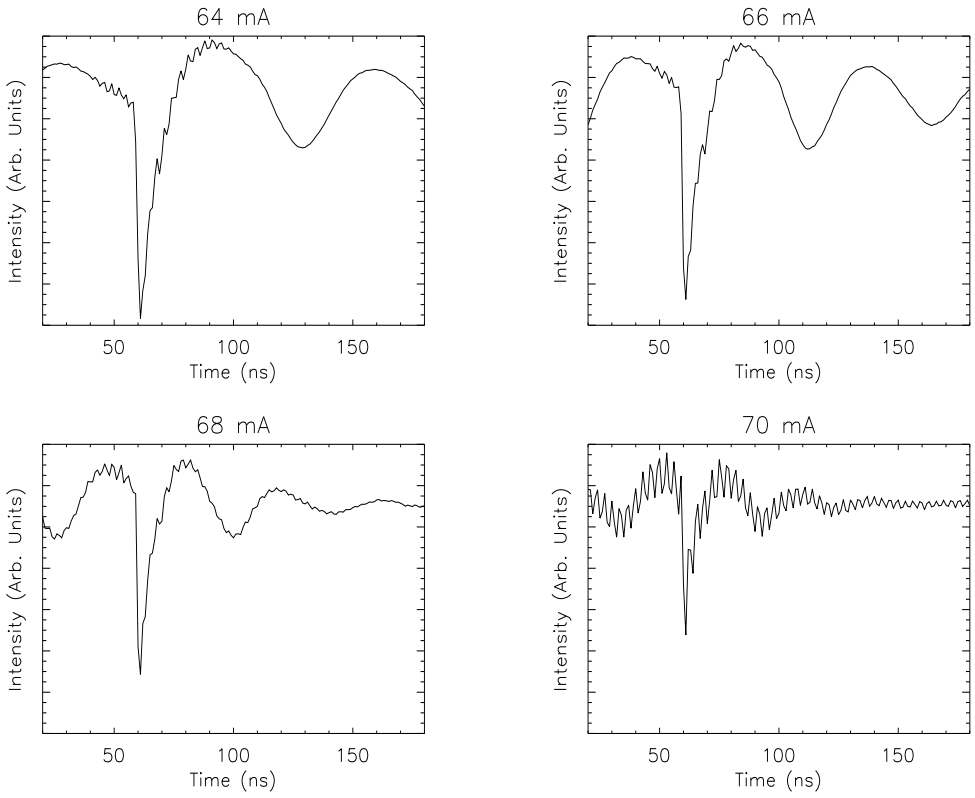

Figure 2.13: Average of the temporal behavior over 10^4 consecutive drops, feedback level = 8%, cavity length = 51.5 cm

then able to discriminate the *events* in the time trace and accumulate in memory only the information on it (time, intensity etc.), allowing for the computation of up to 50000 events. The analysis on the entire time traces would have required huge time and memory size in order to achieve this number of events. The Low-Frequency Fluctuation can be identified in the time-series by setting an intensity level threshold and taking as *event* the fact that the output signal has downward crossed this threshold. In Figs. 2.14-2.17 we show the time-interval distribution between two LFF as the parameters are changed. We also show the return maps of the signal obtained plotting the time T between successive intensity drops. This diagram is made by digitizing the temporal signal and memorizing the times θ_n for which the intensity of the n_{th} pulse reaches a prefixed given value I_0, and evaluating $T_n = \theta_n - \theta_{n-1}$. We have chosen the threshold I_0 in a region of the intensity for which the maps are independent from that value. This return-map

is equivalent to a Poincaré section of the system at constant intensity. In fact, if the signal is periodic, it gives a single point in the return-map, or a finite set of discrete points. If it is aperiodic, the different points are distributed over an extended region. Thus, at least the presence of well defined structures in the return maps indicates the deterministic origin of the dynamics. We perform the measurements over samples of more than 10^3 pulses. It is important to notice that, for computing the return-map, it is necessary the entire sequence of the time-intervals. So, in this case, the analysis has to be performed on a complete time-series rather than on a purely cumulative time-intervals count. The number of events used for building the return-map is necessarily limited to the number of events present in the maximum time length that the scope is able to acquire without loosing in sampling rate (one million of points at 1 GS/s) and, therefore, it is dependent on the values of the parameters controlling the event rate. In Fig. 2.14 we show the distribution curve and the return-map of the LFF time-intervals as the pumping current is increased, for a feedback level of 8% and a cavity length of 63 cm (4.2 ns roundtrip). In Fig. 2.15 we show the distribution of the LFF time-intervals in logarithmic scale and for a feedback level of $\xi = 12\%$. Three different regimes can be distinguished as pumping current is increased:

• **Purely noise-controlled** LFF**.** Increasing the pumping current, the system transits from the stable-regime to the LFF-regime as $I > I_{lff}$. For $I \approx I_{lff}$, depending on the feedback level, there is a small current interval for which the two regimes coexists in time and the system jumps from one to the other with a rate larger than ms. For greater current LFF-regime settles down definitively, we remark that the power drops occur in the time signal with a low rate (Fig. 2.14a, 2.15a). The interval between the drops T is much larger than the duration of a single fluctuation, $t_a \gg t_o$ and T is mainly determined by the firing time of LFF, $T \approx t_a$. The LFF time-interval distributions have a decreasing exponential shape

(Fig. 2.15) peaked at finite time whose value depends on the parameters. We also notice that there is a minimum time allowed between the drops. This refractory time is related to the single LFF duration (t_o) and it is due to the fact that, after a departure, the system cannot exhibit an LFF before the preceding one has recovered. The duration of a single LFF is given by the dropping time, that is very fast, and the recovery stage, which is much slower. This last time value is determined, as we have explained in the preceding section, by the external-cavity round-trip time and it is not affected significantly by the other parameters. Indeed, from the histograms in Fig. 2.14 and 2.15, we notice that the refractory time does not change a lot with increasing the pumping current and its value is $60 - 90\ ns$ (which is equivalent to $14 - 21$ external-cavity round trips).

The shape of the time-interval distribution at the beginning of the LFF-region indicates the major role of noise in the firing mechanism, according to Kramers' theory. Kramers developed a theory for the brownian motion of a particle in a double potential well. The particle may jump from one well to the other one under the action of noise, we define as T the first-passage time between the two potential minima. (Ref. [104]). If the noise is gaussian delta-correlated with zero mean and variance D, the escaping rate or the averaged first-passage time is given by: $\ln(< T >) \propto (1/D)$ (Ref. [105]). Moreover, Kramers' theory says that, if the noise force is small, the average escaping time is approximately the standard deviation of the the first-passage times: $< T > \approx \sigma_T$. For symmetric bistable system the first-passage times distribution for long intervals is an exponential function decaying at the escaping rate. The tails of the distributions of Figs. 2.14a,b and 2.15a exhibit an exponential decaying starting from the refractory time. Kramers' statistic catches the features of the LFF time-interval statistic related to the firing time t_a but, of course, cannot describe the existence of a refractory time which is not present in the problem of the particle in the double

potential well.

The return-map (Figs. 2.14a,b) shows a cloud of points without any structure, as we can expect from a system where the noise rules the dynamics. As a further test, we have plotted also the k-order return maps (T_n vs. T_{n-k}) for several k-values. Such analysis has not revealed the presence of higher-order correlations. Moving the parameters deeper in the LFF-region, increasing the pumping current or decreasing the feedback level, the rate of the LFF increases and the distribution peak moves to smaller time values. Consequently, the cloud of points in the return-map moves to smaller time values and reduces its size.

Finally it is worthwhile to note that the standard deviation of the LFF amplitudes and the LFF duration (t_o) is smaller than 10%, confirming the deterministic origin of the pulse itself ("coherent" build-up of the pulses).

• **noise-controlled LFF with clusters** Increasing the current deeper in the LFF-region we remark, in the LFF time-intervals distribution curves, the appearance (Figs. 2.14c-e; 2.15b-d) of a narrow peak at low time values. As pumping current is further increased, this peak grows in size, but its time value is not significantly affected. In the time-series this peak of probability correspond to clusters of consecutive LFF where the departure occurs immediately after the recovering of the preceding LFF. Inside the clusters $T \approx t_o$ and $t_a \approx 0$. Since t_o is determined with a low dispersion by the external-cavity length, clusters of LFF contribute to the interval distribution with a narrow peak in the histogram at $\approx 70\ ns$ (≈ 17 round trips on the external-cavity). In the time-series we remark also that, in the clusters of consecutive Low-Frequency Fluctuations, the intensity level from which the power drops is lower than the quiescent intensity level from which it drops in the fluctuations where $t_a > 0$.

At the right of the narrow cluster peak, in the intervals distribution curves, there is also a broad peak (at $\approx 200\ ns$ in Fig. 2.14c, at $\approx 750\ ns$ in Fig. 2.15b)

relative to the LFF appearing at intervals for which $t_a \gg t_o$ and $T \approx t_a$. This peak moves to lower values as pumping current is increased since the activation time decreases, but it maintains the same characteristics: the exponential tail and $< T > \approx \sigma_T$. We conclude that, even in this parameter region where LFF appears in clusters, noise is still triggering the LFF. The difference lies on the fact that the system does not necessarily come back to a quiescent-state after an LFF-orbit. It can continue to fluctuate for a certain number of times, showing clusters of LFF. Hence the bi-modal distribution of the time-intervals. Increasing the pumping current, the probability of having two or more consecutive drops is increasing. In the distribution curves the peak relative to the LFF clusters is increasing in size (Figs. 2.14d,e; 2.15c-e) at the expense of the peak where t_a is dominant. Moreover the activation time continues to decrease and eventually the right peak merges into the other one (Figs. 2.14f,g; Figs. 2.15f,g).

The return-map shows the same mixing between an almost-periodic state determined by the clusters and a purely noise controlled firing. By consequence the system exhibits return maps with an almost ordered structure of points (Figs. 2.14d-2.14e) together with a broad cloud of point at (200 ns; 200 ns). The cloud merges in a low size spot in Fig. 2.14f. In this situation, $t_a \approx 0$.

Comparing Fig. 2.14 and 2.15 we remark that for larger feedback levels the average activation time ($< t_a >$) of the system is longer and the peaks separation in the bi-modal distribution curve structure is larger. Moreover, the clusters of LFF settle down and take over more abruptly for strong feedback level: in Fig. 2.15 the right peak almost disappears before merging into the one corresponding to the clusters of drops, while in Fig. 2.14 it decreases in size more smoothly.

• **Determinism takes over** In Fig. 2.14g and 2.15g the low dispersion of the histograms and the size of the spot in the return-map show that the system has a almost-periodic behavior. The histograms (especially the one in Fig. 2.14g) shows

a structure of peaks, enveloped in the distribution curve, whose separation is the external-cavity round-trip time. This structure is indicating that the probability of departure is higher for time interval between LFF equals to multiples of the external-cavity round-trip. Further increase of current determine the settling of the fully-developed Coherence-Collapse. The LFF shape is lost, and the *events* as defined before are not recognizable anymore in the time-series. In Fig. 2.14h we show the return-map and the histogram in the fully-developed Coherence-Collapse regime obtained with the same I_0 used in the 2.14f and 2.14g ($I_0 = 130$, using the reference scale of the time-series). The relevance of the external cavity round-trip time is evident from the very well defined structures in the return-map. The system is exhibiting oscillations separated by an integer number of τ_{ext}. As I_0 is raised the peak in the time-interval distribution moves towards shorter τ_{ext}, but the structure remains. This structure is indicating that the system is now governed by determinism.

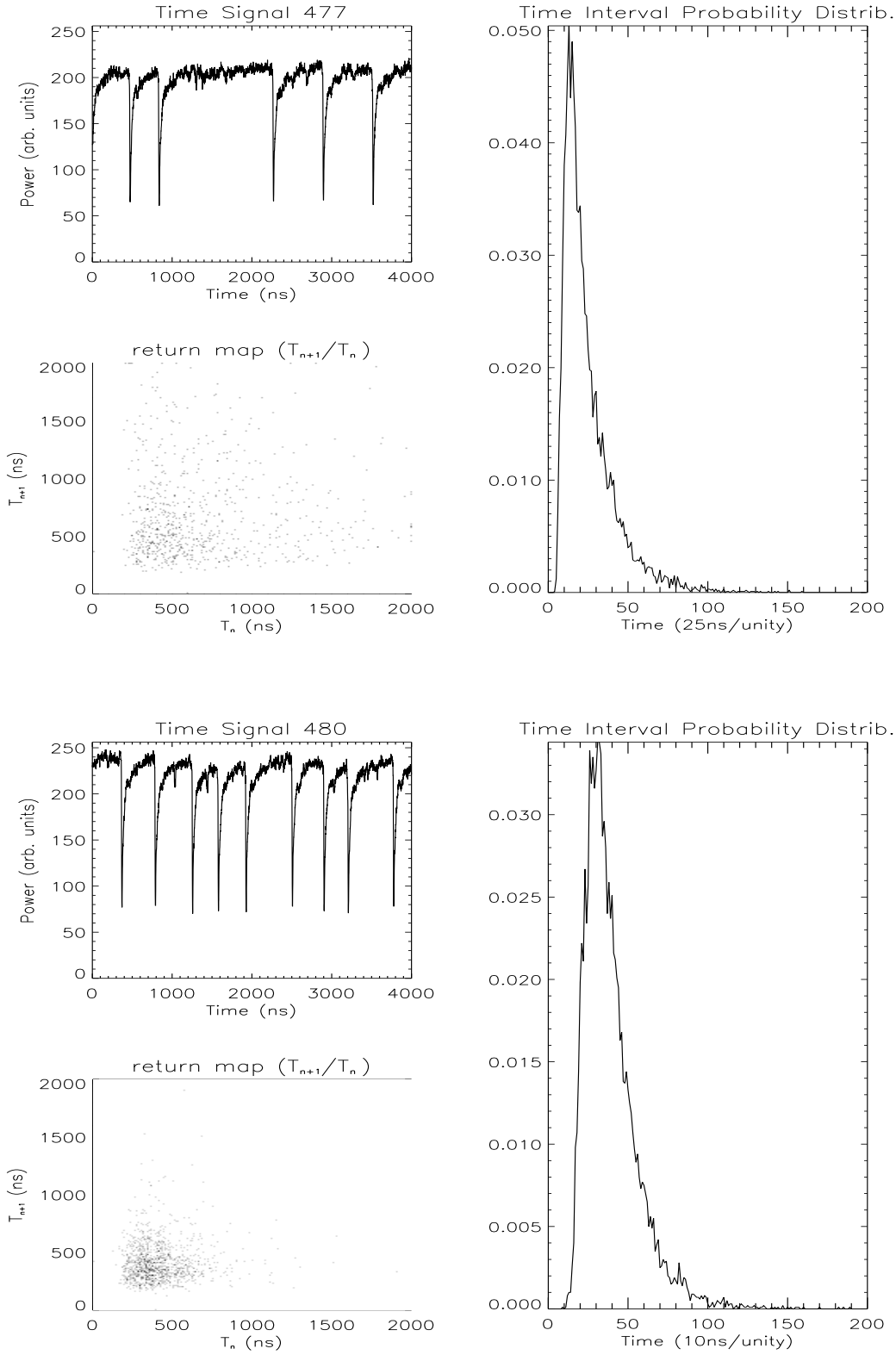

Figure 2.14: (a,b) LFF time-intervals statistical measurements Vs. pumping current for a cavity length of 63 cm ($\tau_{ext} = 4.2\ ns$), ($I_{th,sol} = 48.5\ mA$), feedback level: $\xi = 8\%$, $I = 47.7\ mA$ (above), $I = 48.0\ mA$ (below).

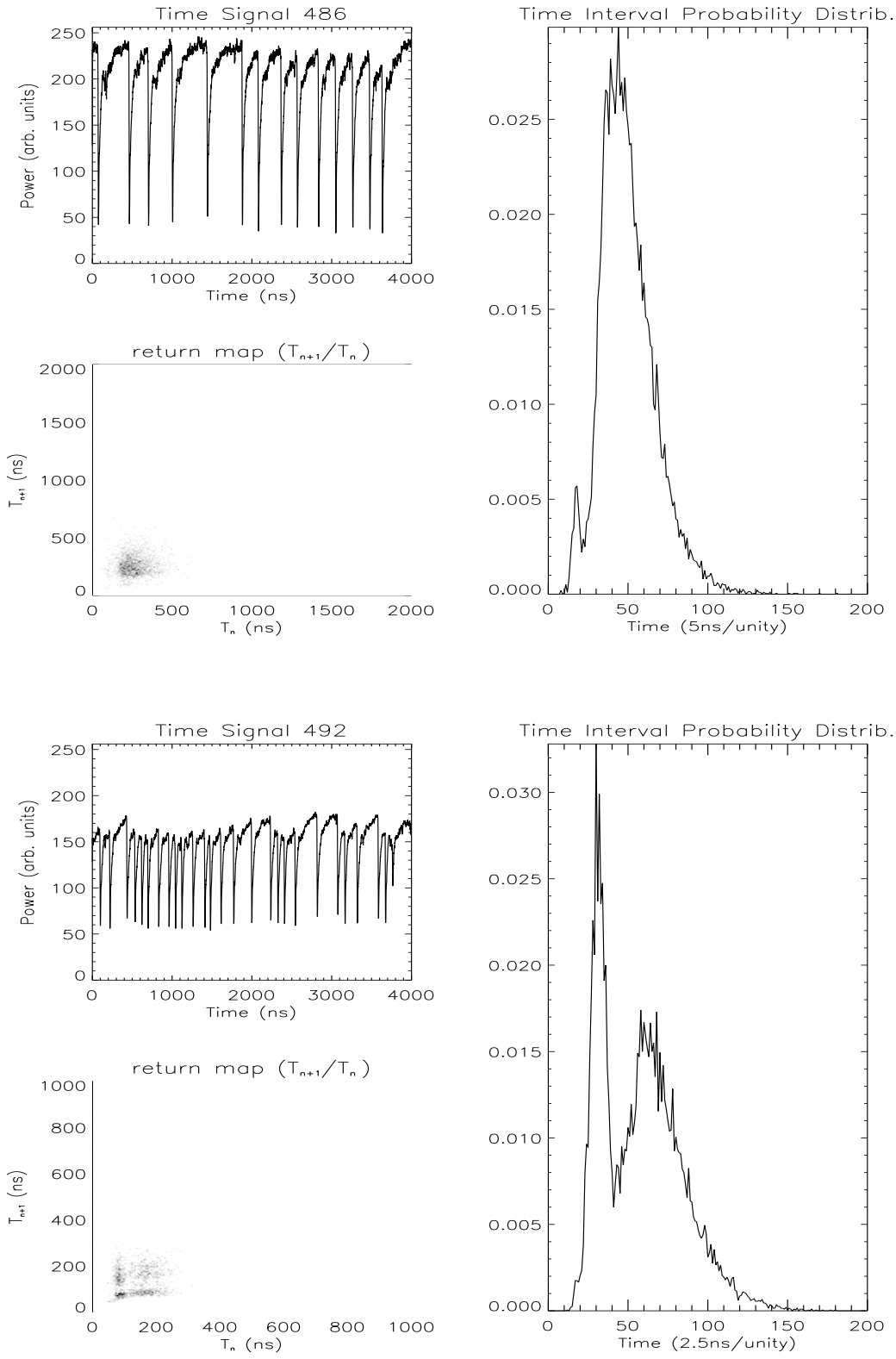

Figure 2.14: (c-d) LFF time-intervals statistical measurements Vs. pumping current for a cavity length of 63 cm ($\tau_{ext} = 4.2\ ns$), ($I_{th,sol} = 48.5\ mA$), feedback level: $\xi = 8\%$, $I = 48.6\ mA$ (above), $I = 49.2\ mA$ (below).

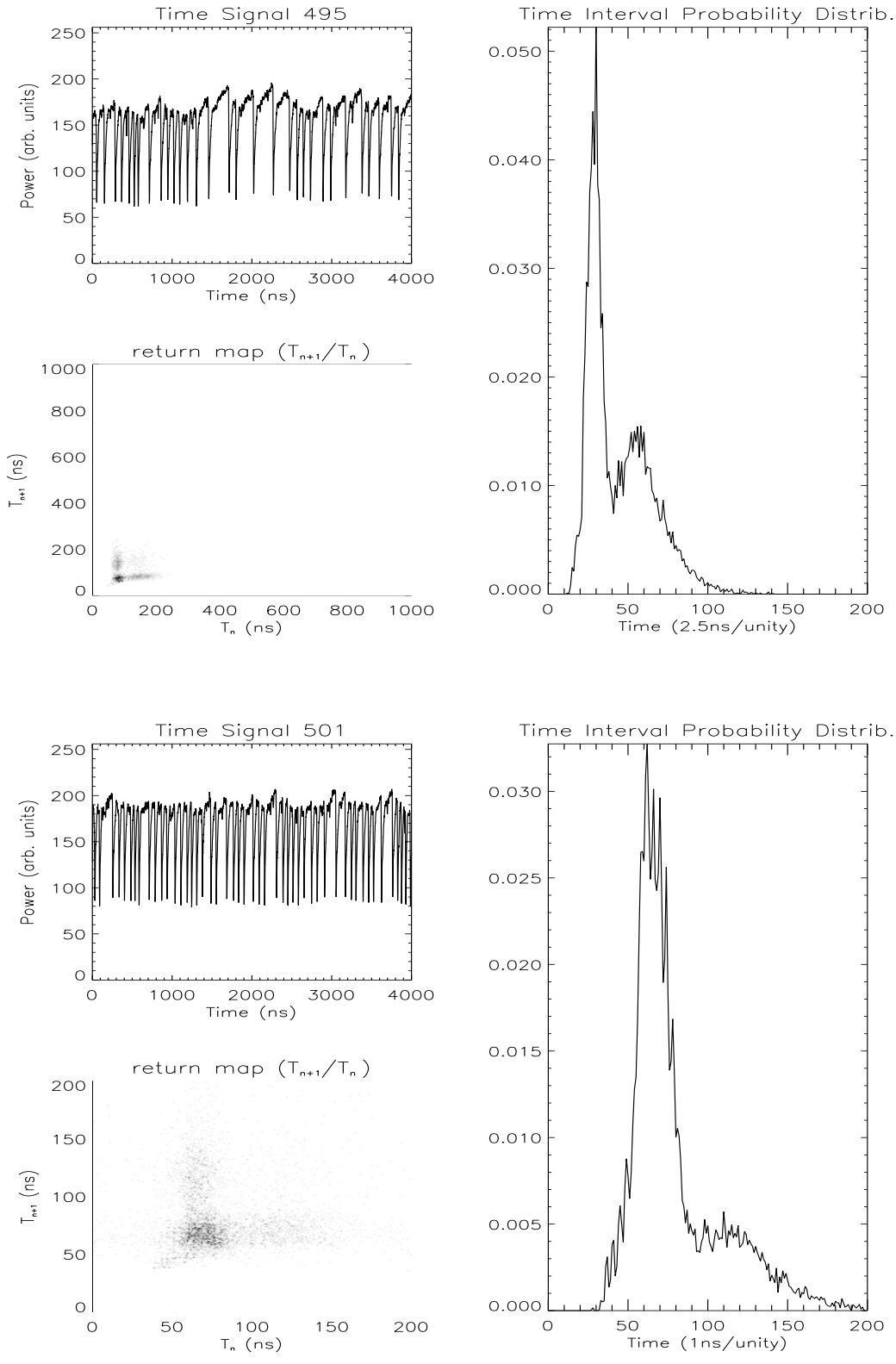

Figure 2.14: (e-f) LFF time-intervals statistical measurements Vs. pumping current for a cavity length of 63 cm ($\tau_{ext} = 4.2\ ns$), ($I_{th,sol} = 48.5\ mA$), feedback level: $\xi = 8\%$, $I = 49.5\ mA$ (above), $I = 50.1\ mA$ (below).

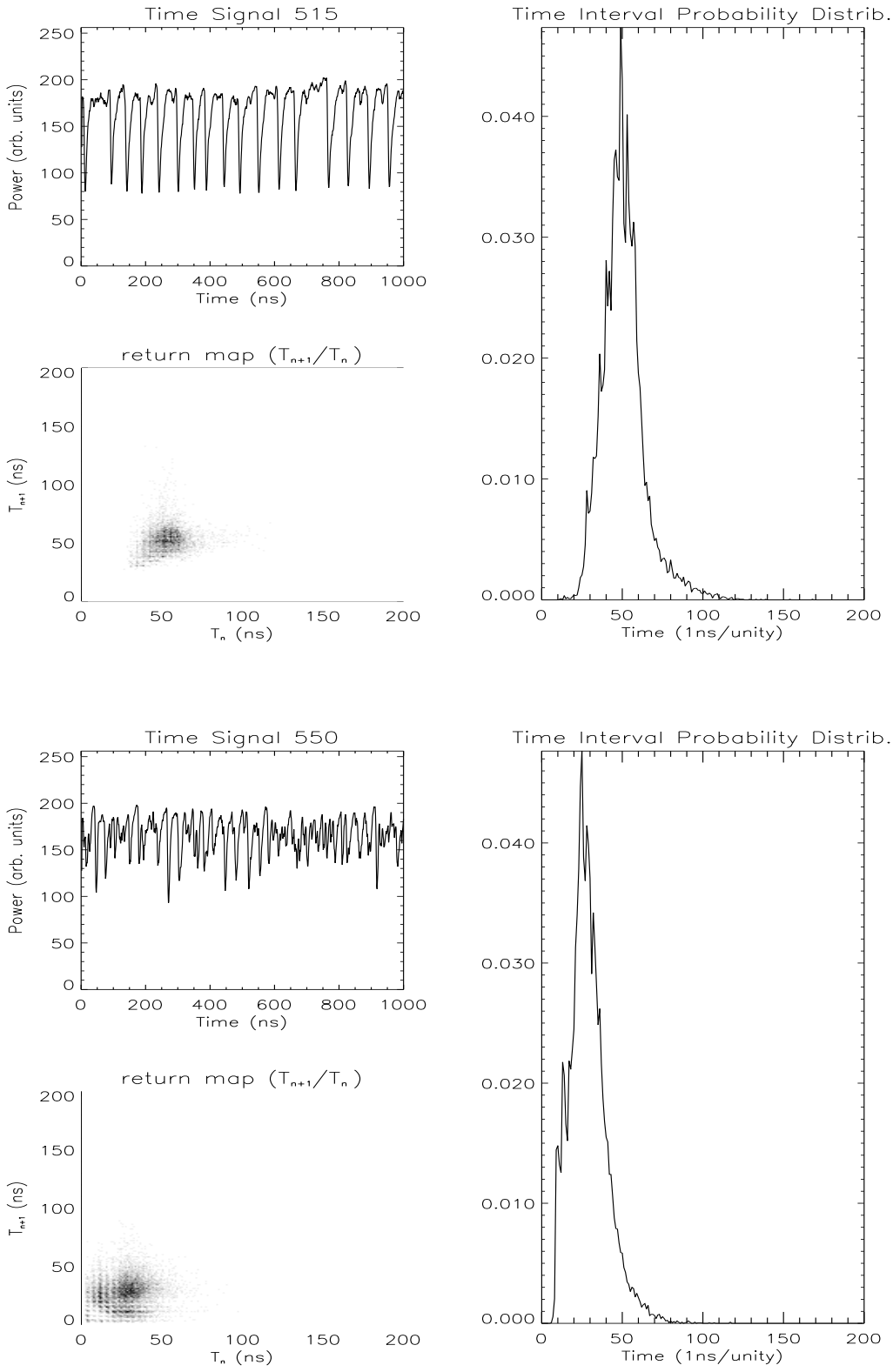

Figure 2.14: (g-h) LFF time-intervals statistical measurements Vs. pumping current for a cavity length of 63 cm ($\tau_{ext} = 4.2\ ns$), ($I_{th,sol} = 48.5\ mA$), feedback level: $\xi = 8\%$, $I = 53.0\ mA$ (above), $I = 54.0\ mA$ (below).

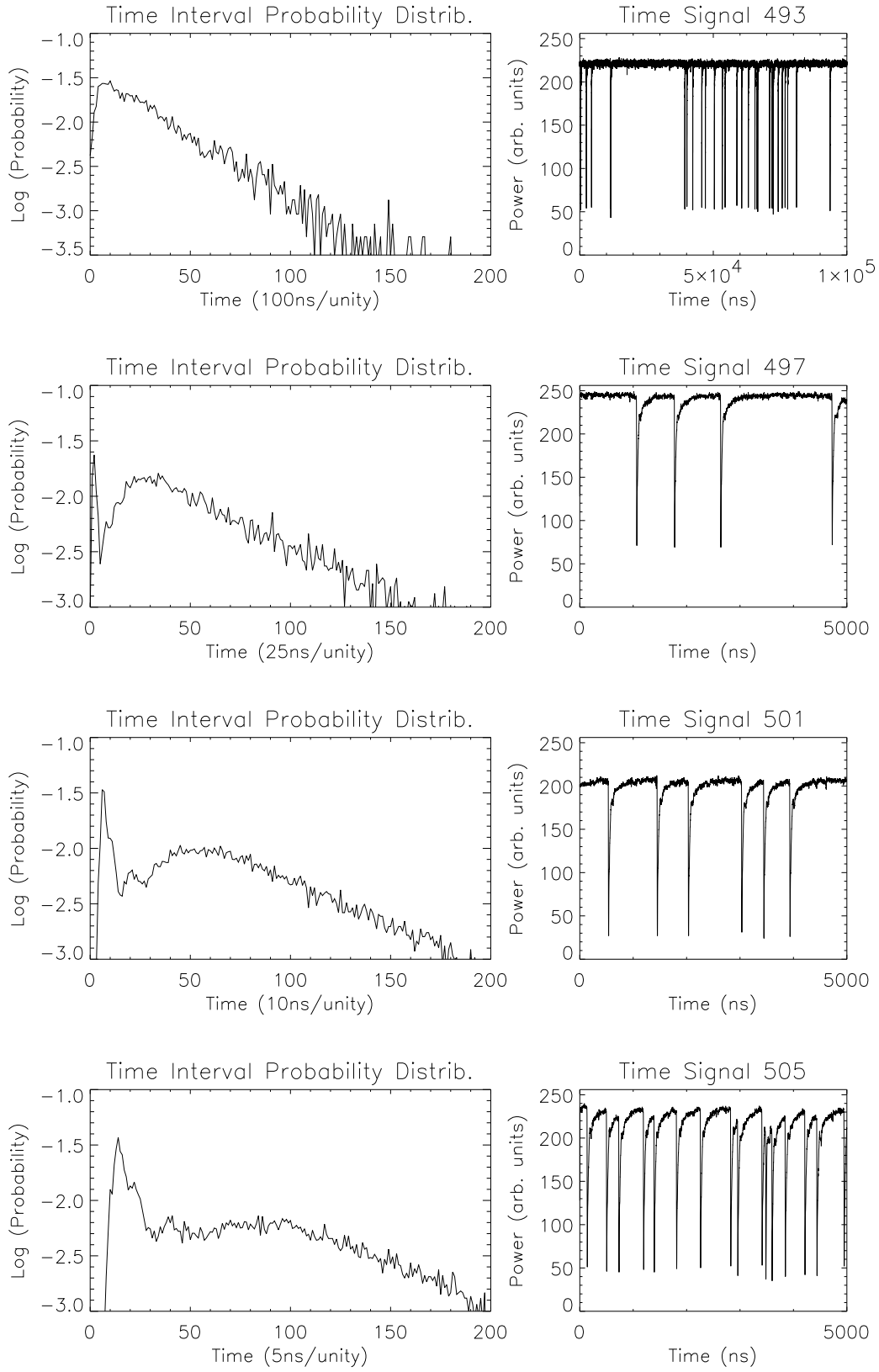

Figure 2.15: (a-d) *LFF* time-intervals statistical Vs. pumping current for a cavity length of 63 cm ($\tau_{ext} = 4.2\ ns$), ($I_{th,sol} = 48.5mA$), feedback level: $\xi = 12\%$, (from the top): I(mA)=49.3 (a), 49.7 (b), 50.1 (c), 50.5 (d).

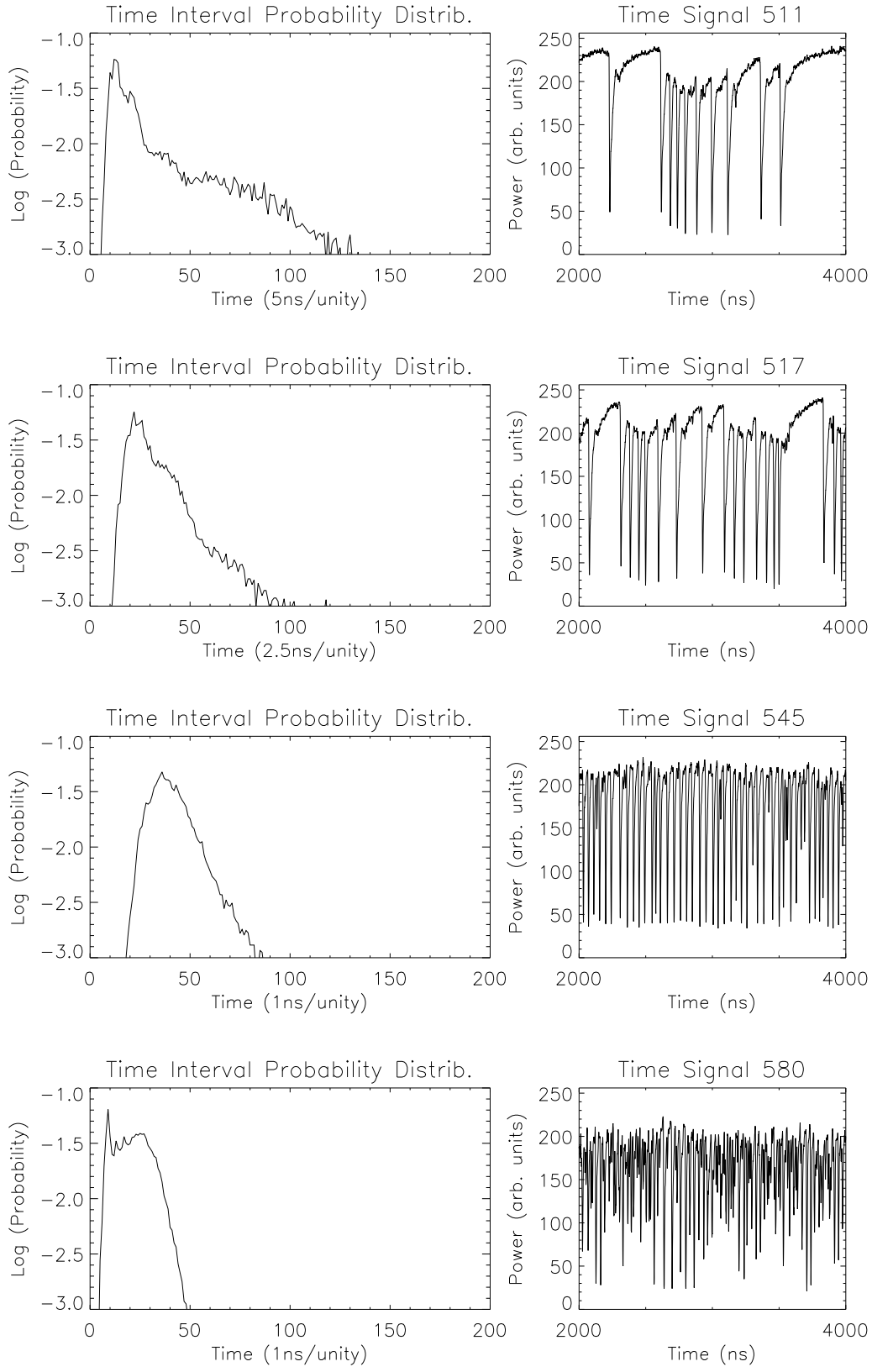

Figure 2.15: (e-h) LFF time-intervals statistical measurements Vs. pumping current for a cavity length of 63 cm ($\tau_{ext} = 4.2\ ns$), ($I_{th,sol} = 48.5\ mA$), feedback level: $\xi = 12\%$, (from the top): I(mA)=51.1 (e), 51.7 (f), 54.5 (g), 58.0 (h).

In the next series of measurements we have changed the feedback level for two different pumping current levels and cavity lengths. The qualitative features observed decreasing the feedback level, are not different from the ones obtained by increasing the pumping current. We notice the same sequence of behaviors, even if we have not reached feedback level low enough to observe fully-developed Coherence-Collapse at the pumping current used. In Figs. 2.16a,b; 2.17 we can remark the presence of the bi-modal distribution: it is worthwhile to note that the right peak in the histograms changes its size at the advantages of the left peak, but does not change its time position as the feedback level is varied. Apparently t_a is not very affected by the feedback level.

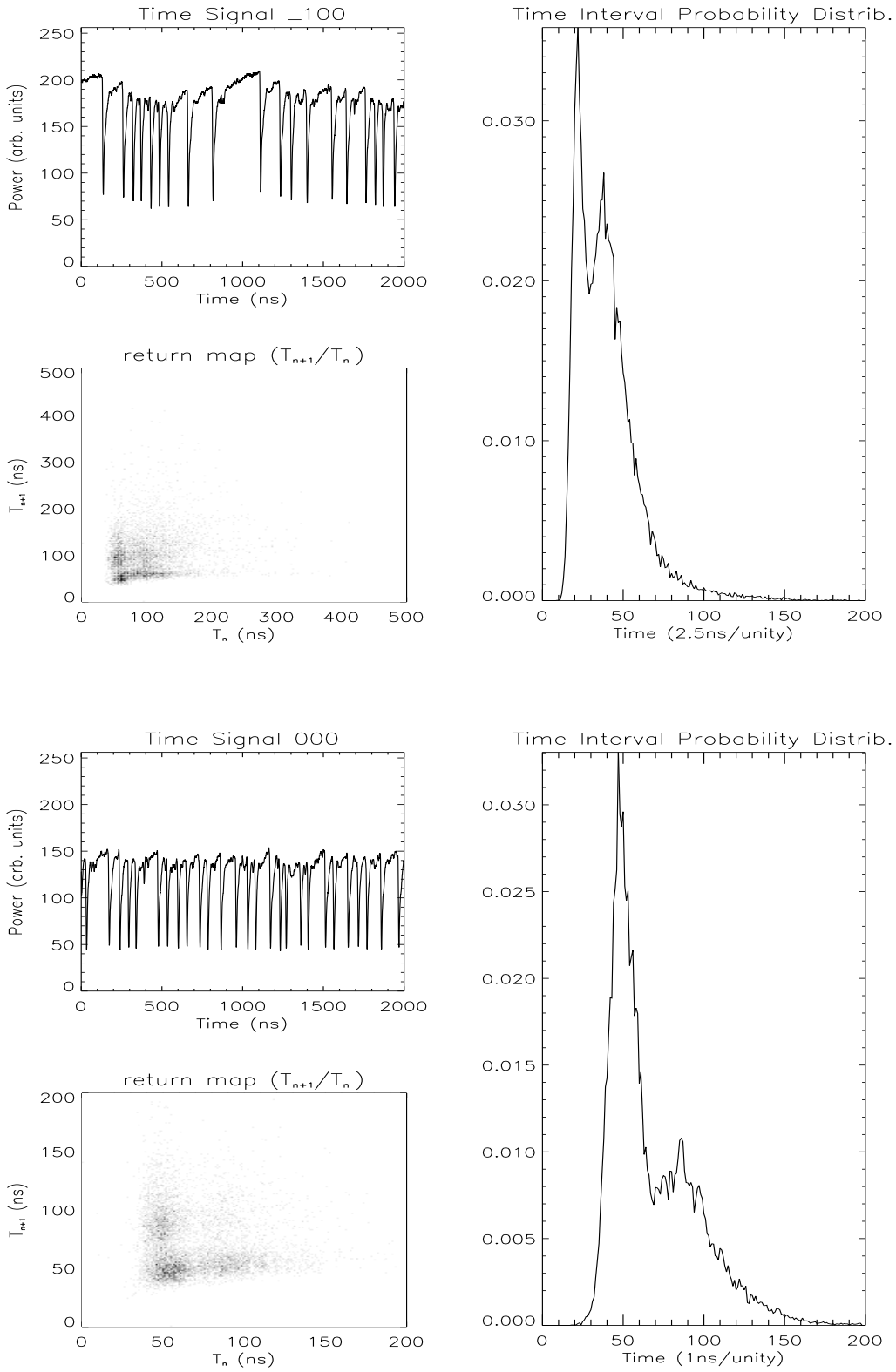

Figure 2.16: (a-b) *LFF* time-intervals statistical measurements Vs. feedback level for a cavity length of 41 *cm* (τ_{ext} = 2.7 *ns*), $I/I_{th,sol}$ = 1.04% and feedback level: ξ = 11.5% (above), 10% (below).

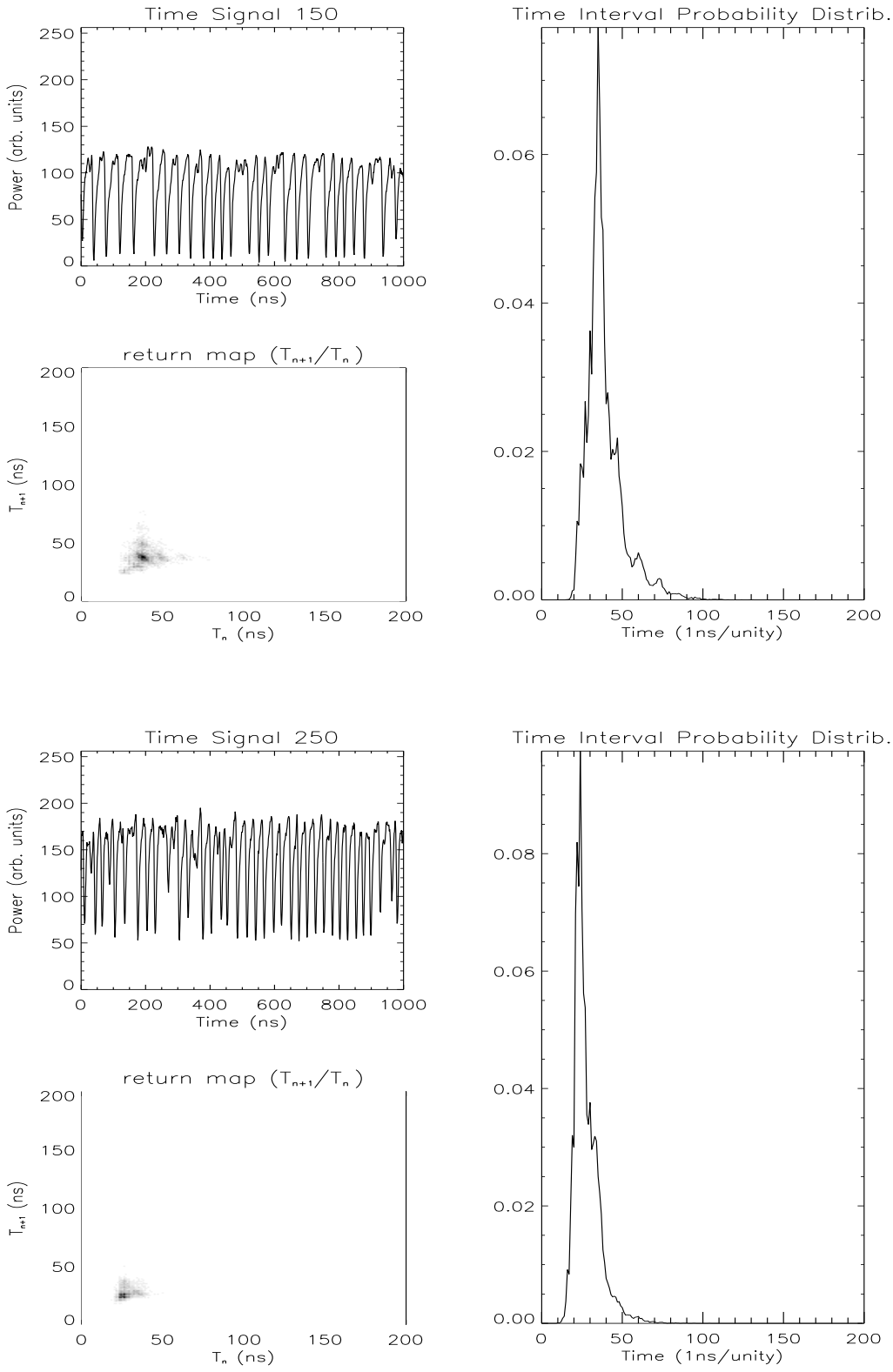

Figure 2.16: (c-d) *LFF* time-intervals statistical measurements Vs. feedback level for a cavity length of 41 cm ($\tau_{ext} = 2.7\ ns$), $I/I_{th,sol} = 1.04\%$ and feedback level: $\xi = 6.8\%$ (above), $\xi = 4.5\%$ (below).

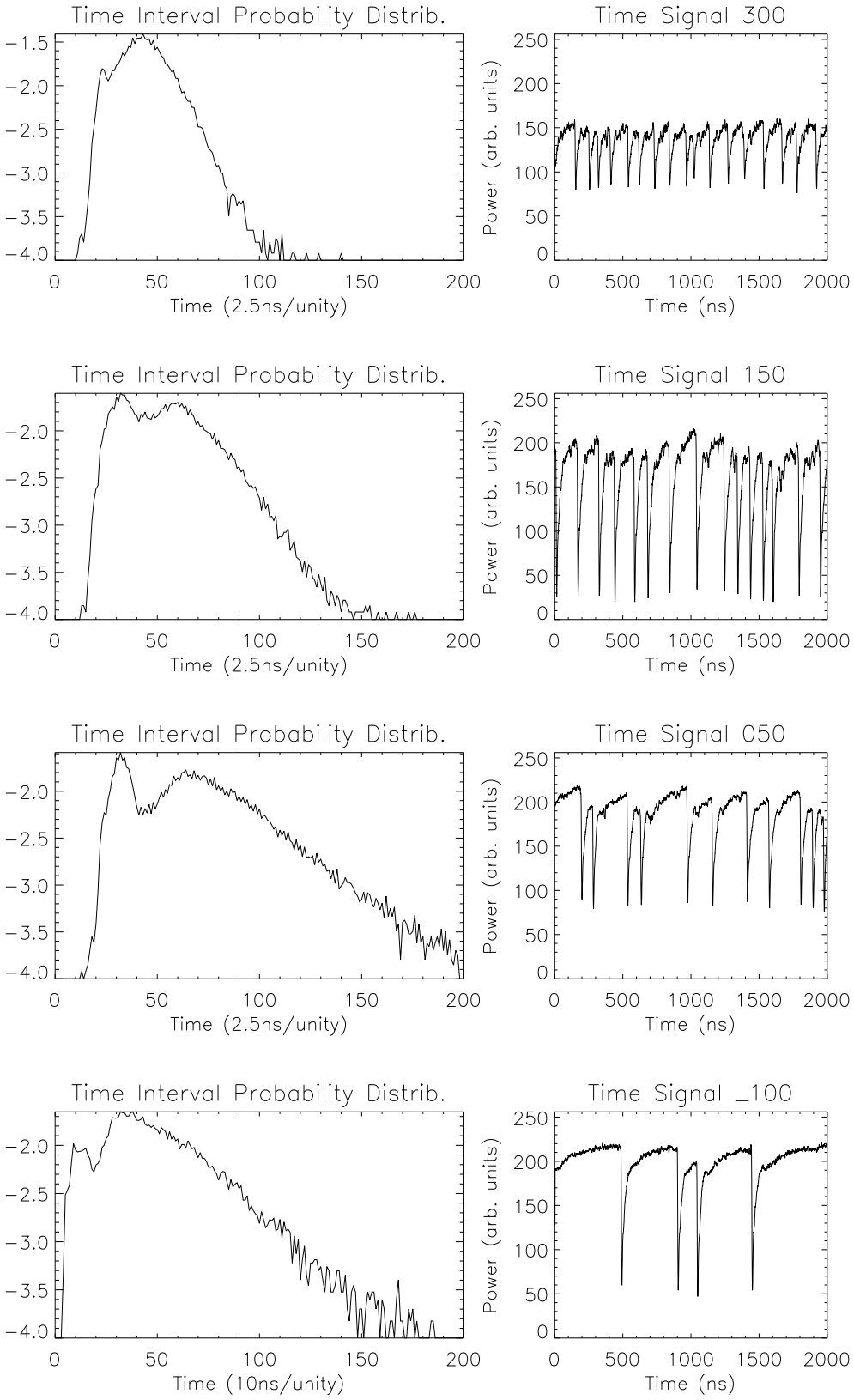

Figure 2.17: (a-d) LFF time-intervals statistical measurements Vs. feedback level for a cavity length of 63 cm ($\tau_{ext} = 4.2\ ns$), $I/I_{th,sol} = 1.02\%$, feedback level = (from the top) $\xi = 3\%$ (a), $\xi = 7\%$ (b), $\xi = 9.3\%$ (c), $\xi = 11.4\%$ (d).

Let's now discuss how the statistical properties of the time between drops change with parameters. In Figs. 2.18-2.19 we show the mean $< T >$ and the standard deviation σ_T of the time interval between pulses as a function of pumping current and of the feedback level. We plot this dependence in logarithmic scale also. The index R, $R = \sigma_T / < T >$, is an indicator of the regularity of the drops. If the index takes values around one or larger, we have the characteristic signature of a noise-induced event (Ref. [106]). On the other hand, if the event is periodic, the index goes to zero. Let's define $e = (I - I_{lff})$, where I is the pump current and I_{lff} is the current at which LFF appear.

Fig. 2.18 shows an exponential dependence of $< T >$ and σ_T with the pumping current for the widest range of e values. This kind of dependence is lost for very low values of e and strong feedback levels (Fig. 2.18, lower panel), when the LFF are very sporadic, and also for large values of e, where CC settles down. The index R decreases from a value close to one down to a minimum as the pumping current is increased. Then, the regularity of the LFF increases with the pumping current and the role of noise, dominating when LFF starts to appear, is overtaken by determinism. The relative maxima of R in Fig. 2.18 is a consequence of the presence of the two peaks in the distribution of the time-intervals, since the regularity is affected by the bi-modality of the time-interval distribution.

The dependence of $< T >$ and σ_T with the feedback level is not so clear as with the pumping current (Fig. 2.19). It seems that we have a different dependence with the feedback level depending on which region is explored. When the feedback level is strong enough ($> 5\%$) $< T >$ and σ_T are not very affected by an increasing of the feedback level. If the feedback level is ($> 9\%$) either $< T >$ either σ_T grow quickly with the feedback. The index also is growing, expressing the fact that noise plays a more important role in controlling the system. If the feedback level is lower than 5% there is a discontinuity in the dependence of R, $< T >$ and σ_T

with the feedback level. We can also remark that the characteristic time ($< T >$) involved in the upper panel of Fig. 2.19 is smaller than in the lower panel, where the external-cavity is longer.

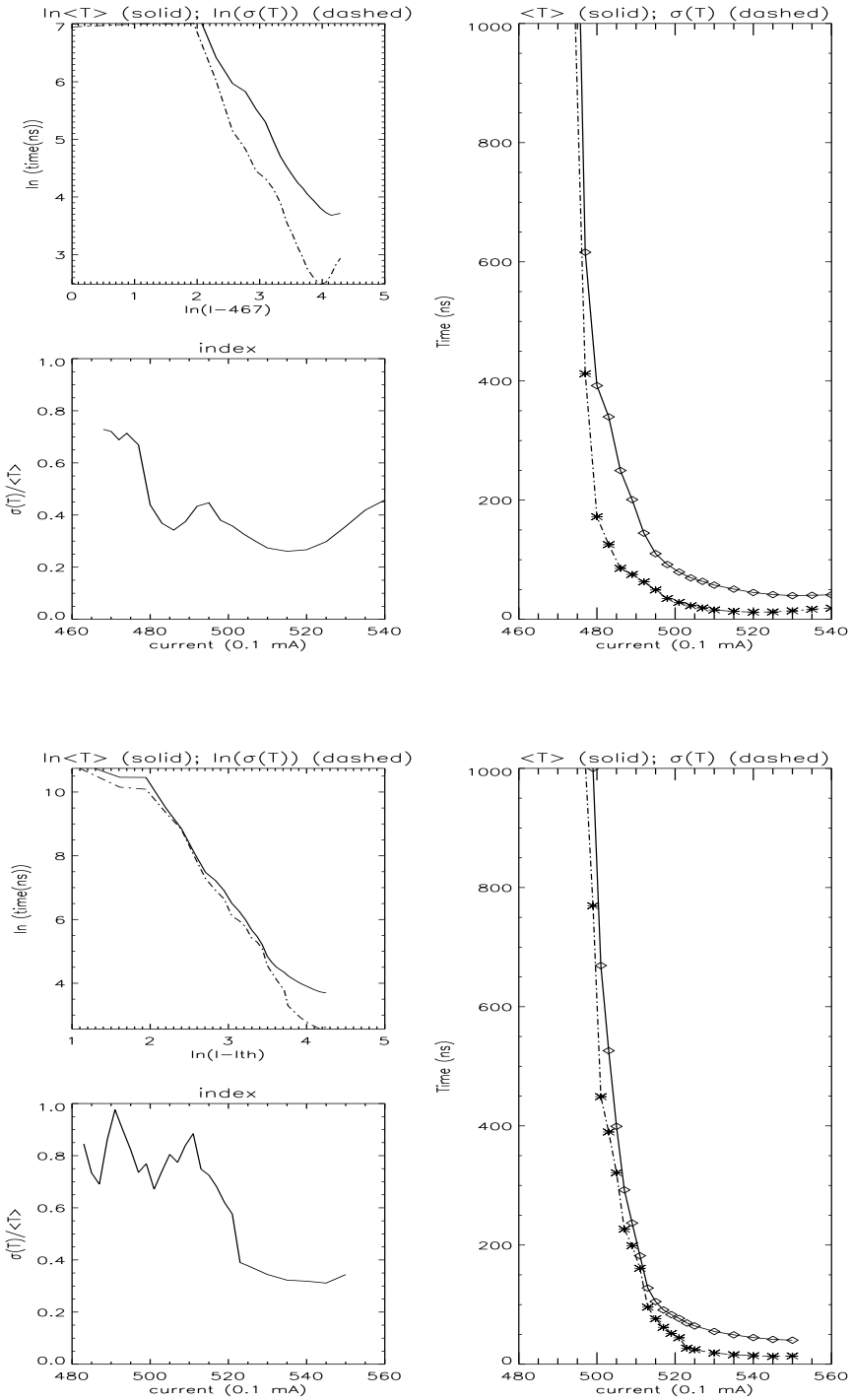

Figure 2.18: $< T >$, σ_T and $\sigma_T / < T >$ vs. pumping current for a cavity length of 63 cm ($\tau_{ext} = 4.2\ ns$) and feedback level: $\xi = 8\%$ (above), $\xi = 12\%$ (below).

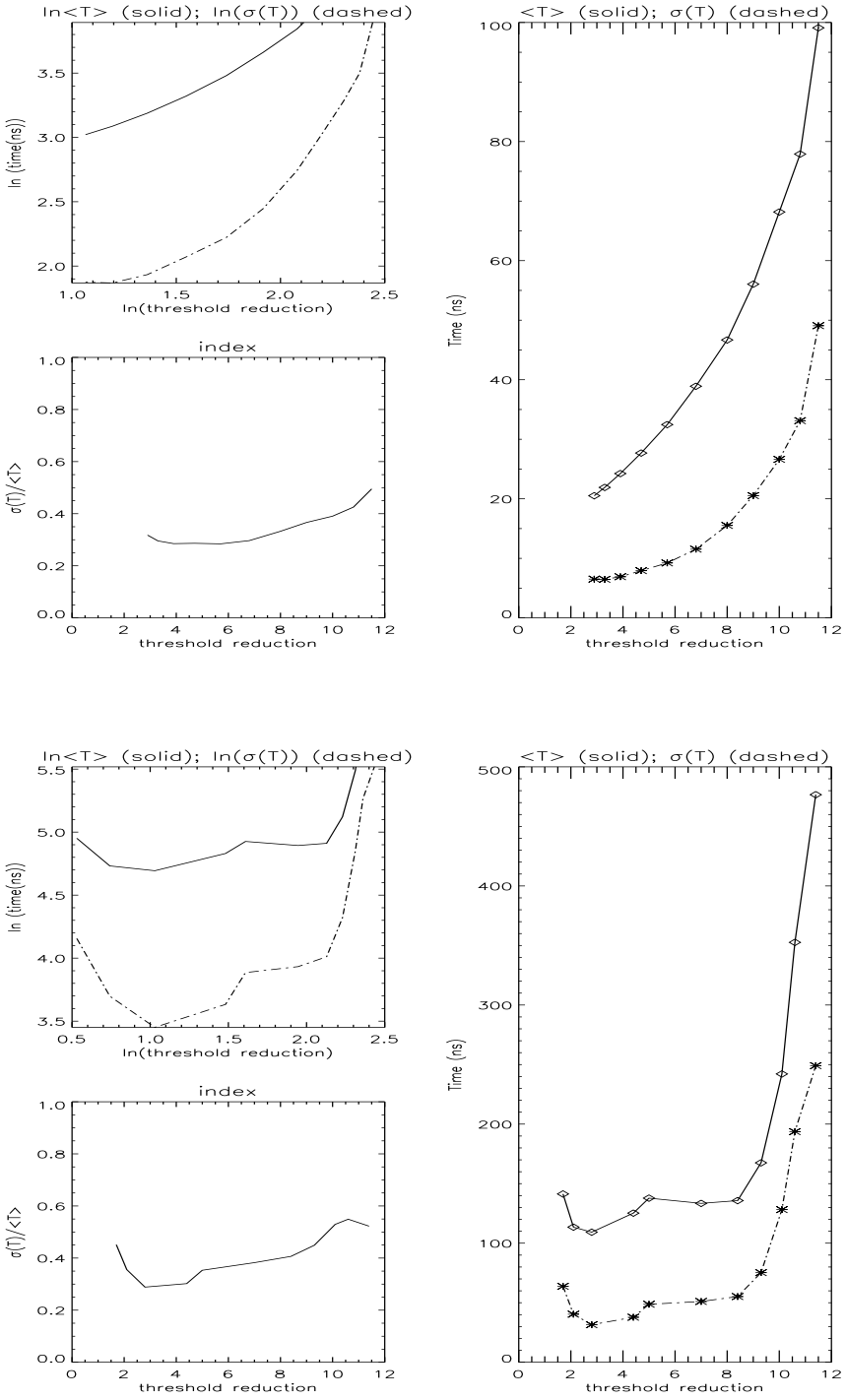

Figure 2.19: $< T >$, σ_T and $\sigma_T / < T >$ vs. feedback level (ξ), for a cavity length of 41 cm ($\tau_{ext} = 2.7\ ns$), $I/I_{th,sol} = 1.02\%$ (above) and of 63 cm ($\tau_{ext} = 4.2\ ns$), $I/I_{th,sol} = 1.04\%$ (below). The threshold reduction is expressed in mA.

2.4.2 Characterization of the bifurcation

From the previous measurements, we can conclude that: i) In the phase-space must exist a "quiescent-state" from which the system may depart; when this occurs the system evolves following a well-defined orbit to which it corresponds a Low-Frequency Fluctuation in the intensity-output variable. ii) In the LFF-regime, for parameters values close to the stable-regime, the system looses memory during the interval T and the statistics of the time-intervals between drops follow the Kramers' rules describing the first-passage times of a noise-driven particle escaping from a potential well. These evidences suggest that noise acts as a trigger for the LFF. iii) LFF appear in the time-series with a finite amplitude and at a low-rate. Increasing the pumping current the rate increases while the amplitude of the fluctuations is not strongly affected. iv) Approaching the CC-regime, deterministic terms play the relevant role in describing the dynamical behavior of the system giving phase correlation among the interval T.

Considering these experimental observations, we can discard the existence of a super-critical Hopf bifurcation ruling the LFF appearing. In fact, this would lead to small amplitude pulses with a well defined frequency, while, in our case, the passage from the LFF-regime to the stable-regime is characterized by the existence of large amplitude pulses with a vanishing rate. In non-linear dynamics a bifurcations that can lead to an oscillatory behavior with these characteristics is the *Andronov-Saddle node bifurcation* (simply Andronov bifurcation hereafter), see Refs. [107, 108]).

An Andronov bifurcation is a global bifurcation involving an unstable fixed-point, a stable fixed-point (node) and a saddle-node whose unstable manifold is the stable manifold of the node (heteroclinic connection). When the bifurcation occurs the saddle-node and the node annihilate as in a simple saddle-node bifurcation, but the presence of the heteroclinic connection originates a closed orbit

(limit cycle) which stays for a long time in the neighborhood of the preexisting fixed-point and suddenly evolves fast far away from it. Such bifurcation is characteristic, for example, of a pendulum in a rotating wind or a laser with injected signal (Ref. [109]) and it is described by Adler's equation. The Andronov bifurcation is characterized by the presence of fluctuations having a fixed amplitude and a frequency vanishing approaching the bifurcation point with the law $\mu^{-1/2}$, being μ the control parameters. The presence of noise on this dynamical scenario makes that the system has a finite probability of departing from the stable fixed-point even for parameter values at which the bifurcation has not occurred. In this situation the statistics of the departures is analogous to the first-passage time problem described by Kramers. Thus, the LFF-regime may be heuristically explained assuming the dynamical scenario of the Andronov bifurcation, and considering the presence of the noise which triggers the drops before the bifurcation has occurred. The control parameters determine the separation between the stable fixed-point and the unstable manifold of the saddle-node in the phase-space or, in term of a first-passage time problem, the depth of the potential well corresponding to the attraction basin of the fixed-point (activation-energy). In this way, for a given amount noise present into the system, the probability of departing and, consequently, the rate of the drops changes with the pumping current and the feedback level. The situation of almost-periodic LFF corresponds to the case where the activation energy is so small compared to the noise level that the average waiting-time (inverse of Kramers' rate) is negligible and there is a very high probability for a system to depart as soon as it has recovered from the preceding LFF. In this situation deterministic processes are less sensitive to the amount of noise.

According to this interpretation, the bi-modal time-interval distribution can be explained in the following way: as the system is returning to the stable point

in the phase-space after a drop, running along the last part of the LFF-orbit, its speed decreases (the last part of the recovery stage is slow, as it is evident from the time trace) and the noise may drive again the system out from the basin of attraction of the stable point. Then, approaching the attractor, the system can depart before having reached the quiescent-state, jumping to an inner orbit very close to the one relative to the first drop. This dynamics could continue for several times before the system could reach again the attractor. Hence, LFF appear grouped in clusters where they are separated by a time $T \approx t_o$ and where the LFF departing intensity level is lower than the departing intensity level of the LFF dropping from the quiescent-state.

It worth noting that the whole LFF-regime can be explained without requiring that the Andronov bifurcation needs actually to occur at some parameter values. The almost-periodic LFF situation can be explained either by assuming an high Kramers' rate of the noise-driven departures, thus without requiring the trespassing of the bifurcation point, either by assuming the occurring of the bifurcation that originates periodic fluctuations whose regularity is somehow affected by the noise present into the system. Because of the unavoidable presence of the noise into the system, it is extremely difficult to provide irrefutable experimental proof that the bifurcation has really occurred.

A system is defined *excitable* whenever its response to a perturbation has the following feature. If the kick amplitude is smaller than a certain threshold the system response is proportional to the perturbation size. Instead, if the kick amplitude overcomes the threshold value, the system responds with a large excursion in the phase-space before returning to the initial state and, therefore, the response becomes independent of the perturbation size. This somewhat vague definition allows us to recognize excitability in a wide variety of systems, most remarkably in biology (Ref. [110]). A system possessing an Andronov bifurcation

is excitable (Ref. [108]). This is evident considering the heteroclinic structure involved in this bifurcation. Let us prepare the system in the stable fixed-point and kick it with increasing size perturbations. Initially, for small size stimulus, the system does not leave the basin of the attractor: it reacts proportionally to the kick size, staying in the neighborhood of the fixed-point, and then returning to the quiescent-state. Increasing the perturbation size we finally reach the threshold for which the system leaves the basin of the attractor. Then the system evolves following the heteroclinic connection between the unstable manifold of the saddle and the stable manifold of the attractor. This topology makes the system to follow a large excursion in phase-space before coming back again to the quiescent-state. Thus the reaction to the kick is fixed by this heteroclinic orbit and it is not anymore related to the perturbation size.

In the frame of the Andronov bifurcation interpretation *Low-Frequency Fluctuations are noise-induced excitable pulses.* This interpretation fits very well with the phenomenology of the LFF and the noise role evidenced by the experimental observations.

We can recognized an excitable medium by its response to a fast variation of a parameter (excitation pulses). In Fig. 2.20 we show the results of the experiment proving the excitable character of our system. The external-cavity length is 21.7 cm (1.5 ns round-trip) and the corresponding LFF time duration is $t_o \approx 22\ ns$. We fix the pumping current close enough to the threshold of the system, such that intensity is constant in time. Through a bias-T, we add to the pumping current pulses whose amplitude and width can be varied. The width of the pulses is of 80 ps and the rate is of 30 ns. Changing this amplitude we have observed the existence of a threshold for the appearance of excitable pulses in the intensity-output of the system. Below this threshold the system reaction is proportional to the kick size ($2-2.6\ mA$); above 3 mA the reaction is independent

of the perturbation both in amplitude and width. Further increasing the kick size increases the ratio between the number of excitable pulses and the number of kicks, approaching unity for perturbation sizes of 10 mA (see the time-intervals histograms of Fig. 2.20). In fact, the unavoidable presence of noise overlapped to the perturbations yields a non constant threshold value for the kick. Hence the situations where just few kicks induce a excitable pulses. Just as noise anticipates the bifurcation, it can, overlapped to the kicks, trigger the departures before the kicks have actually achieved the excitability threshold value. As the kicking size is increased, noise becomes secondary and every perturbation triggers a pulse. It is fundamental to remark the fact that the amplitude of the excitable pulses is not affected by the wide variation of the size of the kicks, nor it is related to the pulse width; the excitable pulses observed in Fig. 2.20 are similar in amplitude and width to the Low-Frequency Fluctuations observed in the LFF-regime, thus confirming the excitable character of our system. To our knowledge this is the first experimental observation of excitability in an optical system.

It worth noting that, in our experiment, we used a pulse rate larger than t_o. Then, there is an high probability that the system has returned to the quiescent-state before the next kick. Increasing the kicking frequency above $(t_o)^{-1}$ prevents, even for huge kick sizes, to excite an LFF for every kick. Moreover, we observed particular excitation frequencies for which no LFF are excited no matter the perturbation sizes. We are currently exploring these features analyzing the ratio between the refractory time and the kicking period (Ref. [111]).

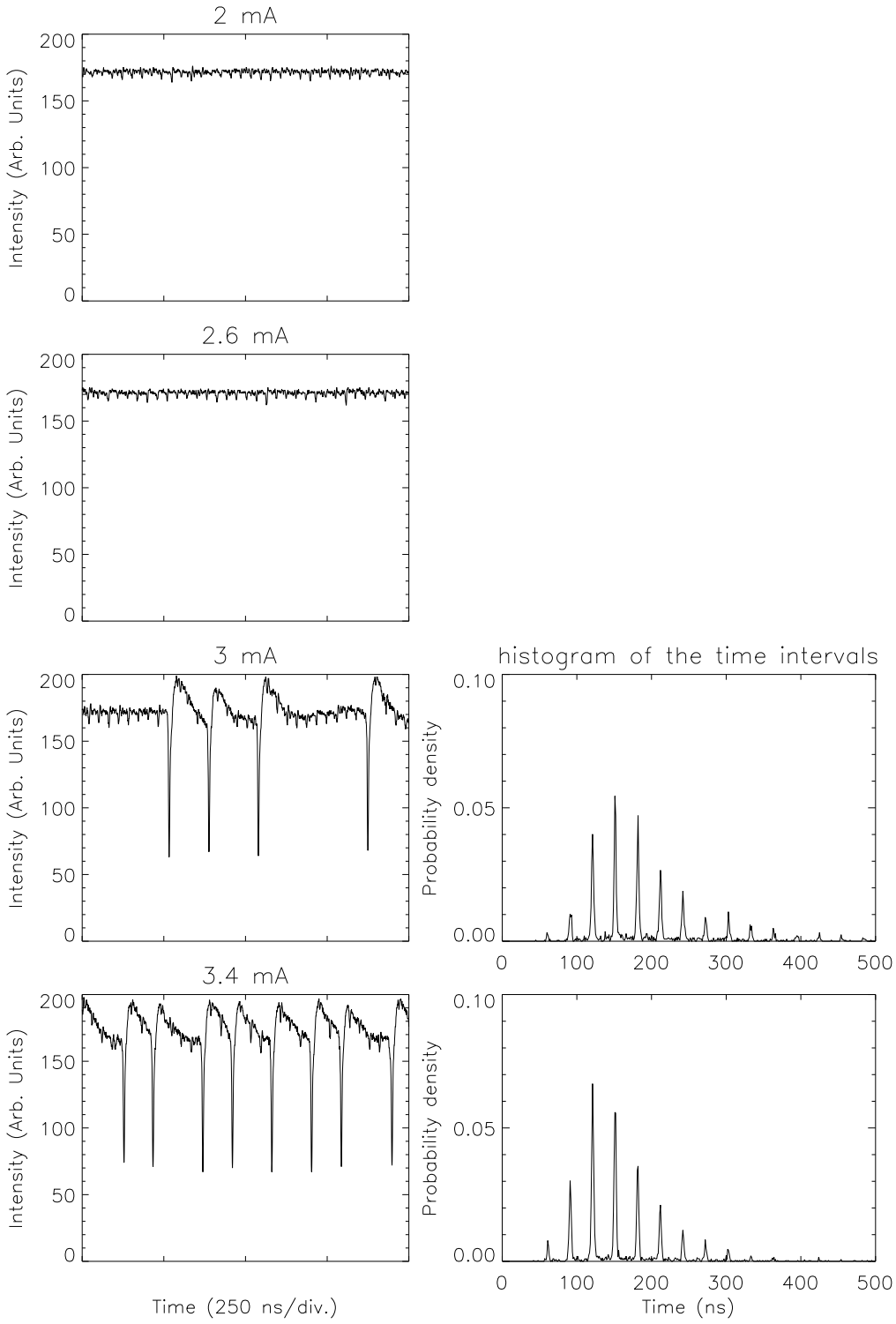

Follows in the next page ⟶

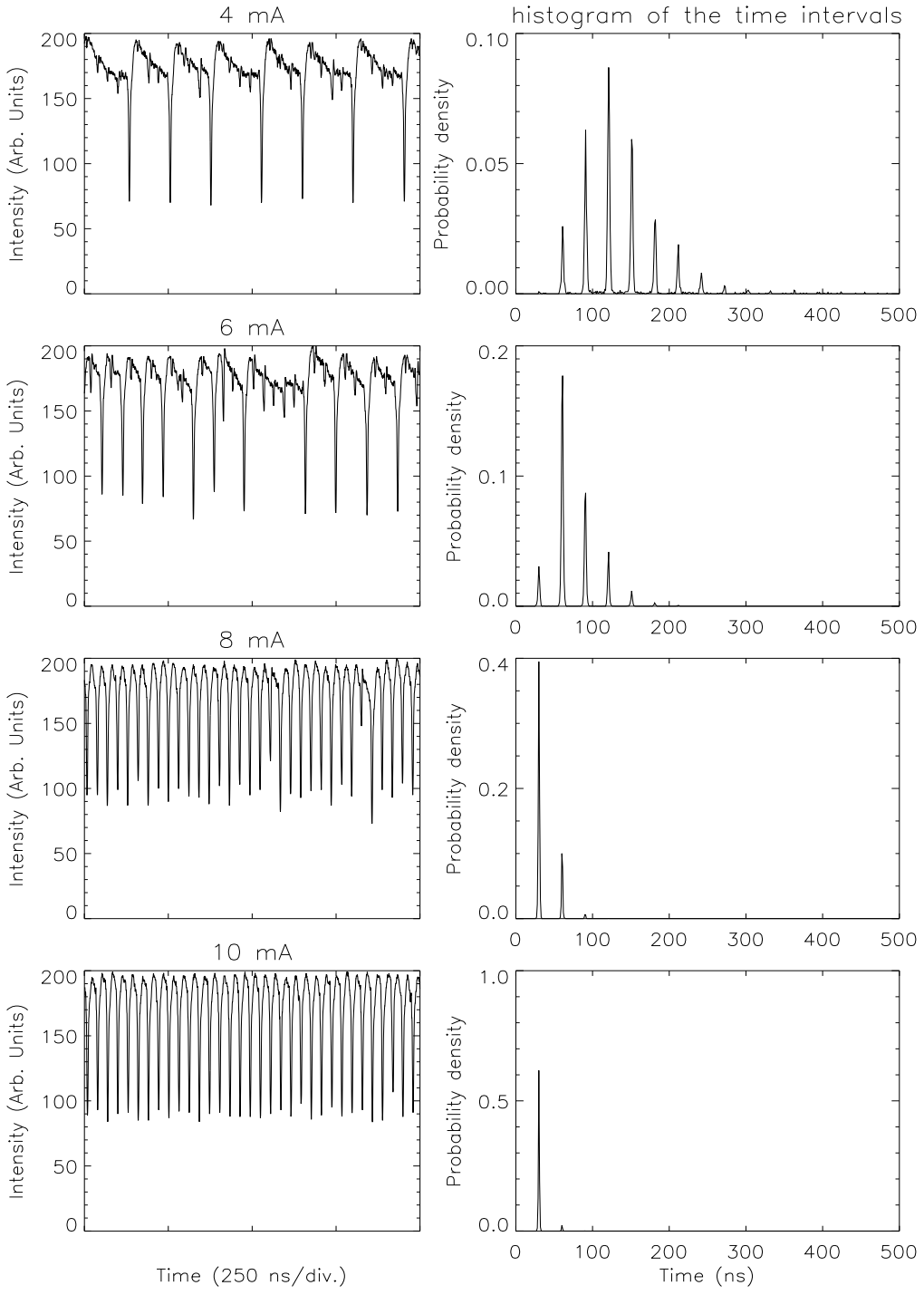

Figure 2.20: Intensity of the system when a small amplitude perturbation (width: 80 ps , period: 30 ns) is added to the pumping current; the amplitude of the perturbation is written on the top of each picture. In the right column we show the probability distribution of the time-interval between excitable pulses. The system is prepared in this way: $I/I_{th,sol}$=1.01, feedback level:ξ = 10%, cavity length=21.7 cm (1.4 ns round-trip).

2.4.3 Noise role: Coherence Resonance

We have shown the very important role of noise in our system. We have demonstrated that noise anticipates the bifurcation that leads the system to exhibit LFF; at the beginning of the LFF-region, noise triggers the fluctuations and the system appears as a noise-driven deterministic system. In order to build the simplest dynamical model able to describe, at least qualitatively, the behavior of our system, the direct analysis of the noise influence on the system dynamics would be very useful.

Controlling the noise in our system is not only useful to argue elements for the dynamical description. We have shown that our system is excitable. Noise-driven excitable systems represent a very attracting issue. By adding noise to a dynamical system in general, it is possible to obtain order in chaotic systems, synchronization, and *Stochastic Resonance* (Refs. [112, 113]). The latter appears typically in a bi-stable system with noise, when a periodic forcing of frequency ν_{for} is applied (Ref. [114]). It has been found that the periodic response or, equivalently, the S/N ratio of the system is maximal for a certain noise level. This is intuitive considering Kramer's theory which establishes a relation between the average interval $< T >$ between noise-driven jumping between the two states and the noise level. When the noise amplitude implies a rate $< T >^{-1}= 1/2 \cdot \nu_{for}$, the S/N response of the system to this forcing is strongly enhanced. Controlling the forcing frequency instead of the noise level, it exists a forcing frequency that verifies the same condition, hence the name of *Stochastic resonance.* Therefore, while in conventional linear systems noise is always perceived as a degrading factor, in some non-linear systems it can improve the regularity of the signal.

Recently the effect of noise on the autonomous excitable oscillator described by the Fitz Hugh - Nagumo system has been analyzed in Ref. [106]. In this work it

has been theoretically proven that the characteristic correlation time of the noise-induced excitable pulses shows a maximum for a finite noise amplitude. Since in this system there is no periodic forcing, this situation does not correspond to stochastic resonance and it has been named *Coherence Resonance* in Ref. [106]. The physical meaning of *Coherence Resonance* can be understood by considering the features of excitable systems, namely, the pulse firing occurs only when a perturbation overcomes a certain (nonzero) threshold and thereafter the response of the system is almost independent of the size of the perturbation itself. Two characteristic times have been defined for each value of the input noise: the refractory time (or orbit-time) t_o, usually close to the pulse width itself, and the activation time t_a between consecutive pulses. The time t_a is just the time T between consecutive excitations if $T > t_o$. In general, the firing process can be initiated by noise and therefore the time T becomes stochastic. For small amount of noise we can intuitively assume that the description of T follows the statistical properties of the noise itself. However, for larger noise amplitudes the average value of T decreases. The excitable character of the system imposes the physical limit $T > t_o$; as a consequence, for increasing noise, an almost periodic pulsing takes place and the variance $\sigma(T)$ decreases. This corresponds to a maximum of the coherence of the system. Further increases of the noise amplitude induce the deformation of the orbit of the excitable pulses and eventually the dynamics is ruled by the noise.

We have experimentally investigated the effect of noise in our excitable optical system. Changing the amount of noise, and choosing the adequate indicators, we report the first experimental evidence of *Coherence Resonance*.

The experimental setup is the same as in Fig. 2.1. The length of the external-cavity is here 36 cm, corresponding to a free spectral range of 416 MHz. The threshold reduction induced by the optical feedback is 12%. The laser is pumped

at 1 % above the solitary laser threshold. We add a broadband (more than 1 GHz), gaussian noise source, with zero mean amplitude into the laser, via the bias-tee. Such a broad-band noise is generated by an Avalanche Photodiode detecting the spontaneous-emission of a semiconductor laser biased just below its threshold. The band limitation of 1 GHz comes from the bandwidth of the detector. Such signal is then amplified using a 20 dB microwave amplifier (1 $MHz - 22$ GHz). The noise level is varied by controlling the amount of light reaching the detector with a polarizer placed between the laser and the detector. The system output signal detection is carried out by a fast avalanche photodiode (2 GHz bandwidth) and a LeCroy digital oscilloscope (500 MHz bandwidth). A DC-100 MHz amplifier allows to select the frequency range of interest. It is worthwhile to note that filtering the signal at 100 MHz allows us to monitor the excitable pulses without the details introduced by faster time scales.

In the absence of added noise, the output intensity is constant in time. As the noise is added, we observe the appearance of excitable pulses, randomly distributed in time (Fig. 2.21a). Increasing the amount of noise, the pulse rate increases, until the signal becomes almost periodic (Fig. 2.21c). For larger noise the signal becomes irregular (Fig. 2.21d), since the amplitude of the pulses starts to fluctuate strongly. It seems that, around some definite noise level, the behaviour of the system is more regular, which would be an indication of *Coherence Resonance*. Following Ref. [106], we study the behavior of the time-interval between pulses T using the indicator R, defined as the variance of the scaled variable $R = \sigma_T / < T >$. In the case of a perfectly periodic signal, R would be identically zero.

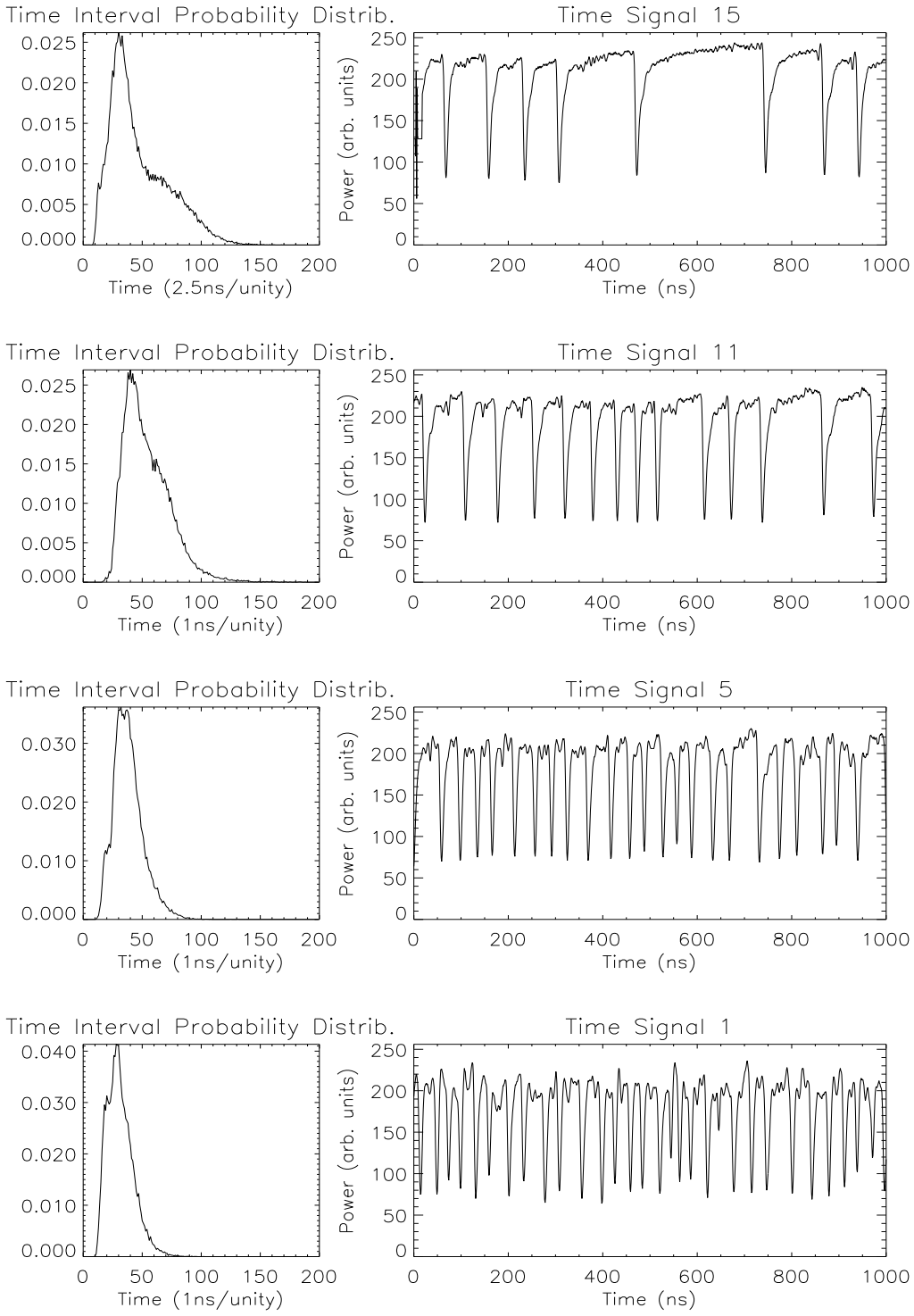

Figure 2.21: time-series and histogram of the time interval probability distribution between drops for increasing (from the top) noise level applied in the pumping current: $-65\ dBm/MHz$ (a), $-57.5\ dBm/MHz$ (b), $-49.5\ dBm/MHz$ (c), $-45\ dBm/MHz$ (d). The system is so prepared: cavity length $= 36\ cm$, $\xi = 12\%$, $I/I_{th,sol} = 1.0$.

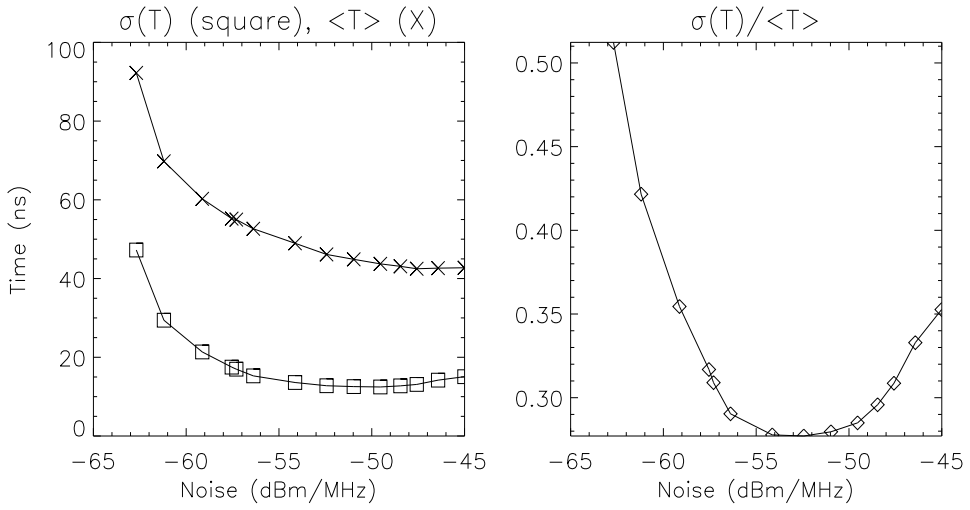

Figure 2.22: $< T >, \sigma_T$ and $\sigma_T / < T >$ versus η for the experiment of Fig. 2.21.

In Fig. 2.22 we plot σ_T, $< T >$ and R as a function of the noise amplitude η. We define the pulse time as the instant when the signal crosses, with negative slope, a fixed threshold value corresponding to 80% of the amplitude of the pulses shown in Fig. 2.21. As noise is increased from its minimum value, R reaches a minimum for $\eta = \eta_{opt} = -57\ dBm/MHz$ and increases afterwards. The minimum is clearly observable for a wide range of threshold choices; the particular threshold value affects only how fast R_θ increases for noise levels above η_{opt}, but it does not modify the statistics for noise levels below this optimum value. This is a clear evidence of *Coherence Resonance*, since around a particular level of input noise we find maximum regularity of the pulse train.

2.4.4 A simple dynamical model

It is a typical strategy in non-linear dynamics to find paradigmatical equations, if possible the simplest ones, whose solutions present a desired feature (Ref. [30]). The purpose of this strategy is to be able to make predictions about the behaviour of a particular problem, regardless of its intrinsic details. In order to study excitability, we can study the phase space organization of the flow of a dynamical system close, in parameter-space, to the point at which an Andronov bifurcation takes place. The most simple equation whose solutions undergo an Andronov bifurcation is the following one:

$$\theta' = \mu - \cos\theta \tag{2.4.1}$$

with $\theta \in S^1$, i.e. and angular variable. Notice that if $\mu > 1$, there are no fixed-points, and the flow consists in a monotonous growth of the variable θ. This growth is interrupted at $\mu = 1$ for a couple of fixed-points that are born at $\theta = 0$. For $-1 < \mu < 1$, these fixed-points (a repulsor and a node) coexist, and the connection between their manifolds is guaranteed by their topological structure in phase space. Let us assume that our system is governed by the eqt.2.4.1 with $\mu = 1 - \epsilon$, and our initial condition is $\theta = \sqrt{2\epsilon}$. A perturbation larger than $2\sqrt{2\epsilon}$ will induce a large response and the system will increase its phase by 2π.

The key element in order to obtain excitability is the connection between the manifolds of the fixed-points. In the model previously described, this connection is provided by the topological structure of the phase-space. In order to draw a model applicable to a larger class of systems, the dynamics has to account for it. The minimal dimensionality in which this can be achieved for euclidean variables is two. A simple model with the desired features is

$$x' = y \tag{2.4.2}$$

$$y' = x - y - x^3 + xy + \epsilon_1 + \epsilon_2 x^2, \tag{2.4.3}$$

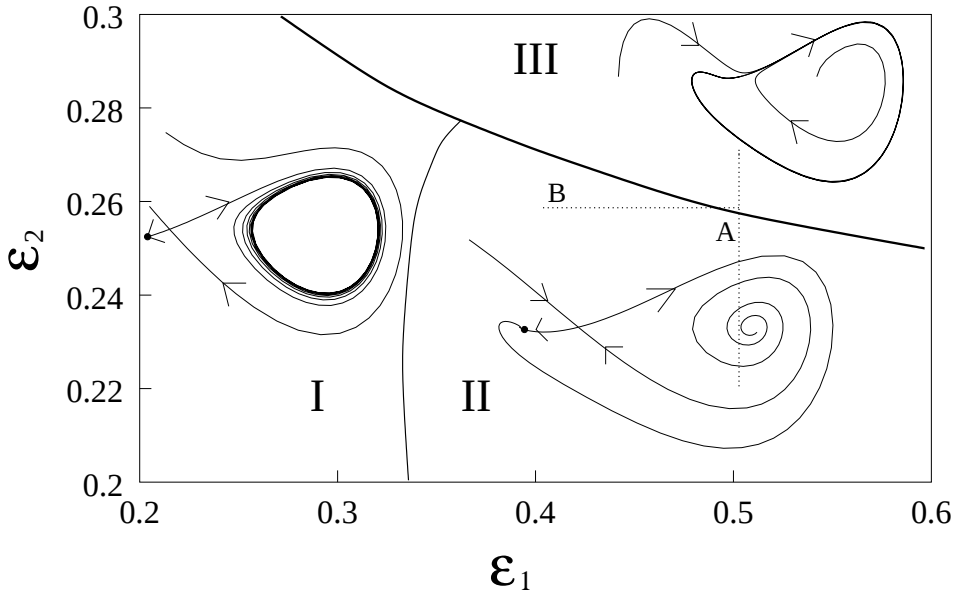

Figure 2.23: Bifurcation diagram and phase portraits for the system described by eqts. (2.2) – (2.3). In regions I and II there are three fixed-points: a node, a saddle and a repeller. Crossing the separatrix to region III, the saddle and the attractor collapses. The three lower regions display a qualitatively different behaviour. In regions I the unstable manifold of the saddle approaches a limit cycle. In region II the unstable manifold of the saddle is the stable manifold of the node and the system behaves as an excitable one. The dashed lines represent the parameters values explored in the histograms of Fig. 2.25.

with $(x, y) \in R^2$, and ϵ_1, ϵ_2, $\in R^+$.

Let us study the structure of the flow of this system. The fixed-points are found at $y = 0$, and at $\epsilon_1 = -x + x^3 - \epsilon_2 x^2$. A double root exists when $\epsilon_1 = -\frac{2}{27}\epsilon_2^3 - \epsilon_2/3 + 2(\epsilon_2^2/9 + \frac{1}{3})^{3/2}$. For $\epsilon_1 < -\frac{2}{27}\epsilon_2^3 - \epsilon_2/3 + 2(\epsilon_2^2/9 + \frac{1}{3})^{3/2}$ a saddle and a node coexist with a third fixed-point that exists for all values of ϵ_1 and ϵ_2. The three fixed-points can be ordered according to their x values, as they all lie in the $y = 0$ axis. For all parameter values, the node has the smallest x value.

In Fig. 2.23 we display the qualitatively different behaviours of the flow in the different regions of the parameter-space. Those regions are limited by curves in which either local or global bifurcations take place. The curve that separates region III from the others contains the parameter values at which the saddle node bifurcation takes place, explicitly written above. Above this curve, there is only one fixed-point that feeds a limit cycle. Below this curve, there are three fixed-points connected as follows. In region I, the unstable manifold of the

saddle feeds the node and a limit cycle. The third fixed-point also feeds the cycle. Regions I and II are separated by a curve in parameter space in which the saddle has an homoclinic connection (from region I towards this curve, the limit cycle approaches the saddle). Within region II, the unstable manifold of the saddle is the stable manifold of the node, and the saddle is connected to the repulsive fixed-point. There is no limit cycle in this region. The flow is orbitally equivalent to the one dimensional flow described above when $-1 < \mu < 1$. Notice that crossing the separatrix in parameter-space from region II to region III implies undergoing an Andronov bifurcation. As mentioned, the system described by eqts. 2.4.2 with parameter values within what we have called region II behaves as an excitable one. The response of the system to a perturbation of an initial state located at the node will be independent of the size of the perturbation, provided that it places the system beyond the stable manifold of the saddle. As the unstable manifold of the saddle is attractive, the response will evolve close to it no matter the size of the perturbation.

We have discussed the excitable nature of our model for parameter values in region II. Let us assume an initial condition in the neighborhood of the attractor. Under the influence of noise, this state might be eventually taken beyond the stable manifold of the saddle. As its unstable manifold is attractive, the state will now evolve following this manifold closely (independently of the original size of the perturbation) until it approaches again the vicinity of the fixed-point. It is important to recall that in this region of the parameter-space, the unstable manifold of the saddle is the stable manifold of the node. Associating this large excursion in the phase-space with a dropout event, we recover the behaviour described in the previous sections for the LFF-regime.

Notice that in our model, a given noise level will give rise to dropout events of higher rate as we approach (from region II), the separatrix defined by the

curve of saddle nodes. From Fig. 2.23 it appears that ϵ_1 rules the approach to the Andronov bifurcation i.e. the distance between the fixed-points, while ϵ_2 controls the distance to a saddle loop global bifurcation. Recalling the definitions of §II.4.1, ϵ_1 controls the activation time t_a i.e. while ϵ_2 controls the "probability" of having LFF clusters.

In order to obtain numerical results for our excitable system we have separated our problem into deterministic evolution and noise. The eqts. 2.4.2 were integrated numerically. In order to simulate the presence of noise in our system we perturb, after each integration step, the x variable by a number given by $\sqrt{2D\delta t}\phi$, being δt the integration time step and ϕ a function that, at each step, generates random numbers Gaussian-distributed with zero mean and variance one. This stochastic term simulate a noise of zero mean and variance (or noise level) D. The square root of the time step arises from the transition probability for a diffusive process.

In Fig. 2.24 we show the time behaviour of the x variable for increasing values of ϵ_1 and ϵ_2=0.4 (Fig. 2.24a) and ϵ_2=0.5 (Fig. 2.24b). The noise level D is set to 10^{-3}.

It is evident the qualitative agreement with the experimental time traces of §II.3, obtained increasing the pumping current. In fact, ϵ_1 plays a role analogous to the pumping current of the laser: increasing ϵ_1 the activation time t_a decreases and LFF rate increases.

The role of the noise in this dynamical model follows the outlines we argued from the experimental results. When, in the parameter space, the bifurcation has not yet occurred, noise may trigger the LFF and, in this case, the activation time t_a of the drops has a statistic distribution following the Kramer' laws.

Comparing Figs. 2.24a and 2.24b we can also remark the role of ϵ_2: for lower value of this parameter the possibility of having clusters of LFF separated just

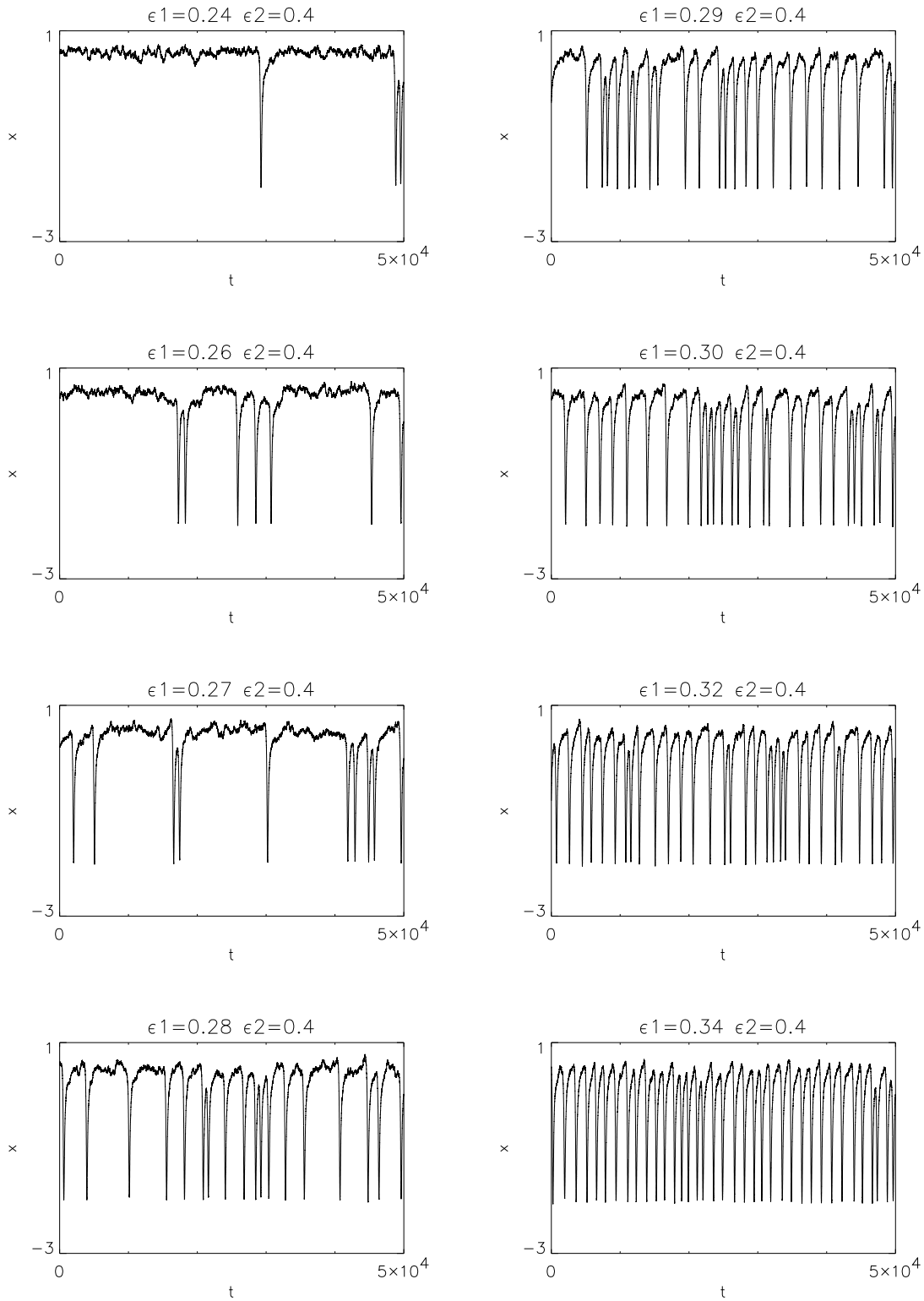

Figure 2.24: Time-series of the x variable when ϵ_1 is varied and $\epsilon_2 = 0.4$, $D = 0.001$, the integration step is 0.01. Setting $D = 0$ we checked that the Andronov bifurcation takes place in $\epsilon_2 = 0.5$, $\epsilon_1 \approx 0.252$.

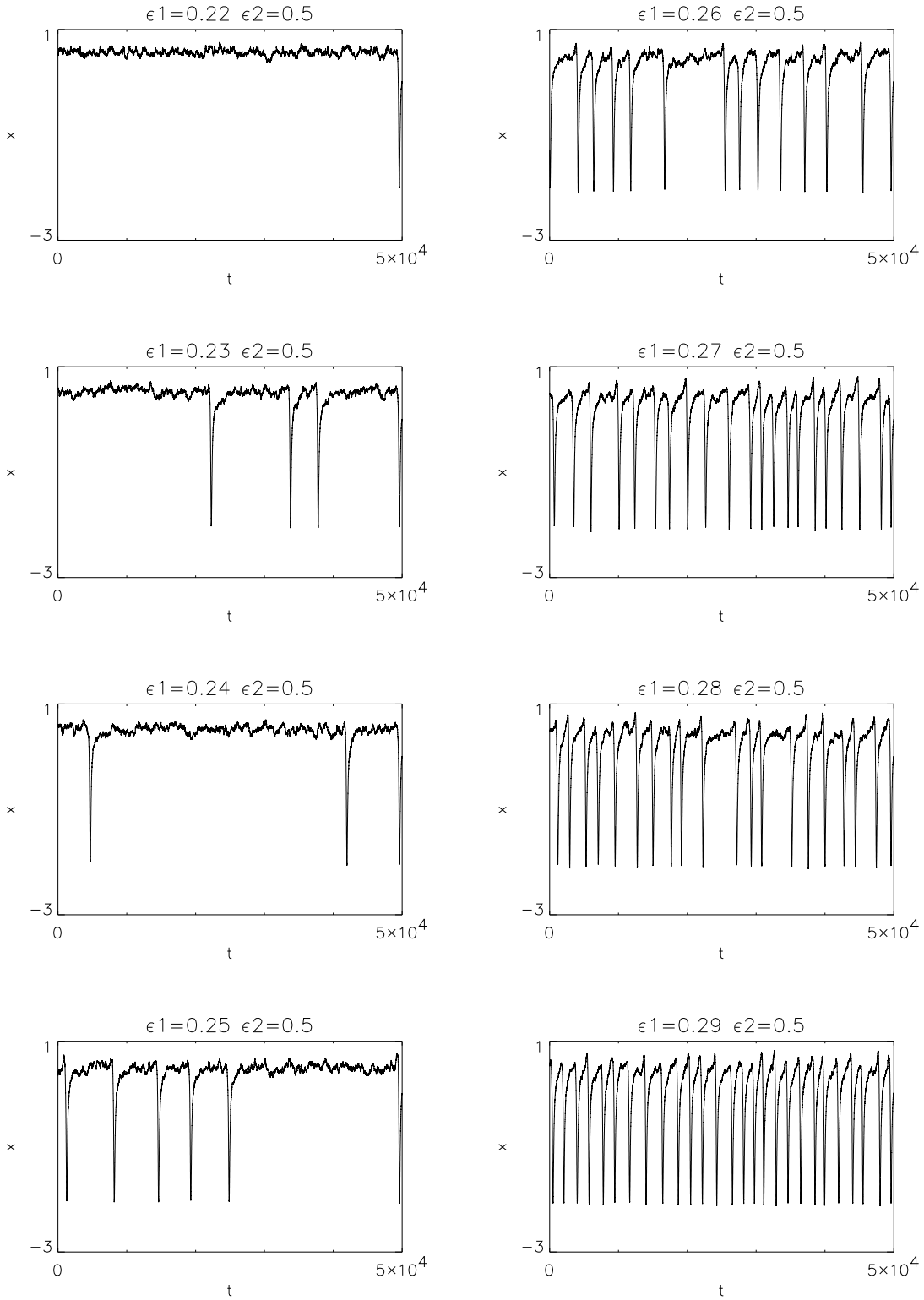

Figure 24b: Time-series of the x variable when ϵ_1 is varied and $\epsilon_2 = 0.5$, $D = 0.001$, the integration step is 0.01. Setting $D = 0$ we checked that the Andronov bifurcation takes place in $\epsilon_2 = 0.4$, $\epsilon_1 \approx 0.268$.

by the orbit time t_o is increasing. Clusters of LFF have been also observed in the experimental time-series and they are at the origin of the bi-modal time-interval histograms of Figs. 2.14-2.17. Equations 2.4.2, exhibit the dynamical features characteristic of the LFF clustering. In a delimited region of parameters (ϵ_2 small), noise can determine, after a drop, a further departure of the system before it has completely recovered its quiescent-state. This originates clusters of LFF separated only by a time $T \approx t_o$, $t_a \approx 0$. Two ingredients determine the occurrence of these early drops: the small separation between the manifolds (set by ϵ_2) and the noise level.

In order to verify more deeply the agreement between this model and the experimental observations, we compare the histograms of the time-intervals between LFF as generated by eqts. 2.4.2 with the experimental ones §II.4.2. The statistical analysis on the calculated time-series has been performed in Ref. [115] and the result is shown in Fig. 2.25.

These histograms shows very clearly the role of ϵ_1 and ϵ_2 in the model. The bi-modal character of the distribution fits well the experimental obtained histograms of Figs. 2.14-2.17. The right-most peak is related to the activation time t_a and it increases in height and moves to lower values as ϵ_1 is increased. The right-most peak in the experimental obtained histogram shows the same features for increasing the current or decreasing the feedback level.

The left-most peak increases in height as a consequence of the higher probability of LFF clusters, while the time location of the peak does not change since it is fixed by the LFF-orbit time t_o which is not significantly affected by the parameter values. The experimentally observed behavior of this peak is very similar: increasing the pumping current or decreasing the feedback level, its height increases together with the probability of LFF clusters while its time location is not affected significantly. The bi-modal distribution holds in the model even after

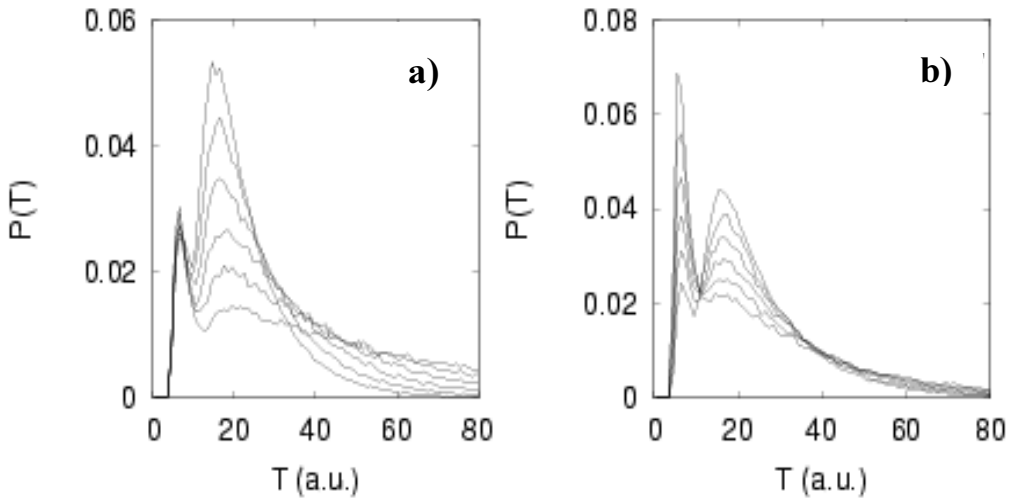

Figure 2.25: Probability distributions of time between dropout events in the model (binsize=1 a.u.): c)ϵ_2=0.5 and ϵ_1=0.22,0.23,0.24,0.25,0.26,0.27 corresponding to increasing rightmost peak amplitudes, d)ϵ_1=0.25 and ϵ_2=0.5,0.48,0.46,0.44,0.42,0.4 corresponding to increasing leftmost peak amplitudes. From Ref. [115].

the Andronov bifurcation. In Ref. [115] this is explained as a "scar of the saddle node bifurcation in the limit cycle". Before reaching the neighborhood where the saddle node was located before the bifurcation, the system can cross the stable manifold of the saddle following a more internal loop in the phase-space. This early-triggered drop adds a count to the left-most peak in the histograms. Noise level and the separation between the manifolds control the probability of this phenomenon. The same mechanism has been argued from the experimental data in §II.4.2. It is worth noting that the presence of noise hides the occurrence of the bifurcation in the variables of the system. The unavoidable noise presence in the experiment makes impossible the determination of the bifurcation boundaries in the parameter space.

The fact that such a simple model, built with the dynamical ingredients argued from the experimental observation, is able to represent successfully all these detailed LFF features, confirms the correctness of the hypothesis formulated in the previous sections on the LFF dynamical origin. On the other hand, it is not

evident to attribute a physical meaning to the variable x and y, and it appears also that neither ϵ_1 nor ϵ_2 can be identified exactly with the experimental control parameters. From the experimental data it follows that both the pumping current and the feedback level control t_a and the height of the leftmost peak in the histograms associated to the LFF cluster presence. In the model, instead, each parameter controls just one of these effects. This loss of information is the price to pay for the simplicity of this model.

2.5 LFF: physical mechanism of the instability

The model presented in section four, built according to the dynamical ingredients inferred from the measurements, identifies the dynamical scenario at the origin of the Low-Frequency Fluctuations. Anyway, as we have pointed out, it does not furnish many elements in order to understand the physical mechanism for which the system looses its stability and starts to exhibit drops in the output intensity. Moreover, the dynamical description has been performed on the averaged intensity-output variable of the system. Even if dynamically this variable is relevant [116], the low bandwidth filtering process may hide several features, fundamental in order to identify the physical mechanism of LFF-instability. This is evident comparing the bandwidth limitation for the time signal (500 MHz) and the time-scales involved in the system. In fact, it has been shown (Fig. 2.9, for example) that the appearance of LFF is associated to the excitation of many external and internal-cavity-modes of the compound laser. In order to resolve the beat note between consecutive external-cavity-modes (1 GHz apart, for example) a time-resolution of the order of 350 ps is required. Such time-resolution is accessible to our detector but it is at the limit of the performances of conventional single shot scopes. Time resolutions of 3.5 ps are required to solve the beating note of two consecutive internal-cavity-modes (separated by 125 GHz) and this is even beyond the limit of our detectors.

2.5.1 Relevance of the internal-cavity laser modes

In order to get information about the roles of the internal-cavity-modes of the laser in the LFF-instability, we may analyze the behavior of the modal components during an LFF, performing a time-resolved optical spectrum. Even if each modal intensity will be filtered by the scope bandwidth, it is possible to gain insight into the dynamics of each mode at the drops and during the recovery.

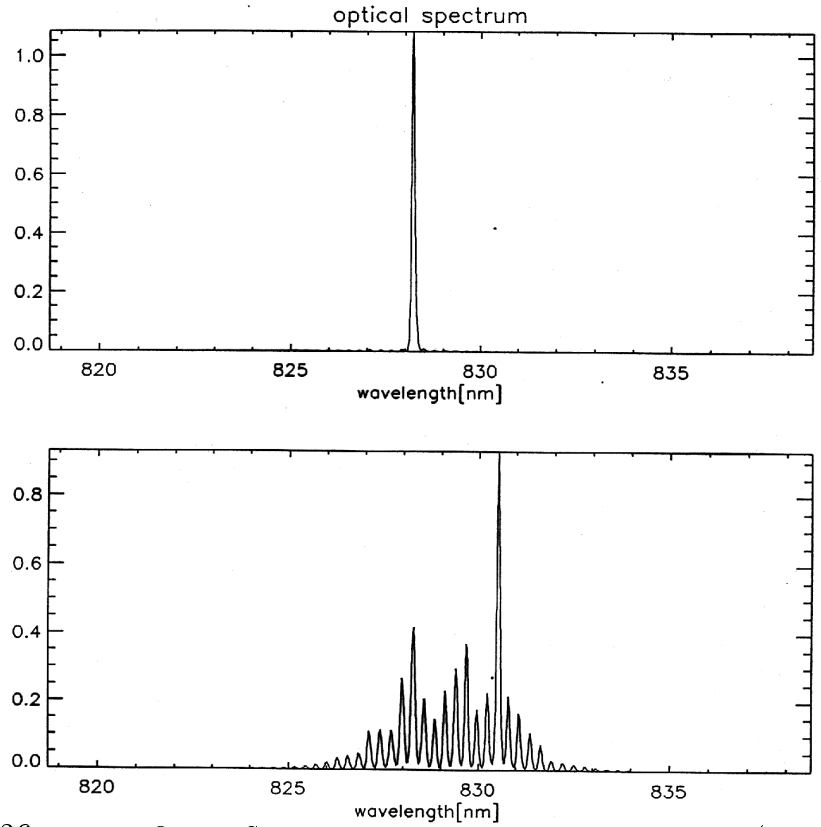

Figure 2.26: Typical Optical Spectra corresponding to the stable-regime (above) and to the LFF-regime (below).

We have shown that the emergence of LFF is associated with the excitation of additional longitudinal-modes of the solitary laser. In Fig. 2.26 we show the optical spectrum, obtained with a monochromator, of the system in the stable-regime and of the system when LFF appear. The use of the monochromator avoids any problem of aliasing, thus enabling the observation of the entire set of lasing modes. Fig. 2.26 shows clearly that the appearance of LFF is associated to the excitation of several solitary-laser-modes. We can quantify this dependence measuring, for different experimental conditions, both the number of drops per time unit and the number of modes above $-20\ dB$ with respect to the maximum peak (Fig. 2.27). The set-up used is the one of Fig. 2.1 where the FSR of the Fabry-Pérot equals 22 times the laser diode mode spacing, i.e. $\approx 2900\ GHz$ and its finesse is around 200. The laser ($Hitachi^{TM}$ HLP 1400) is AR-coated on one facet in order to achieve very large feedback levels, the solitary laser

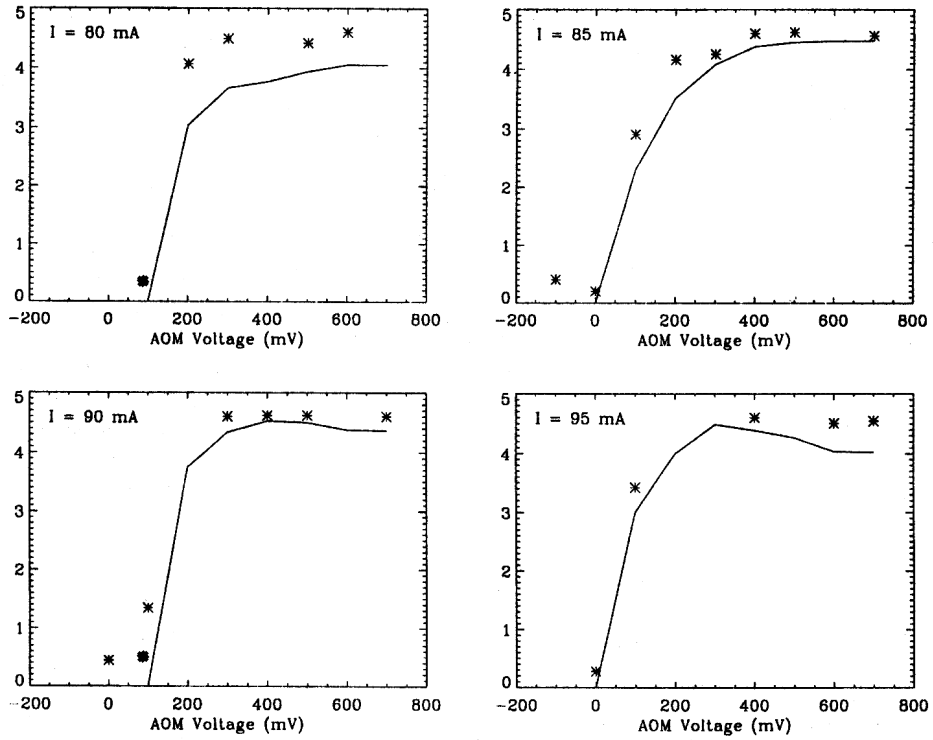

Figure 2.27: Correlation between the number of drops in 1 ms and the number of excited solitary-laser-modes for different feedback levels (ξ) (0 mV = 20%, 100 mV = 14%, 200 mV = 10%, 300 mV = 8%, 400 mV = 6%, 500 mV = 5%, 600 mV = 4%, 700 mV = 3%) and different laser currents: a) 80 $mA = I/I_{th,sol} = 1.03$, b) 85 $mA = I/I_{th,sol} = 1.09$, c) 90 $mA = I/I_{th,sol} = 1.15$ and d) 95 $mA = I/I_{th,sol} = 1.22$. Solid line: decimal logarithm of the number of drops. Symbols: number of excited solitary-laser-modes divided by 5.

threshold is 78 mA. In the LFF-regime, the number of excited solitary-laser modes monotonically increases for decreasing feedback level and saturate at about 22 modes, showing that the presence of LFF is strongly linked to multi-mode behavior.

In order to resolve in time the optical spectrum a second fast Avalanche Photodiode is positioned behind a Fabry-Pérot and replace the conventional slow silicon photodiode of Fig. 2.1. We fix the length of the Fabry-Pérot and we record the total intensity and the intensity transmitted through the etalon simultaneously. The latter corresponds to the component of the optical spectrum at the transmission frequency of the Fabry-Pérot, and its temporal behavior is the

same after every drop of the total intensity.

We record the time-resolved spectrum for different current and feedback levels by repeating the above measurement for all frequencies inside FSR of the Fabry-Pérot (now equal to 6 solitary-laser-modes, $\approx$ 800 GHz) and superposing the data recorded for every frequency. The appearance of an LFF triggers each measurement, which covers a time span of 190 ns with a time resolution of 1 ns. Following a drop of the total intensity (see Fig. 2.28), the active laser modes switch-off. As the power recovers, all solitary-laser-modes within the FSR of the Fabry-Pérot (and possibly more because of aliasing) start emitting with their modal frequencies strongly blue-shifted. Interestingly we see that the maximal value of this shift can be almost equal to the solitary-laser-mode spacing (see Fig. 2.28a and 2.28c)). It is worth noting that, as the total power recovers, all the modal frequencies recover synchronously, with a recovery time below 50 ns, which is of the order of the recovery time for the total intensity.

In addition, the recovery for the modal powers takes longer than 200 ns. On this long time-scale, the solitary-laser-modes exchange energy following dynamics similar to that observed during the switch-on transient of a laser (Ref. [117]). It is worth noting that none of the solitary-laser-modes has an evolution which mimics that of the total power. If there were such a mode, one could then interpret the evolution of the system as dominated by this mode, the others becoming excited because of the non-linear effects associated with the fast, large amplitude modulation of the master mode.

In Fig. 2.28b, one can see the effect of multiple drops (every $20 - 25$ ns). In this case, which is close to the fully-developed CC regime, the time-resolved spectrum is more noisy because the drops are so frequent that the system is no longer able to completely recover its quasi-CW state after every drop.

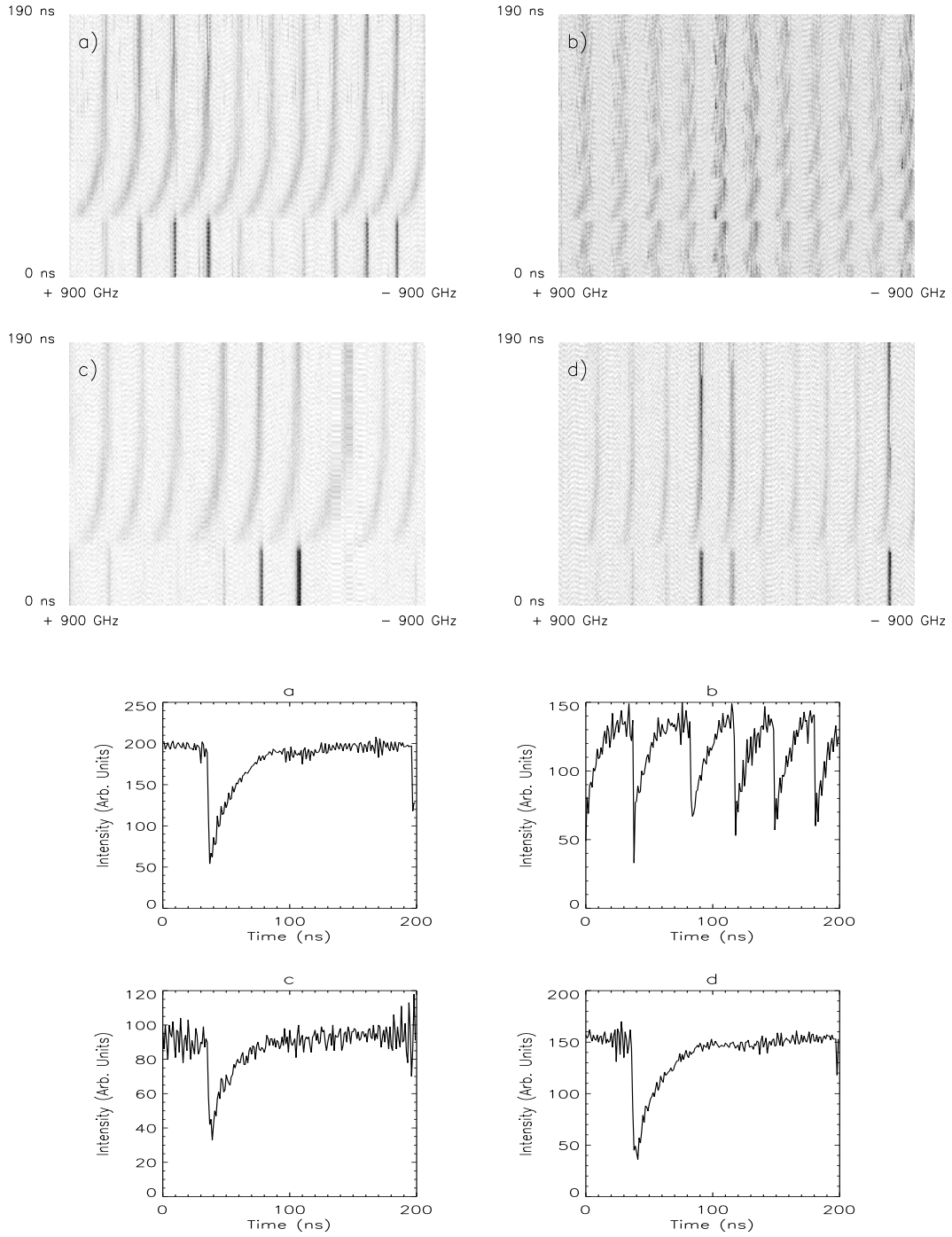

Figure 2.28: (above) Time-resolved spectrum of the laser for currents: $I/I_{th,sol} = 1.13$ with AOM voltages a) 170 mV = 11% threshold reduction and b) 380 mV = 7% threshold reduction, and $I/I_{th,sol} = 1.01$ with AOM voltages c) 170 mV = 11% threshold reduction and d) 380 mV = 7% threshold reduction. Darker areas correspond to larger optical intensity. (below) Total intensity-output of the system in the same time interval at which the time-resolved spectrum was acquired. Each figure is associated to the the one with the same letter in the preceding picture. We can compare the total LFF length with the modal recovery times.

In the LFF-regime, the time-resolved optical spectrum shows that the solitary-laser-modes are synchronized and they drop together. Following the drop, several modes become active, and they start to recover the power level they had just before the drop by means of inter-mode exchange of energy; as a consequence, the recovery for the power in each mode is much slower than the recovery of the total power, which indicates that a single-longitudinal-mode description of such LFF behavior will not capture important underlying dynamics. Because there is strong coupling among the modes on long time-scales, it appears that, in order to describe the LFF, either an effective multi-mode description (Ref. [118]) or a partial differential equation to describe the compound cavity (Ref. [21]) would be required.

Our analysis indicates that even for only two modes, the inclusion of the feedback terms leads to a breaking of the usual antiphase dynamics (as occurring in Ref. [119]). Antiphase dynamics is the dominant effect in between LFF. However, each LFF breaks the phase locking of the modes, which start to oscillate in phase until the modal intensities reach the vicinity of their steady-state values; at this point, antiphase dynamics is again observed.

In Fig. 2.29 we show the time-resolved optical spectrum for a laser with feedback in the LFF-regime, when the FSR of the interferometer contains 62 solitary-laser-modes. The laser is a quantum well GaAlAs laser SDL^{TM} 5400C, with a mode spacing of 58 GHz. The Fabry-Pérot FSR is of 3500 GHz, allowing the monitoring of the almost entire set of laser internal-cavity-modes excited during an LFF. Of course, the large value of FSR implies a lower resolution than in the Fig. 2.28 and we are not able to distinguish the blue-shift at the drop of every mode, as in Fig. 2.28. Fig. 2.29 shows the huge number of modes activated at the drop. Comparing the intensity recovering times in the time-resolved spectrum with the recovering time of the total intensity LFF, it

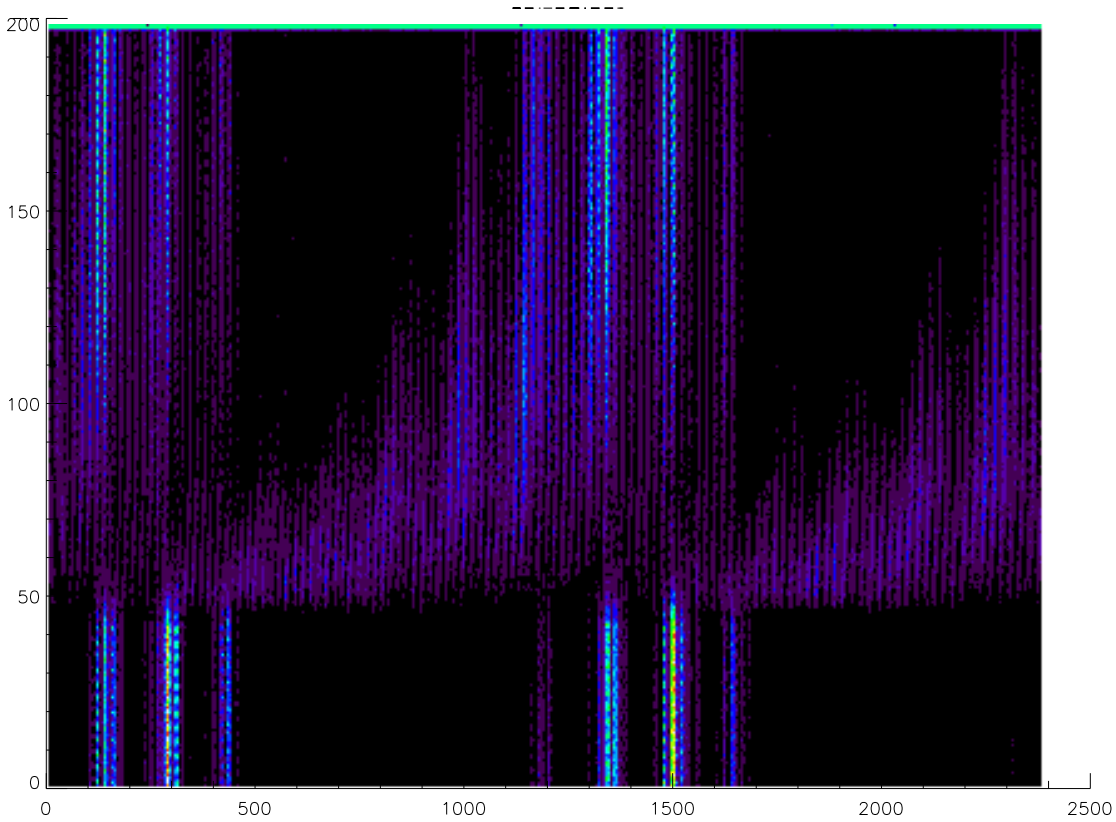

Figure 2.29: (above) Time-resolved spectrum of an SDL^{TM} 5400C with optical feedback. $I/I_{th,sol} = 1.15$ and threshold reduction is of 10%. Lighter areas correspond to larger optical intensity. The horizontal unit correspond to 2.85 GHz (below).

is evident that the inter mode energy exchange lasts much longer than the LFF recovery stage.

2.5.2 The problem of the bandwidth limitation

Looking at the power spectrum corresponding to the LFF-regime (Fig. 2.9, for example) it is evident that very fast oscillations are present in the time signal. These components are not detected in our 500 MHz bandwidth limited time-series. A detecting system, whose rise time is slower than the evolution time-scales of a signal performs a time averaging of the signal monitored. In a dynamical system a bandwidth filtered variable is still a relevant variable for the system [116]: a bifurcation present in the time averaged variable series is necessarily also present in the real-time variable series. The experimental observation of a bandwidth filtered intensity instead of the real-time intensity is equivalent to study a dynamical system where the variable $\int I(t)dt$ replaces $I(t)$. Since the time-scale of the time integrated variable is much slower than the real-time variable, the adiabatic elimination may be applied. In this way the dimensionality of the system is reduced. In terms of phase-space, the adiabatical elimination is equivalent to a projection of the full dimensional phase-space onto a lower dimensional space where the time averaged variable is relevant for the characterization of the flow.

More insights into the real-time variable are advisable in order to understand the physical origin of LFF-instability. The power spectra showed in Fig. 2.9 show frequency peaks up to 3 GHz, covering the whole frequency band at which the Avalanche Photodiode used is sensible. Further measurements with a Shottky photodiode reveals external-cavity peaks up to 22 GHz (Ref. [120]). Moreover, the fact that these peaks are very broad in the power spectra (Fig. 2.9), prevented us from using sampling high speed scope in order to detect them. As explained in

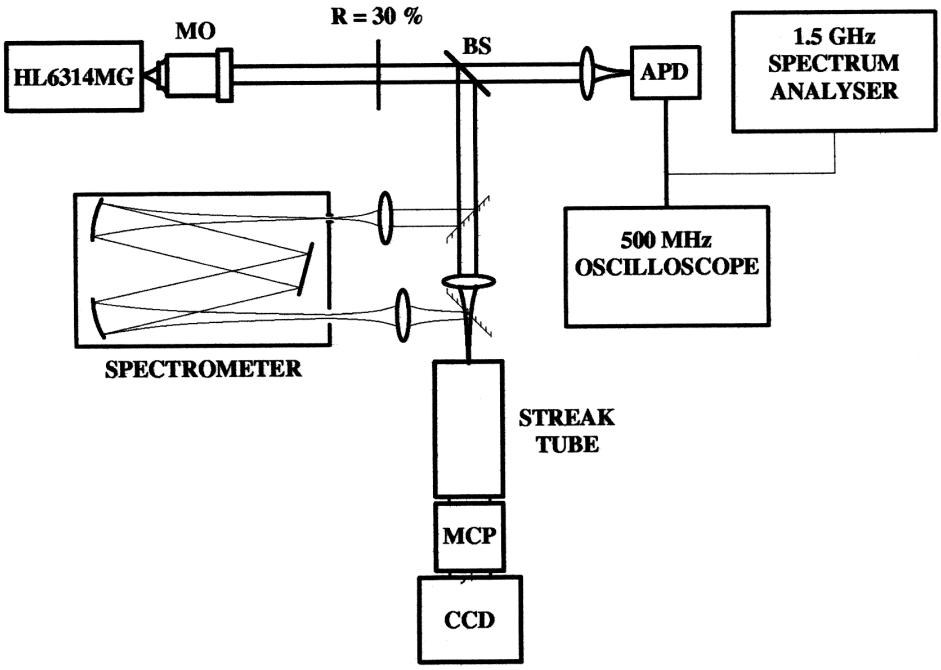

Figure 2.30: Experimental set-up

Appendix A the only possible solutions dealing with very fast non periodic signal is the streak-camera.

2.5.3 The streak-camera measurements

These measurements are performed on an $Hitachi^{TM}$ HL 6314MG laser emitting around 630 nm, with a mode spacing of $\approx$ 135 GHz and a threshold current of 24 mA. In Fig. 2.30 we show the experimental set-up.

An external mirror of 30% reflectivity, placed at a distance of 30 cm from the laser output (delay time $\tau = 2\ ns$), reduces the threshold of the laser down to 22 mA ($\approx$ 8% threshold reduction). Part of the output beam is sent to a 2 GHz bandwidth silicon avalanche photodiode. The photodiode signal is monitored with a digital oscilloscope (500 MHz analog bandwidth) and it can also be sent to a power spectrum analyzer (1.5 GHz bandwidth). The remaining portion of

the laser output is detected by a single-shot streak-camera system. This system is based on a streak tube with an S 20 photo-cathode having a radiant sensitivity of 20 mA/W at 630 nm and a $P-11$ phosphorus screen. A fiber-optics coupled gated image intensifier is used to intensify the output of the streak tube. The intensified image is detected with a two-dimensional, fiber coupled and thermo-electrically cooled CCD array. We operate the camera with different streak speeds, from about 4.5 ns/screen (16 ps time-resolution), to 65 ns/screen (230 ps time resolution), to monitor the laser output on different time spans. The time-resolution of the system and the linearity of the ramp at each speed are tested with a mode-locked Ti:Sapphire laser. In order to maximize the signal-to-noise ratio of our measurements, the input optics of the streak-camera is removed and the laser output is focused directly onto the photo-cathode. A CW $He-Ne$ laser is used to determine the minimum sensitivity of the streak camera. This test rules out any possibility that in our experiments the camera might have been operated below the level at which a continuous signal can appear as a sequence of pulses as a result of a low number of photo-electrons and a high intensifier gain (see Appendix A.4).

In Fig. 2.31 we show the total intensity as a function of time observed with the oscilloscope (a) and the streak-camera (b). In both cases we note that the average intensity increases steadily with time until it suddenly drops to a minimum value. We can also observe that in both cases there are fast intensity pulses, partially filtered in the oscilloscope trace by the limited bandwidth of the detection system. The streak-camera measurement shows that the pulses disappear immediately following the drop of the total intensity. These pulses exhibit a marked pseudo-periodicity at the round-trip time of the optical field in the external-cavity. However, there also exists pulsing at shorter time-scales which suggests the influence of higher frequencies. It must be noted that in the case

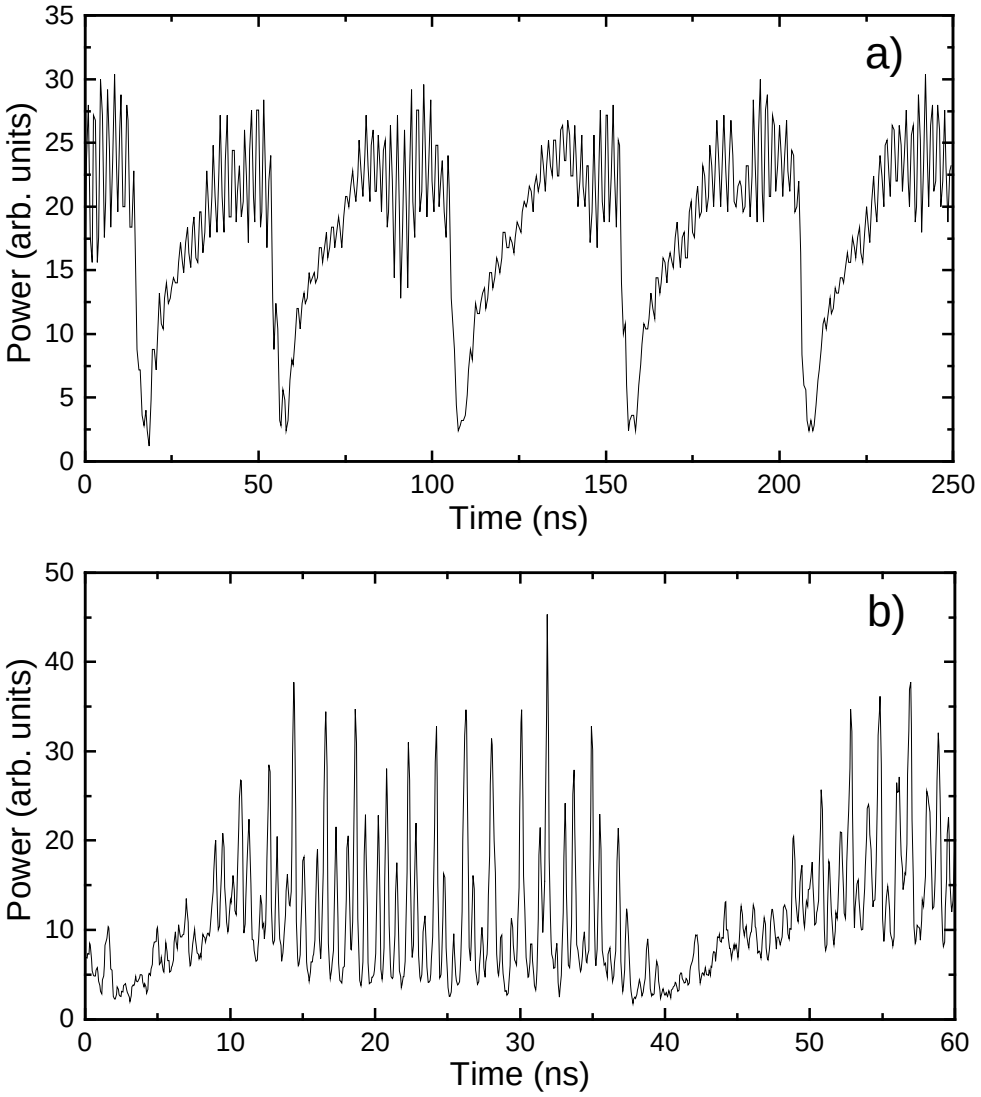

Figure 2.31: Total intensity as a function of time taken with a) the oscilloscope, and b) the streak camera with a time-resolution about 230 ps . Note the pseudo periodicity of the signal at the roundtrip time in the external cavity (~ 2 ns.)

of Fig. 2.31 we have chosen parameter values such that the period of the relaxation oscillations of the laser ($\tau_r \approx 2.5\ ns$) is longer than the delay time. Thus, the faster pulsing cannot be a consequence of undamped relaxation oscillations. We repeat the measurements for several values of injection current and feedback strength over hundreds of intensity drops in each case. As long as the system operated in the so-called LFF-regime, the above qualitative behavior remained unaltered even if the relaxation oscillation frequency is larger than the inverse of the delay time. However, the quantitative details change from one drop to another.

In Fig. 2.32 we show intensity traces covering time spans of 21 ns taken with time-resolution 70 ps (a-c) and time-spans of 4.5 ns and 16 ps time-resolution (d-f). Each trace corresponds to a different drop, and starts at different delay relative to the drop. These measurements confirm that up to our maximum time-resolution there is no underlying dynamics and that Fig. 2.31b illustrates the relevant behavior of the total intensity.

In order to analyze the origin of the pulsing occurring at shorter times than the delay time, we conduct spectral-resolved measurements. We place a 0.3 m grating monochromator ($Acton Research^{TM}\ VM503$) with a resolution of 0.5 Åin front of the streak-camera. Removing the output slit of the monochromator, we obtain a wavelength dispersed beam on the camera photo-cathode. In this way, we are able to record the time-resolved spectrum, with the horizontal axis of the streak image corresponding to wavelength, at the price of a lower signal-to-noise ratio due to the dispersion of the beam. The spectral resolution is $\sim 40\ GHz$, enough to clearly resolve the resonances of the internal laser cavity although insufficient to resolve the external-cavity resonances.

Fig. 2.33 displays typical time-resolved spectra in the LFF-regime taken with the streak-camera with a resolution of 230 ps in time. We clearly observe that

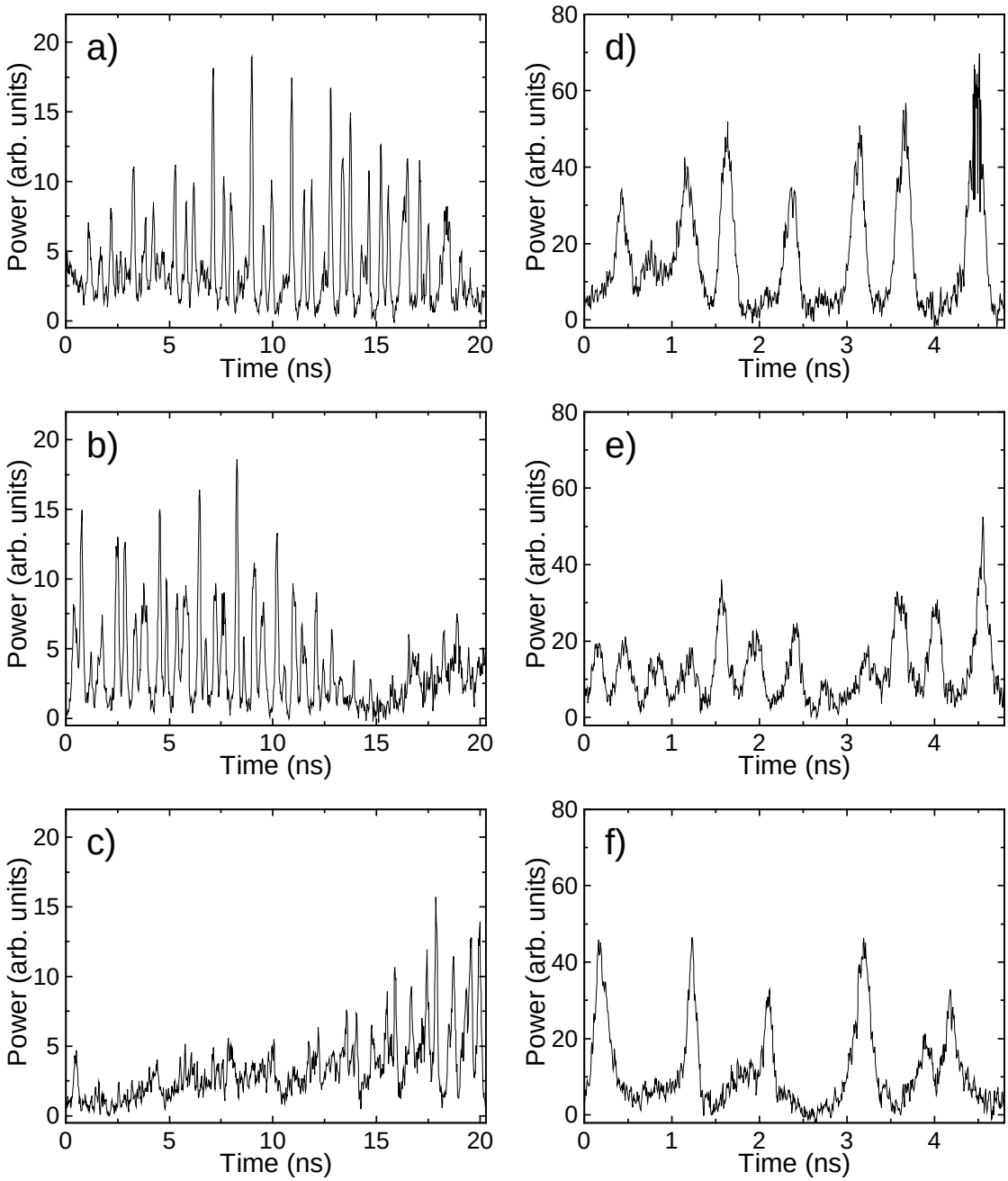

Figure 2.32: Temporal evolution of the total intensity taken with the streak camera over different time spans: a-c) 21 *ns* time-span, 70 *ps* time-resolution; d-f) 4.5 *ns* time-span, 16 *ps* time resolution. Different traces correspond to different drops, and the starting point relative to the drop is changing from one acquisition to the other.

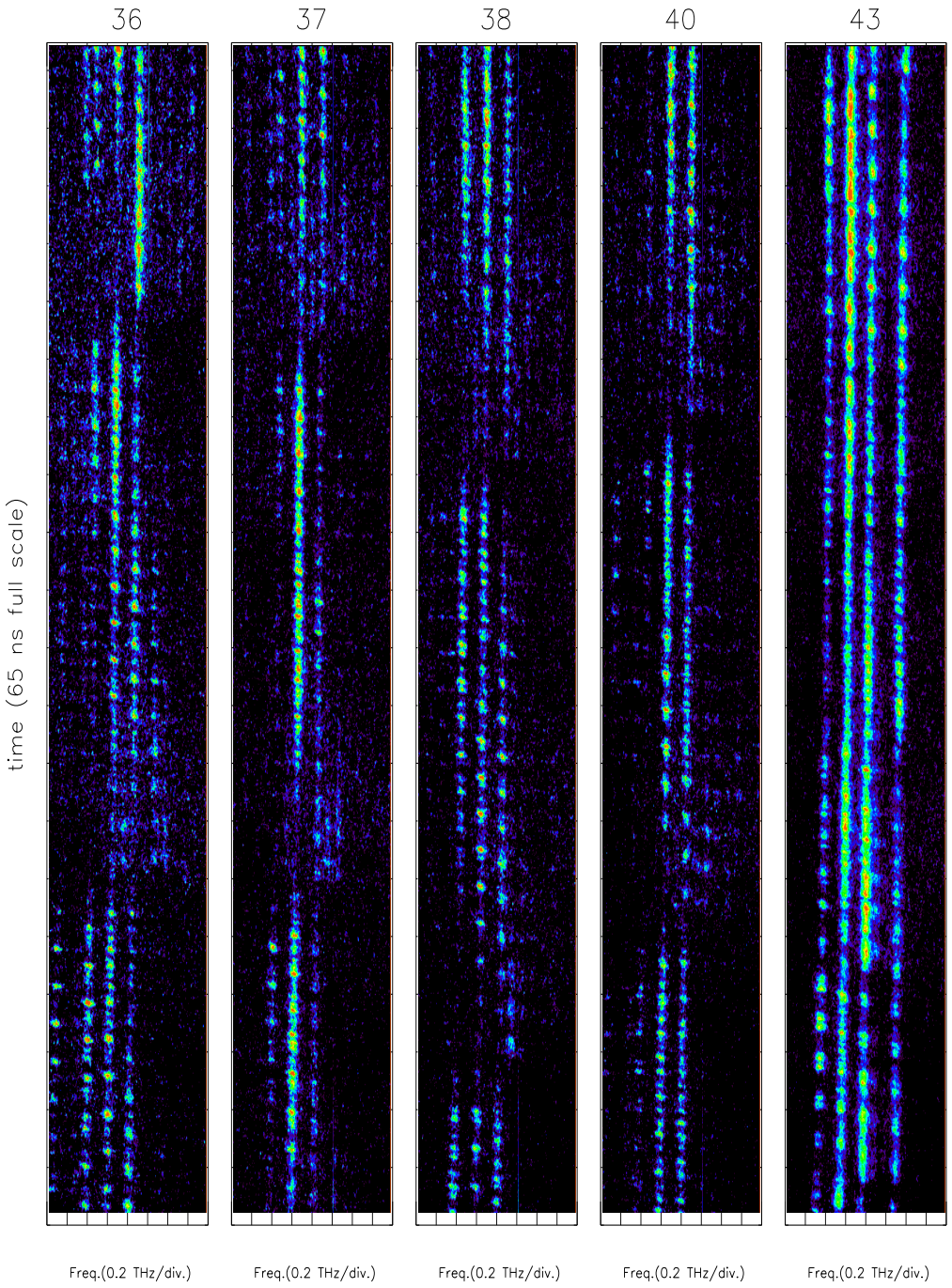

Figure 2.33: Typical streak images showing the time-resolved spectra in the LFF-regime (36,37,38,40) and in the fully-developed CC (43). The first four (from the left) time-resolved spectra are relative to the situation where LFF in the low-frequency time signal appear almost periodic (at a rate of 33.8 MHz). For the four images the current value (25.6 mA) and all the other parameter values are the same. The fifth image is relative to a current of 32.5 mA. The time span is 65 ns with a time-resolution of $\approx$ 230 ps , while the frequency resolution is $\approx$ 40 GHz. The time increases from bottom to top, the frequency from left to right, the power is plotted in false-color logarithmic scale, from purple (low power) to bright red (high power).

most of the time the system operates in multiple modes of the internal laser cavity, in agreement with the results of the last paragraph, and in general the dominant active modes are not consecutive ones. When a drop of the total intensity occurs (see times $\approx 5\ ns$ and $35\ ns$) all modal intensities are below the photo-cathode sensitivity. However after a delay of a few ns, we observe that several diode modes grow from the background. The modal evolution is controlled by the delay time, and until the next drop of the total intensity takes place there is a transfer of energy among these modes.

Important dynamical information can be gained from the analysis of the temporal evolution of the relevant modal intensities, shown in Fig. 2.34. Each mode is pulsing with a repetition rate controlled by the external-cavity round-trip time, but in general the phase of pulsation is different for different modes; in particular, the two dominant modes over a given time-interval operate with different phases. The origin of the oscillations can be understood as a partial phase locking of the external-cavity resonances within each internal-cavity resonance. Since the modal intensities are pulsing with arbitrary phases one relative to the other, the total intensity displays fast pulsing (which looks irregular because of the exchange of energy among the modes) around a non-vanishing average level, in agreement with Ref. [120]. The analysis also reveals that shortly after two or more modes synchronize their amplitudes to pulse in phase, a drop in the total intensity occurs as soon as the pulses are big enough (see lower trace in Fig. 2.34).

It is worth noting that in general, after each drop of the total intensity both the number of modes and the respective phase of the pulsing changes, and that the dominant modes just after the drop are not the dominant ones just before it. However, the repetitive feature is that a total intensity drop happens shortly after several modes start pulsing in phase.

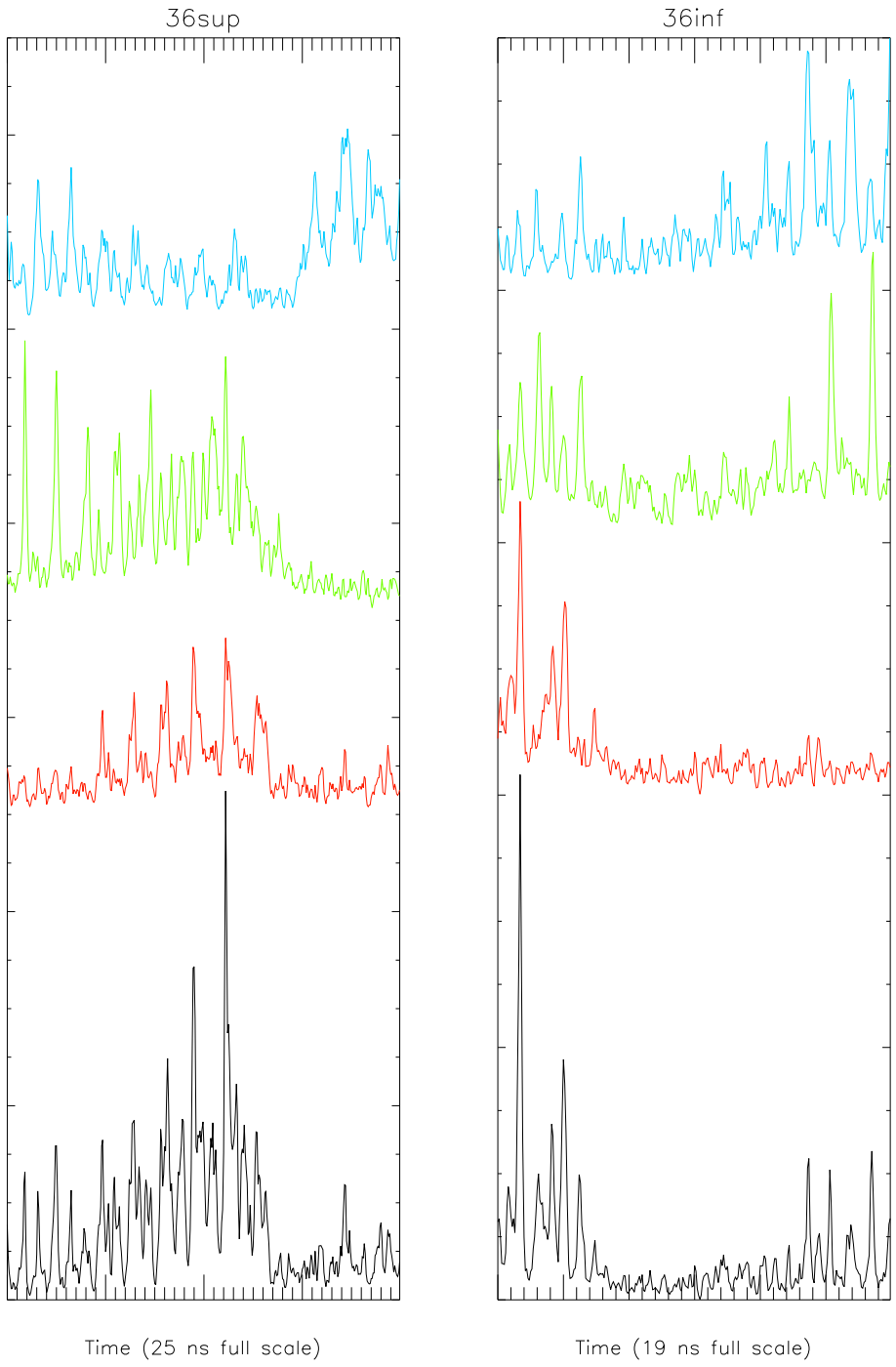

Figure 2.34: (a) Modal intensity traces for the dominant modes in the streak 36 of Fig. 2.33 for times around a Low-Frequency Fluctuation, inf. and sup. indicates which LFF of the streak (the first or the second) is resolved. Blue corresponds to the modes at lower wavelength, red to ones to at higher wavelength. The black trace at the bottom corresponds to the modal correlation, defined as the product of the modal powers above the background level.

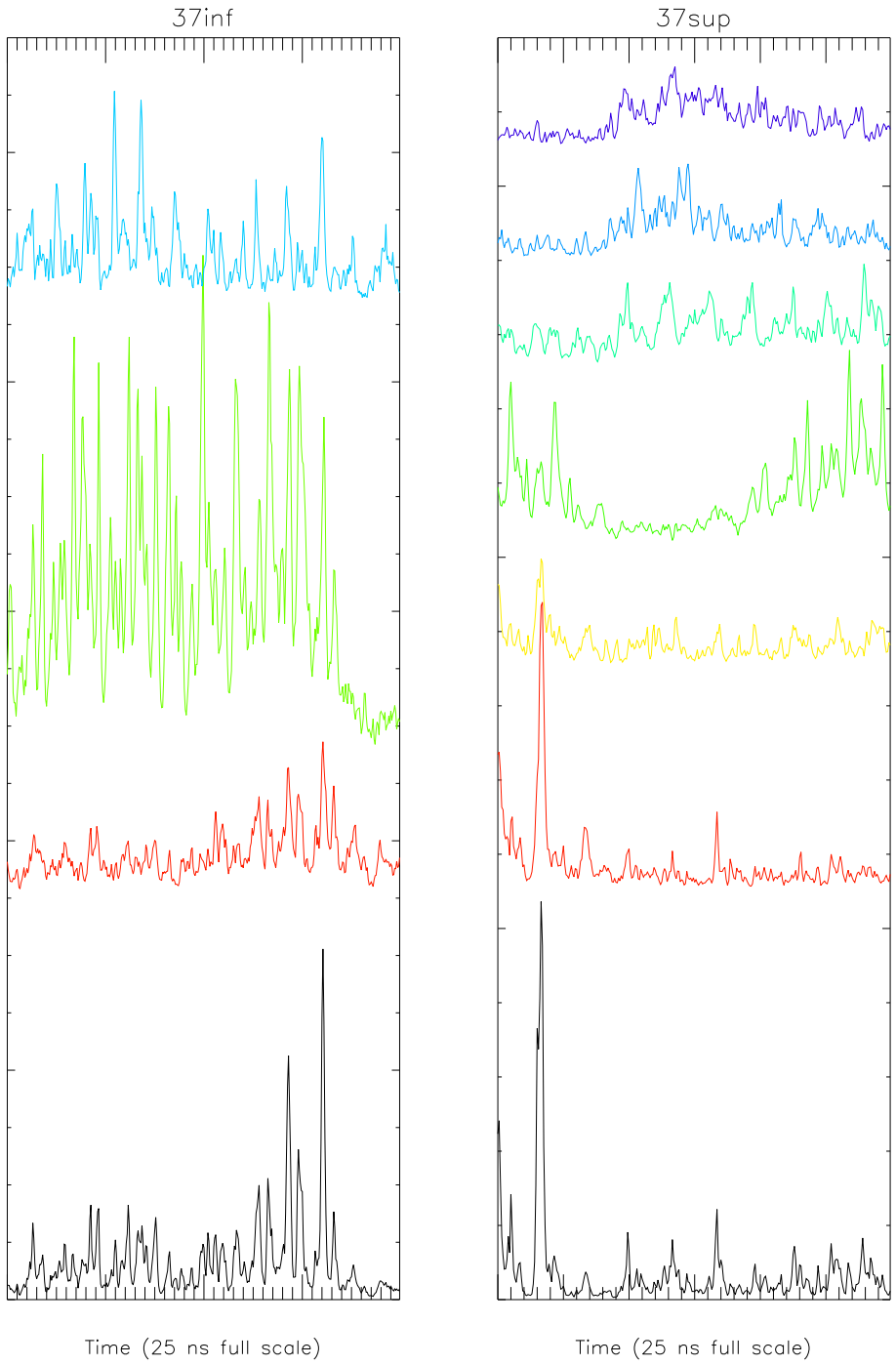

Figure 2.34: (b) Modal intensity traces for the dominant modes in the streak 37 of Fig. 2.33 for times around a Low-Frequency Fluctuation, inf. and sup. indicates which LFF of the streak (the first or the second) is resolved. Blue corresponds to the modes at lower wavelength, red to ones to at higher wavelength. The black trace at the bottom corresponds to the modal correlation, defined as the product of the modal powers above the background level.

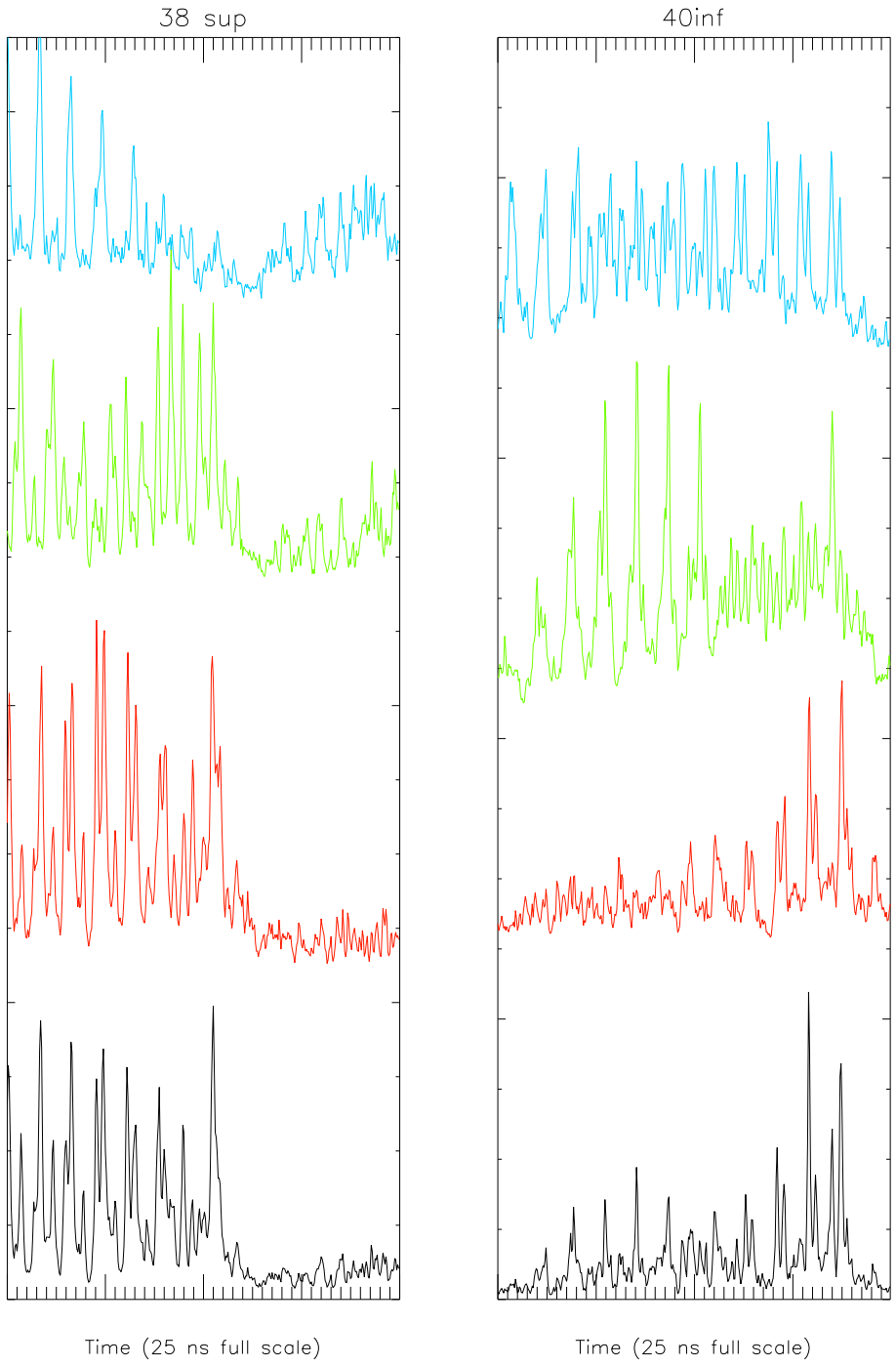

Figure 2.34: (c) Modal intensity traces for the dominant modes in the streaks 38 and 40 of Fig. 2.33 for times around a Low-Frequency Fluctuation. The number on each panel indicates the streak number of Fig. 2.33, inf. and sup. indicates which LFF of the streak (the first or the second) is resolved. Blue corresponds to the modes at lower wavelength, red to ones to at higher wavelength. The black trace at the bottom corresponds to the modal correlation, defined as the product of the modal powers above the background level.

As the injection current is increased, the intensity drops become more frequent, and finally the signal in the oscilloscope looks almost random. This situation is the commonly called fully-developed Coherence-Collapse regime (CC), Fig. 2.33(e). In the CC regime, the signal observed with the streak-camera does not show qualitative differences as compared to the LFF case, although now the signal fluctuates strongly at all times. In fact, the time-resolved spectrum in the CC regime does not show any "dark periods" where all modes are below the sensitivity limit of the streak-camera. In addition, it appears that the different modes are no longer synchronized, as was the case in the LFF-regime.

The above results disclose that the interaction between the resonances of the internal-cavity is at the origin of the total intensity drops. It is worthwhile noting that the operating modes are usually not consecutive ones, as it occurs with the multi-mode instabilities in laser theory (see first chapter or the Refs. [121]). A physical interpretation can be based on a typical multi-mode laser instability. The system is essentially controlled by the delay time, which fixes a resonance frequency at τ^{-1}. For one laser mode, the external-cavity-modes tend to lock in phase during the build-up of the average total intensity, thus leading to pulses. If the delay is long enough the active material can recover before the next pulse is generated, and another laser mode is able to operate and it will grow from noise. The external-cavity-modes inside the bandwidth of this "new" operating mode tend also to lock in phase, but their locking phase will in general be different from that of the previously existing mode. In this way several electro-magnetic modes are able to operate but their non-linear coupling leads to an instability which gives origin to the drop of the total intensity and to fast variations of the material properties like refractive index. As a consequence, there is a shift in frequency and later operation at other unrelated laser modes. The process then initiates again.

In conclusion, the fast pulsing observed in the total intensity with the streak-camera is due mainly to the superposition of the intensities of different longitudinal laser modes and, for each mode, to a phase locking process of the external resonances. The intensity drops are the result of a multi-mode instability and the total intensity value is generally above the spontaneous-emission level. The non repetitivity of the signal from drop to drop leaves unanswered the question about the role of noise and the deterministic character of this particular system. Heuristically we can say that the whole process seems to be dominated by noise. However, the instability giving rise to each drop leads to a short stage of determinism during the recovery, but it is difficult to establish an unambiguous conclusion about the role of noise by just measuring the intensity and operation frequency of the laser.

2.6 Theoretical models

2.6.1 The Lang-Kobayashi model

In the literature about LFF the most commonly model used is the Lang-Kobayashi model (Ref. [16]). This theoretical approach was originally developed for a single-mode semiconductor laser (DFB laser) and weak feedback levels (region I and II of Fig. 2.4). The temporal evolution of the complex amplitude of the electric field coupled to the carrier density is described by semiconductor laser rate-equations 1.2.28. The effect of the optical feedback is included in its first approximation by means of the re-injection of the field itself with a time delay corresponding to an external-cavity round-trip. The influence of this feedback term on the rate-equations is to couple the modulus and the phase of the electric field. The Lang-Kobayashi equations read:

$$\frac{dE}{dt} = \frac{(1+i\alpha)}{2}(G-\frac{1}{\tau_p})E + \digamma E(t-\tau)e^{-i\omega_0\tau} + R \qquad (2.6.1)$$

$$\frac{dN}{dt} = J - \frac{N}{\tau_s} - GE^2 \qquad (2.6.2)$$

τ_s is the carrier lifetime, and τ_p is the photon lifetime. ω_o is the solitary laser frequency. The optical gain is $G = G_N(N-N_o)/(1+\epsilon E^2)$, where G_N is the modal gain, N_o the carrier density at transparency, and ϵ the gain saturation coefficient. α is the linewidth enhancement factor, J is the current density, $\digamma$ is the feedback rate and R is the rate of spontaneous-emission into the lasing mode. The weak feedback approximation means $\digamma << 1$, otherwise all the multiple delays terms of the re-injected field have to be considered. Lang-Kobayashi model describes well the experimental results obtained for weak feedback level (Refs. [101, 16]).

In spite of their limits, Lang-Kobayashi equations have been applied almost universally in the literature, to all the feedback regimes and, in particular, to LFF-regime (Refs. [17, 19]).

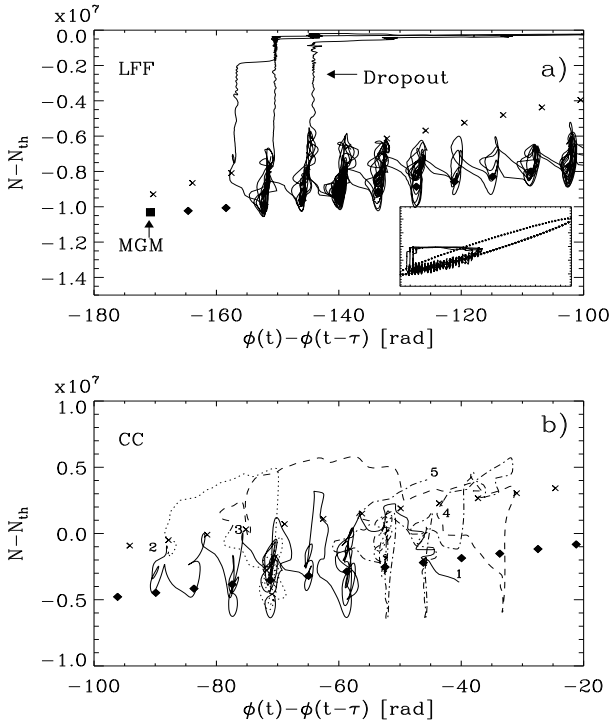

Figure 2.35: Evolution of the trajectory in phase-space for LFF (a) and CC (b). Diamonds denote cavity modes and antimodes. The mode with maximum-gain is denoted with a square. The system evolves towards the maximum-gain mode passing very close to the antimodes and almost reaching the unstable manifold of the saddle generating a drop out event, In the CC regime chaos and antimode dynamics compete. From: J. Mulet C. Mirasso, Phys. Rev. E **59**, 5400, (1999)

Figure 1:Mulet & Mirasso

From the numerical integration of the Lang-Kobayashi model, it has been shown that the laser power exhibits drops similar to those experimentally observed at low-frequency (Refs. [17, 19]). In these simulations a low pass filter was included in order to describe the bandwidth of the detectors commonly used in the experiment. Without any filtering the numerical experiment exhibits strong irregular picosecond light pulses at a rate associated with the relaxation oscillation frequency, typically of a few GHz (Ref. [19]). According to these simulations LFF originate from a deterministic chaotic attractor which encompasses a large number of unstable fixed-points, either saddle-node points or foci (Ref. [17]). This chaotic attractor coexists with one or more stable fixed-points. The trajectory, if in the chaotic attractor, wanders in phase-space around the foci until it approaches a saddle (Fig. 2.35). The collision with a saddle gives rise to a large, fast excursion in phase-space until the evolution recovers towards the foci.

Since this process lasts for several delay times, it generates a long-time-scale dynamics which contributes to the lower part of the spectrum, and it was called *chaotic itinerancy with a drift* because it involves a drift in the laser frequency. The numerical intensity pulses departing from zero intensity level come from the wandering of the system around the foci; the amplitude grows steadily until the collision with a saddle takes place leading to a sudden reduction of the intensity (Ref. [19]).

A first experiment using a single shot streak-camera was performed in order to avoid the low pass filtering of the common detector (Ref. [122]). By comparing the experimental time-series with the numerical ones, the authors concluded the correctness of the Lang-Kobayashi model. However, no information was given about either the location of the picture experimentally taken with respect to the power-dropout or the relation between the amplitude of the fast pulses and the average power. Indeed, from these measurements it is difficult for the reader to conclude the validity of the model. Moreover, further statistical measurements of the intensity distribution with a sampling oscilloscope have shown that the fast fluctuations in general take place around an average intensity value different from zero (Ref. [120]), thus disagreeing with the model.

Our streak-camera measurements provides a more complete experimental picture on the fast pulses observed in Ref. [122]. We have shown, by zooming out from the maximum resolution time span, that this pulses are not randomly occurring in time. They do have a periodicity related to multiples of external-cavity round-trip time. Moreover, the pulsing occurs around a non-vanishing average level, in agreement with Ref. [120].

In our time-resolved optical spectra measurements we have shown that the pulses in the total intensity come from different internal-cavity-modes. At each LFF there is no mode following the total intensity and the number of modes

involved, as well as their dynamics changes widely at every drop. We have also shown that the LFF appears in correspondence of the synchronization of the modal pulsing.

These experimental observations cannot be explained within a single-mode Lang-Kobayashi model, but, instead, they require a description which takes into account the multi-mode character of the solitary laser.

2.6.2 The Duarte-Solari analysis

In a recent work (Refs. [123, 124]) Duarte and Solari analyzed the problem of the optical feedback in semiconductor lasers as a problem of double-cavity boundary conditions. The external optical feedback is then naturally included as a consequence of the boundary conditions, fixed by the external mirror and by the the laser facets. Moreover the semiconductor medium is described in its full spatial extension, hence allowing for multi-longitudinal-mode operation. Therefore they avoid the assumption of single-mode operation and they overcome the inclusion of the external mirror as a perturbative term in the solitary laser rate-equations. The Duarte-Solari analysis considers the complete problem of a double cavity system where one cavity is the solitary semiconductor laser and the second is the external one ($L \gg \ell$) delimited by the external mirror of power reflectivity R. Such a general approach allows for determining the limits of validity of Lang-Kobayashi equations. Two limit cases are evident in the double cavity approach: i) the case with no external mirror ($R = 0$), where the modal solutions of the system are spaced by $\Delta\omega \approx c/(n\ell)$ (being n the refraction index of the semiconductor medium); ii) the case where $R = 1$, where the distance between the modes solutions is $\Delta\omega \approx c/L$. The equations considered in Ref. [123] for the semiconductor media are similar to the one introduced in Ref. [20] and described in the first chapter of this thesis 1.2.33, called *Effective two levels* Maxwell-Bloch

equations. The diffusion terms in 1.2.33 is considered large enough to neglect the spatial dependence of the carrier density, this allows for assuming $N(x,t) = N(t)$. The boundary conditions are written considering the active medium located at $0 \leq x \leq \ell$, while the external mirror is placed at $x = -L$. Then, writing the field, for $x \leq 0$, as $E(x,t) = A_+(ct - x) + A_-(ct + x)$:

$$\begin{aligned} E(l,t) &= 0 \\ \partial N(x,t)/\partial x \mid_{x=\ell} &= \partial N(x,t)/\partial x \mid_{x=0} \\ \lim_{\epsilon \longrightarrow 0} E(-\epsilon, t) &= \lim_{\epsilon \longrightarrow 0} E(\epsilon, t) \\ \lim_{\epsilon \longrightarrow 0} \partial E(x,t)/\partial x \mid_{x=-\epsilon} &= \lim_{\epsilon \longrightarrow 0} \partial E(x,t)/\partial x \mid_{x=\epsilon} \\ A_+(ct + L) &= -RA_-(ct - L) \end{aligned} \tag{2.6.3}$$

The first condition is due to the fact that the mirror in $x = \ell$ is assumed to be a perfect mirror, the second is because the carrier cannot leave the semiconductor, the third and the forth are the continuity conditions for the electric and magnetic fields, the fifth is the boundary condition at the external mirror of reflectivity R. The parameter choice is $\omega_g = 2 \times 10^{15}\ Hz$, $\Gamma = 0.4$, $1/T = 10^{13}$, $\ell = 300\mu m$, $L = 35\ell$. The monochromatic solutions can be found proposing:

$$E_j(x,t) = exp(-i\omega t)[A_j e^{(ik_j x)} + B_j e^{(-ik_j x)}] \tag{2.6.4}$$

where $j = 0$ indicates the external-cavity region and $j = 1$ the active media.

The eqts. 1.2.33 with the boundary conditions 2.6.3 and the ansatz 2.6.4 are resolved at the steady-state by a recursive algorithm. In Fig. 2.36 we plot the complex wave vector k_1 allowed for different values of R. To every contour line it corresponds a value of R, increasing from $R = 0$ (points) to $R = 1$ (real axis). In Fig. 2.37 we plot the stationary solutions in the space Carrier density, frequency.

For $R = 0$ we obtain the solitary-laser-modes (Fig. 2.37, top). For $R \neq 0$ new solutions ("islands"), clustered around the solitary laser solutions, appear

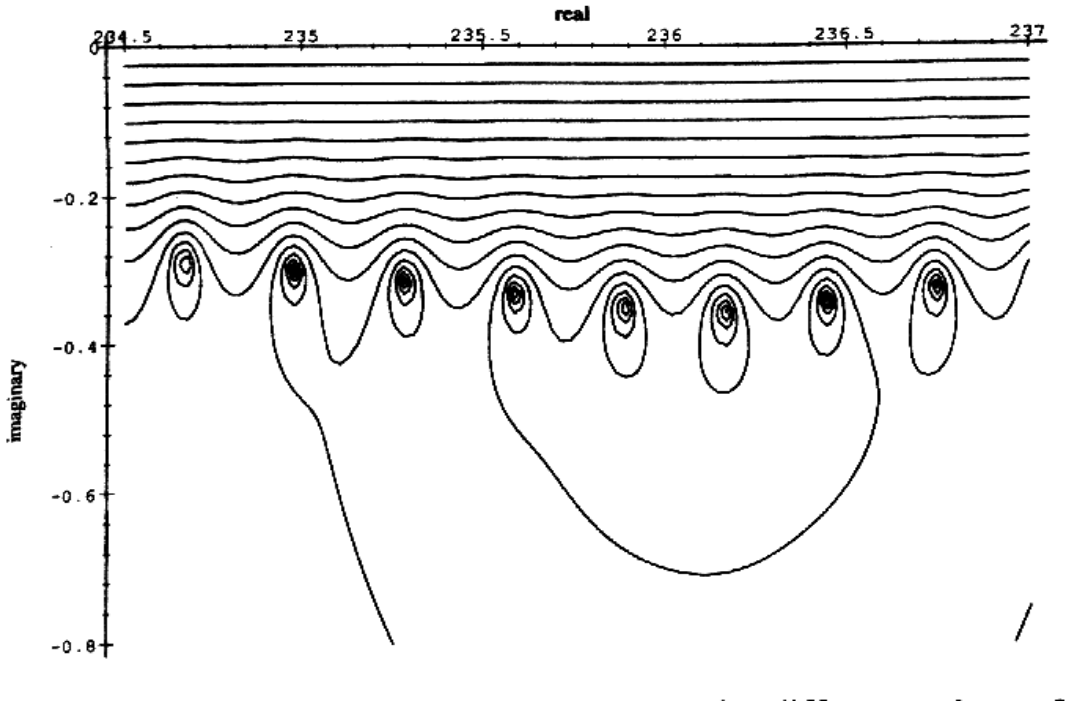

Figure 2.36: Complex wave vector k_1 allowed for different values of R. Contour lines are labeled by R and increase from $R = 0$ (points) to $R = 1$ (real axis). From Ref. [123]

(Fig. 2.37, center). These solutions are created through saddle-node bifurcations as R is increased. Their frequency separation depends on the ratio L/ℓ. The island emerging from each stable solution of the solitary laser corresponds to the solutions found in the Lang-Kobayashi equations. Increasing the feedback level these islands get larger and finally they start to merge into one (Fig. 2.38, top) for low frequencies while, for high frequencies, they still look like islands. Finally, for $R > 0.011$, the spectrum of the monochromatic modes is represented by a single wavy line and the islands have disappeared (Fig. 2.37, lower panel). In Fig. 2.38 we plot a transitional case ($R = 0.01048$ - $R = 0.01055$) showing the merging process between islands. The result of this analysis shows that these changes, increasing R, are beyond the possibilities of Lang-Kobayashi equations since they require the interaction in bifurcations of solutions coming from different solitary-laser-modes, neglected in Lang-Kobayashi. This analysis reveals that Lang-Kobayashi equations are only valid for weak feedback level, but they are

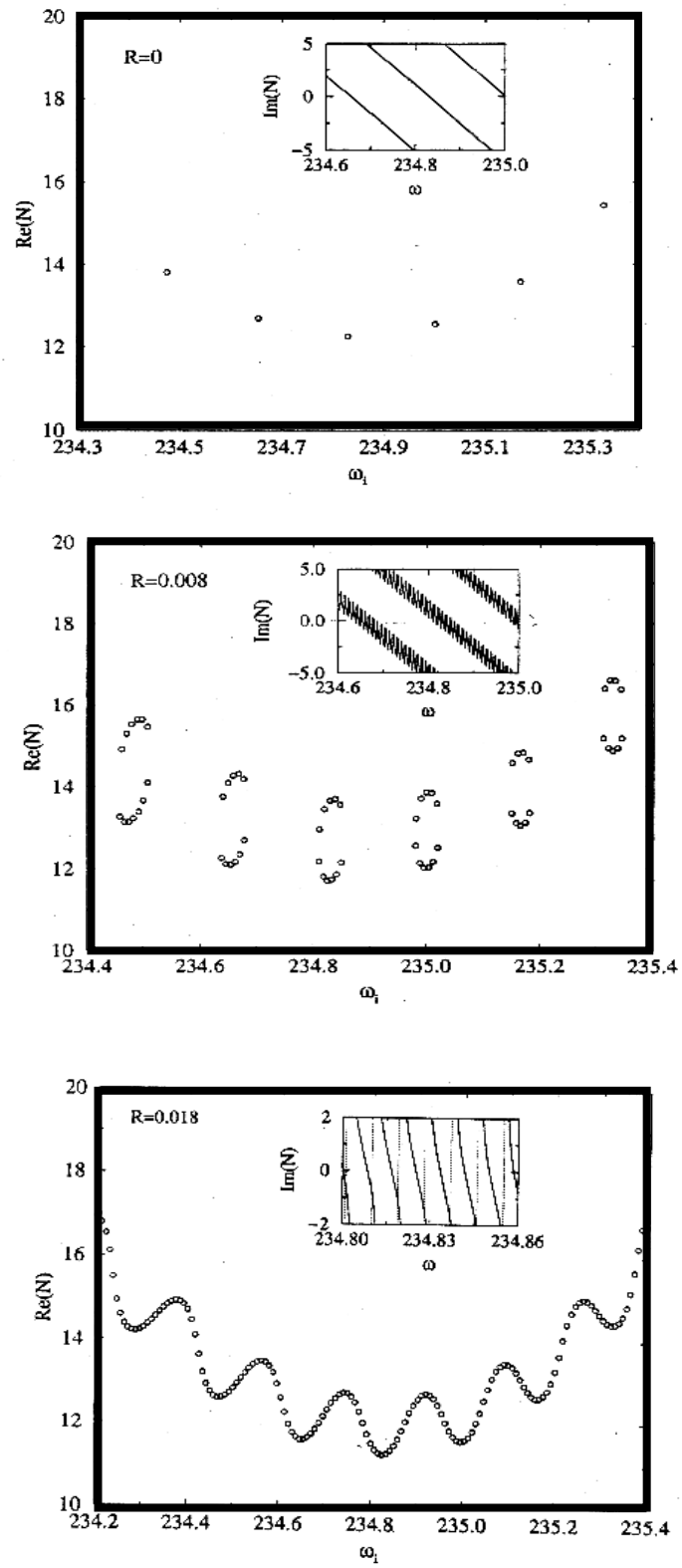

Figure 2.37: Carrier density vs. frequency for the laser with different reflectivity external mirror (from top to bottom: $R = 0$, $R = 0.008$, $R = 0.018$). Inset: the frequencies of the monochromatic modes correspond to the intersection of the lines $Im(N(\omega))$ with the ω axis. From Ref. [123]

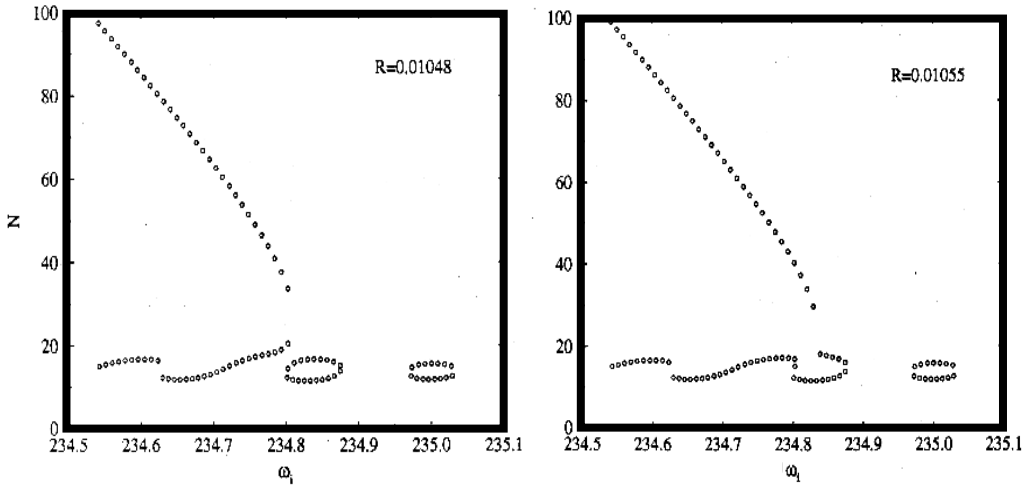

Figure 2.38: Carrier density vs. frequency for the laser with different reflectivity external mirror (from top to bottom: $R = 0.01048$, $R = 0.01055$). From Ref. [123]

unable to describe what happens for $R > 0.011$, when "islands" from different solitary-laser-modes start to merge together.

The stability analysis of the stationary solutions is analyzed in Ref. [124]. In this paper Solari and Duarte describe how the stability is affected by the main parameters (pumping current, feedback level, external-cavity length).

For $J = 40$ and for $R = 0$ the threshold mode is always stable while the others are unstable in one or several directions. For $R = 0.002$ a pair of new modes are created through a saddle-node bifurcation. The two modes with lowest N are stable while the others are unstable. Further increasing R, we have that in the transitional case ($R = 0.01055$) the solution with maximal gain and the two neighboring solutions are stable, but their stability has weakened.

In Fig. 2.39 we show the eigenvalue spectrum of a mode which is unstable for $R = 0.002$. As R increases several eigenvalues approach the imaginary axis and, eventually, they take positive values for the real part (Fig. 2.39, lower panel). Moreover, the difference in the imaginary part between consecutive eigenvalues suggests they can be related to external-cavity-modes, though it is not formally correct to distinguish between external and internal-cavity-modes. In the spectrum of a solution, the presence of an eigenvalue λ with positive real

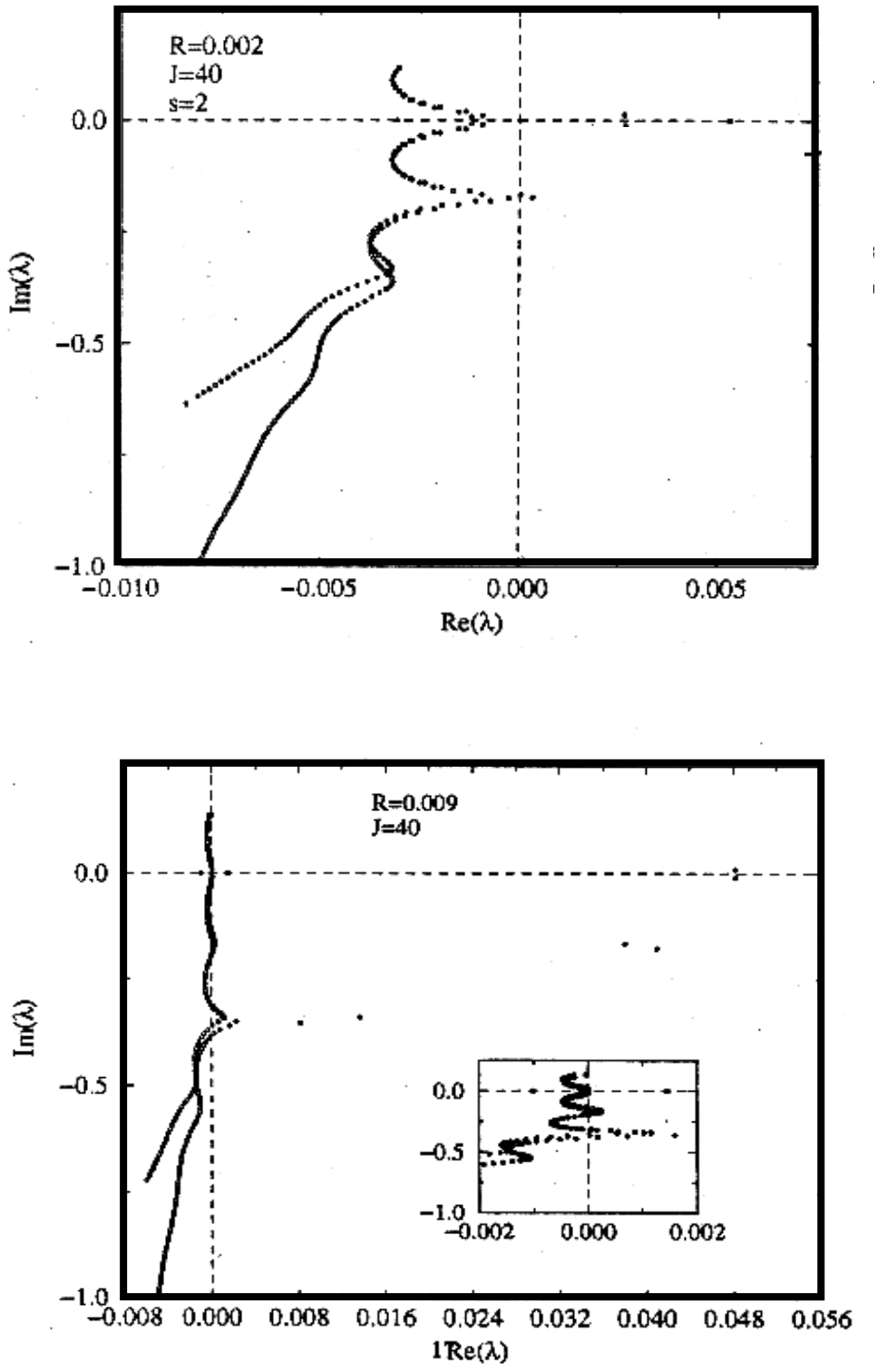

Figure 2.39: Eigenvalue spectrum for an unstable mode for different reflectivity: (top) R=0.002, (bottom) R=0.009. From Ref. [124]

part ($\Re(\lambda) > 0$) means that it exists a perturbation of a certain spatial dependence for which the solution is unstable and for which undamped oscillation at the frequency $\Im(\lambda)$ develops in the system (see chap. 1.1). Then, Fig. 2.39 says that there is a growing number of electrical field spatial structures which may excite undamped oscillation in the mode analyzed. It is worthwhile to notice that these frequencies are grouped in sets whose separation is equal to the separation between solitary-laser-modes. For $R = 0.009$ three clearly separated sets of unstable directions differing in the magnitude of the excitation frequency are observed. Again, the frequency separation between the three sets is equal to the separation between solitary-laser-modes.

For the values of R at which it has been observed the transition between island and merged solutions, the spectra of the solutions depend strongly on the value of N. The solutions with low carrier density are weakly unstable, for moderate N the spectrum is still wavy and the number of unstable directions and the strength of the instability has increased. Finally, for large N the solutions are strongly unstable. Further increasing R beyond the transition value makes that only the solutions corresponding to local minima of the curve N vs. ω (see Fig. 2.37) are stable. The most unstable solutions are the ones located at the local maxima of the same curve.

Solari and Duarte explored also the effect of the pumping current. Here we resume the effect of changing the pumping current on the most unstable eigenvalue of the threshold mode (Fig. 2.40).

For $R = 0$, increasing J affects the stability of the threshold mode lowering the real part and shifting the imaginary part of the most positive real part eigenvalue. These variations are smooth and monotonous with increasing the pumping current.

For $R = 0.009$, $\Re(\lambda)$ vs. J shows a peaked, non monotonous structure. The $\Im(\lambda)$

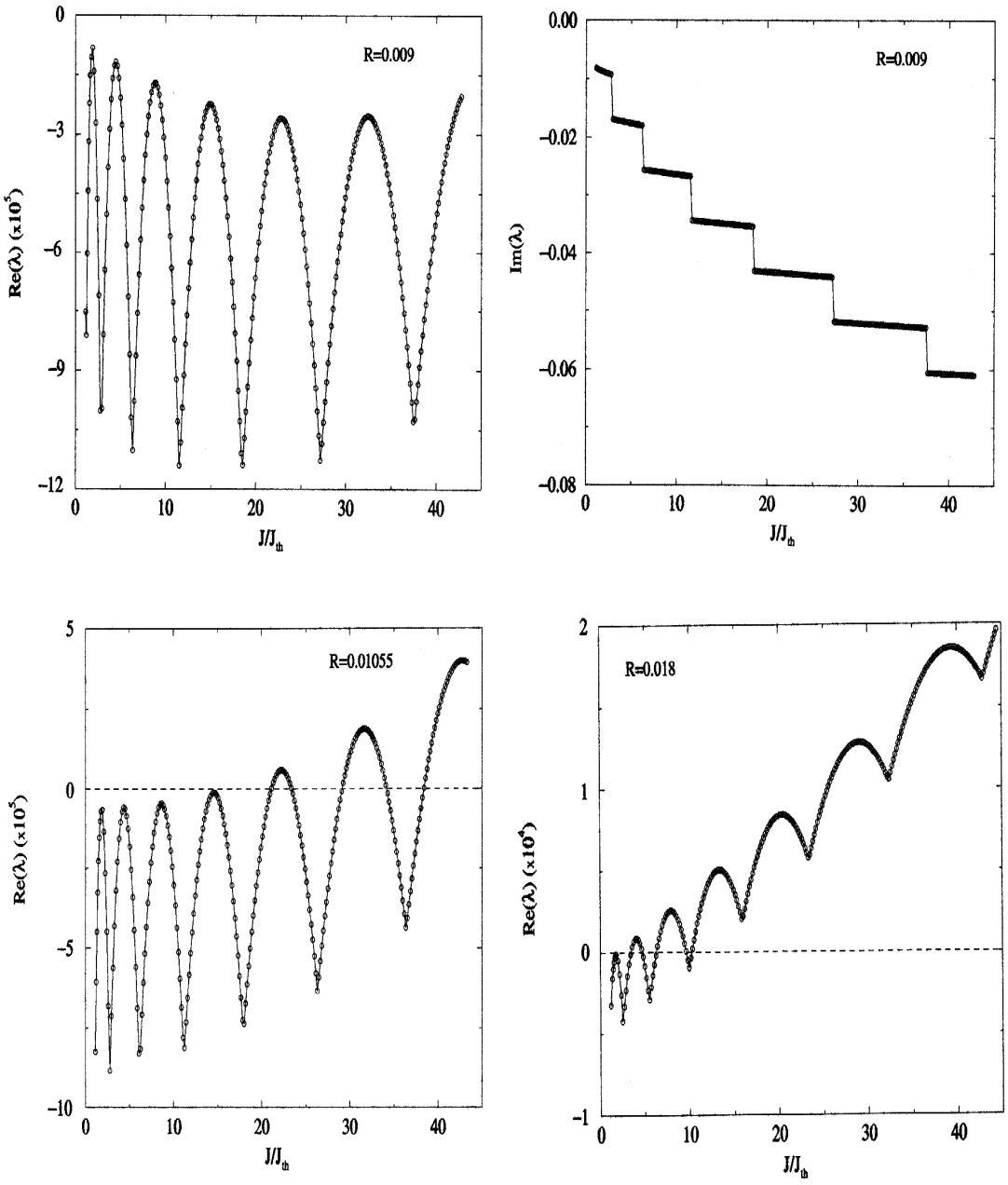

Figure 2.40: Upper panel: (left) Real part of the marginally stable eigenvalue of the threshold mode as a function of J with ($R = 0.009$), (left) corresponding imaginary part. Lower panel: Real part of the marginally stable eigenvalue of the threshold mode as a function of J with ($R = 0.01055$) (left) and once the metamorphis of the spectrum has taken place ($R = 0.018$) (right). From Ref. [124]

vs. J curve shows that, corresponding to each ripple in $\Re(\lambda)$, there is one value for $\Im(\lambda)$. Jumping from one ripple to the next one, as J is increased, there is a jump of the value of $\Im(\lambda)$ equal to the external-cavity-mode separation. In other words, as J increases, the most unstable mode is jumping from one external-cavity resonance to the next one. For $R = 0.009$ the lasing mode remains stable, since $\Re(\lambda) < 0$.

For $R = 0.01055$ the curve of $\Re(\lambda)$ vs. J maintains its ripple structure, but now there is a value of J (≈ 30) for which the lasing mode looses its stability. There are regions of J where the mode undergoes a Hopf-instability and suddenly the system exhibits an oscillation at frequency equal to $\Im(\lambda)$. This Hopf-instability marks the starting point of a possible sequence of instabilities which eventually leads to more complicate dynamical states.

For $R = 0.018$, after the metamorphosis the above effects are significantly stronger and the lasing mode is destabilized for smaller J.

It worth noting that, since $\Re(\lambda)$ may become very small as the pumping current is increased, the lasing mode becomes weakly stable. In this situation the presence of noise in the system (spontaneous-emission) may anticipate the instability, as argued from our experiment. Then, J controls the relevance of the noise, since it changes the degree of stability of the mode. Moreover, since the system may develop undamped oscillation on a wide range of frequencies (containing several free spectral ranges of the internal-cavity), the dynamics will involve the excitation of a great number of laser cavity modes.

The Solari-Duarte analysis determines a maximum feedback level for which the Lang-Kobayashi model is still valid. This limit ($R \approx 0.01$) is much smaller than the feedback ranges where Low-Frequency Fluctuations appear. Lang-Kobayashi stationary states, organized as separated islands of external-cavity-modes, each one centered around the relative internal-cavity-mode, are recovered

for $R < 0.01$. Above this limit, Solari-Duarte model shows that these islands merge together through bifurcations involving solutions coming from different internal-cavity-modes islands. The stability analysis shows that, as J is increased, the lasing solution becomes unstable versus perturbations having different longitudinal spatial structure. Undamped oscillations may develop at frequencies separated by an amount corresponding to the internal-cavity free spectral range. It would be extremely interesting to analyze the dynamics predicted by Solari-Duarte model, unfortunately numerical simulations of these equations have not been performed yet. Anyway, our experimental results seem to confirm heuristically many peculiarities emerging from this analysis: the role of the solitary laser cavity modes in destabilizing the laser solution, the importance of the noise level in the trigger mechanism of the instability, the weak stability (or the instability), of the lasing solution versus perturbations corresponding to a wide number of internal-cavity-modes which determines, together with noise, a modal dynamics deeply irregular and very rich in the number of modes involved.

2.7 The frequency-selective feedback

We have shown that Low-Frequency Fluctuations are strongly related to the excitation of several longitudinal laser modes. A straightforward modification for improving the stability of the system is to replace the external mirror by an optical grating. The presence of a wavelength dispersive element implies a frequency filtering for the re-injected field, possibly limiting the bandwidth of the optical feedback to only one internal-cavity-mode. In this configuration multistability between modes of the external-cavity was theoretically and experimentally reported in Refs. [125, 126]. The macroscopic behavior of such system in terms of tunability and reduction of the spectral width was studied in Refs. [127, 128]. We analyze experimentally the system dynamics as a function of three control parameters: feedback strength, pumping current and detuning between the re-injected frequency of the grating and the resonant frequencies of the laser cavity. We find bistability in the laser operation both below and above the solitary laser threshold. In the last part we sketch a model able to describe our experimental system, and we give an heuristic interpretation of the observed instabilities.

2.7.1 Experimental results

In order to achieve strong feedback levels we use an $Hitachi^{TM}$ HLP 1400 partially AR-coated ($\lesssim 1\%$) on the facet exposed to feedback (Fig. 2.41). A holographic grating (1800 lines/mm, efficiency $\approx$ 90 % at Littrow angle) is placed at 0.5 m from the laser in Littman-Metcalf configuration. This configuration allows, without using a beam expander, to match completely the surface of the grating in order to reach the highest resolution uncoupled from mirror tilting (detuning). We maximize the resolution (18 GHz) of the grating fixing it at an angle of 5° with respect to the incident beam. The first order is sent to a 95% reflectivity mirror which closes the external-cavity and allows the frequency tunability of

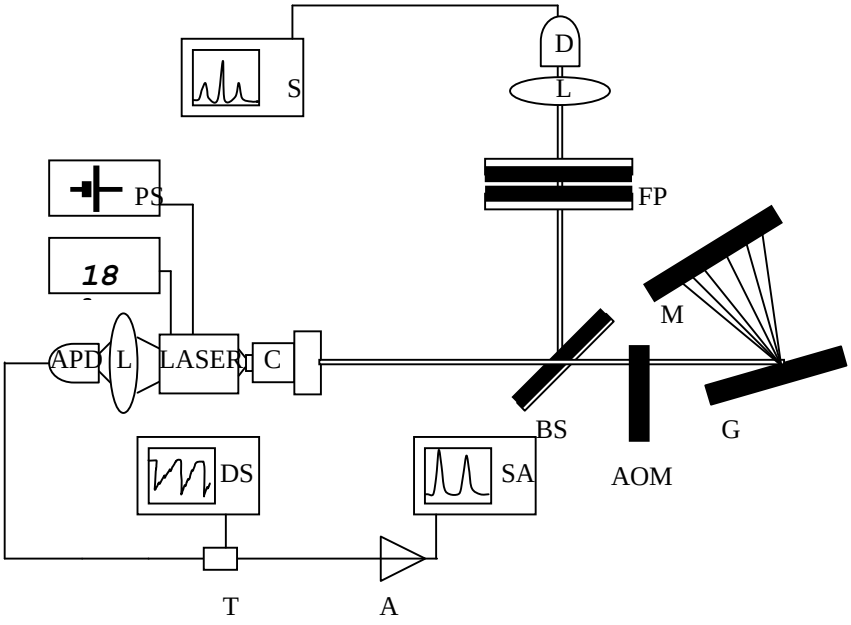

Figure 2.41: Experimental set for the laser with frequency-selective feedback. L lens, S scope, PS power supply, FP Fabry-Pérot interferometer, APD Avalanche Photodiode, C collimating lens, BS beam splitter, AOM acousto-optic modulator M mirror, DS digital scope, SA spectrum analyzer, A microwave amplifier, T T-coupler, G grating

the system. Part of the output beam is reflected into a scanning Fabry-Pérot analyzer (600 GHz Free Spectral Range and finesse of 100) to check the spectral characteristics of the laser output. The remaining elements of the set-up are the same used in the set-up of Fig. 2.1.

The laser without optical feedback has a threshold of 80 mA and it operates multi-longitudinal-mode up to currents of the order of 100 mA. It works primarily in two modes when the current is between 85 mA and 100 mA.

Our frequency-selective element allows, when effective, to select just one single solitary-laser-mode. A single-mode operation of the system depends on two main parameters: the feedback level and the detuning of the frequency selected by the grating with respect to a solitary laser cavity resonance.

We define this detuning in the range $[0, \frac{c}{2\ell}]$, being ℓ the laser cavity length, and we take always as reference the nearest-blue located solitary-laser-mode. This definition is due to the periodicity of the system behavior when the above defined

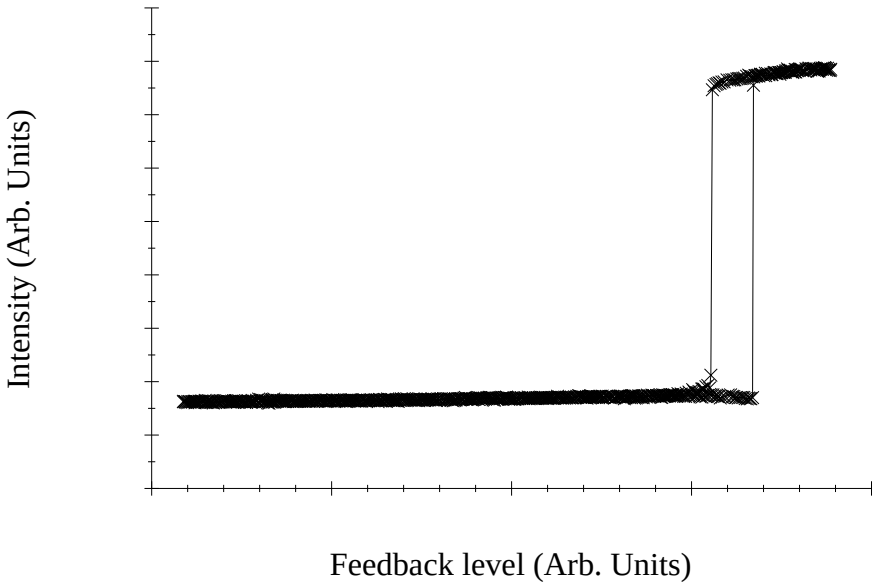

Figure 2.42: Bistability cycle for detuning of 60 Ghz: intensity-output vs. Feedbak Level.

parameter is changed on several internal-cavity free spectral range.

The feedback level is strongly dependent on phase matching and it is maximized by focusing the beam on the plane mirror which closes the cavity. In this condition the acousto-optic modulator is the only element controlling the feedback level. In Fig. 2.42 we show the intensity as a function of feedback level for a pumping value of 84 mA and detuning of 60 GHz to the red of a cavity mode. The system shows clearly a bistable behavior. This bistability is not due to the sweeping of the parameters. In fact, if we fix the feedback level inside the bistability cycle, the intensity-output can be high or low depending on the previous history of the system. This bistable cycle appears at different values of the pump level, and even when the solitary laser is below threshold. The two states of the bistable cycle can be interpreted as: i) one state controlled by the dispersive element which re-injecting the electro-magnetic field decreases the losses and therefore it produces a high intensity-output, and ii) a lower state corresponding to the laser without feedback. Thus, the frequency of the upper state is close to the one selected by the grating, while in the lower state the system operates in an

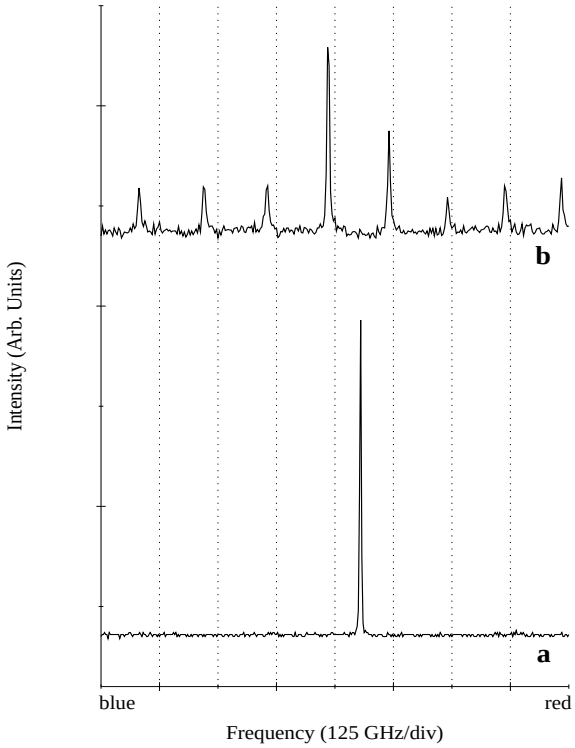

Figure 2.43: a)Optical Spectrum of the system at the upper branch of bistability cycle. b)Optical Spectrum of the system at the lower branch of bistability cycle. The vertical scale is magnified two times in respect with the one in a).

analogous way as the solitary laser does (see Fig. 2.43). If the pumping current is below 80 mA, the intensity of the lower branch vanishes, and its frequency is not defined.

Changing the detuning towards larger values, the area of the bistable cycle increases until the system will not switch anymore to the upper branch even for maximum feedback intensity. For smaller detuning the bistable cycle decreases in size and finally it disappears. The intensity-output grows nonlinearly with the feedback level, and the optical spectrum shifts gradually from the solitary laser frequency to the one imposed by the grating. It must be noticed that the qualitative behavior remains unchanged for all experimentally accessible pumping levels.

Fixing the detuning at a position where the behavior of the intensity is not

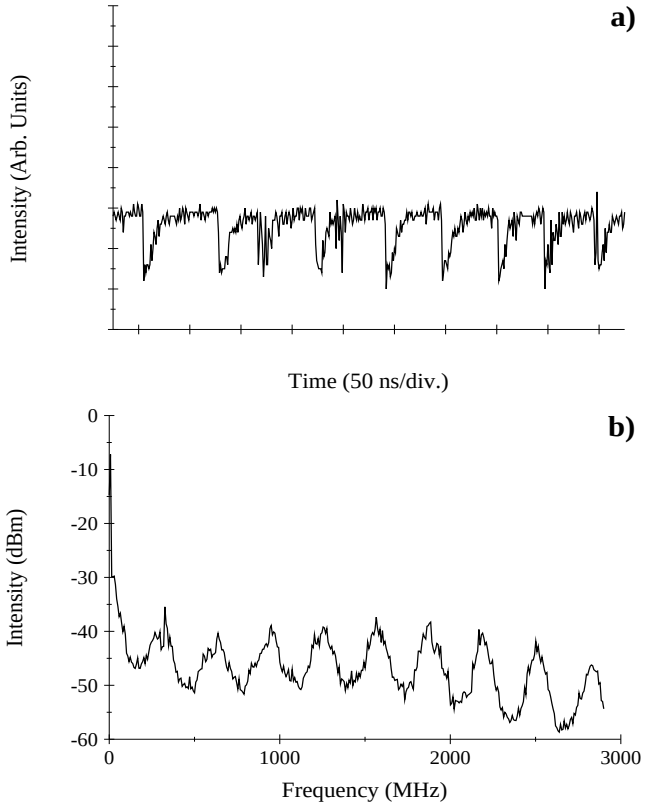

Figure 2.44: a) intensity-output and b) Power Spectrum of the system when the detuning is set to 30 GHz and the feedback level is moderate.

bistable the intensity-output is constant for the maximum achievable feedback level. Decreasing the amplitude of the feedback the intensity-output decreases, the power spectrum shows peaks at the external-cavity resonance frequencies and the optical linewidth increases and the peak shifts back towards the solitary laser frequency.

Below a certain feedback level, Low-Frequency Fluctuations appear in the intensity-output (Fig. 2.44(a)). When this occurs the optical linewidth broadens dramatically to the blue side of the spectrum (Fig. 2.45). The power spectrum shows the characteristic low-frequency component and all the peaks at the external-cavity frequencies broadened (Fig. 2.44(b)). It's important to notice that the optical spectrum shows the existence of several laser longitudinal-modes growing as the fluctuations at low-frequency appear. Their frequency positions

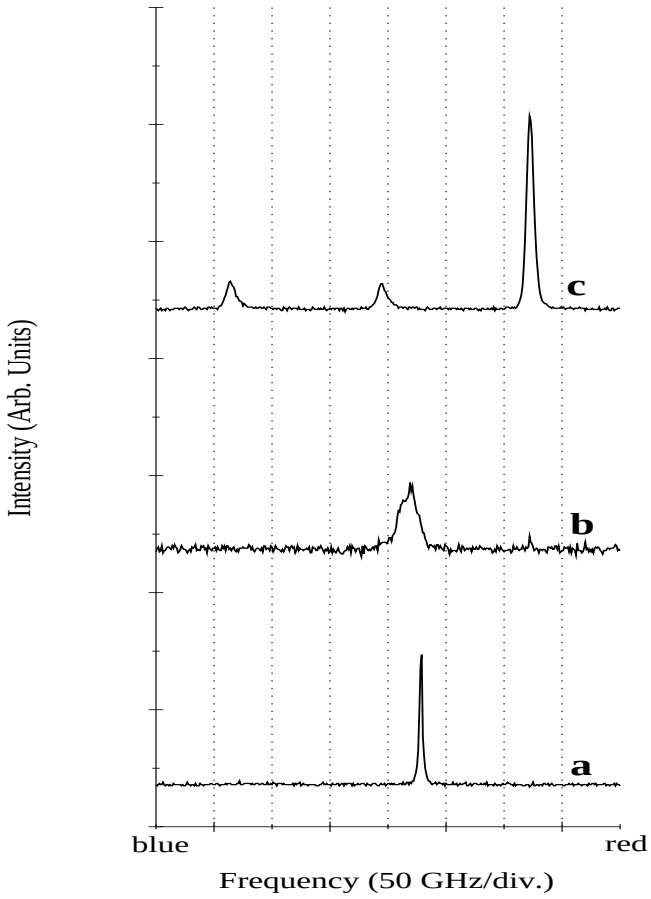

Figure 2.45: Trace b): Optical Spectrum corresponding to Fig. 2.44. Trace a) and c) are added for comparison with b). Trace a) is the optical spectrum of the system for a feedback level slightly larger than in b): the corresponding output intensity is constant in time. The remaining parameters values are the same as in a). Trace c) is the optical spectrum of the solitary laser at the same pumping current as it is in trace a) and b). In a) the vertical scale is compressed four times than in b), in c) is expanded 2.5 times than in b).

are not different from the solitary laser case. Thus when fluctuations at low-frequency are present in the field intensity only the frequency component around the re-injected mode are perturbed. The other longitudinal-modes seem not coupled to this one. However this observation shows only the time averaged behaviors of the spectrum while it does not provide information about correlation in real-time between different modes. Instead, if we detect the temporal behavior of the intensity of each longitudinal-mode, we notice that simultaneously to the dropout of the total intensity, the intensity of the lateral modes grows (Fig. 2.46). Thus the modes are strongly coupled even if just one of them is affected in the frequency

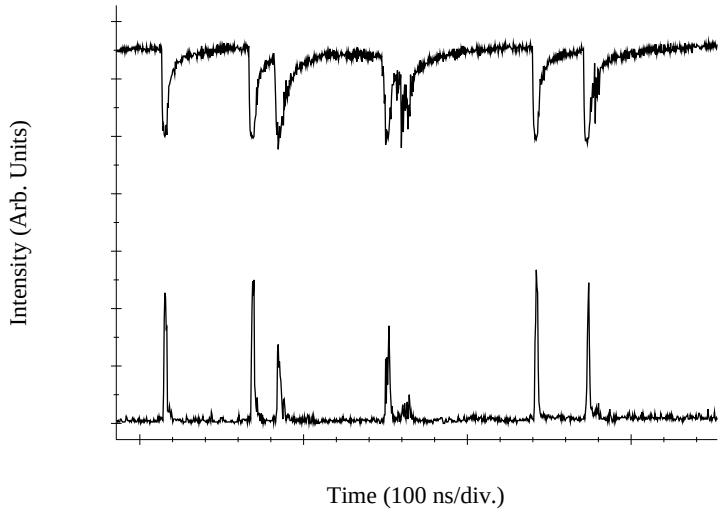

Figure 2.46: Total intensity (upper trace) and intensity of a lateral laser mode (lower trace) as function of time monitored contemporaneously (see text).

domain by the feedback. However there is no frequency shift for them and the duration of the pulse is shorter than the recovery time for the dominant mode. This is the main difference we found on the dynamical behavior of a selective frequency feedback with respect to an optical feedback provided by a mirror.

Our heuristic interpretation is that the dropout process is produced when the dominant mode is destabilized by the presence of the lateral modes. In other words perturbations whose frequencies corresponds to those of the lateral modes tend to grow producing the intensity dropout . However the strongly frequency-selective feedback allows their existence for times of the order of a single round-trip (3.2 ns). In fact the dispersive element will immediately misalign such frequency, and the system returns fast to the dominant mode.

2.7.2 Interpretation

A theoretical model to describe this system was proposed in Refs. [125, 126]. They considered the external grating as element changing the effective reflectivity while not imposing any dispersive effect. With such assumption the model becomes identical to the case of having a conventional mirror for closing the external-cavity. Multiple steady-state solutions occur for parameter values corresponding to semiconductor lasers. However the separation in frequency among consecutive steady-state solutions is of the order of the inverse of the external-cavity roundtrip ($\sim 300\ MHz$ for a $50\ cm$ external-cavity length). We showed experimentally, in agreement with the experimental result of Refs. [125, 126], that the two possible steady-states in the bistable cycle corresponds to a frequency separation of the order of tens of GHz. Such difference can be understood only if we consider that the grating will strongly select the frequency at which the feedback is effective. In other words, the theoretical models previously presented are valid only if the bandwidth of the grating is much larger than the modal separation between longitudinal-modes of the solitary laser. Thus the grating will behave essentially as a conventional mirror whose reflectivity does not depend on frequency. In our experiment the bandwidth of the grating is smaller than the longitudinal-mode separation and the dispersion of the feedback becomes strongly relevant. Furthermore, a complete model able to describe the dynamical instabilities would require a multi-mode description of the laser. Clearly because of the existing coupling among modes, we can not expect a good agreement with a single-mode theory. We are unaware of the existence in literature of such a model containing both a multi-mode description and/or the existence of a dispersive element in the external-cavity. We want to show here that a simple model for a two level atom interacting with an electro-magnetic field but including a multi-mode description and the appropriate boundary conditions for a strongly selective feedback

explains our experimental results when no instabilities are present. A description of the intensity fluctuations would require a numerical simulation which is not the aim of the paper.

We assume a two level atomic medium interacting with an electro-magnetic field in the rotating wave approximation. The frequency-selective feedback is included through the boundary conditions. The well known Maxwell-Bloch equations read:

$$\begin{aligned} \partial_z E + \frac{1}{c}\partial_t E &= gP + i\frac{\omega_\ell}{c}E \\ \partial_t P &= -\gamma_\perp((1+i\delta)P - EN) \\ \partial_t N &= -\gamma_{\|}((N-N_o) + \frac{1}{2}(E^*P + EP^*)) \end{aligned} \tag{2.7.1}$$

where E, P, and N are the electro-magnetic field envelope, the atomic polarization and the population inversion respectively; κ, $\gamma_\perp$, and $\gamma_{\|}$ are their respective loss rates; N_o is the pumping rate, g is the gain , c is the speed of light in the medium, ω_ℓ is the frequency of the electro-magnetic field with respect to a cavity resonance ω_c which was taken as reference; δ is the detuning parameter which indicates the separation in frequency between the electro-magnetic field and the atomic resonance normalized to $\gamma_\perp$, $\delta = \frac{\omega_a - \omega_c - \omega_\ell}{\gamma_\perp}$. Assuming unidirectional ring laser with the medium uniformly distributed along the whole cavity the boundary conditions are:

$$E(0,t) = r_1[E(\ell,t) + r_{eff}\int_0^{t-\tau} E(\ell,t')e^{i(\omega_c+\omega_\ell)(\frac{L-\ell}{c})}\Gamma(t-\tau-t')dt' \,] \tag{2.7.2}$$

where ℓ is the length of the laser cavity, L is the length of the external-cavity , τ is the round-trip time in the external-cavity and $\Gamma(t)$ is the transfer function of the frequency-selective element. Assuming:

$$\Gamma(t) = (\Delta\omega)e^{(-\Delta\omega - i\omega_g)t} \tag{2.7.3}$$

which describes our phase grating we can define:

$$U_\ell(t) = \int_0^t E(\ell, t')(\Delta\omega) e^{(-\Delta\omega - i(\omega_g - \omega_c - \omega\ell))(t-t')} dt' \tag{2.7.4}$$

Then:

$$d_t U_\ell = -\Delta\omega[(1 + i\delta_g)U_\ell - E_\ell] \tag{2.7.5}$$

where $\delta_g = \frac{(\omega_g - \omega_c - \omega_\ell)}{\Delta\omega}$.

So the boundary condition reads:

$$E(0,t) = r_1(E(\ell,t) + r_{eff} e^{i(\omega_c + \omega_\ell)(\frac{L-\ell}{c})} U_\ell(t-\tau)) \tag{2.7.6}$$

and the eqtns. 2.7.1-2.7.5 are the equations of motion. By simple algebra we find the steady-state solutions:

$$\begin{aligned} \rho^2(\ell) &= \frac{2}{1 - (r_1\Theta(\omega_\ell))^2}[(g\ell N_0) - (1+\delta^2) \mid \ln(r_1\Theta(\omega_\ell)) \mid] \\ \omega_\ell &= -\frac{c}{\ell}[\Psi(\omega_\ell) + \delta \ln(r_1\Theta(\omega_\ell))] + 2\frac{c}{\ell}\pi j \qquad j \in \mathcal{Z} \end{aligned} \tag{2.7.7}$$

where ρ is the modulus of electric field and:

$$\begin{aligned} \Theta^2(\omega_\ell) &= 1 + \frac{\alpha}{(1+\delta_g^2)} + \frac{2\alpha^{\frac{1}{2}}}{\sqrt{(1+\delta_g^2)}} cos((\omega_c + \omega_\ell)(\frac{L-\ell}{c}) - arctg\delta_g) \\ \Psi(\omega_\ell) &= arctg\{\frac{\alpha^{\frac{1}{2}} sin[(\omega_c + \omega_\ell)(\frac{L-\ell}{c}) - arctg\delta_g]}{1 + \alpha^{\frac{1}{2}} cos[(\omega_c + \omega_\ell)(\frac{L-\ell}{c}) - arctg\delta_g]}\} \end{aligned} \tag{2.7.8}$$

where α is a constant depending on the reflectivity of the output mirrors and the grating. A complete analysis as a function of the parameters will be presented elsewhere. However we can remark some qualitative features for each mode j:

i) If $\Delta\omega \to \infty$ and $L \to 0$ then we obtain the usual steady-state solutions for a laser. ii) As Θ depends on the frequency ω_ℓ, then 2.7.7 has multiple solutions. iii) If $\Delta\omega$ is small compared to $\frac{c}{2\ell}$, and δ_g is of the same order of magnitude of $\Delta\omega$, then there are, at least, three possible steady-state solutions. One of them is close to the operation frequency of the laser without feedback. A second one is

close to the frequency ω_g defined by the grating. An intermediate value is found to be unstable.

These qualitative feature are able to explain the bistable behavior and the trend of the bistable cycle as we change the value of δ_g. A numerical integration is necessary in order to check the agreement of the model in the parameter region where experiment shows oscillatory behavior: this work will be developed in the future.

Chapter 3

The Vertical-Cavity Surface-Emitting Lasers ($VCSEL's$) with Optical Feedback

3.1 Introduction

It is well known that $VCSEL's$ do not have a strong mechanism for a single polarization selection and may show instabilities because of the polarization dynamics (see §I.3). Such effects were recently studied in the experimental configuration of laser with optical feedback with polarization selection (Refs. [81, 129, 130, 131]). Here we describe the experimental results obtained in the case where the $VCSEL's$ were submitted to polarization preserving optical feedback. This experiments have been motivated by different reasons: i) to check what would happen submitting to optical feedback a semiconductor source that is single-longitudinal-mode. Does Low-Frequency Fluctuations still appears? Are there other kind of instabilities? ii) To characterize the $VCSEL's$ behavior in presence of optical feedback, thus evidencing the dynamics of the polarization components .

It has been argued that $VCSEL's$ should be relatively immune to optical feedback because of large reflectivity of the mirrors forming the cavity (Refs. [132, 133]). However, it has been shown that $VCSEL's$ may exhibit in some cases a

sensitivity to optical feedback comparable to that of edge-emitter lasers (Refs. [134, 135]). In this chapter we show that a $VCSEL$ with polarization preserving and mode-matched optical feedback can display instabilities in the total output power which are linked to fluctuations in the polarization components of the $VCSEL$ emission. We show that for perfect phase matching and alignment of the external-cavity, the total output power is quite stable over a wide range of parameter values, although anti-phase oscillations of the two linear polarization components may occur, with a oscillation period corresponding to the external-cavity round-trip time. As the current injection is increased, instabilities of the total output power which look like the well known Low-Frequency Fluctuations in edge-emitting lasers develop. Fluctuations appear simultaneously in the two polarization modes, in such a way that the dominant polarization mode displays power drops which are simultaneous with bursts in the power of the depressed polarization mode. A theoretical model is presented which explains qualitatively the experimental results. The model is based on the Spin-Flip Model (SFM), (Ref. [86]) which has been often used to explain polarization switching in $VCSEL's$ as described in §I.3. In order to describe the effects of the external mirror, we develop an approximation valid for arbitrary reflectivities of the external mirror which includes all round-trips in the external cavity; the inclusion of multiple round-trips in the external cavity is necessary because of the large reflectivity of the mirrors forming the $VCSEL$ cavity (Ref. [136]). The widely used Lang and Kobayashi approximation (Ref. [16]), which accounts only for one round-trip in the external-cavity, is recovered in the limit of very low optical feedback.

This chapter is organized as follows. In Sect. II we present the experimental results. In Sect. III we develop the model, and in Sect. IV we analyze the numerical results and we compare them with experimental ones.

3.2 Experimental results

In our study, we use a proton-implanted GaAs $VCSEL$ with lasing wavelength λ_0 around 850 nm manufactured by VIXEL^{TM} Corp. The active area is defined by proton implantation, its diameter is around 8 μm (Refs. [54, 83]). The $VCSEL$ is battery powered and mounted on a thermo-electric device to stabilize the temperature. The $VCSEL$ output is focused by an AR-coated aspheric lens onto a distant reflector that provides mode-matched optical feedback.

Two different configurations of the external-cavity have been used. The first one allows for large feedback (threshold reduction of 28%, Fig. 3.1a). The second one (Fig. 3.1b), where mirror M was removed and $BS1$ was substituted by a wedged glass substrate, provides moderate feedback (threshold reduction of 15%). These configurations have been chosen in order to avoid interferometric effects from any optical elements (see appendix A.7). In fact, the symmetric beam shape of the $VCSEL$ together with its high spectral purity easily produce interference effects in optical elements with parallel faces (beam splitters, dielectric mirrors, windows, neutral density filters, etc.), which act as an etalon if anti-reflection coatings are not perfect. This effect has to be avoided in order to maintain the feedback not selective in frequency. Moreover, the incidence of the beam onto the surfaces of the optical elements should be normal in order to preserve the polarization in the external feedback cavity.

The output is polarization-resolved by means of a Glan-Taylor prism. A $\lambda/2$-waveplate placed into the optical path just before the Glan-Taylor prism allows to check the orientation of the analyzer with respect to the polarization emitted by the laser. Thus, a rotation of the polarization axis of the output field can be measured by rotating the $\lambda/2$-waveplate. The two beams emerging from the polarizer are focused onto Si avalanche photodetectors (APD1 and APD2,

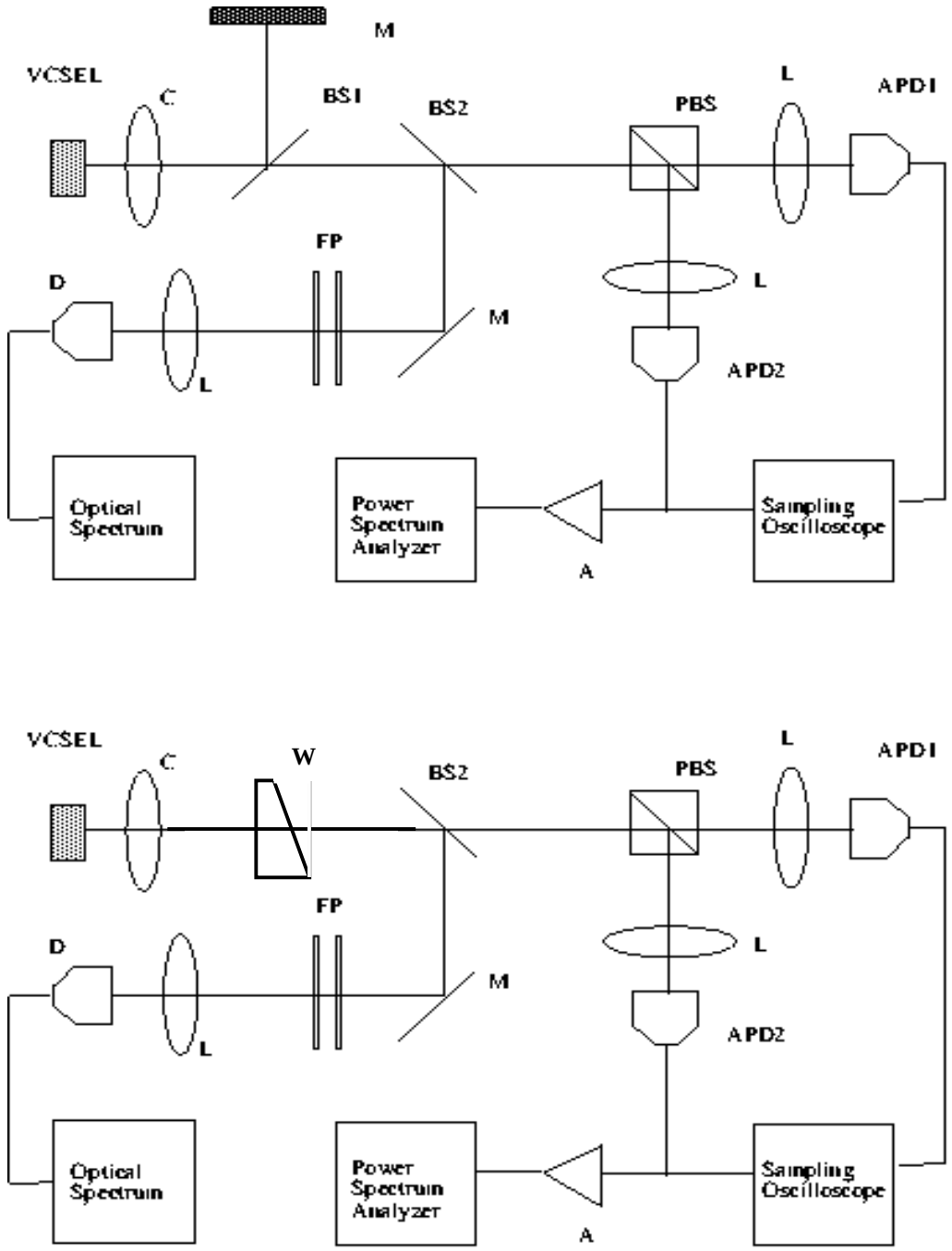

Figure 3.1: (a,b) Schematic experimental setup for (a,above) large feedback (b,below) moderate feedback: C collimator, BS polarization preserving beam splitter, PBS polarizing beam splitter, M mirror, L lens, APD avalanche photodiode, D broad area slow detector, FP plano-planar scanning Fabry-Pérot, A amplifier.

bandwidth $\approx 2.5\ GHz$). Their signals are monitored with a digital oscilloscope ($LeCroy^{TM}$ 7200A, analog bandwidth 500 MHz). An RF-spectrum analyzer monitors the power spectrum of the signals in a range covering the full bandwidth of the detectors. The optical spectrum is obtained with a scanning Fabry-Pérot whose free spectral range is 293 GHz, and its finesse is of the order of 200.

The main characteristics of the solitary $VCSEL$ are shown in Fig. 3.2. The threshold current of the solitary $VCSEL$ is $I_{th,sol} = 2.65\ mA$, and it emits linearly polarized light in the fundamental transverse mode up to 3.7 mA. For currents between 3.7 mA and 4.4 mA, we have bistability between the two linearly polarized modes with noise-induced switching from one to the other, whose frequency splitting is of the order of 2.8 GHz. Above 4.4 mA, the first order transverse mode appears.

In the feedback experiment we will stay always well below this point. The aim of this work is to characterize the dynamical behavior of the $VCSEL$ with feedback in the parameter region where the intensity-output of each polarization component is not stable.

In Fig. 3.3 we show the polarization-resolved L-I curve of the $VCSEL$ with large feedback. The threshold is now $I_{th,feed} = 1.9\ mA$, and the emission is stable and linearly polarized for currents above $I_1 = 2.22\ mA$. At $I \sim 2.65\ mA$, a polarization switching occurs, but the laser emission is still stable and linearly polarized until the larger order transverse mode comes into play.

For currents between $I_{th,feed}$ and I_1 the $VCSEL$ output is unstable both in total power and polarization orientation. Close to $I_{th,feed}$ (see Fig. 3.4a, $I = 2.02$ mA), the output field is almost linearly polarized but there are important fluctuations at low frequency in the two components. The power spectrum of each component shows multiple beat notes of external-cavity modes, and noise excess at low frequencies. For larger currents (Fig. 3.4b, $I = 2.13$ mA) the amplitude of

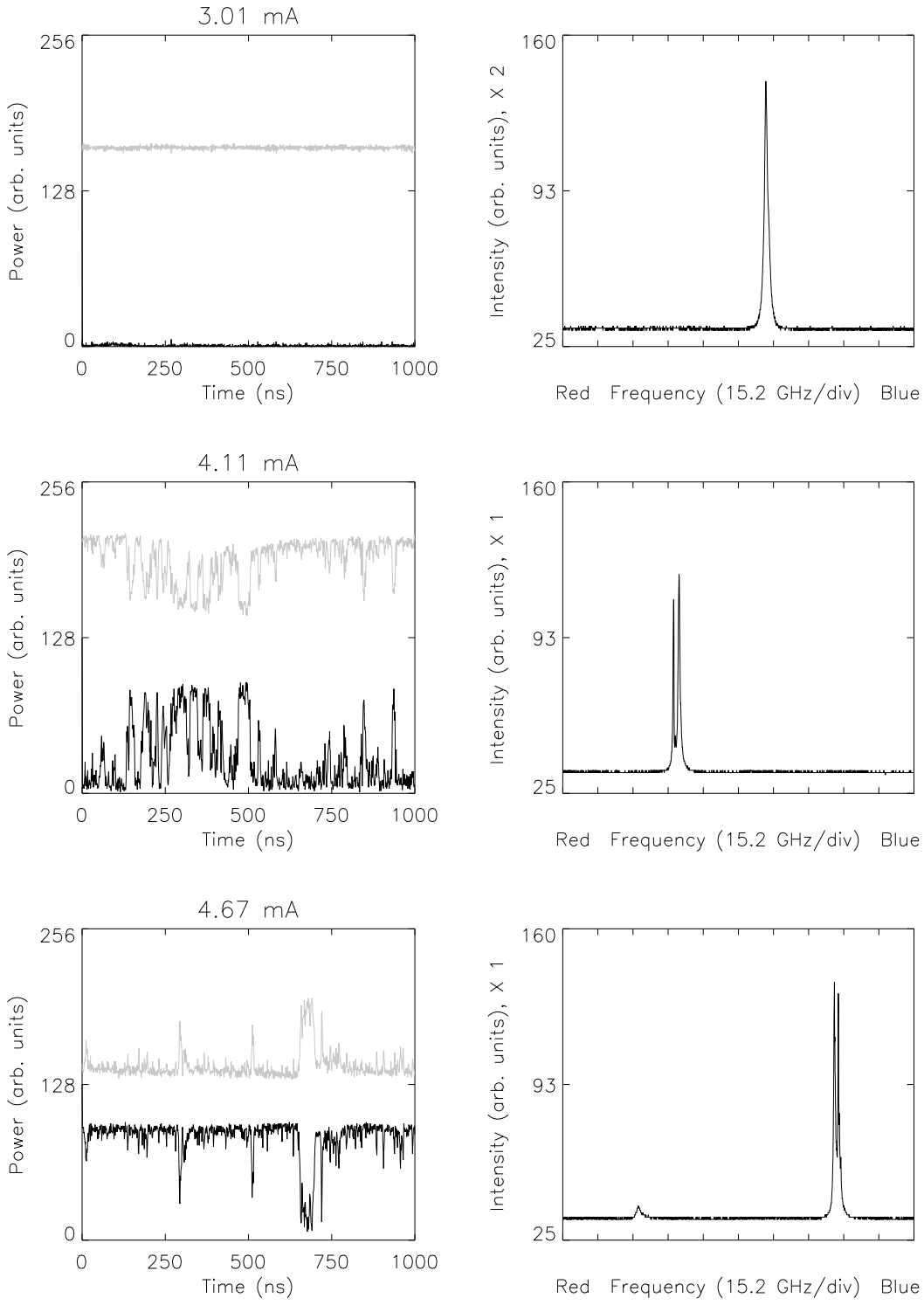

Figure 3.2: Polarization-resolved dynamics of solitary laser for current 3.01 mA (upper left panel), 4.11 mA (central left panel) and 4.67 mA (bottom left panel). Right-hand panels display the corresponding optical spectra.

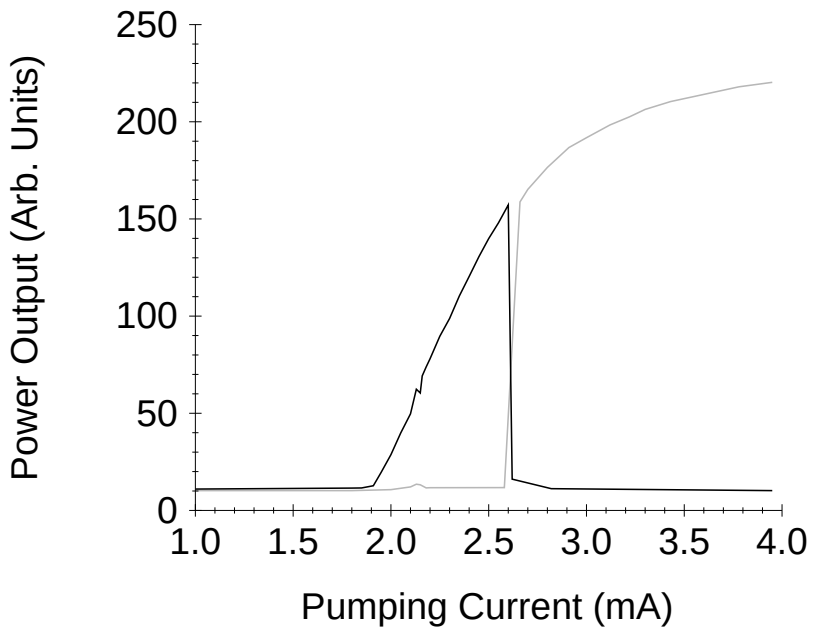

Figure 3.3: Polarization-resolved LI-curve of the $VCSEL$ in the large-feedback configuration.

the Low-Frequency Fluctuations increases, and the two polarization components are in anti-phase.

At this point the fluctuations manifest themselves in sudden drops in the power of the dominant polarization component (and the total power) which is followed by a rather slow stepwise recovery. This shape resembles very much the shape of the power drops in the low frequency fluctuation regime in edge-emitters with feedback. Each drop of power of the dominant polarization component is accompanied by a burst in power of the one which is usually depressed.

Further increasing the current, the Low-Frequency Fluctuations appear grouped in bursts (Fig. 3.4c, $I = 2.19\,mA$) separated by intervals of constant output. The length of the bursts reduces and the time between bursts increases as the current is increased.

Finally, for currents above I_1 the Low-Frequency Fluctuations disappear and

the output is linearly polarized (Fig. 3.5). However, the RF spectrum of each polarized component displays several narrow peaks with side-bands at multiples of the external cavity frequency spacing (Fig. 3.5, upper panels). The two linearly polarized components can be adjusted to interfere with variable amplitude by rotating the $\lambda/2$-waveplate (Fig. 3.5, lower panels). We observe that the RF spectrum is modified by this operation, and there is a position of the $\lambda/2$-waveplate where the central component of the external cavity modes is suppressed while the side-bands remain (Fig. 3.5, 2.36 mA, 66^o). This result indicates that each polarization is oscillating with a period corresponding to the external round trip time but in anti-phase, because the beating disappears if we compensate their difference in amplitude. The side-bands indicate that a second lower frequency exists and the two polarization components oscillate in-phase at this frequency. For currents above 2.65 mA, the system then emits linearly stable on the other component and single external-cavity mode operation is improved if the current is further increased.

It is worth remarking that the orientation of the polarization axes of the $VCSEL$ with feedback is affected by minute anisotropies in the external-cavity. As a consequence, the emission of the $VCSEL$ with feedback has in general principal axes rotated with respect to those of the solitary device. This uncontrolled rotation of the axes can be compensated for by the $\lambda/2$ wave-plate in the output beam thus realigning the emission axes with those of the polarizer. Interestingly, the orientation of the linearly polarized emission from the $VCSEL$ with feedback can be controlled by inserting a highly anisotropic element in the external-cavity (as a $\lambda/4$ or $\lambda/2$ waveplate), whose axes become dominant.

In Figs. 3.6a and 3.6b we show the moderate feedback case. In this case the output of the system is always very noisy with broad peaks in the power spectrum both at low frequency and at the external-cavity resonances. Although antiphase

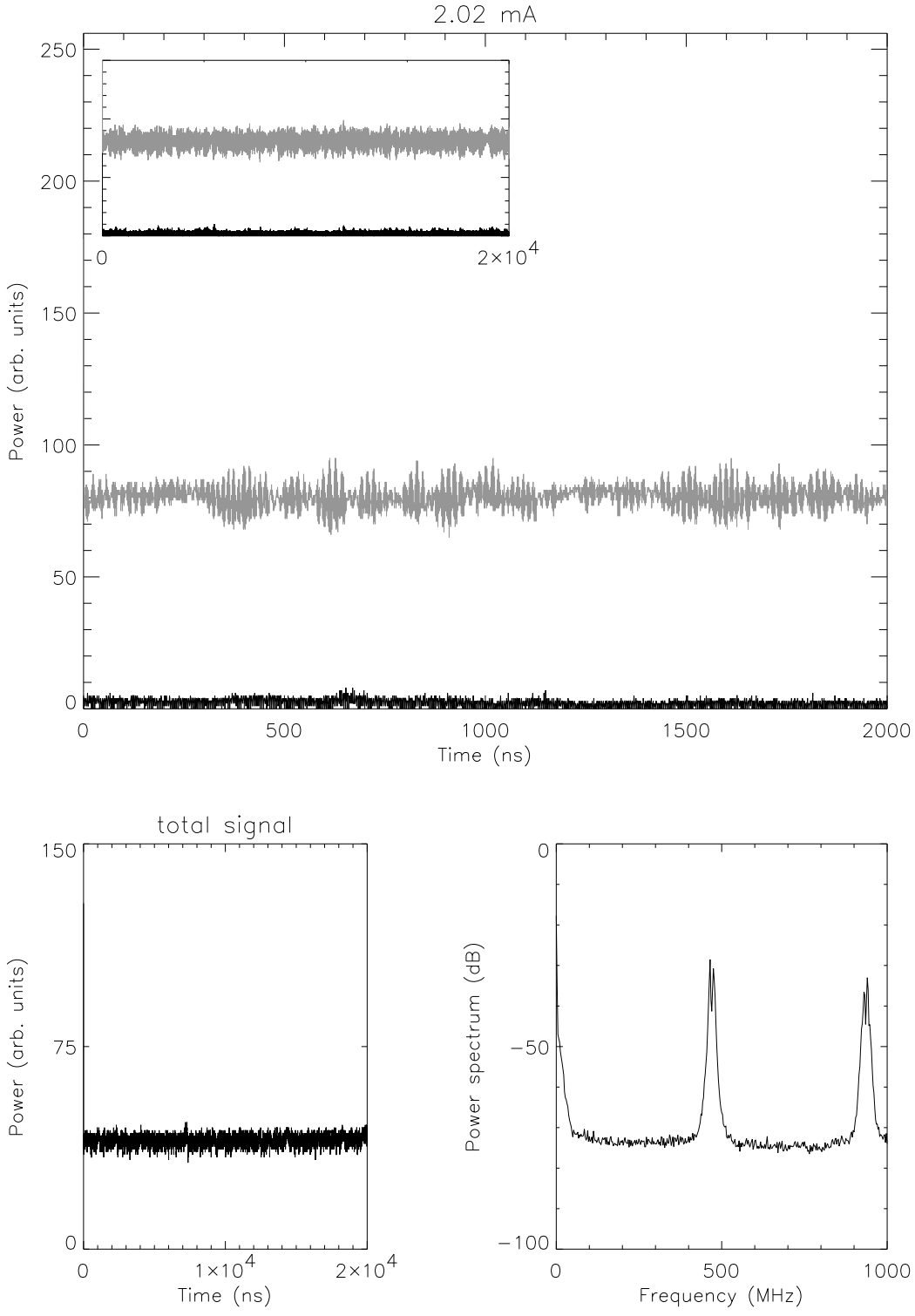

Figure 3.4: (a) Emission characteristics of the $VCSEL$ in the large-feedback configuration for current injection $I = 2.02$ mA. Big upper panel: Time trace of the polarization-resolved powers, (Inset panel) long scale time trace of the polarization-resolved powers. Bottom left panel: Time trace of the total power. Bottom right panel: Power spectrum of one polarization component.

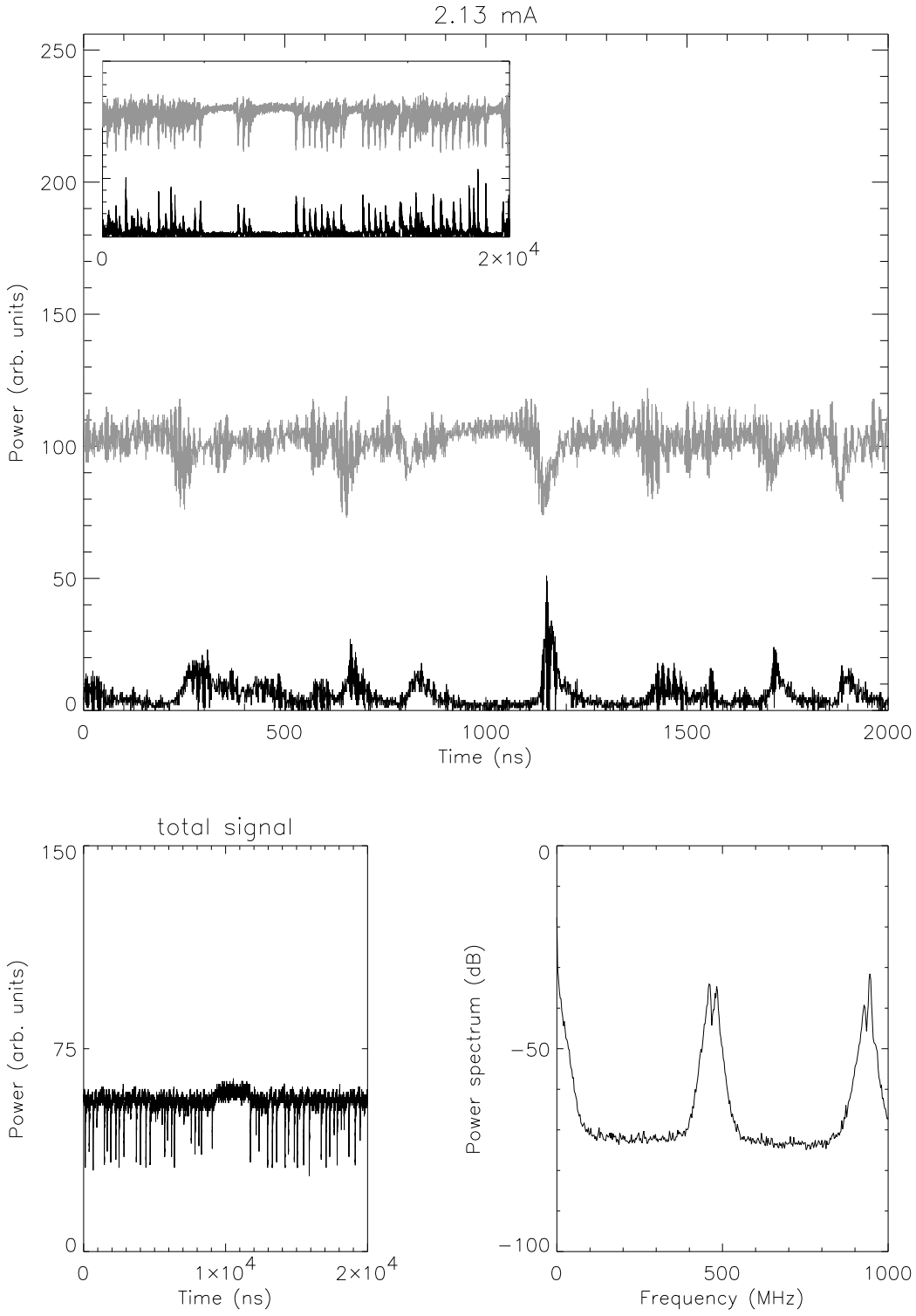

Fig. 3.4: (b) Emission characteristics of the $VCSEL$ in the large-feedback configuration for current injection $I = 2.13$ mA. Big upper panel: Time trace of the polarization-resolved powers, (Inset panel) long scale time trace of the polarization-resolved powers. Bottom left panel: Time trace of the total power. Bottom right panel: Power spectrum of one polarization component.

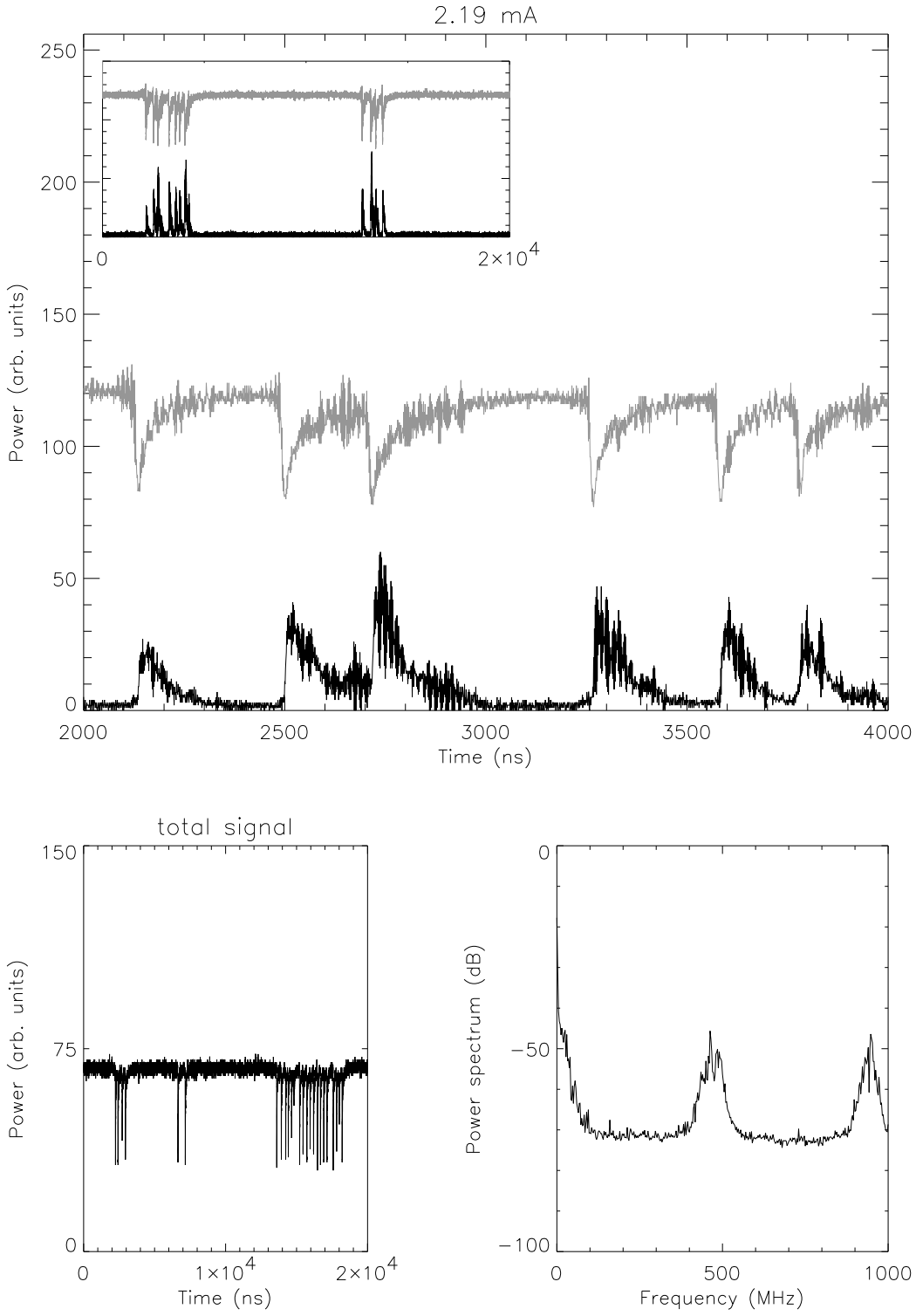

Fig. 3.4: (c) Emission characteristics of the $VCSEL$ in the large-feedback configuration for current injection $I = 2.19$ mA. Big upper panel: Time trace of the polarization-resolved powers, (Inset panel) long scale time trace of the polarization-resolved powers. Bottom left panel: Time trace of the total power. Bottom right panel: Power spectrum of one polarization component.

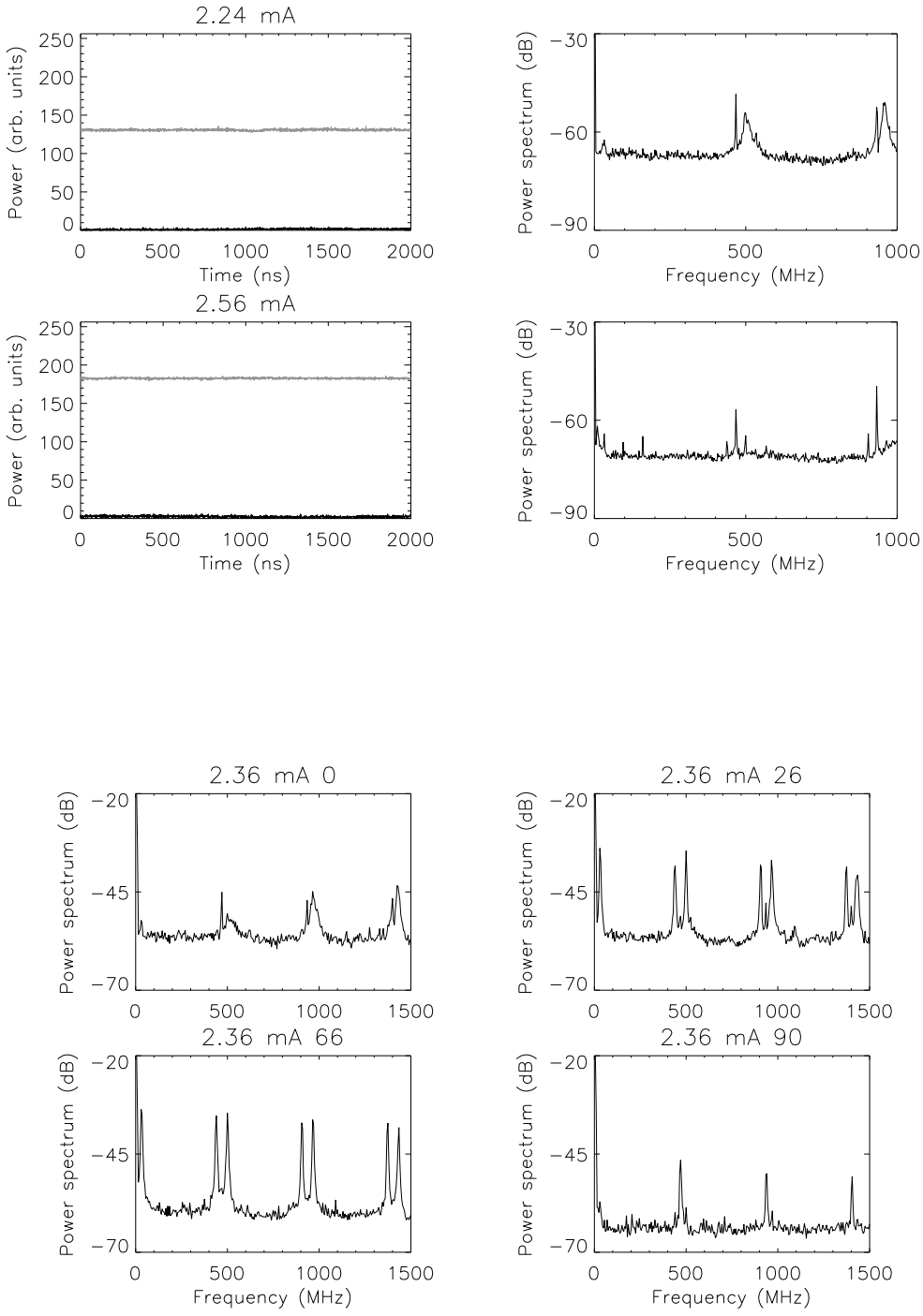

Figure 3.5: (upper half of the figure) Time trace of the polarization-resolved powers and corresponding power spectrum of one polarization component of the $VCSEL$ in the large-feedback configuration for current injection of $I = 2.24\ mA$ and of $I = 2.56\ mA$. (upper half of the figure) Power spectrum of one polarization component of the $VCSEL$ in the large-feedback configuration, for current injection of $I = 2.36\ mA$, as the the $\lambda/2$-waveplate is rotated. Then the polarization axis are rotated before the polarizing beam splitter of 0^o, 26^o, 66^o, 90^o, as indicated above each panel. In this way the two linearly polarized components can be adjusted to interfere with variable amplitude.

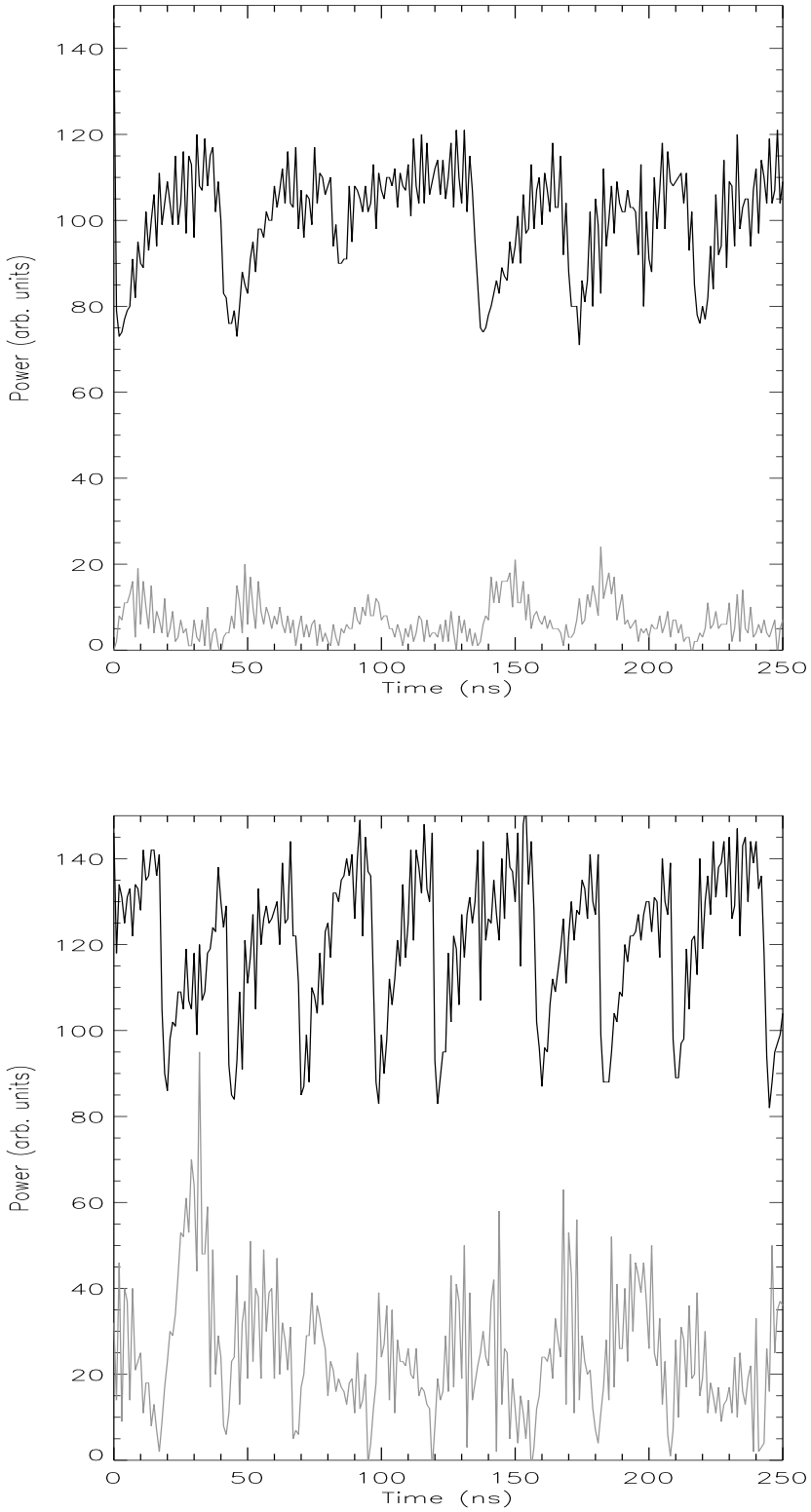

Figure 3.6: (a,b) Polarization-resolved time-series for the moderate feedback configuration when $I = 3.09\ mA$(above) and $I = 3.16\ mA$(below).

dynamics is not as clear as for the strong feedback case, anyway it is evident that the fluctuations in both polarizations are synchronous.

3.3 Model

In order to describe the effects of optical feedback on the output characteristics of the $VCSEL$, we have on one hand to describe the interaction of the optical field with the material in the active region, and on the other, we have to include in the description the effects of the external mirror while keeping the vector characteristics of the optical field.

Our starting point for the description of the $VCSEL$ is the Spin-Flip Model (SFM) developed in Ref. [86] (see §I.3). The original SFM model does not include optical feedback, and therefore the evolution equations for the optical field have to be modified in order to take it into account. Polarized feedback effects in the SFM have been considered previously by adding to the rate-equations for one of the field components a delayed term which represents the effect of the external mirror (see Refs. [130, 81]. For polarization preserving feedback one could follow the same approach for both components of the field (as in Ref. [131]); however, in this limit only one roundtrip in the external-cavity is taken into account for the dynamics, and it has been pointed out (Refs. [136] that because of the large reflectivity of the Bragg mirrors defining the $VCSEL$ cavity, several roundtrips should be considered. Nevertheless, as shown in the Appendix, an approximation taking into account all roundtrips in the external cavity can be developed for any reflectivity of the external mirror based on the fact that the Bragg mirror reflectivity is almost one.

In this approximation, the dynamical evolution of the system is given by

$$R_{\pm}(t) = \frac{c}{2n_g L}\hat{r}_3\frac{1-r_2^2}{r_2}A_{\pm}(t-\tau) - r_2\hat{r}_3 R_{\pm}(t-\tau)\ , \tag{3.3.1}$$

$$d_t N_{\pm} = \frac{I}{2eV} - \gamma_e N_{\pm} - 2g\frac{N_{\pm}-N_t}{1+s|A_{\pm}|^2}|A_{\pm}|^2 - \gamma_J(N_{\pm}-N_{\mp})\ , \tag{3.3.2}$$

where

$$R_{\pm}(t) = d_t A_{\pm}(t) + \kappa A_{\pm}(t) + (\gamma_a + i\gamma_p)A_{\mp}(t) - \Gamma g(1-i\alpha)\frac{N_{\pm}-N_t}{1+s|A_{\pm}|^2}A_{\pm}\ . \tag{3.3.3}$$

In these equations, $A_{\pm}$ is the slowly varying amplitude of the left and right circularly-polarized components of the optical field, and $N_{\pm}$ is the carrier density with spin-down and up, respectively. In addition, $\kappa = 1/(2\tau_p)$ (τ_p being the photon lifetime in the solitary $VCSEL$ cavity), g is the differential material gain multiplied by the group velocity of the transverse mode, c/n_g, N_t is one half of the transparency carrier density (i. e., the transparency carrier density per spin orientation), s is the gain saturation parameter, α is the linewidth enhancement factor, Γ is the field confinement factor to the active region, and γ_a and γ_p are the dichroism and birefringence, respectively. $\hat{r}_3 = r_3\exp(i\Omega\tau)$ is the amplitude reflection coefficient into the $VCSEL$ cavity including the optical phase change after one external-cavity roundtrip. $I/(2eV)$ is the density of carriers with given spin orientation injected into the active region per unit time, γ_e is the nonradiative carrier relaxation rate, and γ_J is the spin-flip rate.

It is worth noting that (3.3.1) and (3.3.2) reduce to the SFM model when there is no external-cavity [$R_{\pm}(t) = 0$], and that the Lang and Kobayashi approximation is recovered in the limit of weak feedback, when only the first round-trip in

the external-cavity needs to be taken into account,

$$\begin{aligned} R_\pm(t) &= \frac{c}{2n_gL}\hat{r}_3\frac{1-r_2^2}{r_2}A_\pm(t-\tau) - r_2\hat{r}_3R_\pm(t-\tau) \\ &= \frac{c}{2n_gL}\hat{r}_3\frac{1-r_2^2}{r_2}A_\pm(t-\tau) - r_2\hat{r}_3\frac{c}{2n_gL}\hat{r}_3\frac{1-r_2^2}{r_2}A_\pm(t-2\tau) + ... \\ &\approx \frac{c}{2n_gL}\hat{r}_3\frac{1-r_2^2}{r_2}A_\pm(t-\tau)\ . \end{aligned} \tag{3.3.4}$$

Moreover, from the numerical point of view they allow us to approximately describe the effect of all reflections in the external mirror with a single additional memory vector, $R_\pm(t-\tau)$, thus memory consumption and computational cost are essentially the same as in the Lang and Kobayashi approximation.

Equations (3.3.1) and (3.3.2), together with (3.3.3), can be recast into the form used in Ref. [88] by scaling the variables according to

$$E_\pm = \sqrt{\frac{g}{\gamma_e}}A_\pm\ , \tag{3.3.5}$$

$$N = \Gamma\frac{g}{\kappa}\left(\frac{N_+ + N_-}{2} - N_t\right)\ , \tag{3.3.6}$$

$$n = \Gamma\frac{g}{\kappa}\frac{N_+ - N_-}{2}\ . \tag{3.3.7}$$

We also include spontaneous-emission noise and injection current fluctuations into the evolution equations, which then read

$$R_\pm(t) = \kappa f E_\pm(t-\tau) - r_2\hat{r}_3R_\pm(t-\tau) + \sqrt{\beta_{sp}(N\pm n)}\chi_\pm(t)\ , \tag{3.3.8}$$

$$d_tN = \gamma_e\left(\mu - N - \frac{N+n}{1+s'|E_+|^2}|E_+|^2 - \frac{N-n}{1+s'|E_-|^2}|E_-|^2\right) + \sqrt{\varepsilon}\chi_N(t)\ , \tag{3.3.9}$$

$$d_tn = -\gamma_sn - \gamma_e\left(\frac{N+n}{1+s'|E_+|^2}|E_+|^2 - \frac{N-n}{1+s'|E_-|^2}|E_-|^2\right) + \sqrt{\varepsilon}\chi_n(t)\ , \tag{3.3.10}$$

where

$$R_\pm(t) = d_tE_\pm(t) + \kappa E_\pm(t) + (\gamma_a + i\gamma_p)E_\mp(t) - \kappa(1-i\alpha)(N\pm n)\frac{E_\pm}{1+s'|E_\pm|^2}\ , \tag{3.3.11}$$

with the other parameters being given as $f = (c/\kappa 2n_gL)\hat{r}_3(1-r_2^2)/r_2$, $s' = \gamma_e s/g$, $\gamma_s = \gamma_e + 2\gamma_J$ and $\mu = (\Gamma g/\kappa)\left[(I/2eV\gamma_e) - N_t\right]$. Finally, the Langevin terms $\chi_i(t)$ are taken as uncorrelated, gaussian white noises.

3.4 Numerical results

We have numerically integrated eqs. (3.3.8)-(3.3.11) for a variety of injection currents and different external-cavity setups. The output of the $VCSEL$ may exhibit a variety of behaviours depending on the injection current and the parameter values. We analyze here the evolution with current injection for quite a typical parameter set for the $VCSEL$ (as in Ref. [88]): $\kappa = 300\ ns^{-1}$, $\alpha = 3$, $\gamma_e = 1\ ns^{-1}$, $L = 0.24\mu m$, $n_g = 3.5$, $r_2 = 0.998$, $r_1 = 1$, $\gamma_s = 50$, $s' = 0.1$, $\gamma_p = 35\ ns^{-1}$, $\gamma_a = 0.1\ ns^{-1}$. For the confinement factor we take $\Gamma = 4.5\%$ and we consider a material gain coefficient of 1400 cm^{-1}, while for the noise strengths we take $\beta_{sp} = \epsilon = 3\ 10^{-4}\ ns^{-1}$.

For an effective reflectivity of the external mirror $r_3 = 0.075$, a 12% maximum threshold reduction is achieved. Emission in a single polarization orientation, in either single or multiple external-cavity modes is found for currents close enough to threshold (see Fig. 3.7). As the current is increased, periodic switching between the two polarization orientations is found, the two polarizations being in an antiphase state which oscillates with a period corresponding to the external-cavity roundtrip time (see Fig. 3.8).

Further increase of the injection current leads to a clearly unstable output of the $VCSEL$ associated with irregular bursts of the depressed polarization mode (see Fig. 3.9, upper panel). In this unstable regime, low-pass filtering of the $VCSEL$ output displays power drops on a slow time-scale corresponding to the time-interval between bursts, which is of the order of $50 - 100ns$. The recovery time of these power drops is of the order of tens of ns, and both these time-scales and the shape of the power drop and recovery time are very similar to the so called Low-Frequency Fluctuations (LFF) observed in edge-emitting lasers with optical feedback. Noteworthy, the polarization-resolved filtered traces show that

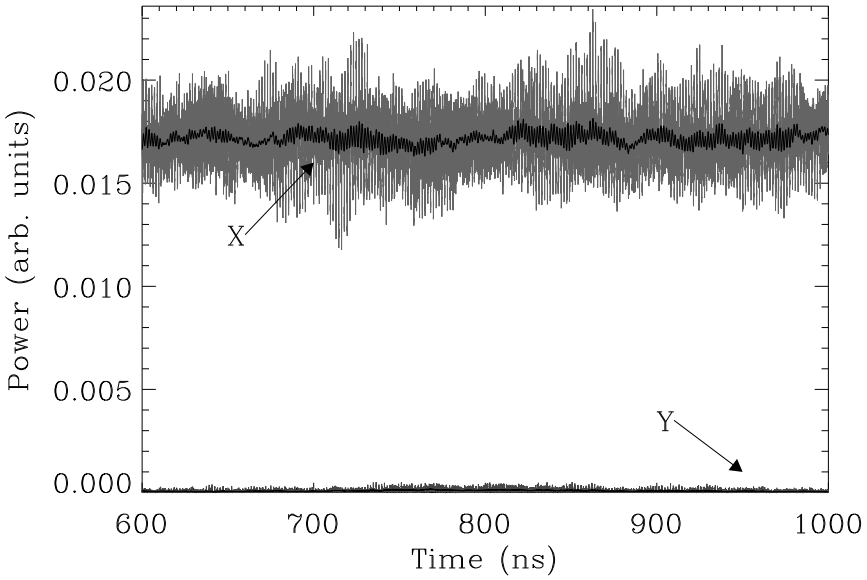

Figure 3.7: Polarization-resolved time traces as obtained by numerical integration of the theoretical model for $\mu = 0.905$ and a threshold reduction $\sim 12\%$. The grey trace corresponds to the unfiltered output, while the black trace is obtained after low-pass filtering with a second order Butterworth filter of 500 MHz bandwidth.

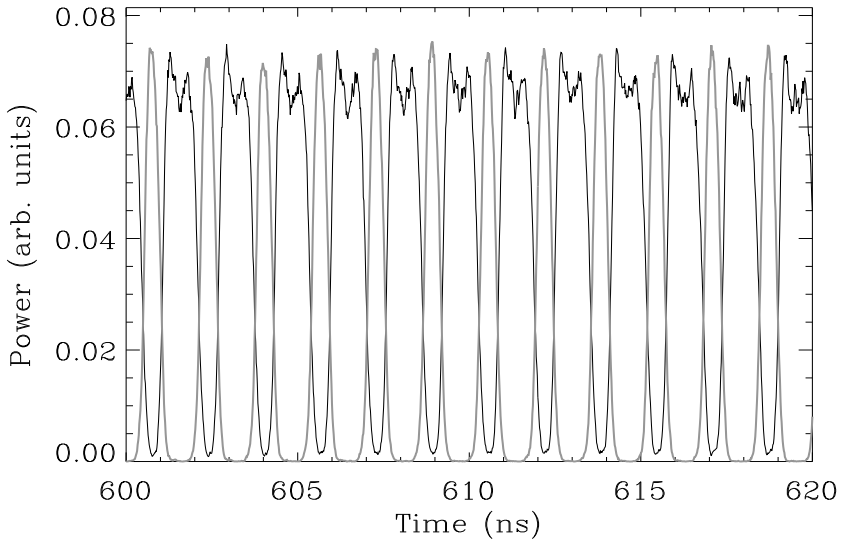

Figure 3.8: Unfiltered traces of the power in the X- (black) and Y-polarization (grey) orientations when the current is raised until $\mu = 0.95$.

the drops in the total power coincide with drops in the power of the dominant polarization compo0nent and with an increase in the power of the depressed one; moreover, the depressed mode remains excited during times noticeably longer than the duration of the drop in the total power, thus leading to two-mode operation during most of the time. When one of the polarization modes is at the noise level, the $VCSEL$ output is either stable or displays dynamics corresponding to multiple external-cavity mode operation. However, it does not exhibit power drops, which occur only when both polarization modes are active, although there are regimes where both are active and the $VCSEL$ output is quiescent.

Since the two linear polarization components have a frequency splitting given by the residual birefringence, the time-resolved spectrum in the LFF-regime shows that total power drops correspond to a power drop in the dominant linear polarization component followed by a power increase in the depressed one, thus leading to a transfer of power from the former to the latter which survives quite longer than the total power drop. This effect has already been observed in edge-emitting lasers with optical feedback in the LFF-regime (chap. 2), although in this case many more than two modes are involved in the dynamics.

In addition, it is clear from Fig. 3.9 (upper panel) that the total power oscillates around a DC level and that it approaches the zero level when a power drop occurs. Therefore, the statistics of the total power on a fast time-scale is peaked around the mean value of the power, and decreases for both high and low power levels (see Fig. 3.9, lower panel). It is worth noting that the decrease on both sides of the maximum is controlled by the non-linear gain saturation s', which forbids high power pulses and the subsequent depletion of carrier density which leads to a deep minimum in the total power; however, even for $s' = 0$ we find a power distribution peaked around its mean value, although the distribution in this case is broader. Similar results were found for edge-emitting lasers with

optical feedback in Ref. [120].

For even larger currents (see Fig. 3.10) the drops become much more frequent, and the optical spectrum displays two peaks corresponding to each of the linear polarization components. Moreover, low power values become more frequent, and as a consequence the statistical distribution of the power flattens (see Fig. 3.10, lower panel).

The dynamics obtained from the numerical simulations and its evolution as the current injection is raised is qualitatively similar to the experimental observations. The ambiguities in parameter values do not allow for quantitative comparisons, and make an exhaustive parameter-space covering useless. However, we have checked that forcing the system to operate with the same density of spin-up and spin-down carriers (i. e., in the limit $\gamma_s \to \infty$) the results are qualitatively the same as when spin dynamics is included in the model. We have also considered the case of a $VCSEL$ with very large dichroism, in such a way that in the absence of feedback only one of the polarization modes is stable in a very broad range of injection current, i. e., a quasi single-mode situation: the $VCSEL$ is now much more stable, but in the unstable regions the phenomenology is the same as discussed previously although LFF appear at larger currents than before. Finally, we have performed deterministic simulations of the theoretical model; in this case we find that LFF occur at much larger currents as compared with the stochastic case. Moreover, the LFF obtained in this case are much more irregular, and reminiscent of the so-called Coherence-Collapse, so it seems that noise leads to an anticipation of the onset of LFF through escape from an otherwise stable state.

The main point of disagreement between the theoretical model and the experimental observations concerns the point where LFF are obtained with respect

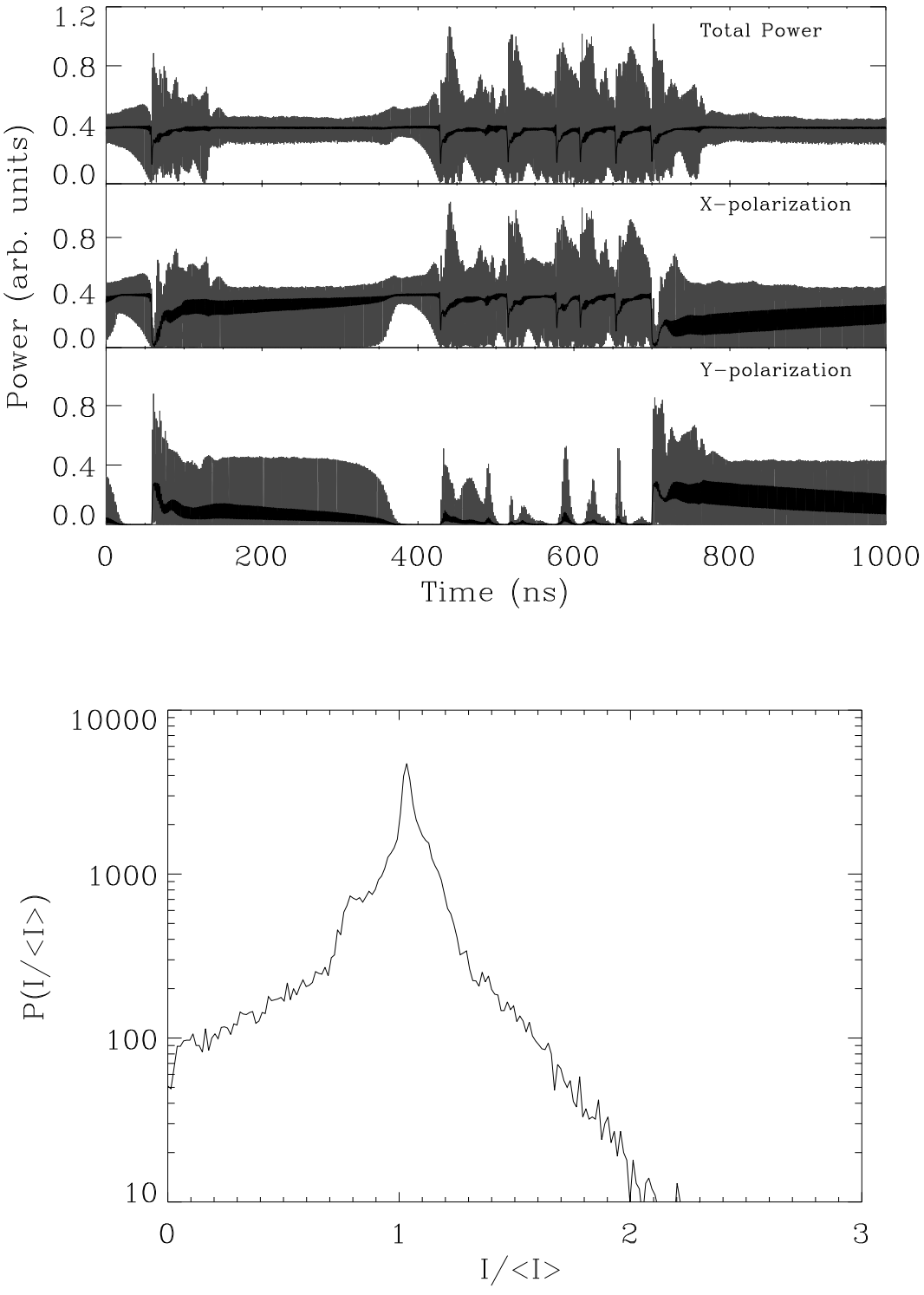

Figure 3.9: (above) Same as Fig. 3.8, but for $\mu = 1.25$, (below) Histogram of the values of the total power for $\mu = 1.25$ during the time span corresponding the figure above

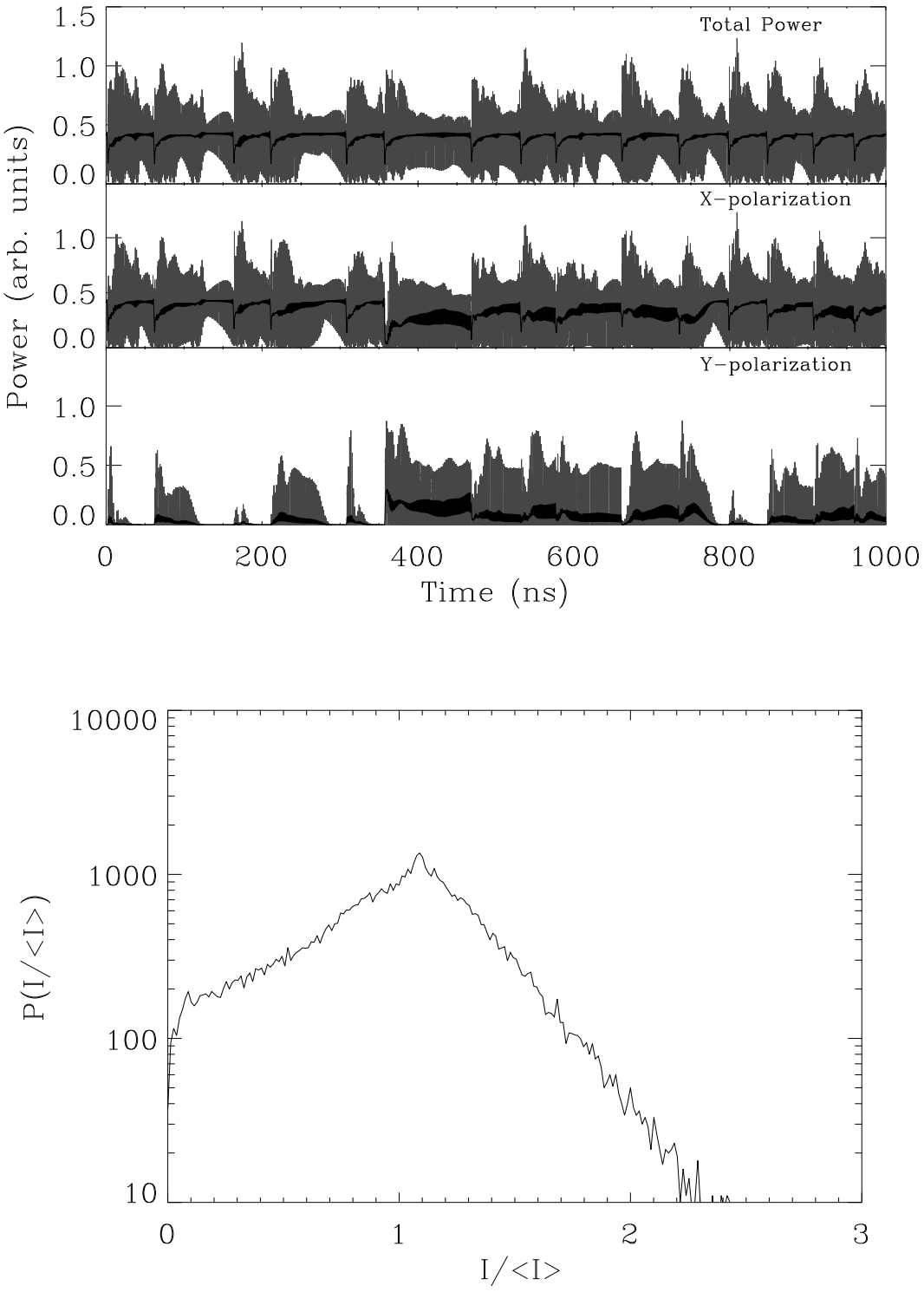

Figure 3.10: (above) Same as Fig. 3.8, but for $\mu = 1.5$, (below) Histogram of the values of the total power for $\mu = 1.5$ during the time span corresponding the figure above

to the solitary laser threshold. In the experimental results, LFF appear in a restricted current range below the solitary laser threshold. Instead, the numerical simulations do not display LFF until $\mu > 1$, i. e. above the threshold of the solitary $VCSEL$, although antiphase oscillations at the external-cavity round-trip time may occur for $\mu < 1$. We think that the reason for such a discrepancy is likely to be that in the theoretical model the frequency dependence of the gain and refractive index (α-factor) have not been considered. The emission wavelength of the $VCSEL$ with feedback is noticeably redshifted with respect to that of the solitary $VCSEL$, which may involve substantial changes in the $VCSEL$ parameter values not taken into account in the theoretical model. The inclusion of such effects requires a dynamical model that includes the spectral dependence of both the gain and the linewidth enhancement factor, and is currently under investigation.

Chapter 4

Conclusions

In this dissertation we have analyzed the dynamics of semiconductor laser when part of the light emitted is re-injected into the laser cavity by a distant mirror. In particular, we have explored the so-called strong and moderate feedback regimes. This parameter region is characterized by the presence of Low-Frequency Fluctuations (LFF) in the output intensity of the system. We have described in details the phenomenology of this instability and we have explored its statistical properties. On the base of these observations we have revealed the dynamical origin of the LFF. The dynamical scenario leading to the saddle node-Andronov bifurcation together with the unavoidable presence of noise in the system appears to be at the origin of these drops. Since a dynamical system exhibiting this scenario is excitable, we have tested the response of our system to external perturbations, finding the threshold-like behavior typical of the excitable media. This evidence provides a further confirmation on the correctness of our dynamical interpretation of the LFF. Moreover, it is the first experimental evidence of *excitability* in an optical system. This first observation opens a very interesting line of research in the analysis of semiconductor laser with feedback. The dynamical scenario on which excitability takes place in our system may be further investigated by changing the excitation rate and analyzing the response of the system. This work, still on progress, can shed light on to the influence of the parameters on the dynamical

properties of semiconductor laser with optical feedback. Moreover, we are going to analyze the behavior of coupled excitable media by using two semiconductor laser with optical feedback systems coupled together.

Noise role in the excitable systems can be very important; we have measured the regularity (or coherence) of the system output as the noise level into the laser is varied and we have found a maximum of regularity for a finite noise level. Thus, below this level, noise improves the regularity of the output signal. This is the first experimental evidence of the so-called *Coherence Resonance*, theoretically predicted in excitable systems.

We have provided the experimental evidences in order to draw one of the simplest dynamical model able to describe the LFF phenomenon. We have found good qualitative agreement between the prediction of this model and the experimentally observed statistical properties of the LFF, confirming the correctness of our dynamical picture.

We have also obtained strong indications about the physical mechanism at the origin of the LFF-instability. We have pointed out the strong dependence between the number of active longitudinal-modes and the rate of LFF. We have shown that LFF appear together with the excitation of several modes of the solitary laser. By means of time-resolved spectral analysis we have showed that the instabilities at low frequency are generated by the interaction among different modes of the laser. Using a streak-camera system with time-resolution of the order of picoseconds we have showed that the fast pulsing of the total intensity is a consequence of the time delay and multi-mode operation of the laser. These experimental observation are beyond the possibility of the widely-used Lang-Kobayashi model which is based on a rate-equation and single-mode description of the solitary laser. Our observations are instead in qualitative agreement to what predicted by the Solari-Duarte analysis, where the laser is described by

an effective two-level model and the optical feedback is considered through the boundary conditions imposed by the double cavity.

In order to force the edge-emitting laser to be single-mode, we have explored an experimental configuration where the optical feedback is frequency-selective, describing the characteristics of the system when the frequency of the feedback is tuned. Even in this case power drops appear bounded to the excitation of side modes of the solitary laser. It can be interesting, for the future, to analyze the internal-cavity-mode dynamics of a DFB semiconductor laser with optical feedback in the LFF-regime. This can provide further confirmation on the role of solitary laser modes as LFF appears.

In this spirit we have analyzed the influence of feedback on a Vertical-Cavity Surface-Emitting Lasers ($VCSEL's$). For the extremely wide separation between longitudinal-modes, $VCSEL's$ is, from this point of view, a single-mode device. On the other hand, not having a strong mechanism for selecting the polarizations, the $VCSEL's$ may have two active polarization modes. Even in $VCSEL's$, a low frequency fluctuation instability appears for moderate-to-strong feedback level. In this device we have shown that the instability is due to the interaction between the two different polarization-modes. We have also worked on a model that provide a qualitative agreement with the experimental evidences. Further work is required to improve the quantitative agreement. In particular, we want to tune the cavity resonance in respect with the gain peak by changing the laser temperature. In this way we can explore regions of the parameter-space not achievable with the usual parameters (current, feedback level), allowing for a complete comparison with the polarization dynamics predicted by the theoretical model.

Appendix A

Experimental Set-up

One of the main difference between the semiconductor lasers and the other kinds of lasers is the order of magnitude of the time-scales involved. As shown in the first chapter, the typical photon lifetime in the cavity is from few ps to few tenth of ps, while the relaxation oscillations are of the order of GHz. Thus, the semiconductor lasers are very fast dynamically. Fast time response is the basic requirements for the semiconductor laser monitoring equipment. The typical bandwidth for the detection system dealing with semiconductor lasers ranges from 1 MHz up to tenth of GHz. Unfortunately the state-of-art of the microwave electronics technology set a limit for the bandwidth of detectors and, most important, of the single-shot oscilloscopes. Actually the maximum analogue cut-off frequency for a commercial single-shot scope is of the order of few GHz. This limit is largely overcome when sampling-mode technique is applicable; commercially available sampling heads reach 60 GHz and more. On the other hand, this working mode requires strictly periodical signals and periodicity is not, in general, guaranteed in the temporal characterization of a dynamical system. Indeed the sampling-mode technique is very useful in the engineering of the semiconductor laser for telecommunications, where the periodicity of the signal is determined by the modulational clock.

The detectors normally used are Avalanche Photodiodes that covers a bandwidth from zero to few GHz (2.5 GHz typical). In Fig. 2.1 we showed the typical experimental configuration for our experiment. This configuration is bandwidth limited by the Avalanche Photodiode (2 GHz) detector and by our scope bandwidth (500 MHz) for the time-series monitoring. The set-up shown in Fig. 2.1 is the one used for the general characterization of the behavior of the system versus the control parameters. Other configurations allows to reach higher cut off frequency but they are not so convenient for compactness, flexibility and simplicity as the one showed. Indeed, other configurations have been used when characterizing a particular phenomenon in details. For example, in order to overcome the bandwidth limit for the single shot monitoring, we used a Streak Camera (time-resolution of 16 ps) as an alternative to the oscilloscope.

The electrical connections must be compatible with the high frequencies into play: we used SMA technology ($0 - 20$ GHz bandwidth) for cables, connectors, attenuators, power splitter, bias-TEE. Great care has been paid in the grounding and connecting procedures of the detectors and of the sources. Microwave detection is very sensible to external noise sources: the wires must be the shortest as possible and axial connection (for the lasers and detectors pins) to the SMA plugs is required.

The fast time-scales involved in the laser present also some advantages: spurious mechanical vibrations of the supports and thermal instabilities interact with the system on time-scales much slower than the ones of the laser and they can be easily distinguished and separated.

The laboratory equipment could be grouped in four main parts: the mechanical parts, the optical parts, the detection parts, the sources parts. The first group is composed by all the parts used for controlling the optical signal: lenses, polarizers, mirrors , beam splitters and so on. The second group is formed by

the supports needed for setting up the experiment in all its parts: the optical table, the supports for the optics, the supports for the sources, the supports for the detectors. The third group is composed by all the detecting and measuring instruments: the detectors, the oscilloscopes, the signal analyzers and so on. Finally the sources group is meant to be the ensemble of optical sources (lasers) with their controlling instruments like power supply and thermal controller. In the following sections we will describe the characteristics of these parts in our semiconductor laboratory.

A.1 The optics

The optical parts used include output couplers, lenses, mirrors, beam splitter, polarizing beam splitter, neural density filters, diffraction grating.

Output Couplers. Since the output beam of the semiconductor laser is strongly divergent, the presence of an output coupler is necessary to reduce the beam spread. In order to couple the maximum amount of light, this coupler must have large numerical aperture. Moreover, the output couplers must be AR-coated for the lasing wavelength for avoiding spurious back reflection. To match these requirements we use $Rodenstock^{TM}$ collimators of the series 1403 (see table A1).

ORD. NUM.	foc. leng.	num. apert.	Wavel.	Img. Field ⌀	Qual. λ^2/x
140-000-20	7.5 mm	0.30	780 - 890	0.12 mm	500
137-000-20	9.0 mm	0.25	780 - 880	0.20 mm	500
108-000-20	5.0 mm	0.50	800 - 850	0.14 mm	400

Table A1: collimators characteristics

Beam Splitters have been used either for the detecting part of the set-up either as part of the external-cavity. In the external-cavity they have been used as external-cavity mirror or as internal splitter to extract light from the compound system. We used:

Eksma^{TM} *P.O. 867/OLI/EKS/96* plano beam splitter AR/R $50/50 \pm 10$ at $800 - 900\ nm$, Angle of Incidence (AOI): 0^o (if it is placed at 45^o we measured different reflection for the two polarizations // and $\perp$: 58% //, 43% $\perp$).
The AR coating of the second face prevents from self-interference of the optical field inside the beam splitter. In this case the beam splitter would behave as a low finesse etalon and the power transmittivity would become wavelength dependent. The angle of incidence indicates the angle at which there is no polarization changes in the reflected (or transmitted) beam in respect with the incoming beam. If the system has just a single polarization axis, like in edge-emitting lasers, the AOI just changes the amount of light reflected or transmitted from the beam splitter, which is not critical for the experiment. On the other hand, when the system has not a well defined polarization axis ($VCSEL's$), it is important to avoid effects of this kind since they destroy the polarization isotropy of the feedback. In order to avoid any alteration of the polarization properties of the laser beam polarization preserving element must be used into the external-cavity. For this purpose we have used a beam splitter $MellesGriot^{TM}$ $03BTL039$ that, at $830\ nm$, for $AOI = 45^o$ assures the same transmission for the p-plane and s-plane and a difference of less than 2% in the range $810 - 850nm$.

Mirrors. We have usually used gold mirrors of a reflectivity larger than 95%. Other materials (like Al) have been used used as external-cavity mirrors for reducing the amount of feedback. Dielectric mirrors has been used sometimes in order to get a transmitted output from the compound system; this avoids the intracavity beam splitter which extracts the monitoring beam. In the $VCSEL$ experiments we have used the *Eksma*^{TM} *P.O 867/OLI/EKS/96* wedged mirror as external-cavity mirror. In fact, due to the beam characteristics of the $VCSEL's$, the self interference effects in the conventional two parallel faces beam splitter persisted in spite of the AR coating (see section A6)

Polarization-resolving beam splitter as Glenn Taylor have been used to resolve the two polarization axis in $VCSEL's$. The orthogonality of the beam with this device may cause spurious back reflection. It is advisable to tilt slightly the beam splitter in order to avoid this problem since an optical isolator would modify the polarization of the field.

Neutral density filter could be used in order to control the feedback level, as far as they do not cause self-interference effect of the beam.

Optical Diodes were used to suppress spurious back reflections. We have used an optical isolators OFR^{TM} *IO-2-840-LP* with an isolation power of -35 dB. This isolator is composed by a Faraday rotator with two polarizers.

Holographic diffraction grating has been used to realize frequency-selective optical feedback. We have used a *Milton* Roy^{TM} *35-83-16-330 Sr 5138*, gold coated, 1800 grooves/mm and absolute efficiency measured in near Littrow (8^o between the incident and diffracted beam): 90% for polarization orthogonal to the grooves, 15% for polarization parallel to the grooves.

A.2 The supports

The mechanical parts of the semiconductor lab include the mountings for the sources, for the optics and for the detectors. The first important element is the optical table. In our case it was a $Newport^{TM}$ board standing on air chamber that provide amortization of the vibrations. The mounting for the sources guarantees good and stable electrical contact, the possibility of grounding the laser terminal when it is switched off, good thermal contact with the Peltier cell (thermal paste has been used to increase the heat conductivity). The mounting for the laser must ensure good heat dissipation and easy accessibility at the two sides of the laser facets for placing the coupling optics. For the output coupler, in order to control accurately the mode matching and the alignment, we have used always

a micrometer positioner with XYZ movements ($Newport^{TM}$ M-466). For the external cavity mirror we used a $Newport^{TM}$ M-600A-3 with micrometer screws, in order to control carefully the alignment.

A.3 The detectors

We used four classes of detectors: Avalanche Photodiode ($Mitsubishi^{TM}$ *PD1002*, *Silicon Sensor*^{TM}*230 -i*). The first were used for conventional measurements. Their bandwidth (up to 3 GHz) covers the analogue bandwidth of the scope and enable the detection of the widest part of phenomena occurring in semiconductor lasers. The silicon photodiode have been used for measuring requiring a low bandwidth and large active region of the detector like the power measurements for the L/I curves or after a Fabry-Pérot spectrum analyzer. We list the avalanche photodiode characteristic in tables A2 and A3:

name	MITSUBISHI PD 1002
Active Aerea	200 μm
Total capacit.(C_j)	1.1 pF
Break-down volt. (V_{BR})	100-200V (150V typ.) (100 μA)
Spectral respons.	0.45 A/W (50 V, 800 nm)
Cut-off freq.	2 GHz (R_L 50 Ω)
Dark current (I_D)	0.8 nA (50 V bias)
Mult. Rate	1000 (R_L 1 KΩ, I=10 nA)
Quantum Efficiency	77% (50 V, 800 nm)
Inverse Current (I_R)	200 μA ($T < 80^o$)
Direct Current (I_F)	10 mA ($T < 80^o$)
NEP	1 X 10 $^{-14}$ W/$\sqrt{Hz}$ (800 nm)

Table A.2: Mitsubishi PD 1002 Data Sheet

name	SILICON SENSOR 230 -i
Active Aerea	230 μm
Total capacit.(C_j)	1.5 pF
Break-down volt. (V_{BR})	166.7 V (I=2μA)
Spectral respons.	0.45 A/W (780 nm)
Cut-off freq.	2 GHz (R_L 50Ω)
Rise Time	180 ps
Optimum Gain	50-60
Gain M	200 (min.)
Excess Noise factor	2.2
Excess Noise index	0.2
Noise current	0.5 pA/ $\sqrt{Hz}$
NEP	1 X 10 $^{-14}$ $W/\sqrt{Hz}$(800 nm)

Table A.3 Silicon Sensor 230 -i Data Sheet

A.4 The instruments

Oscilloscope. We used a $LeCroy^{TM}$ 7200A in order to monitor the time signal of our system. The $LeCroy^{TM}$ 7200A is a two channel digital oscilloscope with a 500 MHz analogue bandwidth and 1 GHz digital bandwidth (extension up to 2 GHz in one channel mode). This scope has a memory of 1 million of points and allows long time-series acquisition. Hence the possibility of employing this instrument for statistical measurements.

Power Spectrum Analyzer. We used a *Hewlett-Packard*^{TM} *HP8593 C* with a frequency range from 9 KHz up to 22 GHz. The electrical signal sent to the spectrum analyzer was amplified using a microwave amplifier *Hewlett-Packard*^{TM} *HP83006 A* with a gain of 20 dB and a bandwidth 10 $MHz - 26.5$ GHz.

Scanning Fabry-Pérot. Two Fabry-Pérot systems were used: A *Tropel* ^{TM} *mod. 350* and a *Thorlabs*^{TM} *MDT 690* piezoelectric driver with the KC1-PZ piezoelctric Kinematic Mount. The mirrors used were two plane mirrors $EKSMA^{TM}$

P.O. 867/OLI/EKS/96 with a flatness over $\lambda/10$, High Reflection Coated at $820 - 900\ nm$, $R > 99.5$ (Finesse of 200) and AR-coated at $820 - 900\ nm$. The Free Spectral Range (FSR) was varied according to the measurement. We have used a FSR up to 3000 GHz in order to monitor the entire set of laser internal-cavity modes, and a FSR of 200 GHz in order to check the spectrum of a $VCSEL's$. In using the Fabry-Pérot we have always checked there was not light fed back into the laser system by the mirrors of the interferometer. In general, for $FSR > 100\ GHz$, a slight tilting of the Fabry-Pérot was enough to misalign the returned beam with the laser system, without loosing a great amount of Finesse. When this procedure was not possible we have used optical isolators (sometimes two of them were required). The output of the Fabry-Pérot has been monitored using a *BPW 32* silicon photodiode. The signal was monitored on a *Tektronix*^{TM} *TDS 420* scope.

Pulse Generator. We used a *Hewlett-Packard*^{TM} *HP8593 C.* This instrument allows to pulse the laser with pulses of variable width (60 ps - 1 ns), amplitude (0.1 V - 1 V) and frequency (33 MHz - 3.3 GHz).

Streak Camera. Streak-cameras are instruments for the detection of ultra-fast optical phenomena. The streak tube is composed by a photocathode, two deflecting electrodes generating an electric field orthogonal to the direction of the photo-electron beam emitted by the photocathode, a Multi Channel Plate Photo-multiplier (MCP) and a Phosphor screen. Light enters into the streak tube passing through a slit and a lens system focusing the slit-image on the photocathode. Light hits the photocathode that generates photo-electrons. These are accelerated by a strong longitudinal electrical field between the photocathode and the meshing electrodes. The accelerated photo-electrons passes in between two deflecting plates to which a voltage signal is applied. The photo-electrons are then deflected of an angle proportional to the voltage difference applied to the

plates. A known signal applied to the plates allows to associate to every deflection angle a known time-interval. In the single-shot streak camera the deflecting signal is a ramp. Since the ramp rise time is known, the deflection induced on the electron beam gives a direct indication of the time. In this way, the temporal information has been transformed into a spatial information and every angle is associated to a time. When deflected, the photo-electrons are spread along the direction parallel to the electrical field between the two plates; they hit the MCP unit that increases their number of a factor of ≈ 5000. Finally the electrons hits a phosphor screen and they are converted in an optical image called *streak image*. This image is a stripe of points of different intensities. Every point of the stripe is associated to a time and the intensity of the point is associated to the intensity of the electro-magnetic field at that time. A CCD detector register and analyze the streak image.

The streak-camera avoids the usual bandwidth problems of the conventional oscilloscope cause there is not a real-time detection of the optical field. The technical problem is just to supply a wide-amplitude, fast rise-time ramp signal to the deflection plates. The ramp characteristics together with the density of MCP channels determines the time-resolution of the streak camera. The time-resolution is also limited by the beam spot size on the photocathode. For this reason, it is advisable to focus at most the light beam onto the photocathode. Finally, it is important to have high density pixel CCD arrays, in order to be able to distinguish the channels onto the phosphor screen.

Using the femtoseconds pulses from a mode-locked Titanium Sapphire laser we have measured the time-resolution of the instruments and we have calibrated the time reference on the streak image. For our streak system we have reached a time-resolution of 16 ps with a time span of 4.5 ns. The time span is variable, by changing the ramp slope, up to 65 ns; in this case the time-resolution drops

to 230 ps.

The biggest problems involved in using a streak-camera are related to the low sensitivity of this instrument. This problem is normally avoided using synchro-scan streak-camera. In this system the signal to be monitored is synchronized with a sinusoidal signal applied to plates. If the signal has a repetitive feature whose frequency is equal to the frequency of the plate signal, this feature appears always at the same position of the streak image. In this way, the signal over noise ratio (S/N) is increased remarkably. Streak-camera are used in synchro-scan when used for monitoring the laser response to modulation or transients. In our case this solution is not applicable, since LFF are not periodical in general. Moreover, previous measurements showed random time intensity fast pulses that would be washed-out by a synchro-scan detection.

The low radiant sensitivity of the photocathode determines the low streak-camera sensitivity. Moreover, there several sources of power losses for the incoming light intensity: the losses at the input system of slit and optics (50%), the losses for the photo-electrons hitting the separation of two adiacent channels of the photo-multiplier and, finally, the losses at the interface CCD/phosphor screen. We avoid the losses at the input optics by focusing the spot size directly into the photocathode, removing the optical system at the entrance of the photo-tube. We also used a fiber coupled and thermo-electrically cooled high-sensitive CCD array in order to reduce at most the losses at the interface phosphor screen/CCD. Our photocathode spectral response curve gives a radiant sensitivity of 0.5 mA/W at 830 nm for a quantum efficiency of 0.1%. This sensitivity is very small in order to monitor the output from a low power semiconductor laser. For this quantum efficiency the probability for the photocathode to generate a photo-electron when a photon hits its surface is extremely low. Therefore, the monitoring of the real optical signal is strongly affected by the shot-noise of the streak-camera

apparatus. In this condition, a weak but constant beam of photons hitting the photocathode (CW optical signal) is monitored as a sequence of pulses as a result of the low number of photo-electrons and the high intensifier gain. This effect is more dramatic when the time-resolution is high and the time span is small as a consequence of the smaller time integration of the photo-electron beam on each point of the phosphor screen. These problems have prevented us to use our streak system to monitor the output from an $Hitachi^{TM}HLP1400$ with optical feedback. The emission power of an $Hitachi^{TM}HLP1400$ with optical feedback in the LFF-region is, in the most favorable conditions, of the order of 0.8 mW. In order to evaluate the reliability of the streak system in this condition, we have monitored the power equivalent CW output power from the laser without feedback. The signal obtained by the streak-camera with time-resolution of 16 ps (4.5 ns time span) showed pulses on a negligible DC component.

In order to estimate the minimal power requirement for getting a reasonable S/N ratio in our detecting system, we have used an $He-Ne$ laser emitting at 630 nm. At this wavelength the spectral response of the tube is 40 time better than at 830 nm: 20 mA/W for a 3% quantum efficiency. We have varied the intensity of the CW incoming beam and we have found that the minimal power for having a S/N ratio of ≈ 5 is 0.2 mW with a time-resolution of 16 ps. The equivalent minimum power requirement value at 830 nm is of 8 mW, well beyond the power characteristics of a laser exhibiting LFF. Then, we have decided to use a 630 nm semiconductor laser, instead of the more conventional $Hitachi^{TM}HLP1400$.

A.5 The optical sources and their control

We have used several different commercial laser devices. These sources were the most used in the literature concerning similar experiments. We list here below

the devices used and their characteristics.

SDL^{TM} 5400 C: edge-emitting $GaAlAs$ laser emitting at 822 nm (rate power of 50 mW), MQW structure. The cavity length is 750 μm long for a FSR of 50 GHz (measured value). The laser emits on the foundamental Gaussian mode. Typical characteristics for these lasers are:

Spectral Width (nm)	3 (typ.) 5 (max)
Slope Efficiency (mW/mA)	0.75 (min) 0.9 (typ)
Conversion Efficiency	30
Emitting Dimensions (μm)	3X1
Beam Divergence (FWHM)	9^o $\parallel$, $30^o\perp$
Threshold Current (mA)	35 (typ) 55 (max)
Series resistance R (Ω)	4 (typ) 6 (max)
Voltage	1.5 V + RI
Thermal resistance	60^o C/W

Table A.4: SDL 5400 C Data Sheet

$Hitachi^{TM}$ HL6314MG: edge-emitter $AlGaInP$ laser emitting at 635 nm, index guided MQW structure, lasing on foundamental Gaussian mode, emitting around 630 nm, with a mode spacing of $\approx$ 135 GHz. Other parameter of the laser are:

Emitting Wavel. (nm)	635 ± 5
Polarization Ratio (@3 mW)	> 350
Beam Divergence (FWHM)	$8^o \pm 2^o$ $\parallel$, $30^o \pm 9^o\perp$
Threshold Current (mA)	25

Table A.5: Hitachi^{TM} HL 6314MG Data Sheet

$Hitachi^{TM}$ HLP 1400: edge-emitting $GaAlAs$ laser, emitting at 840 nm, bulk structure, double-hetero-structure technology and Channel Substrate Planar (CSP) horizontal wave-guiding channel (index guided) whose size confine the emission to single transverse-mode. The cavity length is around 300 μm and the separation between the longitudinal-mode is of 125 GHz (measured value), the reflectivity of the cavity mirrors is defined by the index gap *semiconductor (n≈3.5) / air* and

it is R≈35%. In some experiments we used devices with one mirror AR-coated up to 1%. In the following table we represent the most used parameter for this laser.

Active region(L,W,T)	L_d, w, d	$300, 4, 0.1\ \mu m$
Volume	V	$1.2x10^{-16}\ m^3$
Refr. Index	n_ϕ	3.5
Reflect. at laser faces	$r_1 = r_2 = (n_\phi - 1)/(n_\phi + 1)$	0.5556
Group Index	$n_g = n_\phi + \omega \frac{\partial n_\phi}{\partial \omega}$	4.0
Group Velocity	$v_g = \frac{c}{n_g}$	$7.5x10^9\ cm\ s^{-1}$
Round-trip time	$\tau_c = 2n_g L_d/c$	$8.0\ ps$
Vacuum wavel.	λ_0	$853\ nm$
Absorp. losses	α_a	$45cm^{-1}$
Mirror losses	$\alpha_M = \frac{1}{L_d} \ln \frac{1}{R_2}$	$39.2\ cm^{-1}$
Total loss coeff.t	$\alpha_l = \alpha_a + \alpha_M$	$84.2\ cm^{-1}$
Loss rate	$T_p = v_g \alpha_1$	$6.31 \times 10^{11}\ s^{-1}$
Photon lifetime	$\tau_p = \frac{1}{T_p}$	$1.6\ ps$
Conf. factor	Γ	0.25
Diff. gain	$G_N = \left(\frac{\partial G}{\partial N}\right)_{N=N_{th}}$	$2.8 \times 10^{-12}\ m^3 s^{-1}$
Carrier dens. at transp.	N_0	$1.400 \times 10^{24}\ m^{-3}$
Carrier dens. at thresh.	N_{th}	$2.302 \times 10^{24}\ m^{-3}$
Gain compres. coeff.	ϵ^{NL}	$2.5 \times 10^{-17}\ cm^3$
Non radiative recomb. rate	A_{nr}	$3.6 \times 10^8\ s^{-1}$
Radiative recomb. rate	B	$0.57 \times 10^{10}\ cm^3 s^{-1}$
Auger effect	C	$-0.6 \times 10^{29}\ cm^6 s^{-1}$
Spont. emission lifetime	$\tau_e = (A_{nr} + BN_{th} + CN_{th}^2)^{-1}$	$2.04\ ns$
Spont. emission coefficient	n_{sp}	2.552
Spont. emission rate	$R = \frac{n_{sp}}{\tau_p}$	$1.6 \times 10^{12}\ s^{-1}$
Linewidth enhanc. factor	α	3

Table A.6: Hitachi HLP 1400 data. From Ref. [11]

$Honeywell^{TM}$ $HFE4080-321$ Vertical-Cavity Surface-Emitting Laser emitting at 850 nm.

Parameter	Test condition	Values
Output Power (mW)	$I_F = 10$ mA	0.5 (min) 1.25 (typ)
Threshold Current (mA)		3.5 (min) 6 (typ)
Slope Efficiency (mW/mA)	$I_F = 10$ mA	0.3 (min)
Forward Voltage (V)	$I_F = 10$ mA	1.75 (min) 2.1 (typ)
Reverse breakdown volt. (V)	$I_R = 10$ μA	5 (min) 10 (typ)
Peak Wav. (nm)	$I_F = 10$ mA	820 (min) 850 (typ) 860 (max)
Spectral Width (nm)	$I_F = 10$ mA	0.5
Temp. variation I_{th} (mA/C)^o)		± 0.042
Temp. variation λ(nm/C^o)		0.06
Series resistance R (Ω)		30

Table A.7: Characteristics of $Honeywell^{TM}$ $HFE4080-321$

$Vixel^{TM}$ $LA-S-850-1X16-3s$, $1X16$ $VCSEL's$ laser array emitting at 850 nm. The active area is defined by proton implantation, its diameter is around 8 μm. No data sheets available. The production procedure and the laser characteristics are described in [54]

A.5.1 Laser controlling

Since the semiconductor laser is sensible to environment temperature variations, it is convenient to stabilize the device temperature during a measurement. Every device has been mounted with the laser chip submount in thermal contact with a Peltier cell and with a thermistor. The current in the Peltier cell is driven by an electronic circuit ($Hytek$ $HY-5610$) that compare the resistance of the thermistor with a set value and, according to this, warm up or cool down the Peltier surface in contact with the laser. This thermo-controlling circuit has an output signal that allows to test the amount of temperature stability reached. We

have always performed our measurements under thermal stabilization of the laser submount to better than $0.01^o\ C$. It worth to point out that this stabilization do not prevent the thermal changes inside the chip due to variation on the pumping current flow. The thermal controlling system we have used is useful for helping the laser to dissipate the heat (especially at large rated power) and to avoid over heating of the device, but it cannot help on stabilize the temperature gradient in the laser chip.

The other important controlling element of the laser is the power supply. The power supply must be a stable CW source. We have used a DC battery-based power supply in order to power our devices. The current flow was stabilized at $\pm 0.1\ mA$. Semiconductor lasers are very sensible to electro static discharge (ESD) and could be damaged if a reversed biased is applied. Great care has to be applied in handling these devices. Anti-static wrist must be always worn when it is necessary to operate on the devices. Even the laser switching on/off procedure are delicate; short-circuiting of the laser terminals is recommended during the power supply turning on/off.

A.5.2 Feedback controlling

The feedback level, after mode matching and alignment (see chap. 2.1), can be varied in different ways: i) by a neutral density filter, ii) by a polarizer, iii)by an acousto-optical modulator, iv) by changing the external-cavity mirror reflectivity. The feedback controlling must change the intensity of the returned field without changing the other characteristics of the beam, like the polarization or the frequency. We analyze different solutions versus this criterion:

Neutral density filters. They may generate self-interference of the transmitted beam, as explained before. This problem is strongly present dealing with $VCSEL's$ (see next section), where the beam quality and coherence is very high

and self-interference on two parallel facets occurs easily. In the case of the edge-emitter we have not remarked the presence of such effect, mainly because of the lower quality of the beam shape; we have just tilted the filter in order to avoid spurious back reflections.

Polarizing Filters. It is a valid solution when dealing with edge-emitter beams, as far as the rotation of the polarizer does not affect the alignment. Modifying the polarization state, this method could not be used in the experiment with $VCSEL's$.

Acousto-optical modulator. This method exploits the acousto-optics properties of some crystals. These crystals change their index of refraction when an electric field is applied at the ends of the crystal block. If a sinusoidal electric field is applied to the crystal block at an acoustic frequency (typically 80 MHz) and the crystal length support such a frequency, then an acoustic standing wave settle down along the crystal block. Such a standing-wave determines a modulation of the index of refraction of the crystal and the crystal behaves like a diffraction grating for an incoming optical beam. The efficiency of this grating (i.e. the relative intensity of the first order in respect with the zero order) depends on the modulation depth of the refraction index and therefore on the amplitude of the electric field applied to the crystal. Modulating at low frequency the 80 MHz signal it is possible to tune continuously the intensity of the zero order beam respect with the first order beam intensity. One can also control easily the feedback level by applying a DC signal to vary the amplitude of the 80 MHz signal. The zero order intensity can be varied from the maximum (zero grating efficiency) to a minimum (maximum grating efficiency). The first order intensity can be varied from zero (zero grating efficiency) to a maximum (maximum grating efficiency). It is important to point out that the first order beam is shifted of 80 MHz in respect with the incoming signal. As any other grating, the efficiency is strongly

dependent on the polarization of the field. In the case of $VCSEL's$ this methods can not be applied because it is not polarization preserving.

External-cavity mirror reflectivity. Varying the feedback level by changing metallic mirrors having different reflectivities, avoids all problems of polarization alteration of the feedback field and of self-interference effects. On the other hand, once changed the mirror, re-alignment of the optics is required, and this may not be acceptable during a measure devoted to characterize the laser behavior when sweeping the parameters. If the feedback mirror is a dielectric one, self-interference problems may be reduced if the second face of the mirror is AR-coated or, better, tilted respect the reflecting one (wedged beam splitter). Moreover, normal incidence is required normally to avoid polarization alteration of the reflected beam respect with the incoming one.

A.6 Experimental problems dealing with $VCSEL's$

The feedback level when dealing with $VCSEL's$ cannot be controlled, unless changing the reflectivity of the external mirror, i.e. rebuilding the set up. The presence of a laser dynamics involving modes with different polarization axis excludes the possibility of employing polarization sensitive devices like Acousto-Optical Modulators or Polarizer Filters, otherwise we alter the polarization isotropy of the external-cavity. Moreover, as explained before, Neutral Density filters and Beam Splitters inserted in the external-cavity behave as an interferometer filter (etalon). Indeed, the strong coherence of the $VCSEL$ beam and the regular circular shape of the spot size make the system very sensitive to self-interference effect. The same effect was noticed from the glass window that covers the detectors, and also from AR-coated Beam Splitters, mainly due to residual reflection of the back facet. All these problems were evidenced analyzing the output of solitary $VCSEL$ elements versus pumping current. If we insert optics with parallel

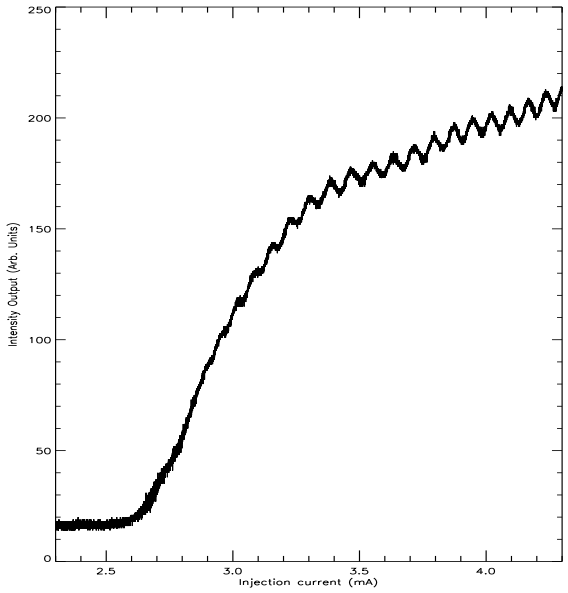

Figure A.1: L/I curve of a $VCSEL$ element showing the undulation originated by self-interference effect in optics interposed between the laser and the detector. In this case self-interference was occurring in a beam splitter placed in front of the detector. The undulation period depends on the incidence angle of the beam onto the beam splitter, the L/I curve of the same laser element does not present any undulation when this spurious etalon effect is removed.

facets between the detector and the collimator, the L/I curve of the $VCSEL's$ shows regular undulations (see Fig. A1) appearing periodically as the current is increased. This periodicity could be changed and eventually eliminated tilting or removing the optical elements interposed between the laser and the detector. In fact, changing the pumping current the emission wavelength of the laser is tuned and the signal is filtered by the Airy function of the parasitic etalon.

This problem has several consequences: i)We cannot use Neutral Density filter to control the feedback level, ii)The use of Beam Splitters for intracavity applications, as external-cavity mirror and in a Fabry-Pérot interferometer, requires great care. In particular it has been found that the AR-coating on the Beam Splitters normally used is not efficient enough to eliminate the problem. Only wedged beam splitters, not having the two faces parallel, can avoid the problem. iii)It is advisable not to use detectors with a glass window. These criteria limit

the possible experimental configurations of the external-cavity. In order to obtain an isotropic feedback, not affecting the polarization and the frequency of laser emission, we have used the configurations of Fig. 3.1. In the first case we used a metallic (gold or aluminum) mirror as external mirror to provide optical feedback. The output beam was obtained by putting an AR-coated, polarization-preserving beam splitter in the cavity and using the reflected beam for feedback and the transmitted one to get the output beam. This beam splitter was tested for not exhibiting any etalon effect at its working angle (45^o). We used this configuration to obtain the strongest feedback. In the second we used a wedged glass substrate to provide feedback: we get then a reflectivity of 4% and we were able to use the transmitted beam to monitor the system. We used this configuration to obtain a weaker feedback level.

When the etalon effect is present in the beam splitters that constitute the two mirrors of a scanning Fabry-Pérot, the measurements of optical spectra are altered. In fact, convolved with the Airy function of the interferometer cavity, there is the Airy function relative to the parasitic etalon. The resulting effect is a modulation in the transmission vs. frequency curve of the scanning Fabry-Pérot, having a period of about 20 GHz that corresponds to the thickness of the beam splitter. When the laser has a narrow emission this effect does not disturb too much if we want to deduce just the qualitative indications from the Fabry-Pérot. On the other hand, if the optical linewidth is broader than 20 GHz, then the optical spectrum exhibits broad peaks separated of 20 GHz that are just an artifact from the set up.

Appendix B

Comparison with LFF statistical measurements reported in the literature

Statistical measurements on LFF have been performed by several groups and there is discrepancy between the results obtained. Sacher et al. [137] have found that, defining $\epsilon = (I - I_{th,sol})/I_{th,sol}$, there is a dependence $< T > \propto \epsilon^{-1}$. They interpret the LFF as a manifestation of time-inverted type II intermittency. This interpretation is justified by considering the LFF time-interval distribution curves and the Poincaré plot of the intensity of consecutive minima of the fast oscillation component at τ_{ext}. Further statistical measurements do not agree with Sacher measurement of $< T >$ vs. ϵ, especially for large feedback level and for low pumping current [138, 139, 102], i.e. at the beginning of the LFF-regime. Our measurements too do not support Sacher interpretation. In our opinion Sacher power-law $< T > \propto \epsilon^{-1}$ is strongly related to the choice of the current value at which LFF appears. In general, the power-law paradigm of a type II intermittency phenomenon scales with the normalized control parameter value $\epsilon = (I - I_0)/I_0$, being I_0 the parameter value at which the intermittent phenomenon takes place [28]. In [137] I_{lff} is assumed equal to $I_{th,sol}$ since LFF appears, for the feedback level explored by Sacher, at the solitary laser threshold.

In fact, this assumption is not justified since noise rules the appearing of LFF. The real value of I_0 for the LFF phenomenon is hidden by the presence of noise which anticipates the bifurcation; then, the methods for the identification of a purely deterministic process are not applicable.

Another model for explaining the statistics of the time-intervals in the LFF-regime is the one proposed by Henry and Kazarinov [140]. Using the dynamical ingredients predicted by Lang-Kobayashi model (see §II.6.1), they analyze the stability of the "maximum gain mode" attractor in presence of a stochastic perturbation. They compare the dynamics of the system to the motion of a particle in a potential well where the spatial coordinate is the deviation of the carrier density from its stationary state value. The escape of the particle over the barrier corresponds to a drop. Then, the statistics of the time interval between drops are described by Kramer's theory. Even if we do not agree on the dynamical scenario arising from the Lang-Kobayashi model for the feedback levels involved in our experiment (see §II.6.1), Henry and Kazarinov model is close to our interpretation of LFF as the system departing from a stable state under the action of noise. The experiments comparing to Henry-Kazarinov model find qualitative but not quantitative agreement with the theory. We can compare these results with ours:

In [138] they find LFF time-interval distribution curves very similar to ours with a refractory time, exponentially decaying tails and double peaks in the distributions for a given range of the pumping current values. They investigate also the dependence of $< T >$ on the pumping current, finding curves very similar to ours. The comparison with Henry-Kazarinov holds for low pumping current values but it fails for large values.

In [139] they investigated dependence of $< T >$ on the pumping current and on the feedback levels. The curves obtained changing the feedback level are in

qualitative agreement with ours for equivalent parameter values. On the other hand, we can not compare the results for $\xi > 12\%$ since we have not reached, in the laser employed for the statistics, such strong feedback level. Moreover we have not observed, for feedback level $\xi > 10\%$, LFF appearing below the solitary laser threshold as they did. In [139] they claimed perfect agreement with Henry-Kazarinov model for the dependence of $< T >$ changing the feedback level. On the other hand, no fitting with this model has been tried versus the pumping current. It worth to note, in [139], the non-monotonic dependence of $< T >$ with feedback level (at $I/I_{th} = 0.98$) similar to what we have observed, which, in addition, is not in agreement with Henry-Kazarinov model.

In [102] they have measured the LFF time-interval distribution curves, finding curves very similar to ours. In particular they have observed that the index R is close to one for low pumping current and then it decreases to $R = 0.3$ for large current values. Instead, their results on the dependence of $< T >$ on the pumping current, showing $< T >$ non-monotonically decreasing I, is in contradiction with ours and with the other experimental results here reported.

Appendix C

$VCSEL's$ with feedback model details

The case considered here corresponds to a single-mode $VCSEL$ which, due to growth-induced stresses, presents some small amount of birefringence and dichroism. The main effect of small birefringence is to induce a frequency shift of the two linear polarization orientations of the fundamental mode, leaving the mode profile almost equal to that of the perfect waveguide. Then, each Fourier component of the electric field distribution inside the $VCSEL$ cavity can be written as

$$\mathcal{E}_{\pm}(\omega, z, \rho) = A_{\pm}(\omega)\Psi_{\omega}(z)U_{\omega}(\rho) \ . \tag{C.0.1}$$

In this equation, $A_{\pm}$ is the amplitude of each circular polarization component of the field, $\Psi(\omega, z)$ is the longitudinal field distribution, and $U_{\omega}(\rho)$ is the modal profile in the unperturbed waveguide.

$U_{\omega}(\rho)$ is given by

$$\nabla_{\perp}^2 U_{\omega}(\rho) + \frac{\omega^2}{c^2}\varepsilon_{\omega}(\rho)U_{\omega}(\rho) = \beta_{\omega}^2 U_{\omega}(\rho) \ , \tag{C.0.2}$$

where c is the speed of light in vacuum, $\varepsilon_{\omega}(\rho)$ is the transverse distribution of dielectric function, and β_{ω} the propagation constant of the mode in the unperturbed waveguide. We assume perfect mode-matching between the field leaving the top mirror and the reinjected field.

The longitudinal field distribution is given by

$$\Psi_\omega(z) = r_1 e^{iqz} + e^{-iqz} \ , \tag{C.0.3}$$

where the boundary conditions at the edges of the cavity select the allowed longitudinal wavevectors q,

$$\begin{aligned} q &= M\frac{\pi}{L} + \frac{i}{2L} ln\left(r_1 \frac{r_2 + r_3 e^{i\omega\tau}}{1 + r_2 r_3 e^{i\omega\tau}}\right) && \text{(C.0.4)} \\ &\equiv q_0 + i\phi(\omega) \ , && \text{(C.0.5)} \end{aligned}$$

r_1, r_2 and r_3 being the effective field reflectivities of the bottom, top and external mirror, respectively, and $\tau = 2L_{ext}/c$ the roundtrip time in the external-cavity. q_0 corresponds to the wavevector when no external-cavity is present,

$$q_0 = M\frac{\pi}{L} + \frac{i}{2L} ln\left(r_1 r_2\right) \ , \tag{C.0.6}$$

while $\phi(\omega)$ takes into account the effects of the external-cavity,

$$\phi(\omega) = \frac{i}{2L} ln\left(1 + \frac{1 - r_2^2}{r_2} \frac{r_3 e^{i\omega\tau}}{1 + r_2 r_3 e^{i\omega\tau}}\right) \ . \tag{C.0.7}$$

We assume that only one of these wavevectors is in the vicinity of the gain peak, hence the $VCSEL$ operates single-longitudinal-mode. Substituting (C.0.1) into the wave equation for each polarization component of the field, and assuming that they are around the carrier frequency Ω given by $M(\pi/L) = \beta(\Omega)$, the frequency components of the slowly-varying amplitudes in each circular polarization component are given by

$$-iuA_\pm(u) = -\kappa A_\pm(u) + i\Gamma P_\pm(u) - (\gamma_a + i\gamma_p)A_\mp(u) + \frac{c}{n_g}\phi(\Omega + u)A_\pm(u) \ , \tag{C.0.8}$$

where $\kappa = 1/(2\tau_p)$, τ_p being the photon lifetime in the solitary $VCSEL$ cavity, γ_a and γ_p are the dichroism and birefringence, respectively, and $n_g = (d\beta/d\omega)^{-1}_{\omega=\Omega}$

is the group index at the carrier frequency. $P_{\pm}$ is proportional to the carrier-induced electric dipole density in each of the polarizations, and describes the carrier-induced gain and dispersion. Finally, Γ is the field confinement factor to the active region for the carrier frequency Ω.

In order to obtain a time-evolution equation for the field amplitudes, we must Fourier transform back to the time domain, but the presence of the external-cavity (through $\phi(\Omega+u)$) does not allow us to obtain a closed form for the evolution equation. The usual approach is then to consider that the reflectivity of the external mirror is very small, and to expand $\phi(\Omega+u)$ to first order in r_3, which means to consider only one reflection in the external mirror and leads to the well known Lang and Kobayashi approximation [16]. Unfortunately, this approximation is not justified for $VCSEL's$ because of the large reflectivities of the Bragg mirrors, and it is essential to include multiple reflections [136]. However, the large reflectivity of the Bragg mirror allows us to find an alternative solution to the problem. If the lasing mode is close to the center of the stop band, then $r_2 \approx 1$, so $(1-r_2^2)/r_2$ is a small quantity regardless of r_3. Hence, for a $VCSEL$ we have that

$$\phi(\Omega+u) = \frac{1}{2L} ln\left(1+\frac{1-r_2^2}{r_2}\frac{r_3 e^{i\Omega\tau}e^{iu\tau}}{1+r_2 r_3 e^{i\omega\tau}}\right) \tag{C.0.9}$$

$$\approx \frac{1}{2L}\frac{1-r_2^2}{r_2}\frac{r_3 e^{i\Omega\tau}e^{iu\tau}}{1+r_2 r_3 e^{i\Omega\tau}e^{iu\tau}} \; . \tag{C.0.10}$$

Substituting it into (C.0.8), multiplying both sides by $1+r_2 r_3 e^{i\Omega\tau}e^{iu\tau}$, and Fourier transforming to the time domain, we find

$$R_{\pm}(t) + r_2\hat{r}_3 R_{\pm}(t-\tau) = \frac{c}{2n_g L}\hat{r}_3\frac{1-r_2^2}{r_2}A_{\pm}(t-\tau) \; , \tag{C.0.11}$$

where $\hat{r}_3 = r_3 e^{i\Omega\tau}$ is the amplitude reflectivity of the external mirror into the $VCSEL$ cavity including the optical phase change after one external-cavity roundtrip,

and

$$R_{\pm}(t) = d_t A_{\pm}(t) + \kappa A_{\pm}(t) - i\Gamma P_{\pm}(t) + (\gamma_a + i\gamma_p) A_{\pm}(t) \ . \tag{C.0.12}$$

The description of the system is completed with the evolution of the material variables. We take the same model as in [87, 88], which has been extensively studied and provides a good qualitative framework for the description of the $VCSEL$ properties. The only difference with [87, 88] is that we consider non-linear gain saturation. Then, the electric-dipole density is given by

$$P_{\pm} = -g(\alpha + i)\frac{N_{\pm} - N_t}{1 + s|A_{\pm}|^2} A_{\pm} \ , \tag{C.0.13}$$

which is obtained by assuming that birefringence is small enough for the two polarization components have almost the same modal gain g, α factor, transparency carrier density N_t and non-linear gain saturation coefficient, s. $N_{\pm}$ is the density of carriers with spin down (spin up) within the active region.

Bibliography

[1] G. Agrawal, N. Dutta, *Long Wavelength semiconductor lasers*, Van Nostran, 1986.

[2] K. Ikeda, H. Daido and O. Akimoto, Phys. Rev. Lett.**45**, 709 (1980).

[3] V. Petrov, B. Peng and K. Showalter, J. Chem. Phys.**96**, 7506 (1992).

[4] S.J. Schiff, K. Jarger, D.H. Duong, T. Chang, M.L. Spano and W.H. Ditto, Nature **370**, 615 (1994); J. Starret and R. Tagg, Phys. Rev. Lett. **74**, 1974 (1995).

[5] I. Györi and G. Ladas, *Oscillation Theory of Delay Differential Equations*, Oxford University Press, New York (1991).

[6] A.P. Bogatov, P.G. Eliseev, L.P. Ivanov, A.S. Logginov, M.A. Manko and K. Senatorov, IEEE J. Quantum Electron. **QE-9**, 392, (1973).

[7] R.W. Tkach and A.R. Chraplyvy, J. Lightwave Technol. **LT-4**, 1655 (1986).

[8] D. Lenstra, B. Verbeek and A.J. den Boef, IEEE J. Quantum Electron. **QE-21**, 674 (1985); J. Cohen, D. Lenstra, IEEE J. Quantum Electron. **QE-25**, 1143 (1989); J. Cohen, D. Lenstra, IEEE J. Quantum Electron. **QE-27**, 10 (1991).

[9] J.Risch and C. Voumard, J. Appl. Phys. 48, 2083 (1977).

[10] H. Temkin, N.A. Olsson, J.B. Abeles, R.A. Logan, and M.B. Panish, IEEE J. Quantum Electron. **QE-22**, 286 (1986).

[11] P. Besnard, B. Meziane and G.M. Stéphan, IEEE J. Quantum Electron. **29**, 1271 (1993).

[12] G.C. Dente, P.S. Durkin, K.A. Wilson, and C.E. Moeller, IEEE J.Quantum Electron. **24**, 2441 (1988).

[13] J. Wang and K. Petermann, IEEE J.Quantum Electron. **27**, 3 (1991).

[14] J. Mork, J. Mark and B. Tromborg, IEEE J.Quantum Electron. **28**, 93 (1992).

[15] J. Mork, Ph. D. Thesis, "Nonlinear Dynamics and Stochastic Behaviour of Semiconductor Lasers with Optical Feedback", Report # S48, March 1989, Technical University of Denmark. See Chapter 4 (pages 50-68).

[16] R. Lang and K. Kobayashi, IEEE J. Quantum Electron. **QE-16**, 347 (1980).

[17] T. Sano, Phy. Rev. A **50**, 2719 (1994).

[18] C. Masoller, Phys. Rev. **A 50**, 2569 (1994)

[19] G.H.M. van Tartwijk, A.M. Levine and D. Lenstra, IEEE J. Sel. Topics in Quantum Electron. **1**, 466 (1995).

[20] S. Balle, Optics Comun. **119**, 227 (1995).

[21] M. Homar, S. Balle, M. San Miguel, Optics Comun. **131**, 380 (1996).

[22] L.M. Narducci and N.B. Abraham, *Laser Physics and Laser Instabilities*, World Scientific, Singapore, 1988.

[23] L.M. Narducci, E.J. Quel, J.R. Tredicce, *Laser and Quantum Optics*, Proceedings of the International School on Lasers and Quantum Optics, Mar del Plata 22-31 Aug 1988, World Scientific, Singapore, 1988.

[24] P. Mandel, *Theoretical Problems in Cavity Nonlinear Optics*, Cambridge University Press, 1997.

[25] O. Svelto, *Principles of Lasers*, Plenum Press, New York, 1982.

[26] R.W. Boyd, M.G. Raymer, and L.M. Narducci,*Optical Instabilities*, Cambridge University Press, 1997.

[27] F.T. Arecchi and R.G. Harrison, *Instabilitites and Chaos in Quantum Optics*, Springer, Berlin, 1987.

[28] P. Berger, Y. Pomeau, C. Vidal *The Order within the Chaos*, Hermann, Paris, 1984.

[29] H. Abarbanel, M. Rabinovich, M. Sushchik, *Introduction to non linear dynamics for physicists*, World scientific Publishing, Singapore, 1993.

[30] H.G. Solari, M.A. Natiello and G.B. Mindlin, *Nonlinear Dynamics*, IOP publishing, London (1996).

[31] A.Yariv, *Optical Electronics*, College Publishing, (1985).

[32] M. Sargent III, M.O. Scully, and W.E. Lamb jr, *Laser Physics*, Addison Wesley Publ. Comp., Reading Mass. (1974).

[33] M. Alonso, E. Finn, *Fundamental University Physics vol. III*, Addison Wesley, (1968).

[34] M. Homar, *Ph.D Thesis*, Palma de Mallorca (1996).

[35] J.Martin-Regalado, *Ph.D Thesis*, Palma de Mallorca (1998).

[36] For a review in this topic see J.J. Coleman, "Quantum-Well heterostructure lasers" in *Semiconductor Lasers: past, present, and future*, Ed. G.P Agrawal, AIP press, New York, (1995).

[37] For a review in this topic see T.E. Sale, *Vertical Cavity Surface Emitting Lasers*, Wiley, New York, (1995).

[38] C.H. Henry, IEEE J. Quantum Electron. **QE-18**, 259 (1982).

[39] K. Vahala, L.C. Chiu, S. Margalit, and A. Yariv, Appl. Phys. Lett. **42**, 631 (1983) and C. Harder, K. Vahala, and A. Yariv, Appl. Phys. Lett. **42**, 328 (1983).

[40] G.Lasher and F.Stern, Phys.Rev. A **133**, 553(1964); M.Lax, Phys. Rev. **160**, 290, 1967; H.Haug and H. Haken, Physik, **204**, 262 (1967).

[41] W.W. Chow, S.W. Koch and M. Sargent, *Semiconductor - Laser Physics.* Springer-Verlag, Berlin, (1994).

[42] F. Stern, J. Appl. Phys. **47**, 5382 (1976).

[43] D.S. Citrin and Y.C. Chang, IEEE J. Quantum Electron. **29**, 97 (1993).

[44] H. Haug and S.W. Koch, Phys. Rev. A **39**, 1887 (1989).

[45] J. Manning, R. Olshansky and C.B. Su, IEEE J. Quantum Electron. **19**, 1365 (1983).

[46] V. Kozlov, A. Salokatve, A.V. Nurmikko, D.C. Grillo, L. He, J. Han, Y. Fan, M. Ringle and R.L. Gunshor, Appl. Phys. Lett. **65**, 1863 (1994).

[47] R. Raghuraman, N. Yu, R. Engelmann, H. Lee and C. L. Shieh, IEEE J. Quantum Electron. **29**, 69 (1993); M. Hofmann, M. Koch, H.J. Heinrich, G. Weiser, J. Feldmann, W. Elsässer, E.O. Göbel, W.W. Chow and S.W. Koch, IEEE Proc. Optoelectron. **141**, 127 (1994).

[48] S.L. Chuang, J. O'Gorman and A.F.J. Levi, IEEE J. Quantum Electron. **29**, 1631 (1993).

[49] S. Balle, Phys. Rev. A **57**, 1304 (1998).

[50] T. Lee, C.A. Burrus, J.A. Copeland, A. G. Dentai and D. Marcuse, IEEE J. Quantum Electron., **QE-18**, 1101 (1982).

[51] M. Homar, J.V. Moloney and M. San Miguel, IEEE J. Quantum Electron. **32**, 553 (1996).

[52] K. Iga, F. Koyama, and S. Kinoshita, IEEE J. Quantum Electron. **24**, 1845 (1988).

[53] G.A. Evans, J.M. Hammer, *Surface Emitting Semiconductor Lasers and Arrays*, Academic Press, Inc., San Diego (1993) and reference there are in.

[54] J. Jewell, J.P. Harbison, A. Scherer, Y.H. Lee and L.T. Florez, IEEE J. Quantum Electron. **27**, 1332 (1991).

[55] S.W. Corzine, R.S. Geels, J.W. Scott, R.H. Yan, and L.A. Coldren, IEEE J. Quantum Electron.**25**, 1514 (1989).

[56] C.J. Chang-Hasnain, J.P. Harbison, G. Hasnain, A.C. Von Lehmen, L. T. Florez, and N.G. Stoffel,IEEE J. Quantum Electron.**27**, 1402 (1991).

[57] C.J. Chang-Hasnain, M. Orenstein, A.C. Von Lehmen, L.T. Florez, J. P. Harbison, and N.G. Stoffel, Appl. Phys. Lett.**57**, 218 (1990).

[58] K.D. Choquette, G. Hasnain, Y.H. Wang, J.D. Wynn, R.S. Freund, A.Y. Cho, and R.E. Leibenguth, IEEE Photon. Technol. Lett. **3**, 859 (1991).

[59] C. J. Chang-Hasnain, Y. A. Wu, G. S. Li, G.Hasnain, and K. D. Choquette, Appl. Phys. Lett. **63**, 1307 (1993).

[60] D.L. Huffaker, D.G. Deppe, and T.J. Rogers, Appl. Phys. Lett. **65**, 1611 (1994).

[61] C.H. McMahon, J.W. Bae, C.S. Menoni, D. Patel, and H. Temkin, P. Brusenbach, R. Leigenbuth, Appl. Phys. Lett. **66**, 2171 (1995).

[62] G. Hasnain, K. Tai, L. Yang, Y.H. Wang, R.J. Fischer, J.D. Wynn, B. Weir, N.K. Dutta, and A.Y. Cho, IEEE J. Quantum Electron **27**, 1377 (1991).

[63] D.B. Young, J.W. Scott, F.H. Peters, M.G. Peters, M.L. Majewski, B.F. Thibeault, S.W. Corzine, L.A. Coldren ,IEEE J. Quantum Electron.**29**, 2013 (1993).

[64] H. C. Casey Jr., and M. B. Panish, in "Heterostructure lasers", (Academic Press, New York, 1978).

[65] J. W. Scott, D. B. Young, B. F. Thibeault, M. G. Peters, and L. A. Coldren, IEEE J. of Sel. Topics in Quantum Electron.**1**, 638 (1995).

[66] H. Li, T. L. Lucas, J. G. McInerney and R. A. Morgan, Chaos, Solitons and Fractals **4**, 1619 (1994).

[67] M.Giudici, G.Vaschenko,J.Rocca,C.Menoni,J.J.Tredicce, Optics Commun. **158**, 313-321 (1998)

[68] K. D. Choquette and R. E. Leibenguth, IEEE Photon. Technol. Lett. **6**, 40 (1994).

[69] F. Koyama, K. Morito, and K. Iga, IEEE J. Quantum Electron. **27**, 1410 (1991).

[70] Z.G. Pan, S. Jiang and M. Dagenais, R.A. Morgan, K. Kojima, M.T. Asom, R.E. Leibenguth, G.D. Guth, and M.W. Focht, Appl. Phys. Lett. **63**, 2999 (1993).

[71] H. Kawaguchi, I.S. Hidayat, Y. Takahashi, and Y. Yamayoshi, Electron. Lett. **31**, 109 (1995).

[72] K.D. Choquette, D.A. Richie, and R.E. Leibenguth, Appl. Phys. Lett. **64**, 2062 (1994).

[73] M. Travagnin, M.P. van Exter, A.K. Jansen van Doorn and J.P. Woerdman, Phys. Rev. A **54**, 1647 (1996); Opt. Commun. **133**, 252 (1997).

[74] J.H. Ser, Y.G. Ju, J.H. Shin, and Y.H. Lee, Appl. Phys. Lett. **66**, 2769 (1995).

[75] S. Jiang, Z. Pan, M. Dagenais, R.A. Morgan and K. Kojima, Appl. Phys. Lett. **63**, 3545 (1993).

[76] M.P. van Exter, A.K. Jansen van Doorn, and J.P. Woerdman, Phys. Rev. A **56**, 845 (1997).

[77] A.K. Jansen van Doorn, M.P. van Exter and J.P. Woerdman, Electron. Lett. **30**, 1941 (1994).

[78] T. Mukaihara, N. Ohnoki, Y. Hayashi, N. Hatori, F. Koyama, and K. Iga, IEEE J. of Sel. Topics in Quantum Electron. **1**, 667 (1995).

[79] T. Mukaihara, F. Koyama, and K. Iga, IEEE Phot. Tech. Lett. **5**, 133 (1993).

[80] A. Chavez-Pirson, H. Ando, H. Saito and H. Kanbe, Appl. Phys. Lett. **62**, 3082 (1993).

[81] F. Robert, P. Besnard, M.L. Chares and G.M. Stephan, IEEE J. Quantum Electron. **33**, 2231 (1997); P. Besnard, F. Robert, M. L. Chares and G.M. Stephan, Phys. Rev. A **56**, 3191 (1997).

[82] A.K. Jansen van Doorn, M.P. van Exter, and J.P. Woerdman, Appl. Phys. Lett. **69**, 1041 (1996).

[83] A.K. Jansen van Doorn, M.P. van Exter, and J.P. Woerdman, Appl. Phys. Lett. **69**, 3635 (1996).

[84] K.D. Choquette, R.P. Schneider, Jr., K.L. Lear, and R.E. Leibenguth, IEEE J. of Sel. Topics in Quantum Electron. **1**, 661 (1995).

[85] A. Valle, K.A. Shore, and L. Pesquera, IEEE J. of Lightwave Tech. **14**, 2062 (1996); A. Valle, L. Pesquera, and K.A. Shore IEEE Photon. Technol. Lett. **9**, 557 (1997).

[86] M. San Miguel, Q. Feng, J.V. Moloney, Phys. Rev. A **52**, 1728 (1995).

[87] J. Martín-Regalado, M. San Miguel, N.B. Abraham, F. Prati, Opt. Lett. **21**, 351 (1996).

[88] J. Martín-Regalado, M. San Miguel, N.B. Abraham, and F. Prati, IEEE J. Quantum Electron., **33**, 765 (1997).

[89] H. Kakiuchida and J. Ohtsubo, IEEE J. of Quant. Electron. **QE30**, 2087 (1994).

[90] J. Sigg, IEEE J.Quantum Electron. **29**, 1262 (1993).

[91] L. Goldberg, H.F. Taylor, A. Dandridge, J. F. Weller, and R.O. Miles, IEEE J. of Quant. Electron. **QE18**, 555 (1982).

[92] J.H. Osmudsen and N. Gade, IEEE J. of Quant. Electron. **QE19**, 465 (1983).

[93] D. S. Seo, J. D. Park, J. McInerney and M. Osinski, IEEE J. Quantum Electron. **25**, 2229 (1989).

[94] B.Meziane, P.Besnard and G. M. Stephan, IEEE J. Quantum Electron. **31**, 617 (1995).

[95] J. Sacher, W. Elsässer, and E. O. Göbel, IEEE J. of Quant. Electron. **QE-27**, 373 (1991).

[96] J. Mork, B. Tromborg, J. Mark and V. Velichansky, SPIE vol. 1837 (1992).

[97] F. Favre, D. Le Guen, and J.C. Simon, IEEE J. of Quant. Electron. **QE18**, 1712 (1982).

[98] R. Wyatt and W.J. Devlin, Electron. Lett. **19**, 110 (1983).

[99] E. Patzak, H. Olesen, A. Sagimura, S. Saito, and T. Mukai, Electron. Lett. **19**, 938 (1983).

[100] G.P. Agrawal, IEEE J. of Quant. Electron. **QE20**, 468 (1984).

[101] J. Mork, J. Mark and B. Tromborg, Phys. Rev. Lett. **65**, 1999 (1990).

[102] F. Cerboneschi, F. De Tomasi and E. Arimondo, IEEE J. of Quant. Electron. **QE-30**, 2277 (1994).

[103] M.P. van Exter, R.F.M. Hendiks, J.P. Woerdman, C.J. Van der Poel, Optics. Commun. **110**, 137, (1994).

[104] H.A. Kramers, Physica **7**, 284 (1940).

[105] H.Z. Risken, *The Fokker-Planck Equation*, Springer, Berlin, (1989).

[106] A. Pikovsky and J. Kurths, Phys. Rev. Lett. **78**, 775 (1997).

[107] A.A. Andronov, E.A. Leontovich, J.I. Gordon and A.G. Majer, *Theory of bifurcations of dynamic systems on a plane*, Wiley, New York, 1973. M. Argentina *Ph. D. Thesis*, Nice 1999.

[108] P. Coullet, T. Frisch, J.M. Gilli and S. Rica. Chaos 4, 485 (1994).

[109] J.R. Tredicce, F.T. Arecchi, G.L. Lippi, and G.P. Puccioni, J. Opt. Soc. of Am. **B2**, 173 (1985).

[110] J.D. Murray, *Mathematical Biology*, Springer-Verlag, Berlin, (1989).

[111] M. Feingold, D. Gonzalez, O. Piro, H. Viturro , Phys. Rev. A **37**, (1988).

[112] R.Benzi, A.Sutera, and A. Vulpiani, J. Phys. A**14**, 453 (1981).

[113] C. Nicolis and G. Nicolis, Tellus **33**, 225 (1981).

[114] G. Giacomelli, F. Marin, and I. Rabbiosi, Phys. Rev. Lett. **82**, 675 (1999).

[115] A.M. Yacomotti, M.C. Eguia, J. Aliaga, O.E. Martinez, G.B. Mindlin, A.Lipschitz, Phys. Rev. Lett. **83**, 292, (1999).

[116] E. Ott, T. Sauer, J.A. yorke, *Coping with chaos*, Wiley series, John Wiley Son, 1994

[117] S.E. Hodges, M. Munroe, W. Gadomski, J. Cooper and M. G. Raymer, J. Opt. Soc. Am. B **14**, 180 (1997).

[118] A.T. Ryan, G.P. Agrawal, G.R. Gray and E. Gage, IEEE J. Quantum Electron. **30**, 668 (1994).

[119] J.Y. Wang and P. Mandel Phys. Rev. A **48**, 671 (1993).

[120] G. Huyet, S. Hegarty, M. Giudici, B. de Bruyn, J.G. McInerney. Europhys. Lett. 40, 619-624 (1997).

[121] H. Risken and K. Nummedal, J. Appl. Phys. **39**, 4462 (1968); V. Benza and L. A. Lugiato, Z. Phys. B **35**, 383 (1979).

[122] I. Fisher, G.H.M. Van Tarwijk, A.M Levine, W. Elasser, E. Göbel, D. Lenstra, Phys. Rev. Lett. **76**, 220 (1996).

[123] A. Duarte, H. Solari, Phys. Rev. A **58**, 614 (1998).

[124] A. Duarte, H. Solari, Phys. Rev. A. **60**, 2403 (1999).

[125] P. Zorabedian, W.R. Trutna Jr., and L.S. Cutler, IEEE J. of Quant. Electron. **QE23**, 1855 (1987).

[126] C. Yan, X. Wang, J. McInerney, IEEE J. of Quant. Electron. **QE32**, 813 (1996).

[127] M.G. Boshier, D. Berkeland, E.A. Hinds, V. Sandoghdar, Opt. Commun. **85**, 355 (1991).

[128] Z.M. Chuang, D.A. Cohen, L.A Coldren, IEEE J. of Quant. Electron. **QE26**, 1200 (1990).

[129] H. Li, A. Hohl, A. Gavrielides, H. Hou and K.D. Choquette, Appl. Phys. Lett. **72**, 2355 (1998).

[130] N.A. Loiko, A.V. Naumenko and N.B. Abraham, Quantum and Semiclass. Opt. **10**, 125 (1998).

[131] C. Masoller and N.B. Abraham, Phys. Rev. **A59**, 3021 (1999).

[132] J. Jewell, Laser Focus World (May 1990), p. 151.

[133] U. Fiedler and K.J. Ebeling, IEEE J. Selected Topics in Quantum Electron. **1**, 443 (1995).

[134] Y.C. Chung and Y.H. Lee, IEEE Photon. Technol. Lett. **3**, 597 (1991).

[135] S. Jiang, Z. Pan, M. Dagenais, R.A. Morgan and K. Kojima, IEEE Photon. Technol. Lett. **6**, 34 (1994); S. Jiang, M. Dageanis and R.A. Morgan, IEEE Photon. Technol. Lett. **7**, 738 (1995).

[136] J.Y. Law and G.P. Agrawal, IEEE J. Selected Topics in Quantum Electron. **3**, 353 (1997).

[137] J. Sacher, W. Elsässer, and E. O. Göbel, Phys. Rev. Lett. **63**, 2224 (1989); J. Sacher, D. Baums, P. Panknin, W. Elsässer, and E.O. Göbel, Phys. Rev. **A 45**, 1893 (1992).

[138] D. Sukow, J. Gardner, and D.J. Gauthier, Phys. Rev. **A 56**, R3370, 1997.

[139] A. Hohl, H.J.C. van der Linden and R. Roy, Optics Lett. **20**, 2396 (1995).

[140] C.H. Henry and R.F. Kazarinov, IEEE J. of Quant. Electron. **QE22**, 294 (1986); D. Lenstra, Optics Commun. **81**, 209 (1991); J. Mork, M. Semkow, and B. tromborg, Electr. Lett. **26**, 609, (1990).